



**MONASH** University

# Aerodynamic Interactions Between Multiple Cyclists

**Nathan Barry**

*BAero Eng (Hons)*

A thesis submitted for the degree of Doctor of Philosophy at Monash University in 2015

Department of Mechanical and Aerospace Engineering



© The author 2015. Except as provided in the Copyright Act 1968, this thesis may not be reproduced in any form without the written permission of the author.

*I certify that I have made all reasonable efforts to secure copyright permissions for third-party content included in this thesis and have not knowingly added copyright content to my work without the owner's permission.*

## Declaration

This thesis contains no material which has been accepted for the award of any other degree or diploma at any university or equivalent institution and that, to the best of my knowledge and belief, this thesis contains no material previously published or written by another person, except where due reference is made in the text of the thesis.

Nathan Barry

September 2015

## Abstract

This research provides a detailed insight into the aerodynamic interactions that occur between cyclists. The force interactions between multiple cyclists are first identified for a range of practical scenarios and encompassing the scope of real world formations. This is followed by an investigation of the flow field around two cyclists in a tandem formation and how this flow structure differs from a single cyclist. Experiments included static cyclist models and extended through to pedalling athletes. As such this work also covers an insight into the dynamic flow behaviour of a cyclist that has not received significant focus previously.

Aerodynamic interactions are a fundamental component of cycling, with cyclists travelling in close proximity in many competition events as well as on the road. To date the investigation of aerodynamic interaction effects in cycling has been limited, especially regarding the flow field. This research sought to provide a more detailed understanding of aerodynamic interactions, the changes to forces and the flow mechanisms responsible.

Loads were measured on full scale cyclists, primarily athletes, in the Monash University large open-jet wind tunnel. Both tandem and transverse formations were studied. Following the quantitative mapping of force interactions, especially drag, a series of experiments were proposed to characterise the flow field around tandem cyclists. By identifying changes from the single rider wake profile, this would lead to an identification of the flow mechanisms responsible for the observed changes in drag. Full scale flow visualisation was conducted on a pair of athletes in tandem in the wind tunnel. This was followed by flow mapping using PIV in the Monash FLAIR water channel using replica reduced scale model cyclists to capture high resolution cross sections of the flow. Flow fields were then linked back to full-scale athletes by capturing wake profiles for a pedalling athlete in both single and tandem cases.

Force measurements showed that the drag of a cyclist varies as a strong function of relative spatial position. Positioned inline to the flow, at small separation there is a small drag saving for the lead rider (2.5%) and a large drag reduction for the trailing cyclist (40%). These reduce with increasing axial and lateral separation distance. Despite the large changes to the inflow conditions, the primary streamwise vortices formed from the hips of a cyclist remain dominant features in the wake of a trailing rider. Some reduction in peak streamwise vorticity was observed and this was found to be proportional to the reduction in streamwise velocity. However, the general distribution of the wake maintains similarity with the single rider case. The similarity in the wake conditions of the single and trailing rider indicate that the large drag reduction is not a product of disruption to the primary wake vortices. Instead it was found to be dominated by the reduction in streamwise velocity at the inlet for the trailing rider, thus reducing the momentum loss over the cyclist. As separation between the cyclists is increased, energy is recovered from the freestream and the inlet momentum impacting on the trailing rider is increased, thus the reduction in drag is smaller.

This research has provided a more detailed understanding of the aerodynamic interactions between cyclists. This understanding can be applied to better exploit the energy savings possible for riders travelling in groups and applied to both high performance and commuters alike. The case of multiple cyclist interactions also presents valuable insights for the study of interactions between other complex, and moving, geometry bluff bodies.



## Acknowledgements

My time at Monash University, both as an under-graduate and graduate student has been a challenging and rewarding experience. The completion of my thesis represents the culmination of many years of study. This feat would not have been possible without the support and contributions of many parties who have assisted me over the course of my candidature.

I would like to begin by issuing my sincerest thanks to my supervisors, Prof. John Sheridan, Mr David Burton and Dr Nick Brown, who have provided me with excellent guidance in all aspects of my research. It has been a privilege to work with such brilliant minds and I am grateful for the lessons they have taught me and the skills developed during my candidature. I would also like to extend this vote of thanks to Prof. Mark Thompson for his contributions as a part of the cycling aerodynamics group and an unofficial advisor.

Special thanks are also due to my colleague Timothy Crouch for his companionship and assistance in all manner of tasks over the course of both of our candidatures. Especially for many hours of assistance in the wind tunnel. Thanks also to Dr Martin Griffith for his contributions as a part of the cycling aerodynamics group at Monash. Thanks are also due to Nick Brown in his capacity at the Australian Institute of Sport along with David Martin for their ongoing commitment to our work in cycling aerodynamics.

I would like to express my deepest gratitude to the technical staff at the Monash University Wind Tunnel for their assistance and expertise in the construction of apparatus and execution of wind tunnel experiments; Steve Dunell, Michael Easton, Don McMaster, Greg Hewes, Gary Preston, Geoff McClure and Andrew Smith.

A note of thanks also to my post-doctoral friends and colleagues James Venning, James Bell, Damien McArthur, Matt Corallo, Derwin Parkin, András Nemes for their professional contributions, running of experiments and friendship over the course of my studies.

I am indebted to the athletes who volunteered their time and energy to participate in my research, without whom this would not have been possible.

On a more personal note, I would like to extend a heart-felt thanks to my parents, Martin and Karen, for their unwavering support. This has been a challenging undertaking and it would not have been possible without all that they have done for me; I can never thank you enough. Thanks also to my siblings, Reagan and Eleanor, for always being supportive of my pursuits. In addition I would like to thank my extended family for being a positive and supportive influence throughout my time as a student.

I would like to thank my friends and extended cycling family who have been a positive influence throughout my athletic and academic career and who have provided motivation, support and friendship over many years. I would like to make special mention to Tom Leaper, Tom Rodgers, Nathan Buschkuehl, Kane Butcher, Jamie Meyer and Wade Edwards for their individual contributions.

This project was financially supported under the Australian Research Council's Linkage Project Scheme (Project Number LP130100955). I would also like to acknowledge the financial contributions of the AIS and Australian Sports Commission. Manufacturing support was also provided to this project by the Melbourne Centre for Nanofabrication.

Finally, I would like to thank the Department of Mechanical and Aerospace Engineering for their financial support and the members of the department for their assistance during my candidature.

## Publications

Barry, N, Burton, D, Crouch, T, Sheridan, J and Luescher, R, 2012, Effect of crosswind and wheel selection on the aerodynamic behaviour of a cyclist, *Procedia Engineering*, 34, p 20-25, DOI:10.1016/j.proeng.2012.04.005

Barry, N, Burton, D, Sheridan, J and Brown, NAT, 2014, The effect of spatial position on the aerodynamic interactions between cyclists, *Procedia Engineering*, 72, p 774-779, DOI:10.1016/j.proeng.2014.06.131

Barry, N, Burton, D, Sheridan, J and Brown, NAT, 2014, Aerodynamic performance and riding posture in road cycling and triathlon, *Proc. IMech, Part P: Journal of Sports Engineering and Technology*, DOI: 10.1177/1754337114549876

Barry, N, Burton, D, Sheridan, J, Thompson, M and Brown, NAT, 2015, Aerodynamic drag interactions between cyclists in a team pursuit, *Sports Engineering*, 18(2), p 93-103, DOI: 10.1007/s12283-015-0172-8

Barry, N, Burton, D, Sheridan, J and Brown, NAT, 2014, Flow interactions between two inline cyclists, *19<sup>th</sup> Australian Fluid Mechanics Conference*, Melbourne, Australia



# Nomenclature

## General

A	Frontal Area
C	Cyclist torso chord length
$C_{DA}$	Drag coefficient Area
$C_D$	Drag coefficient
$C_P$	Pressure coefficient
D	Drag Force
H	Cyclist height
L	Bicycle length
$P_{T,\infty}$	Freestream total pressure
$P_T$	Local total pressure
$r_{x,y}$	Correlation coefficient for two variable x and y
$U_\infty$	Freestream streamwise velocity
U	Streamwise velocity
V	Spanwise velocity
W	Vertical velocity
y	Lateral distance from centreline
z	vertical height above ground plane

## Martin Power Equation

$P_{TOTAL}$	Cyclist total output power
$P_{AR}$	Power due to aerodynamic resistance
$P_{RR}$	Power due to rolling resistance
$P_{WB}$	Power due to wheel bearing friction
$P_{PE}$	Power due to changes in potential energy
$P_{KE}$	Power due to changes in kinetic energy
$E_C$	Chain and driveline efficiency factor
$V_a$	Air velocity
$V_g$	Velocity relative to the ground
$F_W$	Rotational aerodynamic drag coefficient of bicycle wheels
$G_R$	Road gradient
$\mu$	Tyre coefficient of rolling resistance
$m_T$	Total system mass
g	Gravity
$V_{G,i}$	Ground velocity - initial
$V_{G,f}$	Ground velocity – final
$t_i$	Time – initial
$t_f$	Time - final

## Greek Symbols

$\rho$	Air density
$\Delta$	Change in $\Delta C_D A$ between individual and team tests

## Mannequin Dimensions

$\theta$	Crank angle
$\psi$	Knee angle
$\phi$	Hip angle
$\alpha$	Torso angle of attack
$\tau$	Upper arm angle
$\eta$	Elbow angle
$\beta$	Neck angle
HG	Helmet to back gap
Hip <sub>x</sub>	Hip axial location relative to crank centre
Hip <sub>y</sub>	Hip vertical location relative to crank centre
WB	Wheelbase
C	torso chord
HW	Helmet width
SW	Shoulder width
HipW	Hip Width
ES	Elbow Spacing
U <sub>arm,<math>\phi</math></sub>	Upper arm diameter
F <sub>arm,<math>\phi</math></sub>	Forearm diameter
U <sub>leg,<math>\phi</math></sub>	Upper leg diameter
L <sub>leg,<math>\phi</math></sub>	Lower leg diameter

## Tandem Body Open Jet Wind Tunnel Corrections

$\epsilon_S$	Jet expansion factor
$\epsilon_N$	Induced velocity at model due to nozzle blockage
$\epsilon_C$	Induced velocity at the model due to collector blockage
$\epsilon_Q$	Velocity perturbation at the nozzle due to model proximity
$\epsilon_W$	Velocity perturbation at collector due to model proximity
$\tau$	Tunnel shape factor
A <sub>M</sub>	Model frontal area
A <sub>N</sub>	Nozzle area
A*	Effective nozzle area due to jet deflection
A <sub>C</sub>	Collector Area
b	Constant for far field wake effects
C <sub>D</sub>	Measured drag coefficient of model
G	Glauert Factor
L <sub>M</sub>	Model length

$R_N$	Nozzle effective radius $R_N = \sqrt{\frac{2 A_N}{\pi}}$
$R_C$	Collector effect radius $R_C = \sqrt{\frac{2 A_C}{\pi}}$
$V_M$	Model volume
$t$	Model thickness
$x_S$	Source location for nozzle blockage effects
$x_M$	Model location – distance downstream of nozzle exit of model centre
$x_{LE}$	Distance of model leading edge downstream of nozzle exit
$x_{TE}$	Distance from model trailing edge to collector



# Table of Contents

Abstract	iii
Acknowledgements	v
Publications	vii
Nomenclature	ix
<b>Introduction</b>	<b>1</b>
<b>1. Literature Review</b>	<b>5</b>
1.1 Introduction to Cycling Aerodynamics	5
1.1.1 Aerodynamic Drag in Cycling	7
1.1.2 Power Requirements in Cycling	8
1.1.3 The Influence of Cycling Posture	9
1.1.4 The Influence of Cycling Equipment	11
1.2 The Flow Field Around a Cyclist	13
1.3 Multiple Body Aerodynamic Interactions	19
1.3.1 Fundamental Bluff Body Interactions	19
1.3.2 Ground Vehicle Interactions	22
1.3.3 Aerodynamic Interactions in Cycling	24
1.4 Summary	33
<b>2. Methodology</b>	<b>35</b>
2.1 Monash University Wind Tunnel	36
2.2 Flow Corrections for Tandem Bodies in an Open Jet Wind Tunnel	38
2.2.1 Finite Stream Effects	38
2.2.2 Applications to Multiple Tandem Bodies	42
2.3 Cyclist Mounting and Force Measurement	45
2.3.1 Single Rider Cycling Rig	45
2.3.2 Multi-Rider Cycling Rig	48
2.3.3 Repeatability of Drag Measurements	53
2.4 Monash University FLAIR Water Channel	54
2.5 Equipment and Apparatus	57
2.5.1 Four Hole Pressure Probe	57
2.5.2 Dynamic Pressure Measurement System	58
2.6 Test Subjects	60
2.6.1 Athlete Participants	60
2.6.2 Monash Anthropomorphic Cycling Mannequin	61

2.7	Specific Experimental Methodology	64
2.7.1	Effect of Rider Dynamics on Cyclist Drag	67
2.7.2	Force Variation for Drafting Cyclists	69
2.7.3	Force Variation for Overtaking Cyclists	72
2.7.4	Geometry Effects on Drag Interactions	73
2.7.5	Full Scale Flow Visualisation	75
2.7.6	Scale Model Flow Measurements	76
2.7.7	Cyclist Forward Interference	79
2.7.8	Dynamic Athlete Wake Analysis	80
<b>3</b>	<b>The Effect of Leg Dynamics</b>	<b>87</b>
3.1	Static vs Dynamic Drag for a Single Cyclist	87
3.2	The Effect of Leg Dynamics in Two Cyclist Formations	90
3.2.1	Tandem Formation	90
3.2.2	Transverse Formation	91
<b>4</b>	<b>Force Interactions Between Multiple Cyclists</b>	<b>93</b>
4.1	Drafting	93
4.1.1	Phase 1	93
4.1.2	Phase 2	95
4.1.3	Comparison with Literature	98
4.2	Overtaking	99
4.3	The Effect of Geometry on Drag Interactions	104
4.3.1	Drag in a Team Pursuit	104
4.3.2	Influence of the Team Environment on Individual Rider Drag	106
4.3.3	Drag Interplay between Cyclists in a Team Pursuit	109
4.3.4	Statistical Correlation of Drag Interactions between Cyclists	112
<b>5</b>	<b>Flow Topology In A Two Rider Tandem Formation</b>	<b>115</b>
5.1	Full Scale Flow Visualisation of Two Cyclists in Tandem	116
5.2	Velocity fields of scale tandem cyclists	123
5.2.1	Validation of Scale Model Technique	123
5.2.2	Streamwise Vorticity in the Wake of Tandem Cyclists	125
5.2.3	Centreline Streamwise Velocity Profiles in Tandem Formations	130
5.2.4	Flow Between Two Tandem Cyclists	135
5.3	Forward Interference Field of a Cyclist	143
5.4	Wake Topology of Dynamic Athletes	145
5.4.1	Time Averaged Wake Profiles	145
5.4.2	Spectral Analysis of the Dynamic Wake	155
5.4.3	Phase Averaged Wake Profiles	162

5.5	Pressure Distribution in the Wake of a Dynamic Athlete	174
5.5.1	Time Averaged Wake Pressure Profile	174
5.5.2	Spectral Analysis of the Dynamic Wake	175
5.5.3	Wake Profiles of a Static Cyclist	181
5.5.4	Phase Averaged Wake Profiles	185
5.5.5	Modal Decomposition of the Dynamic Cyclist Wake	193
<b>6</b>	<b>Conclusions</b>	<b>199</b>
6.1	Major Findings	199
6.1.1	Drag Variation with Relative Spatial Position	199
6.1.2	Flow Field Around Two Tandem Cyclists	199
6.1.3	Mechanisms Responsible for Drag Reduction in a Tandem Formation	203
6.2	Secondary Findings	205
6.2.1	The Influence of Geometry Interactions on Cyclist Drag	205
6.2.2	Postural Effects on the Wake of a Cyclist	206
6.3	Recommendations	207
	<b>References</b>	<b>209</b>
	<b>Appendices</b>	<b>215</b>
	Appendix A: Validation of Wind Tunnel Corrections for Multiple Tandem Cyclists	215
	Appendix B: Calibration of Force Balance Rigs	217
	Appendix C: Athlete Participant Images	219
	Appendix D: Aerodynamic Loads on Cyclists in a Tandem Formation	220
	Appendix E: Velocity Profiles in the Wake of Scale Model Cyclists	222
	Appendix F: Streamwise Vorticity in the Wake of Scale Model Cyclists	228
	Appendix G: Peak and Mean Vorticity in the Wake of a Scale Model Cyclist	230
	Appendix H: Power Spectral Density in the Wake of a Cyclist	231
	Appendix J: Phase Averaged Wake of a Pedalling Cyclist	235
	Appendix K: The Effect of Posture on the Wake of a Cyclist	237



# Introduction

Cycling aerodynamics is a unique case within bluff body aerodynamics due to the complex and dynamic geometry of an athlete. An understanding of cycling aerodynamics is critical to performance as aerodynamic drag is the dominant form of resistance acting on a cyclist, even at recreational speeds. As a result, there has been considerable investigation into the influence of posture and equipment on the drag of a cyclist as this has specific performance applications. Only recently has the flow field around a cyclist been studied in greater detail. This has highlighted just how complex the flow around a cyclist truly is.

The majority of existing work has studied a cyclist in isolation. This is useful for specific individual events such as time trials and pursuits. However, the vast majority of road cycling events are mass start races. This is in addition to mass start track events as well as team specific events such as the team pursuit on track or team time trial on the road. For this reason, it is necessary to consider how the aerodynamics of a cyclist are influenced by the presence of other cyclists in close proximity. It has been known, anecdotally, by cyclists for over a century that travelling in the wake of another cyclist or vehicle requires significantly less effort than riding in isolation. The case of drafting cyclists has been investigated previously, but a detailed understanding of the forces involved in drafting and overtaking cyclists is still incomplete. Furthermore there has been very little consideration of the flow field surrounding multiple cyclists.

A better understanding of aerodynamic interactions in cycling has the potential to better optimise the performance of athletes and provided more informed tactics involved in team and mass start events. There are also applications for optimising the efficiency of commuters working together. More generally, an understanding of cycling interactions has potential applications to other complex and dynamic geometry bluff bodies.

It is with this motivation the primary question governing this research was derived;

*How are the aerodynamics of a cyclist influenced by the presence of another rider?*

For the purposes of this research this question was dissected into two distinct branches. Firstly, it was necessary to understand and identify the changes in drag that occur for cyclists travelling in group formations. This then leads into consideration of the flow field around multiple cyclists and how it differs from the single rider case. From this it is intended to identify the flow mechanisms responsible for the observed changes in drag. Following this direction the project is refined into several specific research questions;

*How does cyclist drag vary as a function of relative spatial position?*

*How does cyclist geometry and posture influence drag interactions within a team?*

*How does the presence of another rider influence the flow field around a cyclist?*

*What flow mechanisms are responsible for the observed changes in drag?*

*How does the dynamic leg motion of cycling influence the aerodynamics of a cyclist and interactions with others?*

The final question arises from a specific peculiarity of cycling; pedalling legs mean that the geometry is dynamic. This differs dramatically from most bluff bodies which are generally a static geometry with the exception of vehicle wheels or control surfaces. Recently, quasi-static investigations (Crouch et al. 2014) have shown that the leg movement has a significant effect on the aerodynamics of a cyclist. It is therefore necessary to consider how the leg dynamics influence the interactions between multiple cyclists.

The experimental investigations within this thesis were designed in such a way as to answer these questions. The organisation of this thesis is summarised briefly below:

### ***Chapter 1***

A review and analysis of the relevant literature relating to interactions in cycling. This starts with an introduction to the history of aerodynamic evolution in cycling and the study of rider posture and equipment. This is followed by a review of the flow field characterised for a single cyclist. A discussion of literature surrounding bluff body interactions from simplified bodies such as quasi-2D cylinders to ground vehicles is then presented. This chapter closes with a detailed review of previous work on the interactions between multiple cyclists.

### ***Chapter 2***

Description of the apparatus and methodology employed in the various experimental techniques used in this research. Apparatus are discussed first, followed by details of the individual experiments.

### ***Chapter 3***

A preliminary look at the influence of leg position on force interactions between two cyclists and the effect of pedalling legs compared to static. This is important due to potential implications in further experimental work regarding the use of static or dynamic cyclists.

### ***Chapter 4***

A quantitative investigation of the aerodynamic force interactions between two cyclists in close proximity. Cyclists in both drafting and overtaking scenarios are considered. The effect of changing cyclist geometry through posture and interplay between riders is also investigated. This is presented as a case study within the context of a 4 rider pursuit team.

## ***Chapter 5***

A detailed series of investigations designed to build collective knowledge towards the characterisation of the flow field around two cyclists in a tandem formation. Several experimental techniques are utilised including full scale visualisations, scale model flow mapping and wake surveys of pedalling athletes.

## ***Chapter 6***

A summary of the major findings from the experimental investigations and recommendations for future work that would further the understanding of aerodynamics interactions in cycling.

## ***Appendices***

Supplementary data and results from experimental investigations. Includes details of calibrations relating to wind tunnel apparatus.



# Chapter 1

## Literature Review

This chapter reviews the important literature relevant to aerodynamic interactions between cyclists. The significance of aerodynamics in cycling and the motivation for research in this area is first addressed, including a discussion of the fundamental equation governing cycling performance. This leads on to the two key parameters influencing cycling aerodynamics; equipment and athlete posture. Following from this the complex flow field around a cyclist is discussed. This covers the current knowledge base established for the aerodynamics of a single cyclist. Subsequent sections will review literature relating to cycling interactions; beginning with fundamental bluff bodies, followed by ground vehicle interactions and finally a comprehensive review of the limited work presently available on cycling interactions. This will make clear the limitations of current understanding relating to the aerodynamic interactions in cycling and provides context for the scope and direction of this research.

### **1.1 Introduction to Cycling Aerodynamics**

Although academic interest in cycling aerodynamics has only garnered attention in the past three decades, an anecdotal understanding of the importance of aerodynamics to cycling dates back to the end of the 19<sup>th</sup> century. In 1896 E. E. Anderson rode a mile in 1 minute and 3 seconds drafting behind a locomotive carriage (Kyle & Weaver 2004). Later in 1912 a streamlined enclosure for a bicycle was patented by Frenchman Etienne Bunau-Varilla, which was used to set numerous records. In 1933 the first recumbent bicycle was built, which went on to break several human powered speed records (Gross et al. 1983). It was due to these radical changes to bicycle design that, in 1938, cycling's governing body, the Union Cycliste Internationale (UCI), introduced a rule that prevented any modifications to the traditional racing bicycle for aerodynamic advantage. This rule was subsequently revoked in 1976, allowing for renewed research into advancing cycling performance through aerodynamics. The first major change was the introduction of the disk wheel, which was derived from aeronautical research from the WW1 period on exposed biplane undercarriages (Zdravkovich 1992).

The first major adaptation to the traditional riding posture came in the 1989 Tour de France, when Greg LeMond used a set of aerobars and faired helmet during the final time trial to move into first place overall and win the Tour by only 8 seconds. These bars had been developed for triathlons and significantly changed the way a cyclist was positioned on the bike. This marked a turning point in cycling and the start of major investigations and improvements in cycling aerodynamics. Since that time testing and publication of cycling has focussed on the measurement of drag on a rider as a function of posture or component changes. Until recently, there has been a lack of understanding of the flow field surrounding a cyclist or the mechanisms responsible for cyclist drag. The flow around a

cyclist is complex due to the geometry. It is also unsteady, resulting from the dynamics of the legs, and consists of large separated regions (Crouch et al. 2012, 2014).

A prime example of the influence of aerodynamics on cycling performance is the improvement observed in the world hour record. The UCI has an official record for the furthest distance that a cyclist can cover in a single hour. A summary of the hour record is shown in Figure 1.1.1 below. As previously mentioned, until 1976 the UCI had a ruling in place that prevented the modification of the bicycle and equipment for the purpose of aerodynamic improvement. As a result, there was very little difference in bicycle and equipment used in record attempts until this time. After 1976 significant changes could be made to the bicycle and cyclist. This is evident from the evolution of the record, which shows a steep increase after 1980. In the period from 1976 to 1997 there were significant advances in cycling aerodynamics, which incorporated aerofoil shaped bicycle tubes, disk wheels, faired helmets and handlebar setups that allowed dramatic changes to the posture of the cyclist on the bicycle.

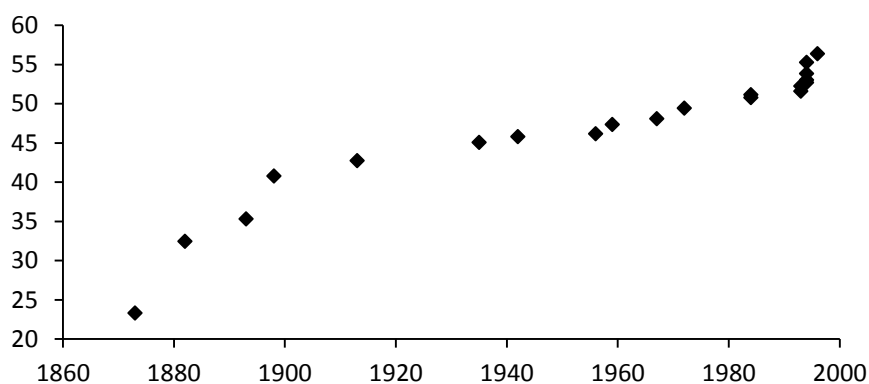


**Figure 1.1.1** - Progression of the world hour record in cycling with time

The first major change to riding posture was triathlon style aerobars, as used by Greg LeMond in the 1989 Tour de France. These bars bring the athlete's arm in front of the torso, inspired by a downhill ski posture. This posture is the basis for modern day time trial and pursuit postures. Two other more radical postures were pioneered by Graeme Obree during the early 1990's. The first had his arms tucked underneath his chest and used a custom bicycle. Using this posture Obree set the hour record twice, in addition to several other world records. The second was termed the 'superman' posture, which positioned the arms stretched out straight in front of the body. This posture was used by other riders, including Chris Boardman in setting the longest recorded distance to date of 56.375 km in 1996. Both of these postures have since been banned by the UCI from all forms of competition (Union Cycliste Internationale, Kyle & Weaver 2004).

The change observed in the trend of the hour record caused the UCI to again change the rules in 1997. This split the hour record into two separate categories. The 'UCI Hour Record' was amended such that riders must compete using equipment equivalent to that used by Eddy Merckx in 1972. This was the last hour record set on a traditional style road bike with circular cross section steel tubing, curved drop handlebars and wire spoke wheels. A second record was then established for the 'Best Human Effort'. This was the ultimate distance record and allowed for aerodynamically optimised equipment and postures. The standing hour record, set by Chris Boardman (56.375 km) was subsequently downgraded to best human effort, as it utilised the superman position, a carbon frame with aerofoil

tubing, a faired front wheel, rear disk and faired helmet. With the introduction of this new ruling, the record holder, Boardman, then set a new hour record by competing on a traditional style bicycle similar to that used by Merckx in 1972. He accomplished 49.491 km in the hour, eclipsing Merckx's mark by only 10m. This highlights how significant the role of aerodynamics is to cycling performance, not only equipment but also posture.

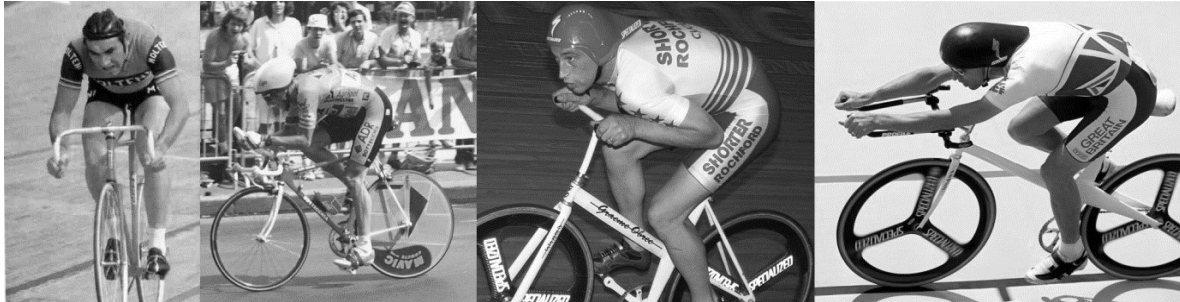


**Figure 1.1.2** - (L-R) Eddy Merckx in traditional posture and equipment, Greg LeMond using triathlon style aerobars in Le Tour de France 1989, Graeme Obree posture, 'Superman' posture

### 1.1.1 Aerodynamic Drag in Cycling

The aerodynamic resistance of a cyclist is described by the equation for aerodynamic drag. This states that the drag force acting on a body ( $D$ ) is a function of the non-dimensional drag coefficient ( $C_D$ ), the projected frontal area ( $A$ ) and the dynamic pressure. Dynamic pressure is itself a function of density ( $\rho$ ) and the relative freestream air velocity ( $V$ ). Both of these are affected by environmental conditions including temperature, pressure, speed and wind direction (Munson et al. 2006).

The non-dimensional drag coefficient is effectively a factor for how streamlined a given body appears to the oncoming wind. Therefore both frontal area and drag coefficient are athlete- dependent factors. Given that the frontal area will vary with posture on the bicycle, it is best practice in cycling to express normalised cyclist drag as the drag coefficient-area product ( $C_D A$ );

$$C_D A = \frac{D}{\frac{1}{2}\rho V^2} \tag{1.1.1}$$

As aerodynamic drag is a function of velocity and density these parameters will affect the resistance acting on a cyclist. It is for this reason that the majority of cycling records were recorded at high altitude, as the lower density decreases the dynamic pressure acting on the cyclist for the same ground speed.

The velocity in Equation 1.1.1 refers to air velocity of the cyclist. As road cyclists are exposed to environmental winds, the air velocity can differ from the cyclist's ground speed. Atmospheric winds can also induce yaw angle on the total wind vector. For ground vehicles yaw angle has been shown to

affect the side force, roll moment and yaw moment as well as drag (Baker 1991). This has also been shown to apply to cycling (Barry et al. 2012).

In experimental investigations cyclist drag is normalised by dynamic pressure in order to eliminate the effect of small fluctuations. This is particularly relevant to wind tunnel investigations. However, testing at Monash University has shown that  $C_D A$  can vary with velocity and is not constant over the range of speeds observed in elite cycling. This is in fact due to a change in  $C_D$  due to Reynolds number sensitivity and is seen for many bluff bodies (Achenbach 1971). Variation of drag with velocity is also dependent on surface treatment of the cyclist. It is therefore necessary to conduct aerodynamic testing at relevant wind speeds when analysing cycling performance.

Kyle and Burke (1984) performed early investigations into cycling aerodynamics and identified the components and areas that had a significant effect on performance; eg. posture, altitude, wheels, tyres, helmets, bicycle frame and wheel size. Four pathways were identified to reduce the drag acting on the cyclist system. These apply to both cyclist and equipment; reduce the frontal area, streamline the body, optimise the surface roughness and relocate components to hide them from the wind.

Kyle and Burke also performed isolated bike tests, which showed that the drag of a bicycle in isolation is 31-39% of the drag of a rider and bicycle combined. However, it was noted by the authors that this neglects any interference effects and parasitic drag. As the presence of the cyclist has a large effect on the flow field around the bicycle, the bicycle and rider can not be treated independently (Gibertini & Grassi 2008). Nevertheless, this result shows that the cyclist is the major contributor to drag acting on the system. This is unsurprising given the relative volume and area of the cyclist is far greater than that of the bicycle. Hence, there is greater potential for performance improvement from modifying the rider posture. This reflects the progression observed in the hour record, where dramatic changes in cyclist posture had a profound impact on the distance covered.

### **1.1.2 Power Requirements in Cycling**

Martin et al. (1998) presented a mathematical model for cycling power, including a validation against real world cycling performance. Previous studies (Davies 1980, Di Prampero et al. 1979, Kyle 1988, Olds et al. 1995, 1993) had proposed power models, but Martin et al.'s differed in that the development of accurate, portable power meters for bicycles enabled a validation against on-road data. Validation against a series of road tests with 6 athletes revealed a correlation function of 1.00 and an  $R^2$  value of 0.97 for fit to the linear function.

Five terms were identified as sources of resistive power acting against the motion of a cyclist. Aerodynamic resistance (AR) accounts for the aerodynamic drag acting on the cyclist and will typically be the dominant term in the power equation. This includes the rotational drag of the spinning wheels. Introducing two velocity terms for the air speed ( $V_a$ ) and ground speed ( $V_G$ ) makes it possible to account for environmental winds changing the effective velocity of the cyclist. This can also be used to account for induced yaw angle in the difference in direction between the air and ground vectors. The rolling resistance (RR) is the resistance due to the tyres' contact with the road surface and is a

function of surface friction and mass. Wheel bearing friction (WB) is derived from an empirical function and modelled on the work of Dahn et al. (1991), where torque in the bearings is a linear function of rotational velocity. The potential energy term (PE) accounts for energy changes due to altitude change and is proportional to the gradient. The final term is the kinetic energy term (KE) which accounts for the energy expenditure during acceleration phases. A chain efficiency factor ( $E_C$ ) is also included to account for losses in the mechanical drive line of the bicycle. In its simplest form, the equation can be presented as;

$$P_{TOTAL} = (P_{AR} + P_{RR} + P_{WB} + P_{PE} + P_{KE}) / E_C \quad 1.1.2$$

$$P_{AR} = \frac{1}{2} \rho (C_D A + F_W) V_a^2 V_G$$

$$P_{RR} = V_G \cos(\tan^{-1} G_R) \mu m_T g$$

$$P_{WB} = V_G (91 + 8.7 V_G) 10^{-3}$$

$$P_{PE} = V_G m_T g \sin(\tan^{-1} G_R)$$

$$P_{KE} = \frac{1}{2} m_T \frac{(V_{G,f}^2 - V_{G,i}^2)}{(t_i - t_f)}$$

This equation represents a complete model of cycling power. However, for many applications this model can be simplified in order to show the effect of aerodynamic drag on cycling performance by representing changes in  $C_D A$  as cycling power. Taking a steady state riding condition on a flat road and still conditions, this equation reduces to a function of only the drag coefficient-area ( $C_D A$ ), ground velocity ( $V_G$ ), system mass ( $m_T$ ) and the tyre coefficient of rolling resistance ( $\mu$ ). Given these conditions and using typical values for elite cyclists it can be calculated that aerodynamic drag will be the dominant form of resistance above 10 km/h; above 45 km/h drag is over 90% of total resistance.

### 1.1.3 The Influence of Cycling Posture

It has already been indicated that the posture of a cyclist significantly affects their aerodynamics and subsequently their performance. As a result, this has been previously investigated by numerous authors (see Zdravkovich et al. 1996, Grappe et al. 1997, Gibertini and Grassi 2008, Gibertini et al 2008, Oggiano et al. 2008, García-López et al. 2008, Defraeye et al. 2010, Underwood et al 2011, Chabroux et al. 2012, Underwood and Jermy 2013). Four general postures are most commonly identified in literature; hands on the flats of bars sitting upright (climbing posture), hands on the brake levers in conventional riding posture (hoods posture), traditional racing posture with hands on the lower curved part of the handlebars (drops posture) and a time trial posture (Figure 1.1.3). The time trial posture is analogous to that used by Greg LeMond (see Figure 1.1.2 above). It is considered the optimal riding posture for a cyclist (under current regulations). However, the time trial posture utilises different bicycle geometry and setup to a traditional road bicycle, which allows the rider to adopt a posture with their arms in front of the torso. Literature has consistently found the same relative

ranking of these postures in terms of aerodynamic performance. The time trial posture has the lowest drag, followed by, in order of lowest to highest drag, the drops posture, hoods posture and climbing posture. However, whilst this ranking is consistent in literature, the drag of a cyclist in each posture differs dramatically. This is summarised in Table 1.1.1 below which highlights the  $C_D A$  for a cyclist in the drops and hoods postures from available literature.



**Figure 1.1.3** - Four key cycling postures as commonly identified in literature (Gibertini et al. 2008).  
L-R Climbing, hoods, drops, time trial.

**Table 1.1.1** - Summary of literature investigations of the aerodynamics of road cyclists

	Posture	$C_D A$	Technique		Wind Speed ( $\text{ms}^{-1}$ )	Blockage
Kyle & Burke	Drops	0.32	Wind Tunnel	Static	8.9 – 15.6	
Zdravkovich et al.	Hoods	0.26 – 0.38	Wind Tunnel	Static	8.2	12.4-16.2 %
	Drops	0.23 – 0.34				
Gibertini & Grassi	Drops	0.275–0.289	Wind Tunnel	Dynamic	13.9	< 5%
Defraye et al.	Drops	0.243	Wind Tunnel	Static	10 - 20	6%
Davies	Drops	0.280	Wind Tunnel	Dynamic	1.5 - 18.5	
Ménard et al.	Drops	0.370	Wind Tunnel			
Grappe et al.	Drops	0.276	Constant Power	Dynamic		
Capelli et al.	Drops	0.251	Towed Dynamometer	Dynamic	8.6 – 14.6	
Di Prampero et al.	Drops	0.308	Towed Dynamometer		5 – 16.5	
Gross et al.	Drops	0.300-0.319	Coast Down			
Kyle and Edelman	Drops	0.272	Coast Down			

Table 1 shows that values of  $C_D A$  for a given posture vary significantly between studies. This is primarily due to differences between the athletes. Whilst all will be in relatively similar postures on the bike, the size and geometry of each individual can have a large influence over the drag acting on the cyclist. Size and geometry affect an athlete's frontal area, but other differences such as limb size, anthropomorphic dimensions, musculature, flexibility etc. can all result in subtle changes to the flow around a given athlete that result in drag differences for each individual. It is therefore evident that drag is athlete-specific. This was most obvious in the work by Zdravkovich et al. (1996) who reported the drag of 4 different postures for two different athletes given identical test conditions.

The experimental method used in the different studies can also contribute to differences in drag. Previous studies have used a range of field testing methods as well as wind tunnel tests. The advantage of wind tunnel testing for studying cycling aerodynamics is that it allows for much tighter control over the parameter space. Field tests are subject to high variability due to fluctuations in the natural atmosphere and environmental wind, as well as the motion of the cyclist. For this reason wind tunnels remain the most effective method for analysing cycling aerodynamics. By minimising the number of uncontrolled variables it is easier to isolate differences that are occurring specifically from a change to the cyclist setup, rather than the environment. This gives significantly lower uncertainty and better resolution. However, even for controlled wind tunnel tests, variations in method are present in terms of blockage effects, equipment used and the dynamics of the bicycle, wheels and athlete legs. Turbulence levels of the wind tunnel can also influence drag measurements but are not reported in many studies. Computational simulations (CFD) offer a very closed parameter space and are modern techniques are able to capture moving geometry of the legs. However, parametric investigations of dynamic bodies are computationally expensive and the model must be carefully validated. To date CFD studies of cycling have been inconsistent in obtaining the correct magnitude of drag on a cyclist (Blocken et al. 2012, Griffith et al. 2014).

Research on cycling posture has, to date, primarily focussed on drag force variation as this directly relates to performance. There has been far less attention to the flow field around a cyclist and how it varies with posture.

#### **1.1.4 The Influence of Cycling Equipment**

As the cyclist contributes the majority of the drag to the system, the greatest gains are typically made by optimising the posture of a cyclist. However, equipment gains can provide an additional advantage to optimisation of the rider. It has been shown that the choice of helmets, wheels, frame tube shape and clothing can all have a significant impact on the drag of a cyclist (Kyle & Burke 1984).

Using aerofoil shaped tubing on a bicycle rather than traditional round tubes has been shown to reduce total drag on the rider and system by up to 4% at zero degrees yaw angle (Kyle & Burke 1984). Significant improvements can also be made to the performance of traditional wire spoke wheels. This was first identified in aeronautical applications where fairings were used on biplane undercarriages during the First World War (Kyle & Burke 1984, Zdravkovich 1992). A fully faired wheel (disk wheel) offers significant drag reduction over an open spoke wheel (Sayers & Stanley 1994, Greenwell, et al. 1995, Tew & Sayers 1999). For wheel only tests this has been reported up to 70%. In some cases disk wheels have recorded zero drag and even propulsive force at yaw. However, when considering the real world performance of a wheel it is necessary to also look at the effect of yaw angle and its effect on other aerodynamic loads. Many studies has considered bicycle wheels in isolation, without bicycle or rider, and modelled them as a flat plate aerofoil with the yaw angle being an effective angle of attack. This defines the drag force as being parallel to the wind velocity vector; in the wind axis. However, in terms of cycling performance the important drag component is that acting against the cyclist's motion. Therefore drag should be defined as parallel to the ground velocity and not the air

velocity; in the body axis. As a result, bicycle drag tends to decrease at high yaw angles, especially for enclosed deep section wheels and disks (Greenwell et al. 1995, Barry et al. 2012). It is with the addition of yaw angle to the flow that such wheels offer the greatest drag reduction over conventional wheels. However, this drag performance comes at the expense of high side loads, in addition to roll and yaw moments. Whilst these do not directly factor into the performance equation of cycling, they do affect the handling and dynamics of the bicycle and can have severe detrimental effects on overall performance (Barry et al. 2012). In addition to the axial component of drag acting on a bicycle wheel, the rotational motion of the surface results in a rotational drag component. Jermy et al. (2008) and Forrester (2008) showed that the rotational component of drag can be significant and contribute resistance of similar magnitude to the axial component of aerodynamic drag. The majority of studies of bicycle wheels have been conducted on wheels in isolation. In reality the wheels are mounted in a frame and in close proximity to the large bluff body of the athlete and their moving legs. It has been shown that the behaviour of wheels as a part of the full cycling system can differ significantly from isolated wheel tests (Barry et al. 2012).

Helmet selection has also been shown to influence the drag of a cyclist. It has been shown that helmet performance is also influenced by the tilt angle of the head and yaw angle of the body (Blair & Sidelko 2008, Chowdhury et al. 2008). For faired helmets with a teardrop shaped tail, the head tilt angle can nullify any reductions in drag over a conventional style helmet (Blair & Sidelko 2008). Under optimum setup helmets can reduce drag by up to 7% for a mannequin torso. Note that this study used a cyclist torso only. Therefore the percentage reduction will be smaller when referencing against a full cyclist system. The same authors also showed that there is significant variation in performance between helmets of similar faired teardrop shape. Chabroux et al (2010) conducted stereoscopic PIV measurements on the flow behind a time trial helmet. The setup used a mannequin and full bicycle system. They found that flow conditions over the back are influenced by the shape of the helmet. This has more complex implications as helmet selection appears to be able to influence the wider flow field of the rider. They show that isolated helmet tests will not capture the proper flow behaviour that occurs as a result of interactions with the flow over the cyclist's back and shoulders. For this reason, helmet selection can be very much athlete and posture specific.

Kyle and Burke (1984) reported that clothing selection, such as the use of a skin suit, can potentially reduce cyclist drag. Understanding of fundamental shapes such as cylinders shows that drag varies as a function of Reynolds number and surface roughness (Achenbach 1971). It follows that the performance of a cycling skin suit will vary with athlete geometry, velocity and surface treatment. An investigation of skin suits for speed skating revealed that design of a suit can significantly influence drag and that drag performance varies as a function of velocity (Saetran & Oggiano 2008).

In terms of equipment selection, changes to the wheels and bicycle can reduce cyclist drag largely irrespective of riding posture. Although the frame and wheels will be influenced by interactions from the rider, the primary influence is the moving legs, which will be present for any upper body posture. Therefore aerodynamic benefits arising from the frame and wheels will be independent of posture. By contrast, pieces of equipment on the cyclist, such as clothing and helmets, are linked closely with the flow over the rider. Therefore, such equipment will be influenced by the posture and size of the rider, as this varies the local flow conditions. As a result, the drag reductions arising from helmets and skin suits can differentially affect the performance of different athletes.

## 1.2 The Flow Field Around a Cyclist

A cyclist can generally be described as an aerodynamic bluff body (Gibertini & Grassi 2008) as a result of the large scale flow separation evident in the wake. They may more precisely be described as quasi-streamlined as the separation point occurs after the point of maximum thickness. Therefore, the major contributor to aerodynamic drag is the pressure force, specifically the low pressure drag from the wake. Despite the volume of research into cycling aerodynamics, there has, until recently, been little work to investigate the flow field around a cyclist. Crouch et al. (2012, 2014) conducted an in-depth study to characterise the flow structures around a cyclist in an effort to understand the origin of the aerodynamic forces at play.

Force measurements were conducted with the legs at different positions around the crank cycle. This revealed that the drag of a cyclist varies significantly as a function of leg position. A regular periodic function was observed such that drag was a minimum when the cranks were close to horizontal and the upper legs were level ( $15^\circ$ ). A maximum in drag was achieved for the case of one leg at its highest point and the other extended (see Figure 1.2.1). Crouch et al. defined the crank angle as the rotation of the crank anti-clockwise from horizontal with the left crank rearward at the zero point.

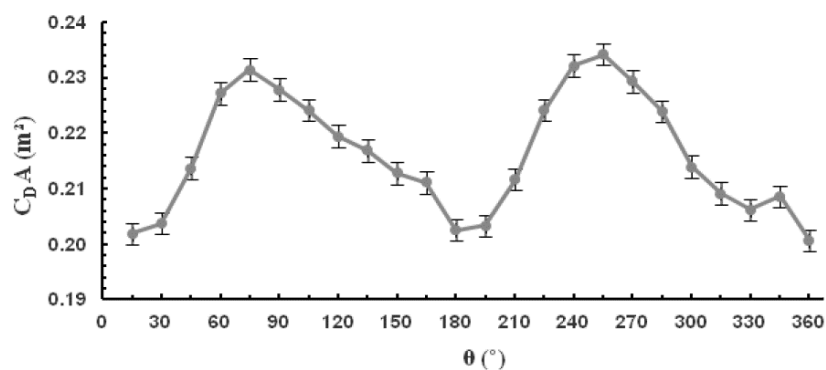


**Figure 1.2.1** -  $C_D A$  of a static cyclist as a function of crank angle position. Crank angle ( $\theta$ ) defined as the angle of rotation of the cranks anti-clockwise from horizontal with left crank rearward (From “Dominant flow structures in the wake of a cyclist,” Crouch et al. 2012 - Courtesy AIAA)

Wake surveys were conducted downstream of the Monash Anthropomorphic Cycling Mannequin at a range of leg positions around the crank cycle to investigate the effect of leg geometry (Crouch et al. 2014). Results showed that the wake of a cyclist can be divided into two key wake flow regimes. The first was a symmetric regime which occurred for crank angles where the upper legs were positioned level. The second was an asymmetric regime which was observed when the legs moved away from level. This asymmetry was most dominant at the extreme point with one leg at its highest point with minimum hip angle and the other leg extended. Correlating with their earlier force results it was observed that the symmetric regime corresponded to the minimum drag case, and the strong asymmetric regime with the high drag case.

The symmetric regime was found to only occur over a small range of crank angles when the upper legs are close to the level position. This is characterised by the wake at a crank angle of  $15^\circ$  where the

thighs are level. As the legs move away from the level point an asymmetry was found in the flow. This became stronger and more prevalent as the legs moved towards their extreme positions. This regime is best characterised by the most asymmetric leg position, with one hip closed and the other leg extended; occurring at a crank angle of  $75^\circ$  (and the opposite leg position at  $255^\circ$ ). The streamwise velocity and streamwise vorticity wake profiles are shown in Figures 1.2.2 and 1.2.3 below, with surveys being taken one torso chord length downstream of the rear of the rider. The interrogation region did not, however, encompass the whole wake down to the ground plane.

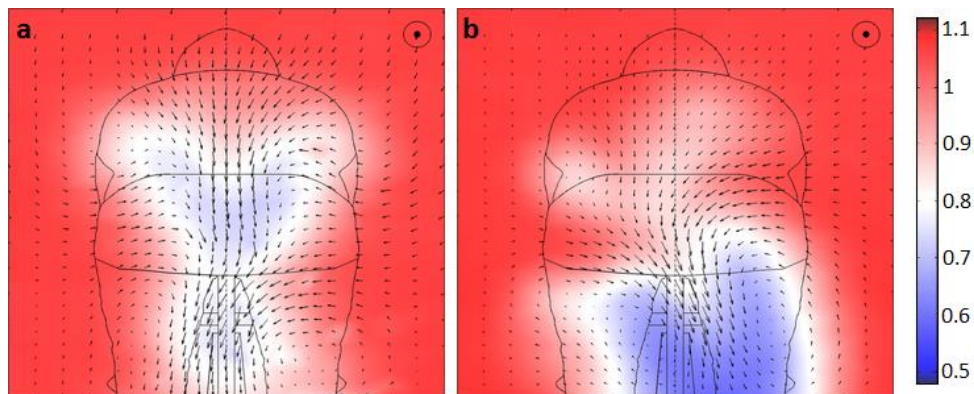


**Figure 1.2.2** - Normalised streamwise velocity in the wake of a static cyclist at; (a)  $15^\circ$  crank angle – upper legs level and, (b)  $75^\circ$  crank angle – left leg raised. Data measured at one torso chord length downstream. (From “Dominant flow structures in the wake of a cyclist,” Crouch et al. 2012 - Courtesy AIAA)

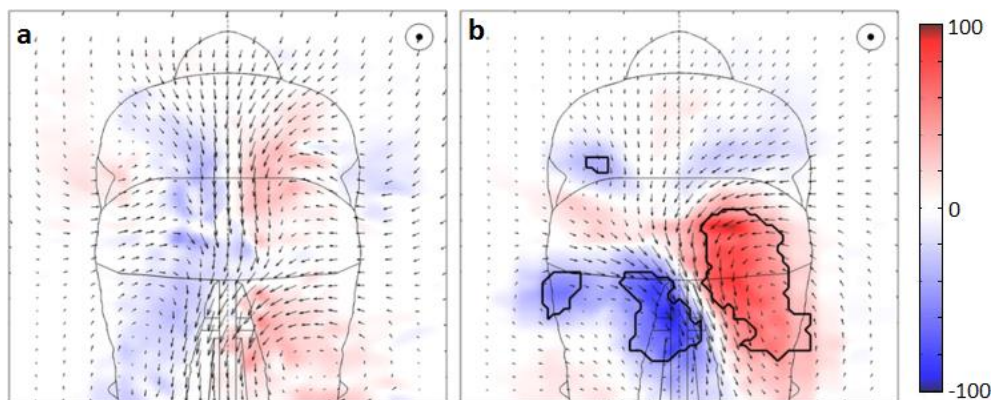


**Figure 1.2.3** - Streamwise vorticity ( $s^{-1}$ ) in the wake of a static cyclist at; (a)  $15^\circ$  crank angle – upper legs level and, (b)  $75^\circ$  crank angle – left leg raised. Data measured at one torso chord length downstream. Contours represent vortex boundaries identified from the swirling strength criterion (Zhou et al. 1999). (From “Dominant flow structures in the wake of a cyclist,” Crouch et al. 2012 - Courtesy AIAA)

The  $15^\circ$  crank angle case shows the wake to be symmetric about the rider centreline. Also, both streamwise velocity deficit and vorticity have significantly lower magnitudes in the  $15^\circ$  profiles. This indicates smaller and less coherent separation regions and correlates with this being the lower drag case.

In the  $75^\circ$  crank angle case (left leg raised) the asymmetry in the flow is evident in the streamwise velocity deficit and vorticity profiles. Velocity vectors indicate that the flow has a strong cross flow

component across the cyclist centreline with flow channelling over and downwards from the left hip. In the vorticity profile two dominant vortices are clearly visible that noticeably distinguish the two flow regimes. This asymmetry is formed from the flow remaining attached over the left hip as the hip to torso gap is closed. This allows the flow to wrap over and down across the rear of the cyclist causing the strong channel of flow across the centreline. On the right side with a fully open hip the flow separates earlier and higher from the side of the torso and top of hip leading to the higher positive vortex on the right of the frame. Other weaker vortices are also evident in the wake but these are secondary to the primary pair which exist over a range of crank angles in the asymmetric regime. For the second half of the crank cycle, when the right leg is raised, the opposite wake profile is evident. Cross flow is from right to left with a high negative vortex on the left and the positive vortex on the right sitting lower in the wake. This profile is strongest at a crank angle of  $255^{\circ}$ .

From this work Crouch et al. developed a detailed description of the flow field of a cyclist at the two key flow regimes. With upper legs level the flow separates evenly from both hips. This creates a balanced wake and vortices in the wake are weak. Flow also wraps around from under both legs forming an additional vortex pair of same rotation to the upper hip vortex. As the legs move away from level the flow behaviour changes dramatically. As one hip closes the flow from under the torso is blocked, this reduces the separation over that hip and the flow is able to wrap around onto the rear of the cyclist. Conversely, on the open hip the flow separates earlier and higher. This asymmetric profile generates a strong vortex pair in the wake, in addition to smaller secondary structures. These two regimes are depicted in Figures 1.2.4 and Figure 1.2.5 below.

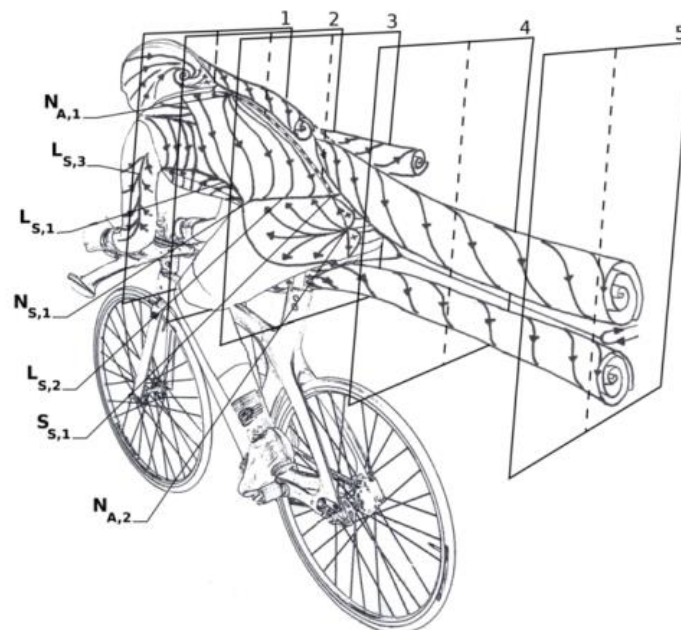


**Figure 1.2.4** - Vortex skeleton depiction of the symmetric flow regime around a cyclist with legs level - Positioned at  $15^{\circ}$  crank angle. Only right side vortices depicted. (From “Flow topology in the wake of a cyclist and its effect on aerodynamic drag,” Crouch et al. 2014 - Courtesy Cambridge University Press)

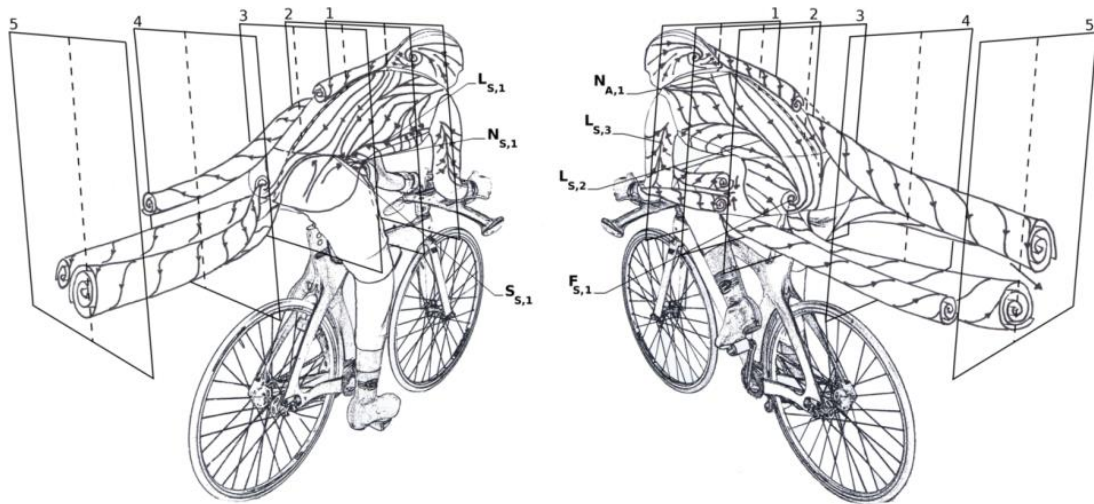


**Figure 1.2.5** - Vortex skeleton depiction of the asymmetric flow regime around a cyclist with one leg at maximum extension (positioned at  $75^\circ$  crank angle). Images show the left and right view of the same leg position. (From “Flow topology in the wake of a cyclist and its effect on aerodynamic drag,” Crouch et al. 2014 - Courtesy Cambridge University Press)

The drag of a model can be calculated from qualitative wake survey data through the application of the integral momentum equation over a control volume in the wind tunnel. This technique was first proposed by Betz (1924) and later by Maskell (1972). Further refinement of the technique for the application to wind tunnel wake survey data has been presented by Brune (1994) and Kusonose (1997). Integrating the streamwise momentum between an inlet and outlet surface it is possible to calculate the drag of a model in a wind tunnel by considering the stagnation pressure deficit, streamwise kinetic energy deficit and the transfer of energy to rotational vortex structures;

$$D = \iint_{Wake} (P_{T\infty} - P_T) ds + \frac{\rho}{2} \iint_S (U_\infty^2 - U^2) ds + \frac{\rho}{2} \iint_S (V^2 + W^2) ds \quad 1.2.1$$

Crouch et al. applied this integral to the series of wake profiles of the mannequin at different static leg positions. Values of the integral reflected the measured force results from wind tunnel tests. This showed that the change in drag with leg position is due to the changing flow structure in the wake. It also indicates that the dominant features in the wake, responsible for the variations in drag, are those captured behind the rider torso and upper legs. Variations with leg position to the flow in the lower part of the wake appear to have less influence on the fluctuating drag of the cyclist.

Following on from the experimental work of Crouch et al., numerical simulations were implemented by Griffith et al. (2014) to model the flow around a cyclist. A cyclist model was constructed to replicate the geometry of the anthropomorphic mannequin used by Crouch et al.. This model was based on the physical mannequin but differed in some features including simplification of certain elements such as hands and feet. The model also included a representative bicycle with deep section wheels. No high level details were included in the bicycle model as these were not expected to significantly influence the primary flow structures. Leg position was varied around the crank angle to assess the influence of leg geometry. Like the experimental results, numerical results showed that drag depends on the position of the legs around the crank cycle. Minimum drag was recorded at  $15^\circ$ , where the upper legs

are level and maximum drag occurred at  $75^\circ$  where the hip angle is at its smallest (closed). The associated wake structures for the two primary flow regimes are shown in Figure 1.2.6, where they are compared with the experimental results of Crouch et al.

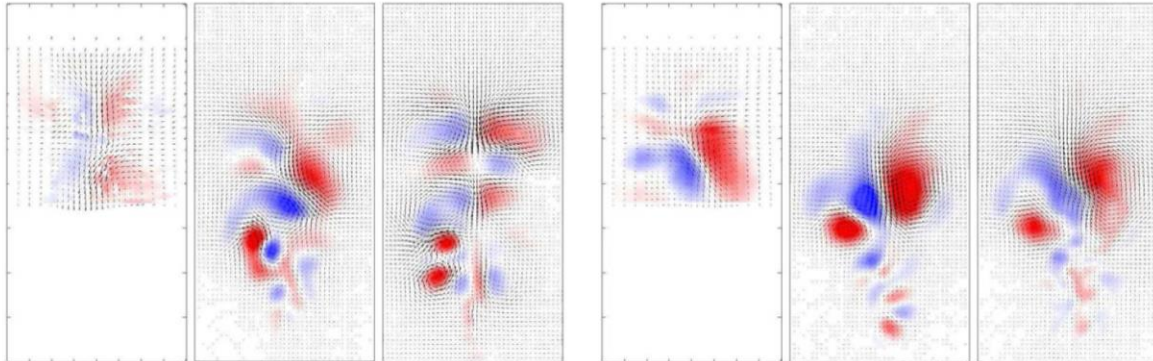


**Figure 1.2.6** - Contours of streamwise vorticity with vectors of cross stream velocity for a cyclist at (left series)  $15^\circ$  crank angle and (right series)  $75^\circ$  crank angle corresponding to the symmetric and asymmetric regimes in experimental results. In each set of three images results are shown for (left) experimental, (middle) numerical steady state solution, and (right) numerical transient average. Planes taken at 0.6m downstream of the model. (From “Computational fluid dynamics study of the effect of leg position on cyclist aerodynamic drag,” Griffith et al. 2014 – Courtesy ASME)

Profiles of the streamwise vorticity (Figure 1.2.6) show that the numerical simulation is able to predict the flow structures observed around a cyclist using the time average of a transient solution. However, using a steady state solution does not produce the same flow field. Although the steady state solution provides reasonable agreement in the asymmetric regime at  $75^\circ$ , at  $15^\circ$  crank angle the flow field does not exhibit the symmetric profile seen in the experimental results and the time averaged transient flow. This shows that it is possible model the flow around a cyclist using numerical simulations. However, transient simulations, such as were used here, are computationally expensive (taking around 6000h per second of real time, running on 64 computer nodes operating in a parallel cluster on the National Computational Infrastructure). The advantage of simulations is that the full flow field is captured in the solution allowing for imaging of other planes and flow components. Figure 1.2.7 (below) shows the streamwise velocity contour on the cyclist centreline at  $15^\circ$  and  $75^\circ$  crank angle positions, respectively. It can be seen that the streamwise velocity deficit in the wake immediately behind the rear of the rider is greater in the asymmetric ( $75^\circ$ ) case. This is consistent with the wake cross sections of Figure 1.2.2 (above). This suggests a greater momentum loss over the cyclist which corresponds with the higher drag at that leg position.

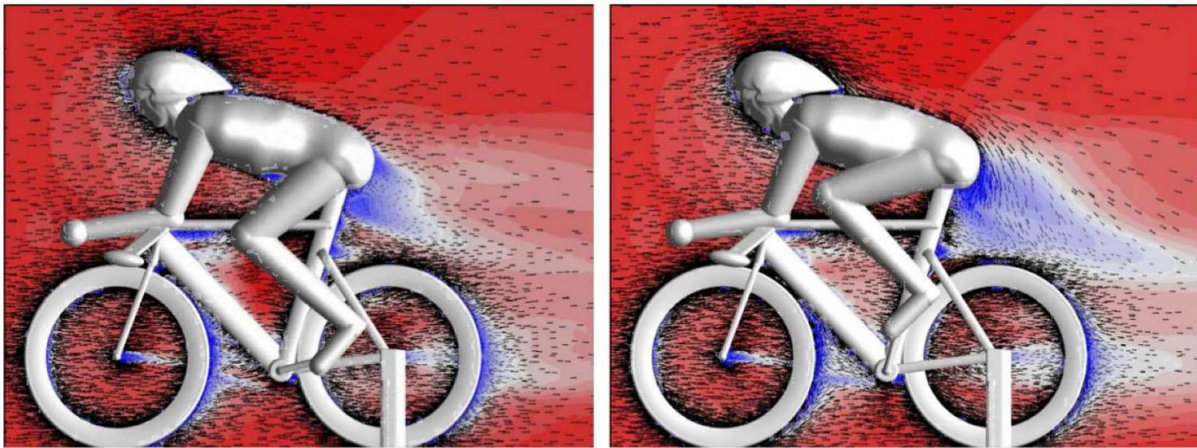


**Figure 1.2.7** - Contours of time averaged streamwise velocity taken from transient numerical simulations in a centreline plane of a cyclist; (left)  $15^\circ$  crank angle, (right)  $75^\circ$  crank angle (From “Computational fluid dynamics study of the effect of leg position on cyclist aerodynamic drag,” Griffith et al. 2014 – Courtesy ASME)

The recent work characterising the flow field around a cyclist provides an essential understanding for future investigations of cycling aerodynamics. Understanding the flow field around a rider and the mechanisms responsible for drag production enable more targeted decisions to be made in terms of optimisation and aerodynamic performance. However, this raises the question of how these flow regimes are influenced by interactions from the presence of another cyclist in close proximity. Do these same regimes prevail when subject to interference from another body? A significant body of literature exists examining the flow interactions arising from flow over simpler, more fundamental bluff bodies, such as cylinders. This should provide a key starting point to understanding more complex bluff body problems such as flow around multiple cyclists.

This work also highlights a potential limitation of existing cycling research relating to the motion of a cyclist’s legs. It has been shown that leg position has a large effect on not only the drag, but also the flow field. It follows then that time averaged dynamic drag of a pedalling cyclist is not necessarily well represented by a static cyclist. However, the comparison of dynamic and static cyclists has not yet been addressed in literature and the two cases are often used interchangeably; as shown in Table 1.1.1.

### 1.3 Multiple Body Aerodynamic Interactions

Aerodynamic research in cycling has, to date, primarily focussed on a single rider because it has been seen that time trial events are where the greatest gains can be achieved from aerodynamics. These events are conducted at maximum sustainable power, meaning any reduction in drag directly translates to greater speed. However, for the majority of road cycling events and in many events on the track the cyclists' performance is strongly influenced by rider interactions.

The benefits of drafting have long been understood in cycling. However, research into the area has not been able to support the anecdotal evidence quantitatively nor have the causes of the benefits been made explicit. There is, however, a large body of knowledge available for other bluff bodies. Research has shown that two bluff bodies in close proximity can have their aerodynamic forces significantly altered as a result of flow interaction effects. For a range of different body shapes drag has been shown to vary significantly with spatial position and separation distance. Studies of complex three-dimensional geometries, such as vehicles, have also shown that these drag interactions are influenced by the geometry of the bodies.

#### 1.3.1 Fundamental Bluff Body Interactions

The earliest bluff body work dates back to investigation of struts and wires of biplane wings in the early twentieth century. Pannel et al. (1915) investigated circular cylinders arranged in-line parallel to the flow (termed 'tandem') and identified that the sum drag of two wires in close proximity was less than double the result for a single wire in isolation. Biermann and Herrnstein (1933) measured the drag on each cylinder individually in a tandem formation and analysed the influence of separation distance on drag. They identified that there is a critical spacing for cylinders at 3 – 3.5 diameters at which there is a discontinuity in the measured drag (Figure 1.3.1).

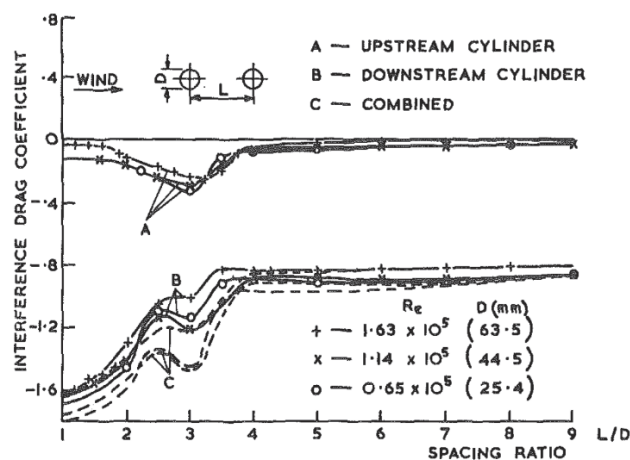


**Figure 1.3.1** - Interference drag coefficient of tandem cylinders (Biermann and Herrnstein 1933)

Notice that there is the potential for drag reduction for both lead and trailing cylinders

Later visualisation studies identified that this discontinuity is due to a transition in the flow regime which occurs between 3 and 4 diameters separation (Ishigai et al. 1972). Below this spacing the flow separating from the lead cylinder reattaches onto the trailing body. Above 3.5 diameters the flow separates from the lead body and forms a secondary stagnation point on the trailing body (Figure 1.3.2). This causes increased drag for both lead and trailing bodies. This is confirmed by surface pressure measurements from the trailing cylinder (Zdravkovich 1977). Interactions between two semi-infinite circular cylinders have been previously investigated by a range of authors (Zdravkovich 1977, Hori 1959, Zdravkovich & Pridden 1977, Lin et al. 2002, Deng et al. 2006).

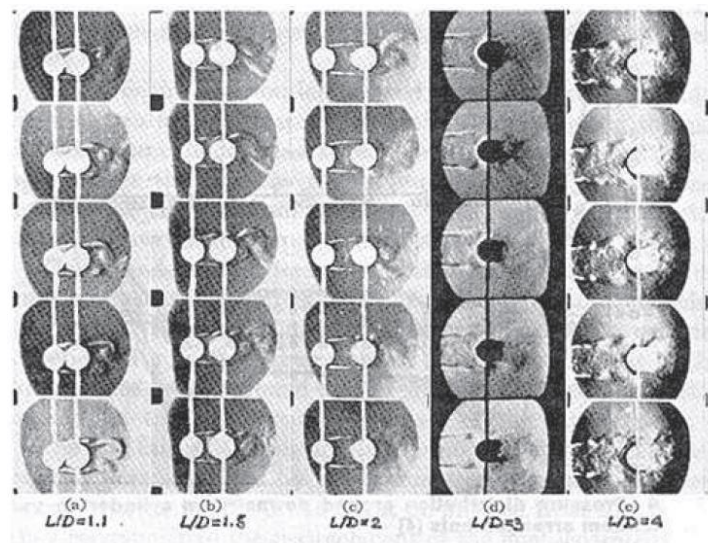


**Figure 1.3.2** - Still images of flow between tandem cylinders (Ishigai et al. 1972)  
Notice the change in flow conditions as spacing increases from 3 to 4 diameters

There are many applications where bodies are not positioned inline parallel to the flow direction. When bodies are positioned perpendicular to the flow it is typically termed a transverse or side-by-side formation. Other formations where bodies are not directly in line with either axis are called staggered formations in cylinder literature. In the case of cycling this applies to cases where the rider is travelling side-by-side with other cyclists as well as in overtaking manoeuvres.

Biermann and Herrnstein (1933) investigated transverse arrangements in addition to tandem formations. It was revealed that when two cylinders are in line perpendicular there are certain separation distances that result in points of dual stability in drag. The drag of each cylinder tended to alternate from one value to another but equal drag was not measured for the two cylinders; evidence of two points of stability. Beyond two diameters this instability was no longer present but drag still exceeded the single cylinder value until separation exceeded 5 diameters. Surface pressure measurements (Hori 1959) confirmed a similar instability when in side-by-side formation. Hori's work in the detailed mapping of staggered formations at all angles relative to the oncoming flow provides a detailed insight of the complexity of interactions between two cylinders. Five different regimes were identified from the range of staggered positions. These are described in Figure 1.3.3 below. Drag and side forces acting on the two cylinders were calculated from integration of the surface pressure measurements. At certain regions relative to a fixed reference body the second body drag is higher

whilst at others it is lower. In addition to the bistable drag, the flow balance on either side of the cylinder induces a component of force perpendicular to drag (side force). Following the investigation of staggered positions it was suggested that the instability in drag that occurs for side-by-side arrangements results from a transition between trailing stagger and leading stagger (Zdravkovich 1977). The flow vectors in Figure 1.3.3 indicate force acting on a second cylinder positioned at that location. A repulsive force is defined as pushing away from the cylinder regardless of whether above or below. Arrows pointing towards the left indicate drag lower than a single cylinder.

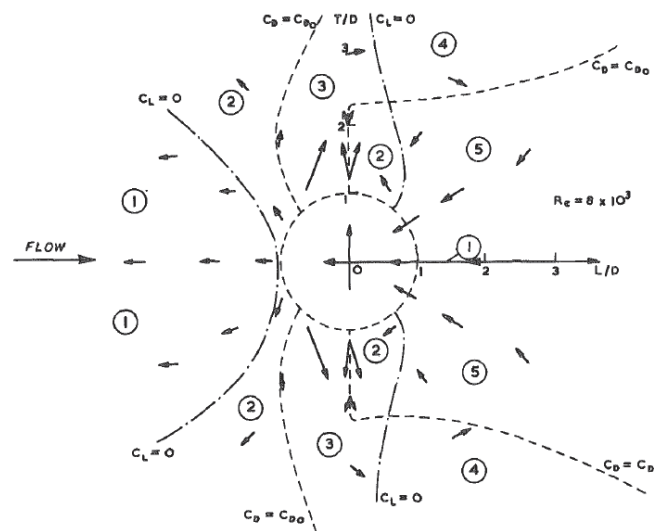


**Figure 1.3.3** - Aerodynamic load regions for staggered circular cylinders (Hori 1959)

Regions of Figure as described by Hori (1959):

Upstream Cylinder Regions

1. Negligible side force – reduced drag
2. Small repulsive side force – reduced drag
3. Repulsive side force – increased drag

Downstream Cylinder Regions

4. Negligible side force – increased drag
5. Attractive side force – decreased drag

The separation point and resulting drag of a cylinder is influenced by Reynolds number (Achenbach 1971). Much of the early interaction work was conducted at a Reynolds number below turbulent transition (sub-critical). For many full scale engineering applications, including ground vehicles and cycling, Reynolds numbers are above turbulent transition. It has been shown that the discontinuity observed for subcritical cylinders is no longer present at supercritical Reynolds numbers (Okajima 1976, Gu 1996). Drag of the trailing cylinder was also seen to be less sensitive to a change in the separation distance between the two bodies. Beyond 2.8 diameters the downstream cylinder is primarily influenced by sheltering from the lead body resulting in reduced incoming velocity and high turbulence intensity for the trailing cylinder. In this way the resultant effect on the downstream cylinder is similar to that found in a highly turbulent flow.

Results for semi-infinite circular cylinders show that flow interactions between two bluff bodies are significant but are complicated, which raises the question of how geometry influences these effects. Flow between two semi-infinite square cylinders parallel to the flow exhibited two distinct flow regimes similar to that of circular cylinders (Kim et al. 2007). The first mode shows reattachment on

the trailing body, the second with a stagnation point on the trailing body. This characteristic was dominated by separation distance with Reynolds number having minimal effect on flow behaviour.

Tandem cubes on a surface introduces more three-dimensionality to the problem as well as ground plane influence. Unlike the quasi-two-dimensional flows a discrete transition point in the drag coefficient was no longer observed (Martinuzzi & Havel 2004). This is a result of the upper shear layer interacting with the shear layers from the side walls in the wake of the upstream cube. This destabilises the flow and inhibits clean reattachment onto the trailing cube. This implies that for increasingly complex geometries the interacting shear layers will smooth out any transitions between flow regimes and subsequently the drag response.

### **1.3.2 Ground Vehicle Interactions**

Automotive applications provide a closer link to cycling aerodynamics, being both complex geometry bluff bodies and in proximity to a ground plane. Several studies have been previously conducted into the effect of the interaction of vehicles in a tandem formation on their aerodynamic drag. These have covered a range of vehicle geometries from simplified vehicle bodies and heavy vehicle shapes through to detailed replica models. The common finding amongst this work is that drag of both lead and trailing bodies is a strong function of separation distance between them. Furthermore, the variation in results for different model shapes indicates that the vehicle geometry also has a strong influence on drag in a tandem formation (Ioannou 1997, Hammache et al 2002, Watkins & Vino, 2008).

Whilst studies have investigated the drag interactions between vehicles, the effects of these interactions on flow fields have received far less attention. One key example of a simplified vehicle shape is the Ahmed body (Ahmed 1984) which replicates the primary wake vortices characteristic of automobile shapes. It has been shown for two Ahmed bodies that as gap size increases the flow has greater downwash as streamlines from the lead body are no longer able to reattach on the trailing body (Watkins & Vino 2008). Rajamani (2006) and Pagliarella (2009) investigated interactions between tandem Ahmed bodies and found that at small separation the axial C-pillar vortices from the lead model impinge on the front face of the trailing body causing flow stagnation on the trailing body near the top and outer edges of the front face. The stagnation point on the trailing body is significantly higher than in the isolated case. Meanwhile, the presence of the trailing model causes an increase in static pressure upstream and a consequent increase in the base pressure of the lead model. For bluff bodies, like an Ahmed body, because rear body pressure drag is a major source of total body drag, reducing this has a large impact on overall drag of the bodies. This explains the drag results observed by Watkins & Vino, which showed lower drag for the lead body, rather than the trailing body, at small separation.

Other vehicle studies have shown, however, that this behaviour is not common to all tandem vehicles. Hammache et al. (2002) showed that the drag interactions of smooth idealised bodies differ significantly from that of more realistic ones (those with greater geometric detail). For smooth idealised trucks (no wheels, no characteristic features and minimal cab gap) the lead body was found

to have lower drag than the trailing truck. However, with a 'dirty' truck model, one with more realistic details, the result was the opposite. The lead body drag was higher than that of the trailing truck for all separation distances. For the detailed car body shape of a 'stock car', small separation distance was shown to increase base pressure for the lead car and decrease pressure on lead face of trailing car (Duncan 1994). However, the drag reduction for the trailing vehicle was much greater than the lead (50% compared to 15% respectively). Romberg et al. (1971) also showed that for 'stock cars' the lead body drag reduction is significantly smaller than the trail. At near zero separation the lead body showed up to 30% drag reduction, however this reduces to zero at a car length separation. The trailing car showed 37% reduction at over a car length downstream but only a slightly greater reduction at smaller separation distances. Romberg et al.'s results exhibited smooth curves with a continuous trend of increasing drag with separation distance for both the lead and trailing cars, with drag approaching but never exceeding the baseline value for a single car. The results showed no discontinuities or inflections as seen for simple smooth geometry bodies. These combined vehicle results suggest that clean separation from the lead body and reattachment onto the trailing body may only be possible for simple geometry bodies. Complex geometry bodies are more likely to follow the drag characteristics of the stock cars where the trailing body drag reduction is significantly higher than the lead. The variation in the drag results for different models highlights the sensitivity of three-dimensional bluff body drag interactions to geometrical features. In cycling terms this could potentially lead to manipulation of team drag results from relatively small changes to equipment and body posture. Furthermore, a better understanding of the characteristic effects on cyclists could translate to wider applicability to other vehicle and complex body interactions.

In addition to a pure tandem formation, Romberg et al. also investigated staggered formations by introducing a lateral offset for the trailing vehicle. For positions with axial separation less than 0.25 car lengths and a lateral offset of greater than 0.37 lengths there was a small drag increase observed for the trailing vehicle (maximum 8%). However, as axial distance was increased the trailing vehicle drag decreased below the baseline value before passing through a minimum at around 0.5 car lengths downstream and then approaching the baseline value again. For small lateral offsets there was no increase for the trailing vehicle and the minimum drag case was at minimum axial separation, similar to the inline tandem case. This behaviour is similar to that seen for staggered cylinders.

The study also investigated the drag behaviour of two cars during an overtaking manoeuvre. This involved one car manoeuvring from a trailing drafting position, pulling out to be side by side and then returning to an in line drafting position in the lead. The vehicle results did not exhibit the same instability in drag force seen in the case of circular cylinders (Biermann & Herrnstein 1933, Hori 1959), however, a significant drag increase was observed. Unlike the case of cylinders, this did not occur at the level transverse position but rather with the nose of one car at the midpoint of the other. That is the vehicle being overtaken experienced the maximum drag increase when the second vehicle was behind the level position. At that position a maximum increase in drag of 37% above the baseline value was recorded. Side force results showed a repulsive force (pushing models away from one another) at transverse positions as was seen for circular cylinders, with a maximum of approximately 30% of the baseline drag.

The full detail of the models in these studies produced smooth, continuous curves compared to the more varied results observed for simplified vehicle models (Watkins & Vino, Ioannou, Hammache et al.).

Flow interactions between three dimensional bodies have shown that drag is a strong function of geometry as well as spatial position. Increasingly complex bodies appear to produce interacting shear layers which inhibit flow from cleanly reattaching onto the trailing model, even at small separation. This eliminates the first mode behaviour seen for quasi-two-dimensional cylinders. As such, the very complex and dynamic geometry of a cyclist could be expected to respond in such a way, with a much smoother trend of increasing drag with separation distance and the lead body always having the higher drag.

### **1.3.3 Aerodynamic Interactions in Cycling**

The benefit of drafting in cycling has been long identified from anecdotal experience. From the early days of cycling in the late 19<sup>th</sup> century, several records were attempted drafting behind vehicles to achieve speeds far in excess of those that could be achieved in isolation. Since that time there have been a select number of investigations that have quantified the performance benefit of riding in the wake of another cyclist (Kyle 1979, McCole et al. 1990, Zdravkovich et al. 1996, Broker et al. 1999, Edwards & Byrnes 2007, Blocken et al. 2013, Defraeye et al. 2014). For a cyclist trailing immediately behind the leader, drag reduction has been reported in the range of 16-49% from experiments. When separation is increased to a bicycle length this saving is reduced to 11-28%. However, surveying the literature shows there is currently considerable variation in reported drag reduction for a drafting cyclist.

Kyle, Zdravkovich et al. and Blocken et al. all investigated the relationship between separation distance and drag for two cyclists in a tandem formation. Results from all studies concluded that the trailing rider drag is a smooth continuous function of separation distance. Minimum drag occurred at minimum separation; monotonically increasing until it approached the single rider value. This behaviour is consistent with that of the complex geometry vehicle models and stock cars observed by Romberg et al. (1971). However, whilst these studies agree on the general behaviour of drag with distance, the gradient of the curve and the magnitude of drag reduction differ significantly between studies.

It is important to note that distance separating cyclists is uniquely different to that of other typical bluff bodies. The majority of the bluff volume of a cyclist is the athlete. However, a rider on a bicycle sits some distance behind the leading edge of the front wheel and ahead of the trailing edge of the rear wheel. In practice, this means that at zero separation distance between riders (no gap between the wheels) there is still a considerable distance between the bodies of the riders. This will vary with bicycle setup but with zero wheel gap the distance from the rear of one rider to the head of the trail is typically of the order of one torso length. For many other bluff bodies the zero separation distance means the two bodies touch. This contributes to the fact that the drag curve is smooth and continuous as there is no case where the flow can reattach onto the trailing body, in addition to the complex separation seen from a cyclist. The one exception to this case is a tandem bicycle where two bodies are on the same bicycle frame and so can be positioned much closer than for two individual cyclists.

Kyle (1979) conducted an early and detailed investigation of cycling aerodynamics. Analysis of cyclist drag was calculated from coast down tests of timed rolling runs over a 200m track. Tests were conducted with cyclists adopting the traditional drops posture ('racing position'), as described earlier. The original results are shown in Figure 1.3.4 below.

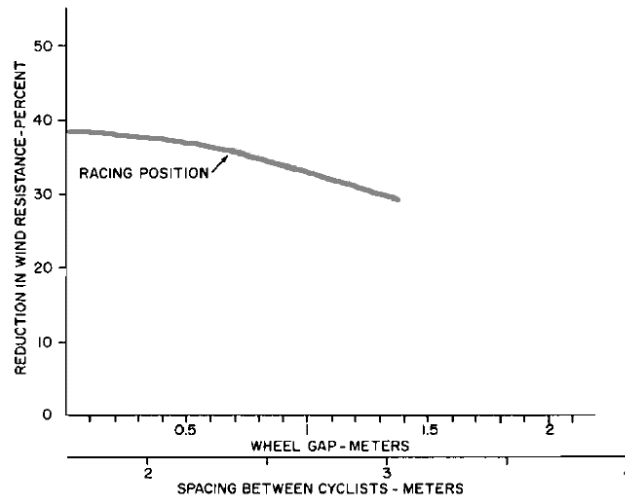


**Figure 1.3.4** - Drag reduction as percentage of solo rider from coast down tests (Modified from Kyle 1979)

Results show that at minimum separation, the trailing cyclist experienced a 38% reduction in drag. As the distance between the riders increased, drag reduction decreased. However, at the maximum spacing of this test there was still a reduction of 28% relative to an isolated rider. The maximum spacing for the racing position was 1.4m between the wheels (a standard road bicycle has a length of approximately 1.7m). Tests were performed for groups 2, 3 and 4 cyclists. However, no further reduction in drag was observed for cyclists in position 3 or 4 compared that found for the first trailing rider, in position 2. Furthermore, the drag of the lead rider did not reduce in any of the formations.

Field testing, such as coast down tests, face difficulty in controlling the parameter space. In particular for cycling, variations in local wind conditions can introduce large uncertainties into the results. For testing such as this there is the added complexity of controlling the relative position of the two cyclists. The plotted results are a regression of the collected data and as such do not show evidence of the variability in the data. However, the author did state that large variation was observed in the results due to variations in separation and distance and lateral alignment, including overlapping. A potential problem inherent in a rolling coast down test is that the lower drag on the trailing rider means they can catch up to the leader. The authors also remarked that during some test runs riders deviated from the inline formation. In some cases where lateral movement was observed there was no measurable reduction in drag. This highlights the large uncertainty associated with field testing. This study was limited by the technology available at the time. More recent field tests of cycling (eg. Broker et al. 1999) have utilised bicycle-mounted power meters to measure cyclist output during field trials. The alternative to field tests is wind tunnel tests. This allows greater control of spatial and environmental variables. However, it requires a large cross section and test section length, which are expensive and in high demand. For this reason, full scale wind tunnel tests have been limited to date.

Zdravkovich et al. (1996) sought to improve on Kyle's work by performing a similar investigation in the more controlled environment of a wind tunnel. In addition to axial separation, lateral displacement from the centreline was also investigated. Drag was measured using a single fixed force balance for the trailing rider. The lead rider was not instrumented and was positioned relative to the trailing one to vary spatial position. The test procedure was then repeated with each athlete acting as the lead and trail in turn. The two test subjects differed significantly in physical size and were shown to have a 30% difference in baseline drag (Figure 1.3.5). All tests were conducted with cyclists using the hoods posture (described previously). As a result two very different profiles were obtained for the two formations. This highlights how the drag depends on the size and geometry of the athletes. To display the more general trend in the data the mean result of the two athlete formations is plotted in Figure 1.3.6 below.

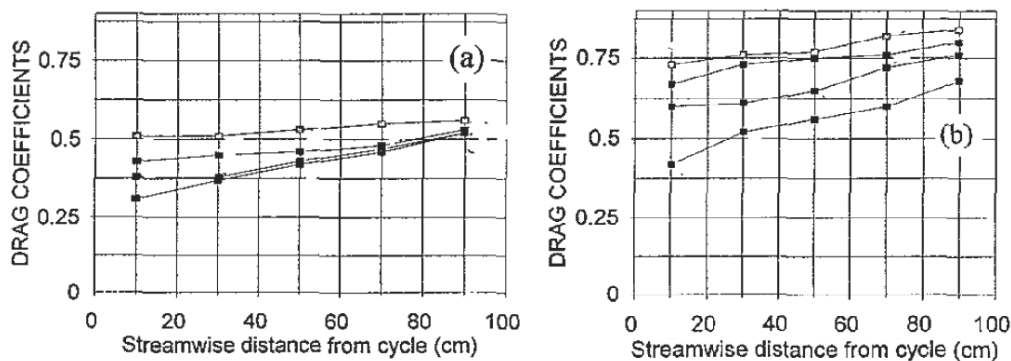


**Figure 1.3.5** - Drag coefficient ( $C_D$ ) of the trailing rider in a tandem formation (from Zdravkovich et al. 1996). (a) Rider 1 trailing, (b) Rider 2 trailing. Baseline  $C_D$  was 0.6 and 0.75 for Riders 1 and 2 respectively. Each series represents a 100mm lateral step from the centreline.

Considering the mean results, it can be seen that the trend is similar to that proposed by Kyle. There are no local inflection points in the drag curve. The maximum drag reduction occurs at minimum distance behind the leader. As separation distance increases so does the drag of the trailing rider. In addition, this result shows that the drag of the trailing rider is a strong function of the lateral displacement from inline. For an increase of only 100mm laterally, there is a 20% increase in the drag acting on the trailing rider. This sensitivity explains the high variability observed by Kyle, especially for lateral displacement.

The drag reduction reported by Zdravkovich et al. is significantly different to that of Kyle. The maximum drag reduction averaged across the two formations was 48%, compared to 38% reported by Kyle. Also, at 0.9 m downstream, the inline case reported a mean saving of only 11% where Kyle observed a 28% saving up to a distance of 1.4 m between cyclists. At any lateral offset, the drag saving experienced at the maximum distance of 0.9 m is very small. This rate of decline in drag reduction appears inconsistent with empirical field data and anecdotal evidence from athletes. The fact that drag reduction is so small (with drag increasing for one athlete) at only 0.9 m separation suggests that the gradient reported by Zdravkovich et al. is not representative of the drafting effect experienced by cyclists in practice. Although wind tunnel testing typically allows for a more controlled test environment than field tests, Zdravkovich et al.'s work has several limitations which potentially compromise the validity of the results. One notable feature of Figure 1.3.5 (b) is that Rider 2 (the larger

athlete) recorded an increase in drag for some of the trailing locations. This contradicts other results for cyclists and many bluff bodies. Whilst the drag reduction would be expected to decrease with distance, an increase in drag above baseline is unsupported by other literature. Additionally, the less controlled experiments of Kyle would be expected to under predict the drag saving, but it is the wind tunnel that presents the higher rate of decay of drag reduction. These tests were conducted at a blockage ratio of the order of 15% and no details of any corrections are given. Drag measurements in a wind tunnel require corrections due to distortion of the flow field from the presence of a model which induces blockage (Maskell 1965, Awbi 1978, Mercker & Wiedemann 1996). For closed wind tunnels blockage is typically recommended to be below 10% (eds Tropea et al. 2007). In addition, the small test section meant that athletes were close to the wall boundaries and potentially influenced by the shear layer. It is possible that having two bodies in the tunnel resulted in flow conditions that were unaccounted for at the trailing, instrumented rider that have resulted in erroneous measurements. The reason for this difference is not certain, but the results do contradict numerous other publications and practical experience. Other more practical limitations included that these were static tests, with no pedalling dynamics, and that no helmets were worn, as they weren't compulsory under cycling rules of the time.

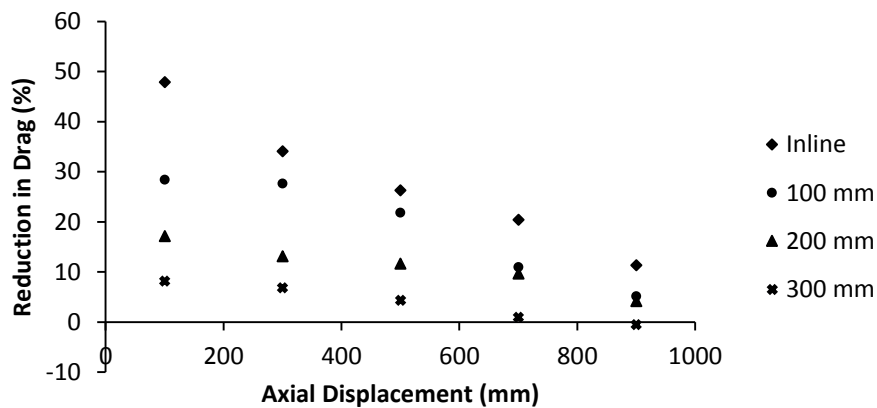


**Figure 1.3.6** - Average drag reduction for the trailing rider from the results of Zdravkovich et al. (1996). Series represent lateral displacement from lead rider centreline.

Tandem interactions were also modelled computationally by Blocken et al. (2013). For the traditional drops posture (as used by Kyle 1979) the study reported a maximum drag saving of only 23% for the trailing rider at zero separation from the leader. In a time trial posture the drag reduction at the same position was only 14%. This is considerably lower than either of the previous experimental studies. Furthermore, power data (Broker et al 1999) from track tests suggest a significantly greater drag reduction at zero separation for two inline cyclists. However, the gradient of the drag curve of the simulation results is closer to the work of Kyle, showing that the interference effects extend further downstream than the results of Zdravkovich et al. indicated.

A particular feature of this work is that the lead cyclist's drag was reduced by 1.7% for the drops racing posture and up to 2.6% in the time trial posture. In both cases this occurred at zero separation between the bicycles. This has been observed previously for fundamental bluff bodies and for vehicles but no forward interference effects had previously been reported for cyclists.

In addition to the force response, the authors also present details of the flow field that occurs around a two rider formation and compare it against that found for a single rider. For a single cyclist the profiles clearly show a high pressure region acting on the front surface and the low pressure behind the rider are caused by the separated wake (Figure 1.3.7). In the two rider case, the majority of the leader profile is similar to the single rider result. The one area of significant difference is behind the hips of the rider where there is a definite increase in pressure relative to the single case. It was concluded that this pressure increase is the cause of the drag reduction observed for a leading cyclist. The pressure field immediately upstream of the trailing cyclist maintains a high pressure region, similar to the single rider case. The pressure coefficient in the lower region of the trailing rider wake is also similar to the single rider case. However, immediately behind the hips there is small region of reduced pressure.

The simulation did not include the bicycles, only suspended rider geometries. To compare with experimental results the drag of the cyclist on the bike was subtracted from the bike in isolation. This procedure ignores any interactions between the rider and the bicycle, which could lead to errors in the simulated results compared to the practical case.

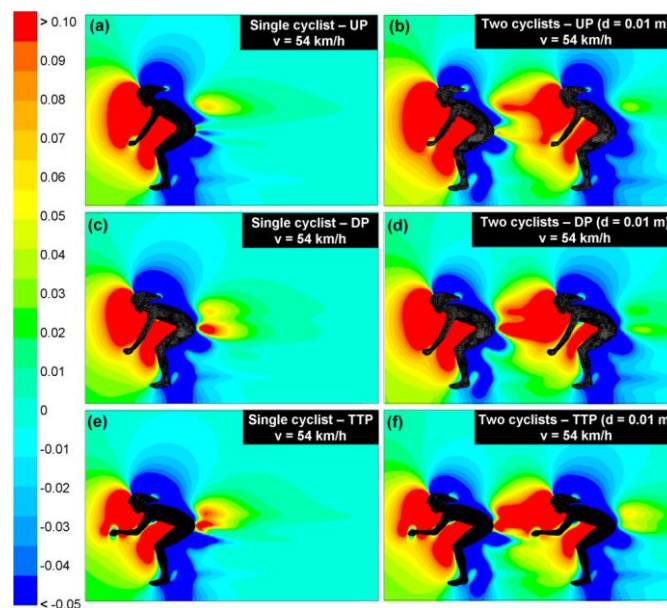


**Figure 1.3.7** - Pressure coefficient in the vertical centre plane for a single cyclist (left and two riders in tandem (right). (a,b) Upright climbing posture, (c,d) drops posture, (e,f) time trial posture (Blocken et al. 2013)

The development of mobile, bicycle mounted, power meters over the past two decades has enabled much better analysis of cycling performance from real world and track data. Such devices typically use strain gauges in the cranks or chain ring interface to measure force and cadence and compute power output. Broker et al. (1999) conducted an investigation of the power requirements during a team pursuit using such devices. A series of team pursuit runs were conducted at several different velodrome locations using groups of 4 athletes. These runs were with a rolling start, not accelerating from rest as is this case in a race. Power data was collected for all 4 riders in the team. Considering the mean of all the published track tests from 3 different velodromes and a range of athletes and equipment, the power required in positions 2, 3 and 4 of the pursuit team was 68.3%, 61.0% and 60.9%

of the leader's power requirement. They also compare their results with wind tunnel data; however, there are limited details of these tests. Wind tunnel force results were converted to equivalent power and presented as a percentage of the leader's power and calculated to be 63.7%, 53.8% and 53.2% for positions 2 to 4 respectively. Compared to wind tunnel tests, field testing has less control over the riders' spatial positions. Zdravkovich et al. (1996), showed that drag is a strong function of both lateral and axial position. Therefore even small fluctuations in spacing and position from the centreline during the track runs would result in increased drag for the trailing rider. This would result in higher mean power than predicted by the wind tunnel for the same modelled separation distance.

Whilst the track tests do provide a realistic model of performance, as even professional athletes will not be able to maintain perfect positioning throughout a race, they do introduce uncertainty when trying to quantify the effect of drag. Furthermore, the track test runs were simulated pursuits, including rotating the time spent at the front of the team. This introduces a further transient factor that has not been accounted for in the modelling. Again, whilst being realistic for competition performance, it is difficult to accurately model the drag with such changes. Another limitation of the Broker et al. study was the use of the lead rider as the reference for the power measurements. The leader was changing during the event, meaning their power will not be a constant reference point. Therefore, these results are useful in that they show the significant reduction in power required, which can be attributed to a reduction in aerodynamic drag but the variability in the test procedure makes it difficult to isolate how the aerodynamics affects the forces.

The studies by Kyle and Broker et al. highlight the value of wind tunnel experiments. Whilst track tests with power meters make data collection relatively simple and provide a good model of expected real world performance they are limited in their ability to detect and assess smaller changes. Due to the sensitivity of drag to spatial position and that field test error margins tend to be quite large, changes in the drag results are dominated by the variation in spatial position and any small changes in drag, due to other variables such as posture or equipment for example, are indistinguishable. Whilst small changes may not be clearly detected from a track test, it does not make them insignificant as the winning margins in cycling can be very small. Wind tunnel tests, however, offer a more controlled environment, particularly with respect to spacing, and this means finer variable changes can be investigated, leading to more reliable quantification of the interaction effects of cycling in groups.

The aerodynamic interactions in a four rider team pursuit were also modelled computationally by Defraeye et al. (2014). Body scan data was used to model 4 different rider geometries. The simulation used these as suspended bodies with static legs; bicycles were not included in the modelling. This work follows on from previous studies by the same authors and uses the same computational method (Defraeye et al. 2010, 2010, Blocken et al. 2013). Simulations were run for 4 possible sequences of the given 4 riders, following that in competition each athlete will rotate through the lead position but remain in the same order. The mean drag reduction for the 4 positions in the team were found to be 3%, 26%, 37% and 43% for positions 1 to 4 in the pursuit team respectively. If the raw  $C_D A$  values are used to determine the trailing rider's drag as a percentage of the leader's drag then these results can be compared to that of Broker et al. mentioned previously.  $C_D A$  for cyclists in positions 2 to 4 are 76.7%, 65.4% and 59.5% of the leader respectively. Note that in this case, as with most multiple body problems,  $C_D A$  is a normalised form of drag referenced to the freestream velocity. For positions 2 and 3 this is considerably higher than both the track tests and the wind tunnel results of Broker et al.. This will be influenced by the fact that only the change in drag has been considered, and not total cycling

power. However, application of Martin et al.'s model reveals that for high speed steady state cycling the change in total power is dominated by the drag component and therefore the percentage change in power is not significantly different from the change in drag. Compared to the 2D ellipsoid model presented by Torre & Íñiguez (2009) there are significant differences in the required power. This confirms that radically simplifying the complex geometry of a cyclist is not a reasonable approximation for performance modelling. It is possible that the lack of the bicycles is contributing to the smaller drag reductions predicted numerically compared to wind tunnel results. The bicycles still contribute a significant amount of drag to the total system and so excluding those bodies has potential to cause differences in drag. It must also be considered that there will be interactions between the bicycle and the athlete and drag of the bicycle is not a linear addition to the drag of the system.

The study also investigated the effect of geometry by testing athletes with arm width set at two positions. In terms of total team drag (sum of  $C_D A$  for each of the 4 riders in a given sequence), the wider arm spacing increased drag for all 4 sequences, although there were significant differences in the magnitude for each sequence. In terms of position in the team, wider arm spacing was reported to increase drag at all 4 positions. However, it was noted that there was variability in the response of athletes, with at least one athlete recording lower drag with the wider arm spacing. No indication of spread of the data for each athlete was published. These geometric changes were applied to all riders in the team. Changing the posture of individual athletes was not investigated.

The authors also presented profiles of streamlines and centreline streamwise velocity profiles of the 4 sequences of the team (Figure 1.3.8). Analysis and review of the flow structures is complex, but velocity contours indicated that the velocity deficit increased with downstream position in the team. Streamlines indicate there are some similarities in the basic flow structure to that of the single rider, but that there were noticeable differences.

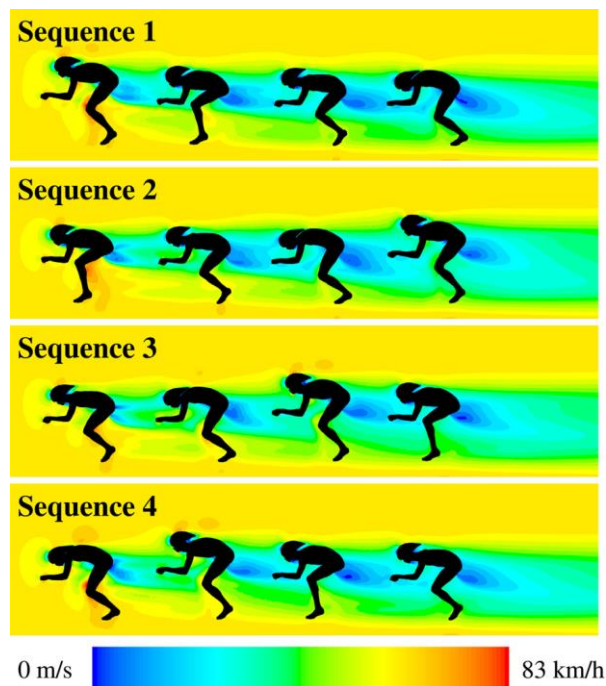


**Figure 1.3.8** - Streamwise velocity contour on the vertical centreline plane for four rider team travelling at a freestream velocity of 60 km/h (Defraeye et al. 2014)

The literature has shown that a drafting cyclist can experience a large drag reduction. The magnitude of the drag reduction has been shown to be influenced by geometric changes and to also differ between athletes. Edwards & Byrnes (2007) investigated how anthropomorphic characteristics influence the magnitude of drafting effects. It has been proposed that the drafting benefit for a trailing cyclist is due to a reduction in the pressure difference across that cyclist (Kyle 1979), thus reducing the pressure drag component. Assuming that the size of a cyclist will influence the size of their wake and that the size of a trailing rider will affect their ability to be contained within that wake region, Edwards & Byrnes suggested that the magnitude of the drafting effect will scale with the size of the lead rider. They conducted constant velocity field tests on a pool of 13 athletes. From these tests the athletes with maximum, median and minimum  $C_{DA}$  were identified and acted as leaders in drafting experiments. Mean results showed that the drag reduction for the trailing rider scaled with the  $C_{DA}$  of the lead rider. Thus, drafting behind a leader with high  $C_{DA}$  will increase the drag saving experienced. Large differences were seen between the three selected leader groups with mean reduction in drag coefficient for the trailing rider of 35%, 41% and 51% for the minimum, median and maximum denoted leaders. It was concluded that the lead rider's  $C_{DA}$  is a strong determinant of the drafting effect experienced by the trailing rider. However, large inter-individual variability within the groups shows that it is not the only important factor. A strong correlation existed across the full data set, however, this was not observed within the individual groups (eg. within the minimum leader data set there was not a strong correlation between leader  $C_{DA}$  and drafting effect). Furthermore, the leader  $C_{DA}$  has a more consistent effect on the drafting effect than that of the trailing rider. Correlation between the trailing rider's characteristics and the drafting effect revealed much more variation in the results.

A mean saving of 42% reduction in drag coefficient was recorded across all tests. This is well within the range of other literature for two tandem cyclists. No clear forward interference effect was observed for the tests. A small and inconsistent effect was observed but this was below the experimental uncertainty threshold. Previous work has shown that the drag reduction for the trailing rider is sensitive to spatial position of the riders. As this study was conducted using field tests there is an inherent uncertainty in the data as a result of the difficulty in controlling the position of the cyclists. Separation distance was designated as a 0.5 m wheel gap but the position was not tracked during testing. Multiple trials and statistical analysis helps to eliminate this from mean results but it does result in large variability when combined with the 3% accuracy of the power meter.

Measuring power is a practical, performance-based approach to assessing the effects of drafting in cycling. Direct force measurement in a wind tunnel provides detailed aerodynamic information and control of a greater number of parameters. However, power is a measurable output for athletes and coaches and so is more closely linked to performance. Another method for assessing the benefits of drafting is to look at the energy expenditure of an athlete. McCole et al. (1990) investigated drafting during cycling from the athlete's change in oxygen uptake. Tests were conducted on a flat stretch of road with an expired gas collection system mounted from a chase vehicle which supported the mouthpiece and tubing. The  $VO_2$  was reduced for drafting cyclists by  $18 \pm 11\%$ ,  $28 \pm 10\%$  and  $26 \pm 8\%$  at speeds of 32, 37 and 40 km/h respectively. Separation distance from the lead rider was of the order of 0.2 – 0.5m. There were negligible differences in drag reduction for cases where there were 1, 2 or 4 trailing cyclists inline. However, when cyclists were following a pack of 8 other cyclists or a vehicle the reductions in consumption were significantly greater. The oxygen consumption is affected by total resistance on the bicycle, not just aerodynamic resistance. Therefore it can be expected that reduction

in oxygen consumption will be less than the reduction in aerodynamic drag when comparing to literature. The result of 18% oxygen consumption reduction at 32 km/h is significantly lower than the drag reduction reported from experiments. However, given the relatively low speed compared to other experiments, aerodynamic drag will contribute less to the total resistance. This may explain why the oxygen consumption is reduced by less at 32km/h than at higher speeds. The results of 28 and 26% reduction at 37 and 40 km/h respectively are closer to the reported values of drag reduction. This fits with cycling power models, which indicate that the majority of a rider's power at racing speeds is expended in overcoming aerodynamic drag.

### ***Experimental Tools for the Investigation of Cycling Aerodynamics***

Existing literature investigating cycling aerodynamics has utilised numerous different methods. Track testing is the closest recreation of practical performance, but variability in parameters limits its application to the study of large scale changes. Smaller changes in force are easily hidden in the large uncertainty margin. It also lacks facility for studying the flow field. Computational Fluid Dynamics allows for tight control of parameter space. However, accurately replicating a pedalling cyclist remains a challenge. New techniques with sliding meshes make this a possibility, but the resources required for multiple rider problems and iterative changes to parameters such as spacing and geometry present a high degree of difficulty. Such a complicated simulation also requires validation against accurate experimental data. Wind tunnel testing offers practical testing of real athletes with exact recreation of posture, geometry and dynamics but with more a more controlled parameter space than track testing. Experiments also provide direct measurement techniques for both force and flow data that could potentially be used in the future for validation of computational simulations.

## **1.4 Summary**

Aerodynamics is critically important to cycling performance. The governing power equation for cycling shows that at elite racing speeds, at least 90% of total resistance acting on a cyclist is aerodynamic drag. Even at relatively lower speeds, such as is the case for commuting, aerodynamics still comprises the majority of the resistive load. Therefore an understanding of aerodynamics in cycling is important not only for elite performance, but in terms of optimising cycling as a transport solution.

The evolution of cycling equipment and riding posture has led to significant increases in speed over the past three decades. This is particularly evident in the progression of the cycling hour record and shows the practical importance of aerodynamics. Several authors have investigated the effects of changes to cyclist posture and equipment on performance, with the athlete posture having a much larger effect on the total drag of the system (Kyle & Burke 1984, Zdravkovich et al. 1996, Grappe et al. 1997, Gibertini and Grassi 2008, Gibertini et al 2008, García-López et al. 2008, Oggiano et al. 2008, Blair & Sidelko 2008, Underwood et al 2011, Defraeye et al. 2010, Chabroux et al. 2012, Underwood and Jermy 2013, Barry et al. 2014, Zdravkovich 1992, Sayers & Stanley 1994, Tew & Sayers 1999, Forrester 2008, Jermy et al. 2008, Barry et al. 2012). Recent work has provided a detailed characterisation of the flow field around a static cyclist (Crouch et al. 2012, 2014). This has shown that the wake structure and drag varies as a function of the leg position around the crank cycle.

Understanding of the interaction effects between multiple cyclists has received relatively less attention but is, however, no less important. The aerodynamics of individual cyclists has been studied from the perspective of individual time trial performance. Such events are conducted at maximum exertion where the athlete is isolated. It is simpler to model the performance of an individual and the effects of aerodynamic optimisation are more directly evident. However, the majority of road cycling races are mass start with riders travelling in close proximity. This also occurs in track events and specific team events, such as the team pursuit and team time trial. This leads to the overarching question of this research:

### ***How are the aerodynamics of a cyclist influenced by the presence of another rider?***

Existing work on cycling specific interactions is limited, but has shown that drag is a strong function of spatial separation. This is consistent with other bluff bodies and ground vehicles. However, there is large variation in the reported drag reductions for cyclists in a tandem formation due to the range of techniques and methodologies used, and the limitations associated with each. For a cyclist at minimum separation results have reported a drag reduction in the range of 14% to 49%. At the greater separation distance of one bicycle length the range is still large, reported to be between 12% and 28%. Furthermore, to date, there has been no investigation of the forces acting on cyclists travelling side-by-side and associated staggered positions encountered during overtaking. This leads to the first specific research question:

*How does cyclist drag vary as a function of relative spatial position?*

Existing research on aerodynamic interactions between ground vehicles has shown that drag reduction is influenced by geometry, as well as spatial position. Edwards & Byrnes (2007) also showed that the magnitude of drag saving for a trailing rider is a function of the relative size of athletes. Extensive testing on single cyclists has shown that drag varies with riding posture. Blocken et al. (2013) and Defraeye et al. (2014) also showed that there is a geometric dependence of drag reduction on posture for cyclists in a team formation. Therefore, it follows that changing rider posture within a group may have a significant impact on the drag interactions between team members. However, the drag interplay between riders in a team has not been investigated in detail to date. This poses the question:

*How does cyclist geometry and posture influence drag interactions within a team?*

Interaction between multiple cyclists have been shown to have a strong influence on the drag. However, the mechanisms responsible for these changes have received little attention. Crouch et al. (2014) have shown that the flow field around a cyclist is a complex function of the leg position. However, an understanding of how the flow field around cyclists travelling in close proximity varies from the single rider case remains largely absent from the literature. An understanding of the flow field around tandem cyclists will provide understanding to the origins of changes in force and has potential applications to other complex bluff body flows. This leads to two key questions:

*How does the presence of another rider influence the flow field around a cyclist?*

*What flow mechanisms are responsible for the observed changes in drag?*

To date there has been little consideration of the effect of a cyclist's dynamic leg motion on the aerodynamics. Many studies have used static and dynamic cyclists interchangeably in aerodynamic testing. Crouch et al. (2014) showed that the flow field, and subsequently drag, vary with leg position in static tests. However, the effect of the leg dynamics on drag and the evolution of wake flow structures have not been well explored. This leads to a final question:

*How does the dynamic leg motion of cycling influence the aerodynamics of a cyclist and interactions with others?*

The research proposed aims to further the current frontier of knowledge surrounding aerodynamic interactions between cyclists. Experimental investigations were designed to answer each of these questions in turn to develop a knowledge base surrounding aerodynamic interactions in cycling. This begins with a comprehensive investigation of the force variation between two cyclists. This is followed by investigations aimed at understanding how our knowledge of the changes in the flow field around a single rider can also provide explanations for the resultant drag found when cyclists travel in close proximity. This will provide better understanding for optimisation of cycling performance in team and group riding scenarios. It also has the potential to provide insight for the interactions between other complex geometry bluff bodies.

## Chapter 2

### Experimental Methodology and Equipment

This section will discuss the experimental methodology, facilities, apparatus and test subjects used for the various experimental investigations undertaken to answer the key research questions of the project. It will begin with a description of the facilities, force balance rigs and equipment that were used across the experiments. This will be followed by the detailed methodology for each individual experiment.

Two key research facilities were utilised during the course of this research; the Monash University Wind Tunnel and the FLAIR water channel. A methodology is outlined for the correction of force measurements of multiple tandem bodies in an open-jet wind tunnel. Due to the different needs of each experiment two different force balance and mounting rigs were utilised during wind tunnel testing; the Single Rider Cycling Rig and Multi-Rider Cycling Rig. Different experiments also necessitated different wind tunnel configurations, resulting in differing flow profiles for each setup. Following the detailed facility description and characterisation the key pieces of apparatus utilised in experiments are described. The cyclist participants used during this investigation are then outlined, including the Monash Anthropomorphic Mannequin. Subsequent to the description of facilities, equipment, apparatus, and participants the specific methodology for each individual experiment are then outlined.

## 2.1 Monash University Wind Tunnel

All wind tunnel experiments were conducted in the Monash University Large Wind Tunnel (MUWT or wind tunnel). This facility is a three-quarter open jet, closed circuit, recirculating wind tunnel. Flow is driven by two 5m diameter axial fans rotating in the same direction. Each fan is powered by two DC electric motors with a combined maximum power of 1.4 MW. A tunnel schematic is shown in Figure 2.1.1. Maximum wind speed in this test section is approximately 180 km/h, significantly in excess of that required for cycling testing.

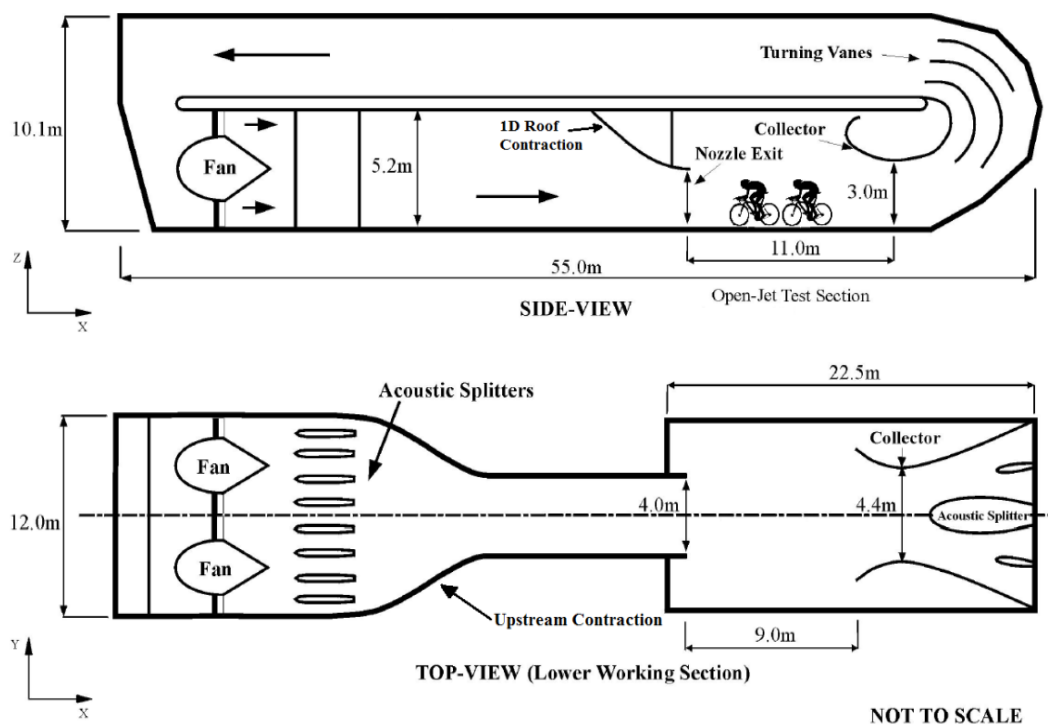


**Figure 2.1.1** - Schematic of the Monash University Wind Tunnel showing cyclists in primary test section (Gilhome 2002)

The wind tunnel has a two stage contraction. Upstream there is a two dimensional contraction followed by a one dimensional contraction from the roof into the nozzle of the main open-jet test section. Ongoing development of the facility, set up timing issues and separate requirements for different experiments meant that different wind tunnel configurations (size) were adopted (Table 2.1.1).

**Table 2.1.1** - Tunnel configurations that apply to each experimental investigation (refer to Section 2.7).

	Jet Dimensions	Experiments	Test Rig
<b>Configuration 1</b>	2.6 m high by 4 m wide	2.7.1, 2.7.2, 2.7.3, 2.7.7	Single Rider Cycling Rig
<b>Configuration 2</b>	3.2 m high by 4 m wide	2.7.4	Multi-Rider Cycling Rig
<b>Configuration 3</b>	3 m high by 4 m wide	2.7.2, 2.7.5, 2.7.8	Multi-Rider Cycling Rig

Descriptions of specific experimental studies will detail the setup in place for each (Section 2.7). These will be described in the following sections. Tunnel configuration slightly altered the flow conditions for the experiments. Freestream velocity was corrected on an individual experiment basis to account for any changes to setup and so this was factored into calculation of force coefficients.

Dynamic pressure in the wind tunnel is measured by an array of 6 Pitot static tubes mounted upstream of the final contraction. By positioning probes upstream of the primary test section it ensures that the presence of the model and apparatus does not influence the pressure field at the Pitot tubes. For each experimental investigation a Pitot static tube is used to correlate the upstream velocity at the Pitot array to the freestream velocity in the test section. The calibration pitot is mounted in the test section at the test location and dynamic pressure recorded. This is then mapped against the upstream response to determine a relationship. This allows dynamic pressure to be measured upstream, independent of influence from the model and without a probe in the test section.

Dynamic pressure is measured from the Pitot tubes using a differential pressure sensor. Two sets of three pitot tubes mounted on each wall of the tunnel feed into two individual pressure transducers (ABB 600 T series Smart Pressure Transmitters). A thermo-couple upstream of the test section is used to measure temperature. A digital barometer measures barometric pressure in the wind tunnel control room. This data is used to calculate the air density in the test section and subsequently the flow velocity is computed from the dynamic pressure.

## **2.2 Flow Corrections for Tandem Bodies in an Open Jet Wind Tunnel**

As a result of testing in a finite volume, all wind tunnel tests have limitations in terms of recreating accurate flow conditions to simulate an atmospheric flow field. To compensate for these changes to the flow, numerous authors have developed correction methods to apply to force measurement in a wind tunnel (see Glauert 1928, 1933, Mercker & Wiedemann 1996, Cooper 1998, Mercker et al. 2005). Due to the differences in flow profile, these corrections are different for open and closed jet wind tunnels. Mercker and Wiedemann (1996) developed a detailed correction methodology for the automotive testing in an open jet wind tunnel. As such this methodology is suitable for application to general bluff body testing. However, this technique was designed for a single body. Additional considerations are necessary for testing multiple bodies in tandem with simultaneous force measurement.

The investigation of a four cyclist team introduces a more complex set of parameters for correcting finite jet effects. Care must be taken as the lead body is a significant distance from the rear body and so is potentially subjected to very different flow conditions. The method of Mercker & Wiedemann (1996) and Mercker et al. (2005) was adapted for specific application to multiple tandem bodies such as a team of cyclists.

In their original work Mercker & Wiedemann identified 5 separate effects that distort the flow field conditions from that of an idealised infinite stream. These are jet expansion, nozzle blockage, jet deflection, collector blockage and horizontal buoyancy. A perturbation velocity term ( $\epsilon$ ) is defined for each effect to correct the drag results measured in an open jet wind tunnel. Each of these is outlined briefly. For full description consult Mercker and Wiedemann (1996) and Mercker et al. (2005). These figures are reprinted with permission from SAE paper 960671 © 1996 SAE International. This paper may not be printed, copied, distributed or forwarded without permission from SAE.

### **2.2.1 Finite Stream Effects**

#### ***Jet Expansion***

Jet expansion is a solid blockage effect but in an open jet tunnel it has the opposite effect to a closed jet tunnel. With a model present in the test section the upper streamline is distorted to accommodate the model volume. This causes an over expansion of the jet. Continuity informs that this will result in a lower local velocity than would be experienced in an infinite jet and thus a lower drag will be measured.

$$\epsilon_S = \tau \left( \frac{V_M}{L_M} \right)^{\frac{1}{2}} \left( \frac{A_M}{A_N} \right)^{\frac{3}{2}} \quad 2.2.1$$

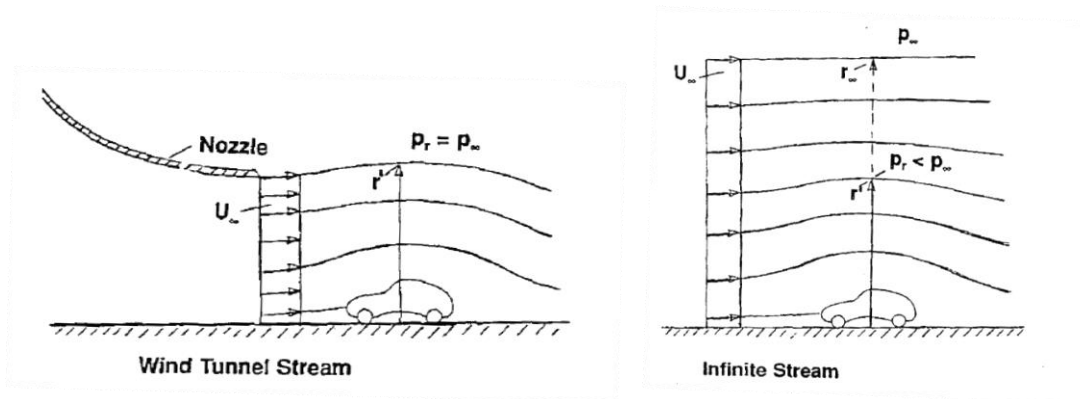


**Figure 2.2.1** – The stream in an open jet tunnel (left) and an ideal infinite stream (right) – (Mercker and Wiedemann 1996)

### Nozzle Blockage

In open jet testing, as opposed to closed jets, the model is often positioned close to the nozzle exit. The high pressure region ahead of the model may extend upstream and into the nozzle. This induces a solid wall blockage similar to a closed tunnel. The area for the exit flow is effectively reduced which speeds up the flow at the exit of the jet. This effect is felt at the model as a far field interference effect. Mercker et al. modelled this effect using Biot-Savart principles with the nozzle replaced by a vortex ring.

The perturbation velocity at the nozzle is described by;

$$\epsilon_Q = \left( \frac{A_M}{2A_N} \right) \left[ \frac{1 - x_S}{(x_S^2 + R_N^2)^{\frac{1}{2}}} \right] \quad 2.2.2$$

$$\text{Where } x_S = x_{LE} - \frac{L_M}{2} + \left( \frac{A_M}{2\pi} \right)^{\frac{1}{2}}$$

The induced velocity at the model position as a result of the perturbation is then;

$$\epsilon_N = \epsilon_Q \frac{R_N^3}{(x_{LE}^2 + R_N^2)^{\frac{3}{2}}} \quad 2.2.3$$

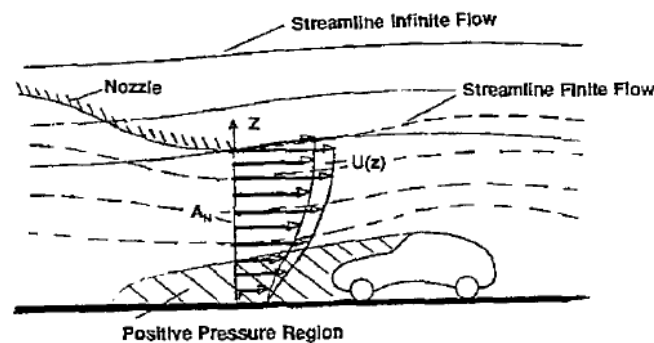


**Figure 2.2.2** – Nozzle blockage; distortion of streamlines due to positive pressure region ahead of a model (Mercker and Wiedemann 1996)

### Jet Deflection

Jet deflection is similar to the solid blockage that causes jet over expansion. The proximity of a model close to the nozzle will deflect the boundary streamlines further than for a model far from the nozzle exit. This results in further expansion of the jet and a lower drag force will be measured. The effect is modelled by calculating an effective jet area which is smaller than the actual nozzle exit area and using this in the jet expansion factor.

$$A^* = \frac{A_N}{1 + \epsilon_Q} \quad 2.2.4$$

$$\epsilon_S = \tau \left( \frac{V_M}{L_M} \right)^{\frac{1}{2}} \left( \frac{A_M}{A^*} \right)^{\frac{3}{2}} \quad 2.2.5$$

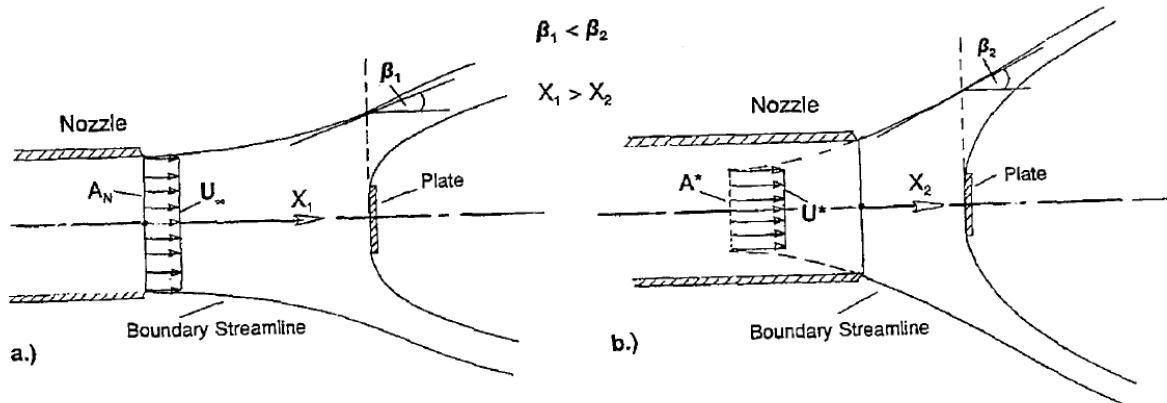


**Figure 2.2.3** – Jet deflection due to proximity of a model; a) Nozzle at infinity; b) model close to nozzle (Mercker and Wiedemann 1996)

### Collector Blockage

The collector blockage effect is analogous to the nozzle blockage described above. If the model is sufficiently close to the collector the wake will extend into the collector and cause a solid blockage; constraining the flow. This is experienced at the model as a far field interference effect. The equations for calculating the influence are similar to those for the nozzle.

$$\epsilon_W = \frac{A_M}{A_C} \left( \frac{C_D}{4} + b \right) \quad 2.2.6$$

Where 'b' is a constant for far field wake effects. For bodies with a small wake (such as fast-back cars) this constant can be neglected. For regular vehicles Mercker and Wiedemann state this at a value of 0.41.

$$\epsilon_C = \epsilon_W \frac{R_C^3}{(x_{TE}^2 + R_C^2)^{\frac{3}{2}}} \quad 2.2.7$$

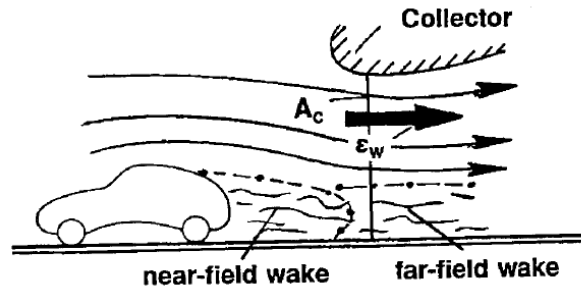


**Figure 2.2.4** - Collector blockage; flow constrained by downstream presence of wake volume (Mercker and Wiedemann 1996)

### **Horizontal Buoyancy**

Due to the expansion and contraction as the nozzle and collector respectively, most open jet tunnels do not have a constant static pressure along the full test section length. This generates a gradient along the test section length. When a model is placed in the tunnel, the static pressure generates a force on the model that corrupts the measured drag force. This axial force is termed horizontal buoyancy, or solid body buoyancy. This can be corrected by mapping the static pressure gradient of the empty tunnel at the model location. Munk (1921) and Glauert (1928) showed that the pressure force actually acts on an effective volume that is greater than the actual model volume. The Glauert factor ( $G$ ) is used to account for the increased effective volume of the body on which the pressure forces act.

$$\Delta C_{D,HB} = G \frac{V_M}{A_M} \cdot \frac{dc_p}{dx} \quad 2.2.8$$

Where:  $G = 1 + 0.4 \frac{t}{L_M}$

$$t = 2 \sqrt{\frac{2 A_M}{\pi}}$$

In their follow up paper (Mercker et al. 2005) the authors propose that horizontal buoyancy effects can also act on the wake of a bluff body. The presence of a horizontal pressure gradient over the wake region can distort the wake which alters the base pressure and subsequently the drag of a model. However, due to the relatively small volume of a cyclist wake, compared to a vehicle for which this methodology was intended, this effect will be small and so has been neglected from these corrections. This was confirmed by empirical tests (See Appendix A).

### ***Application of Correction Terms***

Once all of the relevant correction factors have been calculated they can be applied to the measured velocity and drag force to minimise the interference and approach the results for an infinite jet.

$$U_{corrected} = U_{\infty}(1 + \epsilon_S + \epsilon_N + \epsilon_C) \quad 2.2.9$$

$$q_{corrected} = q_{\infty}(1 + \epsilon_S + \epsilon_N + \epsilon_C)^2 \quad 2.2.10$$

$$C_{D,Corrected} = (C_{D,M} + \Delta C_{D,HB}) \frac{q_{\infty}}{q_{corrected}} \quad 2.2.11$$

These corrections are defined for incompressible flow and are all approximate. They are assumed not to interact with each other. As such they are defined for relatively small corrections where the model is sufficiently smaller than the test section. For a complete description of the methodology see Mercker and Wiedemann (1996).

## **2.2.2 Applications to Multiple Tandem Body Testing**

### ***Velocity Perturbations***

The four velocity perturbation factors described by Mercker & Wiedemann (1996) are the representation of deflection of the flow streamlines which results in differences from an ideal infinite jet. Each is a result of the presence of a model within the test section deflecting the boundary streamlines. Whilst the final rider is a long distance from the nozzle and their individual influence on distortion at the nozzle will be small, it is the presence of the three riders upstream, particularly the leader, which will be impacting on the nozzle interference and jet deflection. The lead rider may be the primary contributor to the deflection of streamlines at the nozzle, but the distortion to the velocity field then acts by all subsequent bodies downstream. The reverse case can be applied to collector blockage effects. These distortions affect the entire velocity field and are due to the presence of whatever objects are placed in the test section. As such, when calculating the velocity perturbations for the 4 rider team, or any other multiple body case, it can be treated as a single body. In the presented equations for perturbation factors the model dimensions should describe the team of bodies. For the case of collector blockage, the drag coefficient used was the sum of the values for all 4 cyclists. This represents a conservative case for the long model volume.

An important consideration for the correcting the velocity interference is the method for determining velocity. The wind speed in the test section of the tunnel is correlated to the speed upstream so that velocity can be monitored during tests without the model interfering with the freestream flow around the probe. For this testing the velocity in the test section was calibrated to the upstream pitot tubes with the base rig already in place. As such, any interference effects due to the rigs presence in the test

section are empirically built in to the correlation factor between the upstream velocity and the test section. Therefore, the dimensions used for the calculation of the velocity perturbation factors need only include the values for the cyclists and not the additional volume and area of the test rig. If the velocity calibration was to be performed on an empty tunnel prior to the rig being installed then the calculation of the factors would need to include all items in the tests section; both test subjects and supporting rig. The location of the reference velocity measurement is also an important consideration. If close to the nozzle exit, a large model may have a pressure field that extends upstream (nozzle blockage) and corrupts the wind speed measurements. This is not a concern at the MUWT as the reference velocity is measured far upstream.

### ***Horizontal Buoyancy***

As is common with open jet wind tunnels, the static pressure in the Monash tunnel varies along the test section length. Generally for automotive testing in such a tunnel, the horizontal buoyancy force is relatively small as the static pressure gradient tends toward zero across the middle of the test section. Such a profile is evident in the MUWT and is discussed in Section 2.3. However, close to the nozzle and collector there is a significant gradient and this will impact long models or testing of multiple bodies such as the team of cyclists. In the case of the cyclists the gradient acting over riders 2 and 3 is small but the lead rider is close to the nozzle and the trailing rider to the collector and there are significant gradients over these regions. To account for this, each cyclist requires an individual correction for static pressure forces. This is unlike the velocity perturbations which require a global set of corrections. For the cyclists the pressure gradients were calculated across the bicycle wheelbase. This is a better representation of the length of the bluff body component as the total bicycle length includes a large volume of empty space due to the wheels extending further up and downstream of the cyclist's body. Static pressure gradients were determined by measuring the static pressure at the hub of the front and rear wheel for each position along the rig. From these values, individual horizontal buoyancy correction factors were calculated for each of the 4 cycling rig mounting locations. Static pressure was measured in the empty tunnel. This is the conventional approach for horizontal buoyancy corrections as it eliminates interference due to the model pressure field. Assuming an equal pressure field upstream and downstream of the model, gradients measured in this way should be representative of the gradients during model tests.

It is noted that the rear rider is close to the collector and therefore in a higher gradient region of the pressure field. This has the potential to lead to greater error in force measurements for the final position. However, validation of the correction methodology in Appendix A shows that the applied method results in only small errors (0.6%) due to different pressure gradients over the final rider position. Furthermore, the corrected drag at Position 4 resulted in a calculated error of only 0.75% relative to the forward 3 positions. In addition, measurements in this research are primarily differential from a reference state and so errors due to collector effects are assumed to be small.

### ***Simplifications to Terms in the Correction Equations***

Some simplifications were applied in the calculation of terms within the correction methodology. However, the magnitude of error associated with these approximations has a small impact on the overall correction factor. The volume of each cyclist and their bicycle was not known so an approximate value of  $0.075\text{m}^3$  was applied for all riders. This is based on an average adult male density of  $1050\text{ kg/m}^3$  (Ward 1967) and an average rider mass of  $71.5\text{kg}$  calculated from the athletes used in this research (Athlete's A-D). In addition to the athlete there is also the volume of the bicycle which is difficult to determine but is a relatively small proportion of the total system. The difference in volume between the heaviest and lightest riders equates to an error of less than 0.25% error in the buoyancy correction term. This was deemed to be appropriate for this testing given the uncertainty in drag due to variations in athlete body position. It is acknowledged that it would be possible to refine the interference corrections based on the actual athlete mass and assuming a constant bicycle volume. For alternative bodies where precise mass is known it would be possible to individualise the corrections to each specific body. The frontal area of the cyclists was approximated at  $0.45\text{m}^2$  based on the frontal surface area of riders of similar dimension (Debraux 2008, Zdravkovich et al. 1996, Crouch 2012, 2014, Barry 2014). This is complicated for cycling testing as the area varies with position in pedal stroke and the different size of each rider, in addition to postural changes that may be applied. Due to the small error these approximations contribute to the overall result, relative to the uncertainty associated with athlete testing, further refinement of the corrections was deemed unnecessary. These same approximations were used in the calculation of the velocity perturbation factors. Similarly, the error arising from using constant values for all cyclists is small compared to the correction shift. A 10% change in frontal area results in a 0.25% change in  $C_D A$  ( $0.0006\text{ m}^2$  for the lead cyclist) and a change in the delta by approximately 0.01%.

### ***Implementation of Correction Methodology***

The 4 rider team testing (see Section 2.7.4) was conducted with a truncated false floor plain that ended immediately downstream of the final rider. To determine the effect of the floor conditions on the results a set of comparison tests were conducted with a 2.3m extension to the ground plane with riders in positions three and four only. The changed ground plane had a significant effect on the static pressure gradient, reversing the gradient across the final rider. There was also an associated change in force for the rider in the fourth position. However, after applying the correction methodology outlined above to the two data sets with two different buoyancy corrections the drag measurements converged. This resulted in an error of 0.6% for both riders between the two floor conditions. In this test procedure the average uncertainty in back-to-back repeatability was 0.6% which is dominated by the variations associated with dynamic athletes. Since the error for the different floor conditions is within the order of the experimental uncertainty it was concluded that any error due to wake buoyancy effects is small and thus it is acceptable to neglect wake effects for this work. It is noted that this is a special case and wake buoyancy effects will not be negligible for all other bluff body cases. A validation of the technique can be found in Appendix A.

## **2.3 Cyclist Mounting and Force Measurement**

The Monash University Wind Tunnel is used for many different applications and has flexibility in terms of test configuration depending on the project. For cycling testing in this research two different rigs were used to mount the cyclist in place and measure aerodynamic loads.

### **2.3.1 Single Rider Cycling Rig**

The single rider cycling rig was developed for the measurement of aerodynamic loads acting on a single cyclist (see Figure 2.3.1). It utilises the wind tunnels inbuilt Kistler (Kistler Instrumente AG Type 9067 3-Component Force Sensor) load cell array to measure the aerodynamic loads. These are a solid state quartz force sensors. They have high range, high rigidity and small cross talk between channels (specifications in Table 2.3.1). Using these in an array of 4 allows the aerodynamic moments to be determined. The four load cells were arranged in a rigid steel sandwich plate to distribute the loads. From the four sets of forces the full 6-axis of aerodynamic loads can be determined. The upper surface of the sandwich plate arrangement provides a rigid mounting point for a range of test bodies. Depiction of the cycling apparatus is shown in Figure 2.3.2.



**Figure 2.3.1** - Single Rider Cycling Rig with bicycle mounted on force balance with athlete

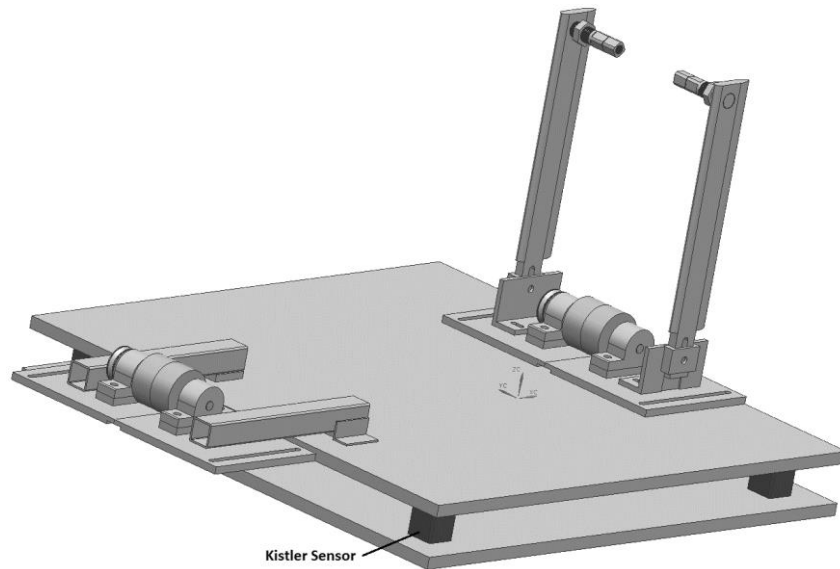


**Figure 2.3.2** – Schematic of Single Rider Cycling Rig showing load cells in sandwich plate and bicycle mounting apparatus

**Table 2.3.1** - Technical Data for Kistler 906x Series Force Sensors

Range		$\pm 20$ kN
Threshold		$< 0.01$ N
Sensitivity		8 pC/N
Linearity		$\leq 0.5$ % FSO
Hysteresis		$\leq 0.5$ % FSO
Cross Talk	$F_z$ into $F_x, F_y$	$\leq 1$ %
	$F_x$ and $F_y$	$\leq 3$ %
	$F_x, F_y$ into $F_z$	$\leq 2$ %
Temperature Sensitivity		-0.02 %/ $^{\circ}$ C

For cycling tests a set of rollers is mounted to support the front and rear wheels of the bicycle. For athlete testing, a pair of struts held the rear axle of the bicycle fixed in place. This holds the rear of the bicycle rigid, however, the front wheel does have some degree of movement through flex in the bicycle and rig frame. This means that the athlete must provide control inputs into the bicycle to keep the front wheel as still as possible during testing. Whilst the movement of the front wheel does introduce some variability into the setup, this setup is advantageous as it limits the amount of interfering rig structure. The use of struts on the front wheel introduces additional rig structure that contributes additional drag that is not representative of true bicycle drag. Front struts also introduce an upstream disturbance ahead of the rest of the bicycle. Rear struts have minimal components of the rider and bicycle system further downstream and so provide minimal interference. Rollers under front and rear wheels of the bicycle were connected by a drive belt. The pedalling of the athlete would drive the rear wheel and in turn the front wheel via the rollers and belt. This ensured that front and rear wheels rotate at the same speed.

For a description of the force calibration procedure see Appendix B.

### **Velocity Profile**

The Single Rider Cycling Rig was fitted with a flat stationary ground plane to house the force measurement and rig supporting structure which sat above the wind tunnel floor. The elevated ground plane had a bevelled leading edge which helped to minimise the height of the boundary layer (see Figure 2.3.1).

To date there have been no published works to investigate the effect of ground boundary layer treatment on the drag of a cyclist. However, given that the majority of a cyclist volume, and the dominant wake region, are positioned at a large distance from the ground plane, there is a reduced effect of the flow interacting with surface. The near ground region of a bicycle is occupied only by the lower wheels and lower leg. The displacement thickness of the boundary layer is only a small proportion of the overall height of the cyclist. For the Single Rider Cycling Rig, boundary layer displacement thickness at the centre was 12.5mm. This is only slightly greater than the thickness of the tyre. It is therefore assumed that the static ground plane has a negligible influence on the drag of a cyclist measured in a wind tunnel. Figure 2.3.3 below shows the velocity profile for the Single Rider Cycling Rig. As reference, a cyclist on bicycle has a height of the order of 1500 mm to the top of the helmet.

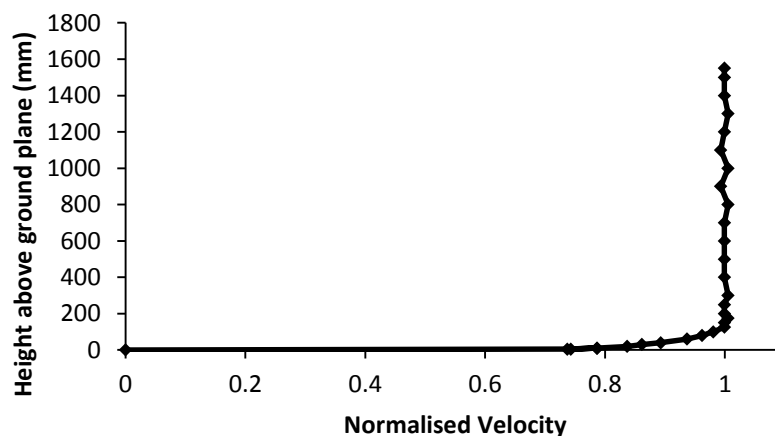


**Figure 2.3.3** - Velocity profile at the centre of Single Rider Cycling Rig

### **Static Pressure Profile**

The pressure profile of the tunnel test section was also characterised to determine the axial variation in static pressure. Static pressure was measured using a calibrated Pitot static tube. This was mounted to a stand above the ground plane boundary layer and positioned along the centreline of the wind tunnel test section. As described earlier (Section 2.2), large gradients in static pressure over the cyclist can induce a horizontal buoyancy force which will affect drag measurements. Figure 2.3.4 below shows the static pressure coefficient in the MUWT test section. This profile is typical of open jet wind tunnels (eds Tropea et al. 2007).

For testing with the Single Rider Cycling Rig the cyclist is positioned in the centre of the test section. It can be seen that the change in static pressure over a model in this position is small. This is desirable as it minimises the error in drag measurement.

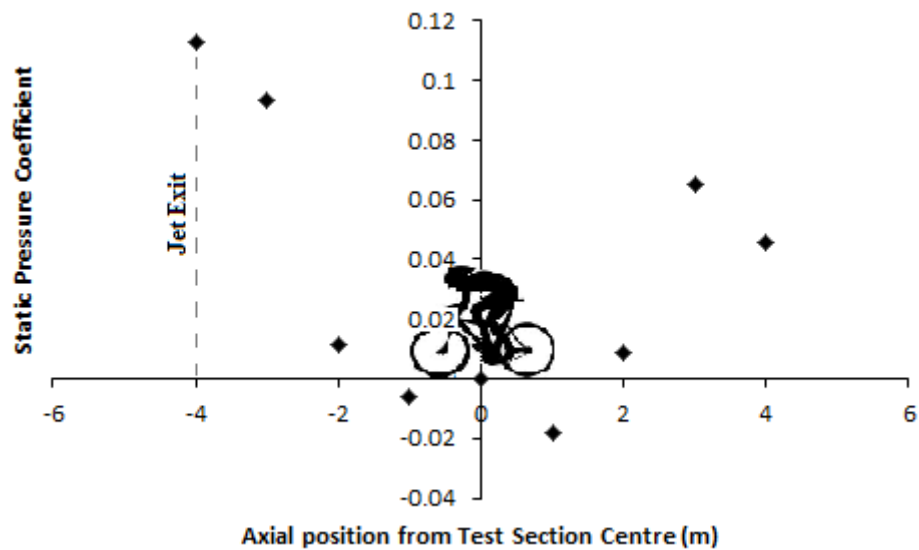


**Figure 2.3.4** - Static Pressure Coefficient ( $C_p$ ) in the MUWT test section with Single Rider Cycling Rig installed

Using the horizontal buoyancy correction described earlier, the resulting correction equates to a 0.3 % change in  $C_D A$  ( $0.0006 \text{ m}^2$ ). Given the relatively small shift, and the fact that results from this work are presented as differential drag, being a shift from a reference condition, the effect of horizontal pressure gradient is sufficiently small so as to have a negligible effect on the results and have been neglected.

### 2.3.2 Multi-Rider Cycling Rig

To meet the specific needs of this research an additional test rig was required that could measure loads on multiple cyclists simultaneously, with specific applications to cycling events such as the four rider team pursuit. A rig was developed at Monash University that allows for the measurement of axial force (drag) on four cyclists simultaneously (see Figure 2.3.5). The rig utilises a series of planar air bearings in two planes to isolate the axial force component. Air bearings offer a great benefit in force balance design as they can accommodate large loads, in this case in the vertical and lateral directions but allow near frictionless motion in the axial direction. A linear single axis strain gauge was then used to measure loads on the suspended plate. This system has an instrumented platform to which a range of models can potentially be attached. In this case a system similar to that described earlier for the Single Rider Cycling Rig was employed. A roller was positioned under the front and rear wheels of the bicycle to allow the wheels to rotate. A timing belt arrangement connected the front and rear rollers whilst allowing for adjustment to the wheel base of the system. This belt connection meant that the

pedalling of the rider would drive the rear wheel and in turn rotate the front wheel at the same speed. The bicycle was held in place by a pair of struts at the rear axle. The fixed rear struts hold the bicycle firmly in place and provide a constant load transfer to the instrumented platform. This setup minimises the amount of interference from the supporting rig by only having a single set on the rear axle.



**Figure 2.3.5** - Multi-Rider Cycling Rig shown with mannequin mounted at Position 1. Struts are visible for each of the four force balances that mount at the bicycle rear wheel.

The Multi-Rider Bicycle Rig uses four of these individual balances in series to allow the mounting of four cyclists in a tandem formation. The four rigs were securely mounted to a sub-frame to ensure rigs were stable and level after each installation. This resulted in fixed separation distance between cyclists. Distance was set at approximately 100mm. This would vary slightly depending on bicycle wheelbase. As the wheelbase for each rig was adjustable it could alter the separation distance up to 50mm. It will be shown that, at small separation distances below 200 mm the change in drag as a function of downstream distance is very small. Therefore this is an acceptable simplification as it does not significantly affect the drag of either cyclist.

For details of the calibration of the Multi-Rider Cycling Rig see Appendix B.

### ***Ground Plane***

The four individual rigs were housed in a continuous fairing with static ground plane elevated above the wind tunnel floor (see Figure 2.3.5 above). This ground plane extended 2 m upstream of the lead cyclist. This protruded upstream into the nozzle. A sharp bevelled leading edge and elevated ground plane helps to assist in the minimisation of the boundary layer height. However due to the length of the rig, there is still some growth of the boundary layer over the trailing cyclists. Given that the majority of cyclist drag and the volume of the cyclists are elevated well above the ground plane it is assumed that the static ground plane and associated boundary layer have small influence on the drag. Even at the heights seen for the fourth rider position, this is well below the torso and so the effect is assumed to be small. It is noted that due to structural changes to the tunnel during the course of this

research, this rig was used with two different jet configurations. This resulted in slightly different flow profiles which will be presented in the following sections.

### Velocity Profiles

Two different jet configurations were used with the Multi-Rider Cycling Rig as a result of ongoing development of the wind tunnel. As a result two slightly different flow profiles exist for this rig. Given the high ground clearance of a cyclist and the nature of the individual experiments these changes are not expected to have a great effect on the results.

Testing with the 4 rider team pursuit simulation was conducted with a unique jet setup; Configuration 2 (See Section 2.3.4). This had the jet exit raised to a height of 3.2 m. The top wall of the nozzle protruded further downstream than the side wall sections. The velocity profiles at each bicycle mounting position as well as an upstream point close to the jet exit show that the boundary layer is uniform over the full length of the rig (see Figure 2.3.6). Displacement thickness at each location was 43.2, 43.8, 38.3, 40.1 and 30.7 mm for 1m downstream of the jet, and Positions 1 to 4 respectively. This equates to less than 3% of the total height. It would be expected that there would be growth in the height of the boundary layer with distance downstream, however this is not seen in this profile. It is suggested that this is occurring due to the pressure gradient over the rear of the rig in this configuration.

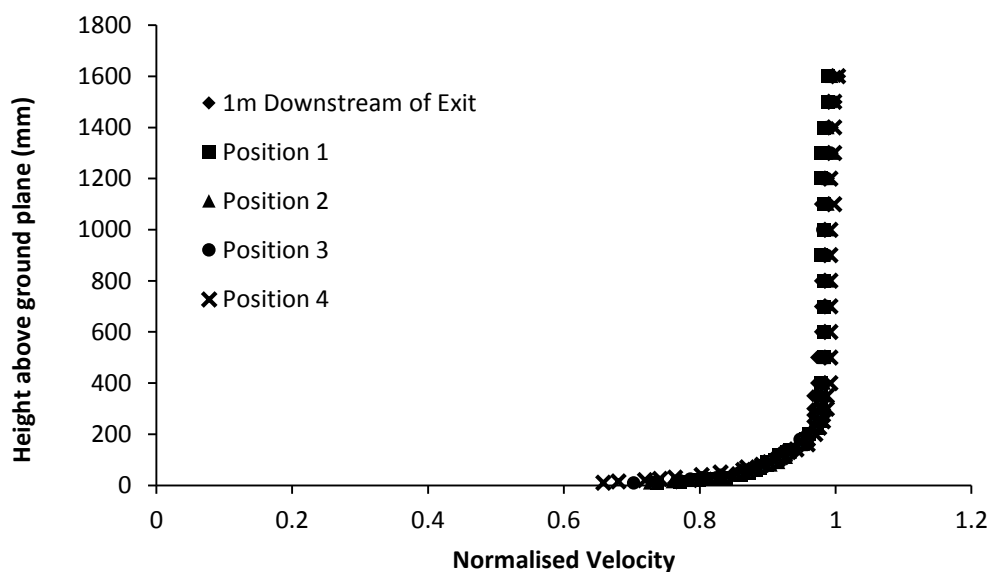
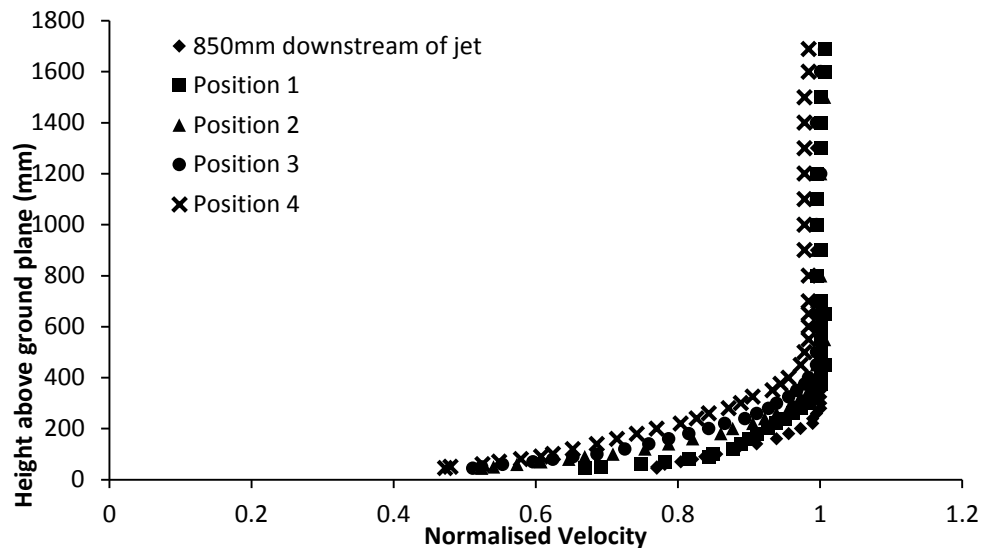


Figure 2.3.6 - Velocity profiles on the centreline of the Multi-Rider Cycling rig at Wind Tunnel Configuration 2.

All other testing conducted on the Multi-Rider Cycling Rig was conducted with Configuration 3. This jet setup resulted in a nozzle exit of 3 m x 4 m with an extended constant area section before the exit. This was seen to affect the velocity profile over the rig. Figure 2.3.7 shows the velocity profiles at each bicycle mount location, as well as an upstream position closer to the jet exit. It can be seen that the velocity profiles are no longer uniform over the whole rig as there is some growth with distance downstream. Boundary layer is greatest at the last rider location (Position 4) where uniform velocity

is achieved above 450mm. This is higher than the leading positions, however, due to the nature of the bicycle setup, this is still well below the height of the cyclist torso where the primary wake structures are present. Displacement thickness at each position was 23.0, 27.7, 49.9, 61.4 and 104.9 mm for the upstream position close to the jet exit and Positions 1 to 4 respectively.



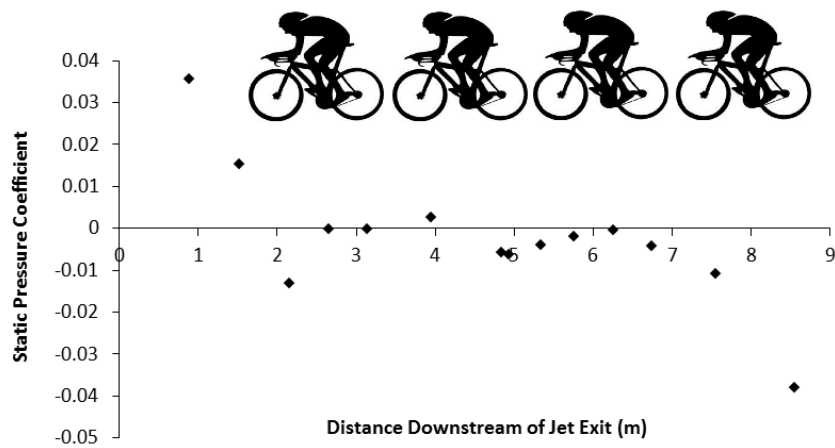
**Figure 2.3.7** - Velocity profiles on the Multi-Rider Cycling rig with Wind Tunnel Configuration 3.

### **Static Pressure Profiles**

Static pressure profiles also differed on the Multi-Rider Cycling Rig due to the changes in jet setup and small changes with rig setup. The axial static pressure gradient through the tunnel is particularly important for this rig as multiple bodies are instrumented at different positions in the test section. This can result in variation in flow conditions for different bodies in the test section and potentially inconsistent error in drag measurement.

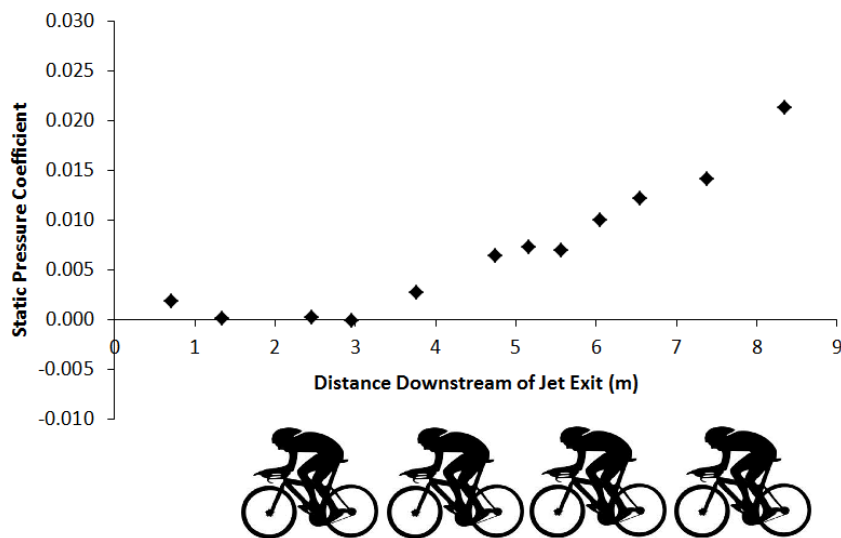
Static pressure was measured by installing pressure taps into the ground plane along the length of the rig. This allowed pressure to be measured simultaneously and eliminated temporal variations. Pressures were referenced to the wind tunnel plenum static pressure. Pressures were measured using a digital pressure measurement system (TFI DPMS). Vertical traverses at each rig location showed that static pressure gradients along the rig did not vary significantly with height. Therefore measuring static pressure gradients at the ground plane are representative of distribution over the cyclists.

Figure 2.3.8 shows the static pressure profile for the rig with the MUWT in Configuration 2 as used in the 4 rider team pursuit tests. The cyclist silhouettes indicate the axial position of the cyclists on the rig. It can be seen that static pressure decreases dramatically from the jet exit due to over expansion, before stabilising and being close to constant over the centre of the test section. However, at the rear of the rig there is a further pressure drop. This was due to the back of the rig which was truncated close to the rear cyclist. Due to the variation in pressure gradients over the four balances it was necessary to apply corrections for horizontal buoyancy as described in Section 2.2 above.



**Figure 2.3.8** - Longitudinal static pressure distribution over the Multi-Rider Cycling Rig in Configuration 2.

Configuration 3 in the wind tunnel with the Multi-Rider Cycling Rig resulted in a different static pressure profile across the rig. This is shown in Figure 2.3.9 below. The cyclist silhouettes indicate the location of the 4 rig positions within the test section. It is seen that the pressure gradient is quite constant over the first half of the rig before steadily increasing towards the back. The flat profile at the jet exit is the result of the jet redesign. This has greatly reduced the upstream pressure gradient. The other significant change is the downstream pressure which steadily increases towards the back of the rig. This is due to the change in the ground plane of the rig which was extended further downstream. This resulted in the collector effect dominating the pressure over the rear of the test section and resulting in increasing static pressure approaching the collector. The presence of these pressure gradients will affect the drag on the cyclists, particularly the trailing riders. It was therefore necessary to correct the measured drag using the method described in Section 2.2 above. Note that the methodology does not change, but the calculated correction factors will differ depending on the pressure gradient applied.



**Figure 2.3.9** - Longitudinal static pressure distribution over the Multi-Rider Cycling Rig in Configuration 3

### 2.3.3 Repeatability of Drag Measurements

Due to the majority of this research being conducted with athlete participants, the major source of uncertainty in drag measurements was due variation in athlete body position. The variation in drag due to the athletes is significantly greater than uncertainty associated with the force balances.

As different athletes were used for different experiments the uncertainty associated with force measurements for each rig is experiment and athlete dependent (see Section 2.6 for descriptions of cyclists). To provide an indication of the total system uncertainty the mean uncertainty and standard deviation for each experiment is tabulated in Table 2.3.2 and 2.3.3 below. In all cases the data is looking at athlete baseline tests only. Results indicate the back to back repeatability of a given cyclist on each force balance rig. Note that this does not account for reproducibility over the course of test series.

In all cases the mean uncertainty associated with the athlete testing is less than 1% of the athlete's baseline  $C_D A$ . In fact, with the exception of two cases mean uncertainty is less than 0.5%. It is noted that Athlete D had noticeably higher variation in  $C_D A$  than other athletes. This is not a property of the Multi-Rider Cycling Rig force balances but is due to variation in the athlete's position between tests.

**Table 2.3.2** – Repeatability of baseline force measurements on the Single Rider Cycling Rig showing mean uncertainty and standard deviation ( $\sigma$ )

	<b>Athlete</b>	<b>Uncertainty</b>	<b>Uncertainty %</b>	<b><math>\sigma</math></b>	<b><math>\sigma</math> %</b>
2.7.1 Dynamics Part 1	E	0.0018	0.65	0.0025	0.92
2.7.1 Dynamics Part 2	E, F	0.0006	0.22	0.0008	0.27
	E	0.0007	0.24	0.0022	0.81
	F	0.0002	0.09	0.0003	0.12
2.7.2 Drafting - Phase 1	Mannequin	0.0004	0.17	0.0005	0.23
2.7.3 Overtaking	B	0.0008	0.36	0.0011	0.44

**Table 2.3.3** – Repeatability of baseline measurements on the Multi-Rider Cycling Rig with mean uncertainty and standard deviation ( $\sigma$ )

	<b>Athlete</b>	<b>Uncertainty</b>	<b>Uncertainty %</b>	<b><math>\sigma</math></b>	<b><math>\sigma</math> %</b>
2.7.2 Drafting - Phase 2	B	0.0008	0.36	0.0013	0.53
2.7.4 Four Rider Team	A, B, C, D	0.0009	0.39	0.0010	0.47
	A	0.0002	0.09	0.0003	0.12
	B	0.0005	0.21	0.0006	0.27
	C	0.0003	0.15	0.0005	0.22
	D	0.0020	0.94	0.0027	1.27
2.7.8 Dynamic Wake – Part 1	B	0.0008	0.33	0.0011	0.46
2.7.8 Dynamic Wake – Part 2	B	0.0008	0.37	0.0010	0.43

## 2.4 Monash University FLAIR Water Channel

The Monash University Fluids Laboratory for Aeronautical and Industrial Research (FLAIR) free surface recirculating water channel was used for the testing of scale model cyclists (see Figure 2.4.1). This facility offered high resolution, non-intrusive imaging techniques that were not possible in the wind tunnel. The water channel has a working section with dimensions; width 600 mm, height 800 mm, test section length 4000 mm. The channel has a maximum freestream velocity of 0.4 m/s with turbulence intensity within 0.5% and non-uniformity of velocity of +/- 1% outside the boundary layer.

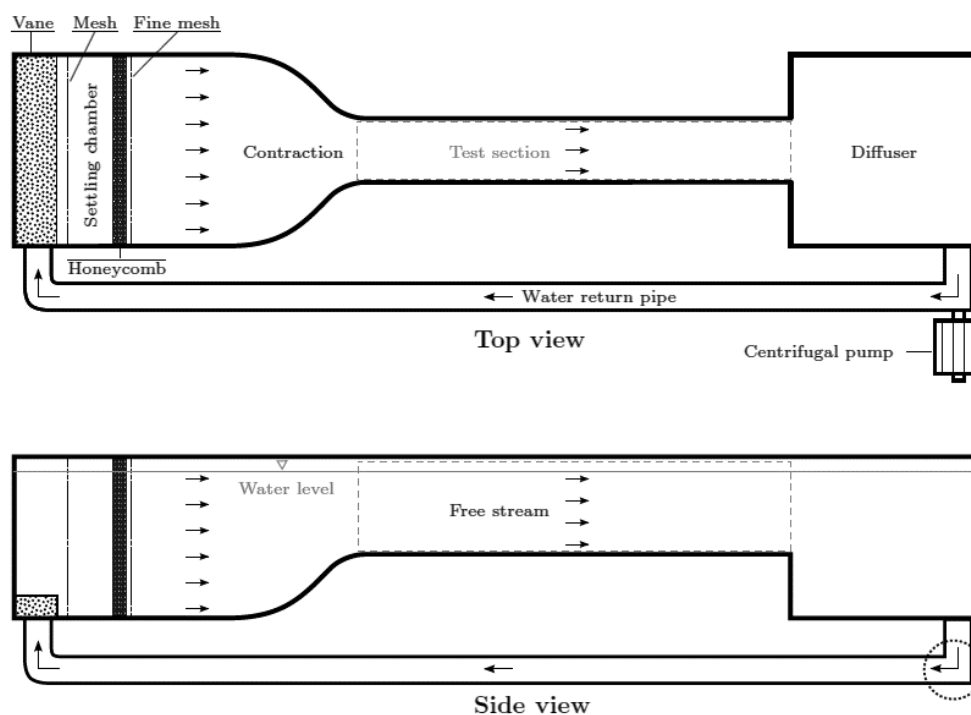


**Figure 2.4.1** - Schematic of the FLAIR free surface recirculating water channel (Sherry 2012)

Cyclist models were mounted on an artificial ground plane suspended in the centre of the test section to minimise wall and free surface interference. This extended the full width of channel over a length of 1200mm. The ground plane extended 1 bicycle length (front wheel leading edge to rear wheel trailing edge,  $L = 0.23$  m) upstream of lead rider and minimum of 1.4 lengths downstream of trailing rider. This varied depending on the separation distance of the lead and trailing riders. The ground plane leading edge had an elliptical profile and resulted in a boundary layer displacement thickness of  $0.01H$  ( $H$  being top of helmet height = 0.216 m) at the location of the leading edge for the first cyclist. This equates to approximately 0.023 wheel diameters in height. Based on previous discussions surrounding ground plane treatment for cycling, this was sufficiently low so as to have a negligible effect on the majority of the flow over the cyclists. Velocity profiles on the empty plane are displayed in Figure 2.4.2 below. Legend refers to distance downstream of leading edge. The first cyclist was located 0.23 m downstream of leading edge. Although some boundary layer growth is evident, the height is significantly smaller than the scale of the cyclists such that even for the trailing rider the

influence will be negligible for the majority of the body. With the cyclist models in place Blockage was less than 1% of channel cross section.

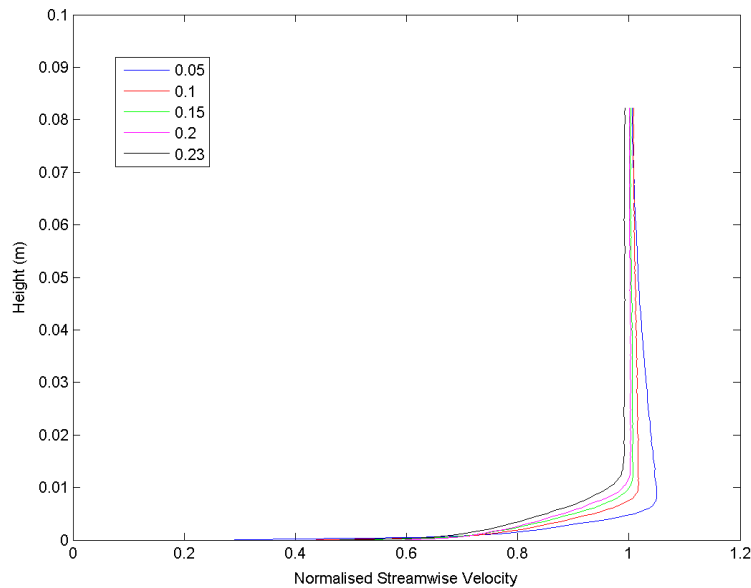


**Figure 2.4.2** - Velocity profiles of the empty ground plane. Series refers to downstream distance from the ground plane leading edge (m). First rider leading edge located at 0.23m

Maximum flow speed of the water channel is approximately 0.4 m/s. All testing was conducted at maximum pump speed so as to maximise the Reynolds number of the cyclists. As with full scale wind tunnel tests, the Reynolds number was calculated using the cyclist torso chord as the characteristic length. At a flow speed of 0.38 m/s this equates to a Reynolds number of 33,000. This is of the order of 15 times less than a typical full scale Reynolds number of a cyclist travelling at 50km/h. The Reynolds number of these tests was limited by the maximum size and operating speed of the water channel.

Whilst previous wind tunnel investigations of cycling have been conducted at Monash University using full scale cyclists at real world Reynolds numbers, that facility does not currently have the capability for high spatial resolution, non-intrusive planar flow mapping such as PIV. The use of scale models in the water channel has this capability and, while the reduced Reynolds numbers of scale models is a limitation, it represents a compromise in pursuit of a greater understanding of the detailed flow field interactions between cyclists.

The lower Reynolds number has potential to generate differing flow behaviour to that of full scale cyclists. However, the existing body of work by Crouch et al. (2014) and simulations by Griffith et al. (2014) provide a basis for comparison with the flow field of a single scale cyclist. The first stage of the study was to validate the approach by comparing the single rider scale results with the full scale results. This showed that despite the lower Reynolds number, the scale model wake flow structures did not differ significantly from those around a full scale cyclist, suggesting at least some degree of Reynolds number independence over this range.

Particle Image Velocimetry (PIV) using a single camera setup was used to capture two dimensional in-plane velocity components in cross sectional planes. The flow was seeded with hollow glass

microspheres with a nominal diameter of  $56\mu\text{m}$  and a density of  $1.016\text{gcm}^{-3}$  (Vestosint, Germany). Two miniature Nd:YAG pulsed lasers produced the laser sheets for illumination of the particles (Minilite II Q-switched lasers, Continuum). Lasers had a nominal wavelength of 532 nm and produced a laser sheet of 2 mm thickness. A charge-coupled camera was used to capture the PIV image pairs (either PCO 2000 or PCO 4000). Data was analysed using in-house software applied to  $32 \times 32$  pixel interrogation windows with 50% window overlap (Fouras et al. 2008). Each velocity profile was generated from the mean of at least 360 image pairs to provide a stable time average. Vector grid spacing for velocity fields was within  $0.01H$ . For a description of the fundamentals of Particle Image Velocimetry see Tropea et al. (eds 2007, Ch 5.3.3).

## **2.5 Equipment and Apparatus**

### **2.5.1 Four-Hole Pressure Probe**

A four-hole dynamic pressure probe, commonly referred to as a Cobra probe due to the head shape, was used for flow mapping in the wind tunnel (Turbulent Flow Instrumentation - TFI - Cobra Probe).

Multi-hole pressure probes resolve the pressure measured on different faces angled to the flow to determine three components of velocity in addition to static pressure (Hooper & Musgrove 1997). This makes them a useful tool for point measurement of flow in the wind tunnel. Multi-hole pressure probes are commonly used in the measurement of turbulent flows in the wakes of bluff bodies and in wind engineering applications.

The TFI cobra probe is a semi-self-contained unit and houses pressure transducers within the probe body. Short steel tubes connect the transducers to the head apertures on the faceted surfaces. The measured fluctuating pressures acting on each surface are corrected for amplitude and phase distortions that arise due to the tubes connecting the transducer to the probe head. This correction is based on the method of Bergh & Tijdeman (1965) which corrects the amplitude and phase response at one end of a tube due to fluctuations at the other.

The pressure transducers have a frequency response up to 2000 Hz allowing for high frequency flow mapping for wind speeds ranging between 2 m/s and 100 m/s. The angle of the faces on the four-hole probe allow for a  $\pm 45^\circ$  cone of acceptance at the head. This limits the probe to certain applications as it cannot measure recirculating flow. With a total head width of 2.8 mm, the probe is able to resolve usable velocity components with a spatial resolution of the order of 5mm. This makes it capable of detecting large scale turbulent structures but not those of small scales. The work of Crouch et al. (2014) showed that the primary vortex structures in the wake of a cyclist exceed an order of magnitude above the size of the probe head. The cobra probe is therefore appropriate for the characterisation of the flow field around a cyclist.

The probe has an internal pressure transducer and provides a direct voltage output. The resolution of velocity from the pressure at the head is internal. Probes come pre-calibrated from TFI, who recommend annual recalibration. Data acquisition and tubing correction is through manufacturer software which converts the voltage outputs to velocity and pressure components.

**Table 2.5.1** - Estimated measurement uncertainty associated with the Cobra Probe as stated by manufacturer Turbulent Flow Instrumentation (TFI)

<b>Flow Quantity</b>	<b>Uncertainty</b>
Velocity (U, V, W)	$\pm 1\%$ of total velocity
Yaw and Pitch Angles	$\pm 0.5^\circ$
Static Pressure	$\pm 1\%$ of dynamic head
Turbulence Intensity	$\pm 5\%$ of total turbulence level

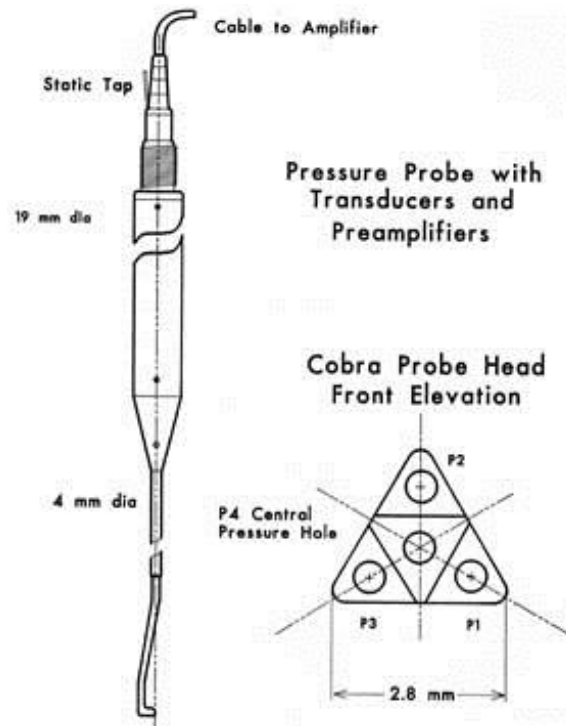


**Figure 2.5.1** - Schematic of Turbulent Flow instrumentation (TFI) Cobra probe

## 2.5.2 Dynamic Pressure Measurement System

A dynamic pressure measurement system was used for direct measurement of pressure for experiments in the wind tunnel. The units used were two multi-channel pressure measurement systems by Turbulent Flow Instrumentation (type; TFI DPMS). These have the ability to measure mean and time varying pressure response for a large number of channels. Each unit has 64 individual pressure channels, equating to a total of 128 simultaneous pressure channels available for experimental measurements.

**Table 2.5.2** - Specifications of Dynamic Pressure Measurement System (TFI DPMS) units

	<b>Module 1335</b>	<b>Module 1336</b>
Type	Differential	Differential
Channels	64	64
Pressure Range	$\pm 3$ kPa	$\pm 7$ kPa
Accuracy	0.3 % Full Scale	0.3 % Full Scale

The DPMS units come calibrated from the manufacturer. However, pressure modules are checked using a peristaltic pump and Betz manometer to apply a known pressure to the channels of the DPMS. This showed a sensitivity of  $\pm 1$  Pa.

Pressure fluctuations measured with the units are corrected in the device control software for the amplitude and phase distortion effects caused by the size and length of tubing between the unit and the measurement location. The correction methodology involves first obtaining a Fourier transform of the measured pressure signal at each channel. In frequency space a transfer function is applied to the signal. This transfer function varies depending on the diameter and length of tubing used and includes consideration of the internal connection between the unit-tube interface and the transducer. The signal is then transformed back into the time domain with an inverse Fourier transform. TFI provide a software function for generating a theoretical transfer function depending on the tube length and diameter being used. This process is based on the method of Bergh and Tijdeman (1965), which showed a strong correlation between theoretical and experimental response.

In this research the pressure measurement units were used to measure pressure in the wake of a cyclist from an array of forward facing pressure tubes. The precise method of these experiments will be described in Section 2.7.8. PVC tubes of length 2200mm and inner diameter 1.5mm were used running from the array to the DPMS units. The theoretical transfer functions for amplitude and phase response are shown in Figure 2.5.2.

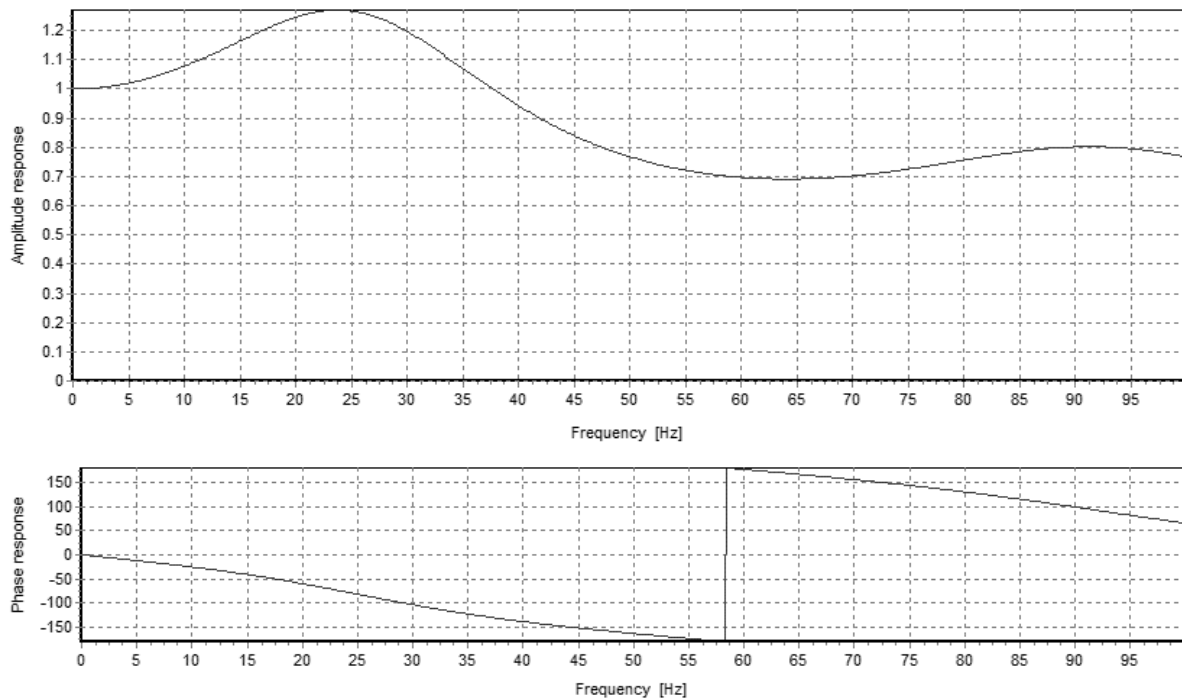


**Figure 2.5.2** - Theoretical amplitude (top) and phase (bottom) transfer functions used to correct measured pressure response

## **2.6 Test Subjects**

### **2.6.1 Athlete Participants**

All testing reported in this work was conducted according to approval from the Monash University Human Research Ethics Committee. Project Number CF13/1326 – 2013000679

Athlete volunteers were used as test subjects throughout this research project. Due to availability and commitment, different athletes were used for different experiments over the course of the project. However, within each experiment the same athlete(s) were used. All athletes are experienced elite level cyclists or triathletes and male.

The basic biometrics of each athlete is presented in Table 2.6.1 below. In this case the baseline  $C_D A$  is the critical parameter as size and weight do not have a direct correlation with aerodynamic drag. It is important to note that these are basic metrics for each athlete. As such, height is the standing height of the athlete. In moving an athlete from standing posture, to a cycling posture the geometry changes dramatically. As such, the difference in standing height of an athlete is not directly proportional to their height on the bicycle or the athlete's  $C_D A$ .

As both size and geometry affect drag and are individual characteristics of an athlete, it is most practical to refer to drag coefficient area ( $C_D A$ ). Unlike conventional vehicles, the area of the cyclist is a unique factor of their size and geometry. Area for an athlete also varies with their riding posture, which was varied for some experiments. Furthermore, the frontal area of a cyclist varies with leg position around the crank cycle and is therefore not a constant, even for a given posture. Consequently all results in this research are presented as drag area rather than drag coefficient. Images of each athlete can be found in Appendix C.



**Figure 2.6.1** – Athlete B depicted in Monash Wind Tunnel.

**Table 2.6.1** - Basic dimensions of athletes used throughout this research.

\* The  $C_{DA}$  of Athlete G was not measured as they were not used in force measurements

	Height (cm)	Weight (kg)	$C_{DA}$ (m <sup>2</sup> )
Athlete A	193	78	0.252
Athlete B	183	78	0.224
Athlete C	183	70	0.225
Athlete D	176	60	0.214
Athlete E	188	105	0.280
Athlete F	183	78	0.264
Athlete G*	183	84	NA

### 2.6.2 Monash Anthropomorphic Cycling Mannequin

A piece of apparatus used throughout this investigation was the Monash Anthropomorphic Cycling Mannequin (mannequin), developed by Crouch et al. (2012, 2014). This was developed at Monash to investigate the flow field around a cyclist. Dimensions of real athletes were used to generate a representative geometry of a male cyclist in a time trial posture. The mannequin is mounted to a track bicycle. This setup was constant for all tests. The mannequin geometry is shown in Figure 2.6.2 and described in Table 2.6.2 below. At a crank angle of  $15^\circ$  the mannequin had a  $C_{DA}$  of  $0.193 \text{ m}^2$ .

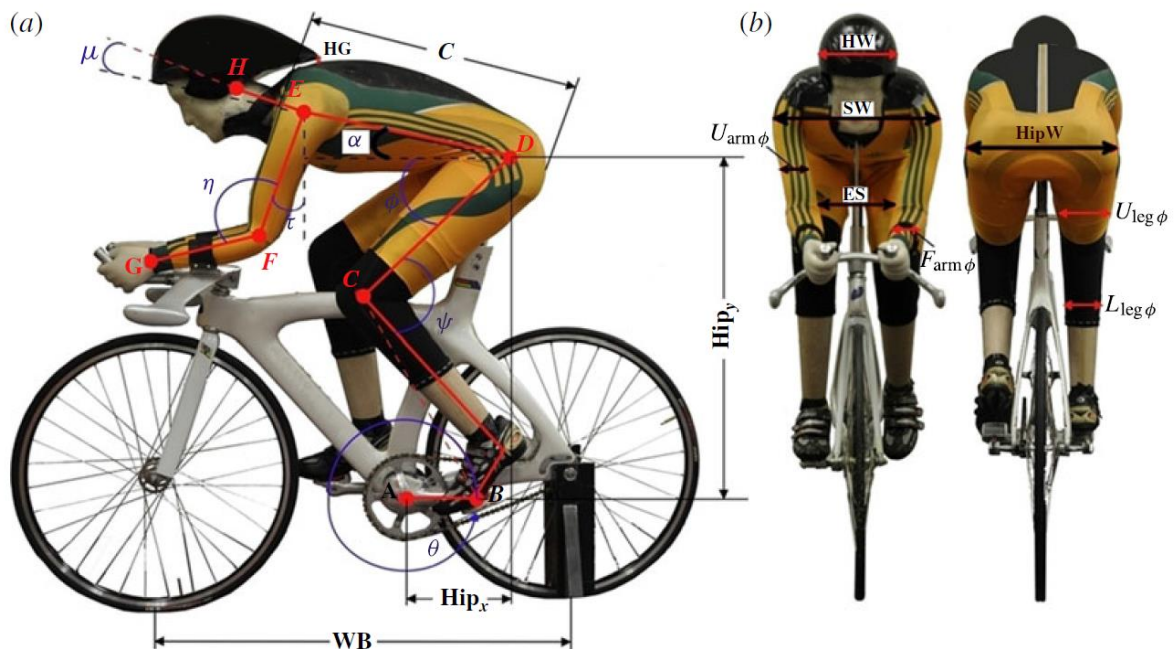


**Figure 2.6.2** - The Monash Anthropomorphic Cycling Mannequin. Dimensions refer to Table 2.5.2

**Table 2.6.2** - Monash Anthropomorphic Cycling Mannequin dimensions

Name	Symbol	Dimension	Name	Symbol	Dimension
Crank angle	$\theta$	$0^{\circ} - 360^{\circ}$	Foot-knee	B $\rightarrow$ C	558 mm
Knee angle	$\psi$	$f(\theta)$	Upper leg	C $\rightarrow$ D	448 mm
Hip angle	$\phi$	$f(\theta)$	Torso	D $\rightarrow$ E	485 mm
Angle of attack	$\alpha$	$12.5^{\circ}$	Upper arm	E $\rightarrow$ F	300 mm
Upper arm angle	$\tau$	$20^{\circ}$	Forearm	F $\rightarrow$ G	250 mm
Elbow angle	$\eta$	$110^{\circ}$	Neck	E $\rightarrow$ H	120 mm
Neck angle	$\mu$	$5^{\circ}$	Helmet width	HW	200 mm
Helmet-to-back gap	HG	20 mm	Shoulder width	SW	420 mm
Hip location (x)	Hip <sub>x</sub>	200 mm	Hip width	HipW	350 mm
Hip location (y)	Hip <sub>y</sub>	806 mm	Elbow spacing	ES	160 mm
Wheelbase	WB	970 mm	Upper arm diameter	U <sub>arm,<math>\phi</math></sub>	80 mm
Wheel diameter		700C	Forearm diameter	F <sub>arm,<math>\phi</math></sub>	72 mm
Torso chord	C	640 mm	Upper leg diameter	U <sub>leg,<math>\phi</math></sub>	145 mm
Crank	A $\rightarrow$ B	175 mm	Lower leg diameter	L <sub>leg,<math>\phi</math></sub>	90 mm

Note that the arms and legs of the mannequin are tapered. These diameters are of a cross section at approximately mid-section. The leg taper ratio and dimensions were approximated from the measurement of athlete proportions.

The key experimental benefit of a mannequin, rather than athletes, for cycling testing is the ability to create a repeatable and reproducible body position on the bicycle. This minimises variability in the results due to variation in position that can occur with athlete participants. It is a challenge for athletes to maintain a constant body position; not only for back to back tests, but to return to a given position over the course of a test block. Some experienced athletes can achieve low variability in their positioning, however, all athletes are subject to fatigue. The mannequin offers benefits in that much greater volume of data can be collected as testing is not limited by athlete comfort or fatigue. Where the mannequin is limited is that the legs, whilst movable, can only be tested statically. This means that full pedalling dynamics could not be replicated. For this reason athlete testing still offers a significant advantage in terms of replicating the full dynamics of cycling for the most practical application of results.

Crouch et al. (2012, 2014) showed that the flow field and the drag of a cyclist varies as a function of the leg position. It is therefore necessary to characterise the position of the legs to ensure consistency in any testing using static cyclists. Given the complexity of the leg motion and difficulty in defining a clear reference point on the leg, it is more convenient to define the leg position in terms of the crank arm. The zero point for the crank angle position is defined with the left crank arm rearward and horizontal. Looking at the left side of the bike, the cranks rotate in an anti-clockwise manner so that angle increases as the left crank is raised above horizontal. The crank angle ( $\theta$ ) and the resulting hip angle ( $\phi$ ) are depicted in Figure 2.6.1 above as shown on the mannequin. Figure 2.6.1 shows the mannequin at a  $0^{\circ}$  crank position. This definition of the crank angle will be used throughout to define the position of the legs of cyclist subjects.

The hip angle is important as it is the motion of the upper legs relative to the torso that was shown to have the dominant influence on the flow (Crouch et al. 2014). As the crank angle increases from horizontal the hip angle closes. For the mannequin,  $75^{\circ}$  crank angle corresponds to the minimum hip angle and subsequently the maximum drag and most asymmetric flow regime. At a crank angle of  $15^{\circ}$ ,

the thighs of the mannequin are level. This corresponds to a minimum point in the drag curve and the symmetric wake regime. It is noted that the relationship between hip angle and crank angle is not necessarily a constant for all cyclists. The mannequin has a fixed ankle joint which maintains this constant relationship. Different ankle flexion will alter the hip angle, even for a given athlete. For athletes this means that hip angle can vary slightly for the same crank angle such that the hip angles may not be in the same phase with the cranks as seen for the mannequin. Also differences in limb length and size as well as torso position and size will all have effects on these measures. Note that whilst hip angle is defined from the horizontal, it is the interaction with the torso that influences the flow behaviour. This complexity is inherent in cycling testing due to the complexity of the geometry and the number of variables and degrees of freedom in an athlete.

## **2.7 Specific Experimental Methodology**

The following section describes the specific experimental methodology used for each of the separate investigations conducted as a part of this research. Each experiment is targeted towards answering the key research questions outlined in Section 1.4.

The first experiment investigated the effects of a cyclist's leg dynamics on drag and with particular focus on the effect on aerodynamic interactions. Force measurements were conducted on the Single Rider Cycling Rig in the Monash Wind Tunnel. This provides some insight into the effect of leg dynamics but was primarily intended as a validation to identify possible error arising from using static models in the study of cycling aerodynamics.

A series of experiments were then conducted to provide a detailed understanding into the variation of drag with spatial position between cyclists in two rider formations. Force measurements were conducted in the Monash Wind Tunnel using both the Single Rider Cycling Rig and Multi-Rider Cycling Rig; depending on the experiment. This incorporated a range of spatial positions for drafting and overtaking cyclists; encompassing tandem, transverse and staggered formations.

A case study example of a four rider pursuit team was used to investigate drag interactions between cyclists as a function of geometry and posture. Simultaneous drag measurements were recorded for each athlete in the team in the wind tunnel using the Multi-Rider Cycling Rig. Drag interplay between athletes within the team could then be studied.

Following the detailed investigation of the drag interactions that occur between cyclists in close proximity, a series of experiments was conducted to characterise the flow field. Full scale visualisations were conducted using athletes in the wind tunnel. Detailed flow mapping was then conducted on reduced scale models using PIV in the FLAIR water channel. The forward interference field of a cyclist was then measured in the Monash Wind Tunnel. This was followed up by wake mapping of a dynamic athlete in the wind tunnel. From this collective data set it becomes possible to piece together a description of the flow field around a two rider tandem formation and identify the mechanisms responsible for the measured changes in drag.

Table 2.7.1 summaries the experiments conducted in this research and the facility, rig and test subjects used.

**Table 2.7.1** - Summary of experiments and facility and test subject overview

<b>Experiment</b>	<b>Facility</b>	<b>Details</b>
2.7.1 Effect of rider dynamics	Wind Tunnel	Single Rider Cycling Rig Athletes
2.7.2 Force variation in drafting cyclists	Wind Tunnel	Single Rider Cycling Rig Multi-Rider Cycling Rig Athlete & Mannequin
2.7.3 Force variation in overtaking cyclists	Wind Tunnel	Single Rider Cycling Rig Athlete Primary – Mannequin Secondary
2.7.4 Geometry effects on drag interactions	Wind Tunnel	Multi-Rider Cycling Rig Athletes
2.7.5 Full scale flow visualisations	Wind Tunnel	Multi-Rider Cycling Rig Athletes
2.7.6 Scale model flow measurements	Water Channel	FLAIR Water channel Static scale models
2.7.7 Cyclist forward interference	Wind Tunnel	Single Rider Cycling Rig Static Mannequin
2.7.2 Dynamic wake analysis	Wind Tunnel	Multi-Rider Cycling Rig Athlete Primary – Mannequin Secondary

### **Cycling Formations**

Investigations of multi-body formations are usually divided into two groups; those inline parallel to the flow, and those inline perpendicular to the flow. These are termed tandem and transverse, respectively. Any formation that deviates from the inline position is described as a staggered formation. Cycling formations of multiple riders can be assigned more practical definitions. For formations where one cyclist is following another, this is termed drafting. This is analogous to the tandem formation. However, in terms of this investigation, drafting will also encompass tandem type formations with a lateral offset between the centrelines of the lead and trailing cyclist. This accounts for deviations from the idealised inline formation to simulate on road behaviour. Drafting is common place in cycling; occurring in breakaway groups on the road as well as team specific events on the road and track. The second key formation in cycling is an overtaking manoeuvre. This includes transverse formations where two cyclists are positioned side-by-side and inline perpendicular to the flow. However, overtaking is a dynamic behaviour and so also encompasses staggered formations by introducing axial displacement fore and aft of the side-by-side position. Experimental description of cycling formations will utilise these definitions to distinguish the different characteristic behaviours.

### Wind Speed and Reynolds Number

All tests in this project were conducted at 18 m/s (65km/h) unless stated otherwise. This test speed was selected as it represents the steady state speed of an elite men’s pursuit team. During such an event there is a transient period at the beginning while the riders accelerate, followed by a section of constant velocity. At an elite level this is in excess of 60 km/h. When calculating the Reynolds number, the athlete torso chord length was used as the characteristic length (see Figure 2.6.1 mannequin dimensions). For the athletes used in this research the torso chord is of the order of 600 mm. This equates to a Reynolds number of approximately  $7 \times 10^5$ . The Monash University Wind Tunnel is not temperature controlled and so atmospheric conditions varied between tests depending on the time of the year. Tests were controlled by maintaining constant velocity. Therefore, variations in temperature and density resulted in variations in Reynolds number for a given wind speed. Reynolds numbers were in the range of  $6.1 - 7.3 \times 10^5$  for temperatures in the range of  $12^\circ\text{C} - 31^\circ\text{C}$  as the extreme conditions.

The constant test speed was selected as a fixed parameter across tests to remove one variable from experiments. Including Reynolds number effects is an additional consideration beyond the scope of this work. Figure 2.7.1 below shows the drag of a cyclist varying as a function of Reynolds number. Cyclist in these tests was the Monash mannequin with legs positioned at  $15^\circ$  crank angle. The torso chord length was used as the characteristic length. Test speed was varied between 7 and 26 m/s. This sensitivity to Reynolds number is consistent with cylinders and other bluff bodies (Achenbach 1971). This also highlights the necessity to validate testing in a water channel at smaller Reynolds numbers to evaluate flow similarity.

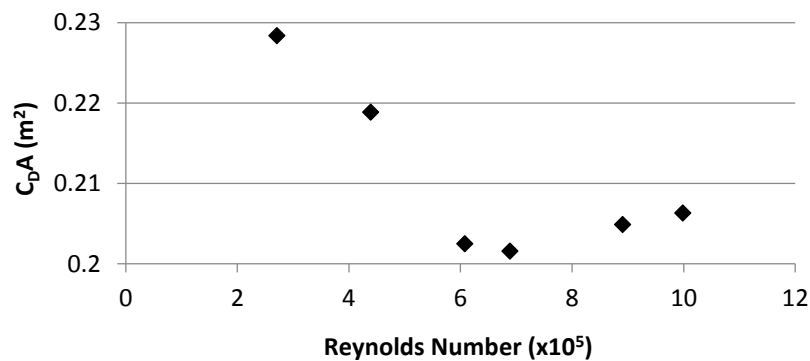


**Figure 2.7.1** – Variation of cyclist drag with Reynolds number calculated using cyclist torso chord as characteristic length. Cyclist was Monash mannequin with legs at  $15^\circ$  crank angle.

### 2.7.1 Effect of Rider Dynamics on Cyclist Drag

Tests were conducted to investigate the effect of leg dynamics on cyclist drag as well as the effects in a two rider formation. Existing literature has investigated cyclist aerodynamics with studies interchangeably using static and pedalling (dynamic) models of cyclists. Recent literature (Crouch et al. 2012, 2014) has shown that drag varies significantly with static leg position. However, the link between static and dynamic drag has not yet been investigated in detail. These tests serve as a reference for understanding any limitations that may arise from the use of a static cyclist model rather than a dynamic rider in subsequent experiments in this research.

Two experiments were conducted. The first looking at the link between the drag of a cyclist with static legs compared to dynamic pedalling legs. The second extended this to two rider formations and the influence of leg position and dynamics on the interactions. Testing was conducted in the Monash University Wind Tunnel using the Single Rider Cycling Rig. The ground plane was extended in the two rider tests from the single rider setup to accommodate the two bicycles. With a single cyclist on the rig, blockage ratio was 6%. With two riders positioned side-by-side the blockage ratio increased to 11%.

Experienced athletes were used for all experiments (Riders E & F). In the two rider formations only a single athlete was instrumented (Athlete E). The second was positioned to act as interference, but was not connected to a force balance (Athlete F). The athlete used for the single rider tests was the instrumented rider in all the two rider formations tests. As drag is a strong function of rider geometry, any two riders in the same general posture will not have drag of the same magnitude. For this reason it is most useful to compare differential drag using a reference state in all aerodynamic investigations of cycling. This allows for presentation of results that are more generally applicable.



**Figure 2.7.2** – Athlete E mounted on Single Rider Cycling Rig in Monash University Wind Tunnel

### ***Static vs Dynamic Cyclist Drag***

Static force measurements were taken at 15° crank angle increments for a half crank rotation; assuming symmetry for the second half of the cycle (as seen by Crouch et al.). In addition, drag measurements were recorded with the athlete pedalling (dynamic) to model the full cycling dynamics. Test duration was 40 seconds sampled at 100 Hz so that data could be averaged over a sufficient number of pedal cycles for the average drag to be independent of start and end positions. The athlete was permitted to set their own pedalling frequency as this would enable the most stable riding posture and test repeatability. Tests at Monash University (unpublished) have shown that time averaged drag is largely independent of pedalling frequency in typical ranges. Wheel speed was not match to wind speed due to limitations of the rig and required physiological load on athletes. This will result in lower circumferential drag on the wheels, a component not measured, and result in an error in the axial drag associated with the wheels. As this study was on differential drag, this error is minimised in final results. Furthermore, allowing athletes to have lower pedalling load reduces fatigue and improves repeatability.

Testing with an athlete allowed testing of the same identical geometry in both static and dynamic tests. Mean variation for static tests with an athlete was 0.9% in  $C_{DA}$  for back-to-back tests. Repeatability for the pedalling tests showed an average variation of 0.6% across the duration of the test program. Although the fluctuations in force are greater in dynamic tests, because it is more natural for athlete to hold, time averaged values can be more repeatable than static tests. Feedback from the athlete suggests that this is likely more closely linked to human factors such as muscle activation and comfort, rather than an aerodynamic instability in the flow.

### ***Two Rider Interaction Tests***

The primary instrumented rider was mounted to the Single Rider Cycling Rig. The secondary rider was mounted on a stand that reflected the profile of the rear struts used on the cycling force balance. A standard bicycle magnetic resistance trainer unit was mounted to the rear wheel to provide resistance and enable the rider to pedal and the rear wheel to turn. The front wheel remained static for all tests. The leg dynamics were expected to have a much greater influence on the results than the static front wheel and so any associated errors were deemed negligible to the experiment. Two athletes were utilised so that dynamic and static positions could be tested for both tandem and transverse formations (inline parallel and perpendicular to the flow respectively). Two static leg positions were selected; the low drag case at a crank angle of 15° and the maximum drag case at 75°. These also coincide with symmetrical and highly asymmetric wake regimes. Static positions were tested in combination with dynamic leg tests. The mean experimental uncertainty for the two rider interaction tests was 0.6% across all runs.

For the tandem formation the two riders were positioned inline, parallel to the flow with 100mm wheel gap between them. Spacing and body position were constant for all tests. For transverse tests, riders were positioned side-by-side with front wheels level and 750mm between bicycle centrelines. The instrumented rider was positioned on the left relative to the flow (Figure 2.7.3 - rider on the left of image acting as interference only). Rider size is acknowledged to have some influence on drag (as described earlier – Edmunds & Byrnes 2007). However, in practice no two athletes will be of equal

dimensions. Also, in terms of the induced change in drag, this is a stronger function of the size of the interfering body.



**Figure 2.7.3** – (Left) Riders in tandem formation with instrumented rider trailing; (Right) Riders in side-by-side (transverse) formation with instrumented rider on right of image.

### 2.7.2 Force Variation in Drafting Cyclists

Tests were conducted in the Monash University Wind Tunnel to investigate the effect of spatial position on the drag of two drafting cyclists. Forces were measured using the single Rider Cycling Rig. As this is a single force balance, only one cyclist was instrumented during testing. The second cyclist was acting as interference only. The force balance has a fixed location in the wind tunnel. For the measurement of trailing cyclist drag, the secondary rider was positioned upstream of the instrumented cyclist. For lead cyclist drag the formation was reversed with the secondary cyclist was mounted downstream of the instrumented cyclist on the balance. For the first phase of the investigation, the Monash Anthropomorphic Cycling Mannequin was used as the instrumented rider. Using the mannequin necessitated the addition of supporting struts at the front axle. As the mannequin is capable of maintaining very high repeatability it was selected to minimise uncertainty in the drag results. An athlete participant was used as the secondary cyclist (Athlete G). As they were not instrumented, variation in the athlete's position would have only small influence on the primary cyclist. The athlete was dynamic for all tests. The rear wheel was mounted to rollers by a pair of struts at the rear axle. This replicated the wind tunnel balance setup and enabled the rider to pedal naturally and the rear wheel to turn. The front wheel, however, remained stationary. As previously stated the influence of a stationary front wheel is negligible to the outcomes of this experiment. However, this setup is limited by as the mannequin is only static. Legs were set at  $15^{\circ}$  crank angle for all tests. This leg position creates a symmetric wake and was thus assumed to provide greater similarity to the time averaged wake of a dynamic cyclist. Mean uncertainty for back to back tests was 0.3% using the mannequin.

Due to the fixed location of the force balance the maximum range of the experiment was limited by the location of the balance relative to the jet exit. Positions were tested with an axial wheel gap of up to 700 mm between lead and trailing cyclists and lateral separation up to 275 mm. Figure 2.7.4 below shows the profile view of the setup. Minimum separation distance is shown (5 mm).



**Figure 2.7.4** - Depiction of the athlete (G) and mannequin in tandem formation at minimum separation distance.

To overcome limitations of the first investigation (Phase 1), a second investigation was undertaken (Phase 2). This would increase the axial range to explore the limits of the interaction effects with separation distance. Phase 1 tests were limited by the single rider rig which had a fixed location in the tunnel. To overcome this, the second set of drafting tests was conducted using the Multi-Rider Cycling Rig (see Section 2.3.2). By utilising the force balances at Position 1 and Position 4 on the rig it was possible to greatly extend the axial range of the experiments. A similar method was used to that described previously. Only a single cyclist was instrumented; with the other acting as interference. This made setup significantly simpler as it did not require a moving force balance. To measure the drag on the leading cyclist, the primary rider was mounted on the position 1 force balance. The secondary cyclist was then positioned downstream. For the trailing cyclist drag, the primary rider was mounted to the position 4 balance. This was significantly further downstream and so the secondary rider could be positioned at greater distance ahead before impinging on the jet exit. Using this setup the maximum axial distance between wheels was extended up to 5m. Given the larger range and the high spatial resolution of the first data set, a coarser spatial grid was used in Phase 2.

In order to best replicate the practical case, the Phase 2 tests were conducted with an athlete (B) acting as the instrumented cyclist. The mannequin was then used as the secondary interfering rider with legs positioned at  $15^{\circ}$  crank angle. Using the athlete as the primary subject reintroduces the full pedalling dynamics. This maintains setup as close to the practical scenario as possible. The setup is shown in Figure 2.7.5 below.

Back to back test repeatability using the athlete as test subject resulted in an uncertainty of 0.4%, which is of the same order as the mannequin results from Phase 1. Reproducibility over the test block was within 0.5%. This accounts for the athlete being able to recreate the same posture on the bike from the beginning to the end of day. Although back-to-back repeatability is an issue, the ability of an

athlete to hold and reproduce a position over the course of a test day is equally important so that there is a fixed reference point. These figures show that, although athletes have a typical weakness in variability, experienced, stable athletes can perform to similar levels as a model cyclist. It is noted however, the experience has shown that this is not common for all athletes. For athlete testing an uncertainty margin within  $\pm 0.001\text{m}^2$  is satisfactory.



**Figure 2.7.5** - Phase 2 drafting tests conducted on the Multi-Rider Cycling Rig. Depicted here measuring lead rider drag on Athlete B. Mannequin mounted downstream is acting as interference only.

Due to the different test setups adopted between Phase 1 and Phase 2 the measured drag at the force balance was subject to change. This is an expected result due to the tunnel flow field being influenced by the change to the test rig, tunnel configuration, test athlete and mannequin. Despite applying the flow correction methodology, reference tests with the mannequin showed differences in the measured drag between the two sets of experiments. For this reason, results are presented as a difference in drag, referencing the baseline condition of the test. Using the local reference minimises error associated with the changing configuration of the experiments. As the changes in baseline drag are due to differences in the flow field, the drag reduction should be proportional as it is also a function of the same flow conditions. For this reason it is not representative to compare the magnitude of drag at each location. It will be shown that results from both sets exhibit similar behaviour over the intersection region of the data sets. As stated above the test uncertainty with the athlete was not significantly greater than the mannequin; providing confidence in the validity of the data.

### 2.7.3 Force Variation in Overtaking Cyclists

Drafting and tandem formations are not the only significant form of interactions in cycling. Cyclists in groups often travel side-by-side in addition to overtaking manoeuvres. In terms of bluff body descriptions this encompasses transverse formations and staggered formations as axial movement is incorporated. Two cyclists were tested in a range of staggered positions encompassing rider's travelling side-by-side as well as axial displacement forward and aft from the level position. Minimum lateral separation between cyclists was 500mm, taken from the bicycle centreline. This represents the minimum possible during competition without coming into contact (see Figure 2.7.6). The zero point is defined where the front wheels of the two cyclists are inline. Axial distance forward and aft of the level position as well as lateral distance was increased up to 1000 mm. The range of positions is shown in Figure 2.7.6.

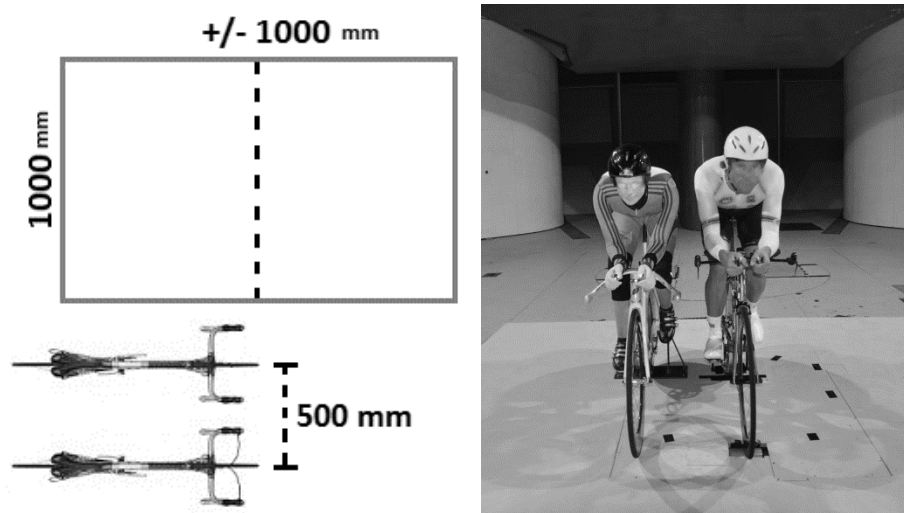


**Figure 2.7.6** - (Left) Depiction of spatial grid of positions tested; (Right) Athlete and mannequin at minimum separation mounted in the wind tunnel.

Experimental method was similar to that described previously for drafting studies (see Section 2.7.2). Tests were conducted in the Monash University Wind Tunnel. With two riders positioned side by side on this rig the total blockage is 11%. Experiments were conducted on the Single Rider Cycling Rig with a single instrumented rider. The second cyclist was acting as interference only. Athlete B was used as the primary instrumented rider and was pedalling for all tests. The mannequin was used as the secondary cyclist with legs positioned at a crank angle of  $15^{\circ}$  for all tests. This setup is the same basic apparatus previously described for the dynamic and drafting tests. The force balance is fixed in the centre of the wind tunnel turn table and the secondary cyclist (mannequin) was positioned relative to the primary to vary spatial position. The mean uncertainty for back to back repeatability was 0.5% with the dynamic athlete. Reproducibility of the baseline position over the course of the test program was 0.2%.

## 2.7.4 Geometry effects on Drag Interactions

The effect of geometry on aerodynamic interactions in cycling was investigated in the context of a pursuit team. This is four rider event conducted on a velodrome with riders travelling in a tight tandem formation. Four athletes (A - D) were selected as to act as a pursuit team, simulating the track event. The group was comprised of elite level triathletes and cyclists. All were riding road specification time trial bicycles and wearing aerodynamic teardrop helmets. Athletes were using their own equipment and natural riding position but with identical skin suits. The individuals ranged in size and body shape, which is representative of natural variation in team dynamics (see Table 2.6.1). The setup is depicted in Figure 2.7.7 below. See Section 2.6.1 for athlete details.

Testing was conducted in the Monash University Wind Tunnel (see Section 2.1). This experiment utilised Configuration 2 with a jet exit area of 3 m x 4m. Test section length was increased by 0.5 m by changing the position of the nozzle exit. Forces were measured for all four cyclists simultaneously using the bespoke Multi-Rider Cycling Rig force balance (Section 2.3.2). This was developed specifically for team pursuit testing as it allows tracking of drag changes across all athletes in the team. Due to the large length of the force rig and variation to flow conditions within the test section a specific correction methodology was developed based on the work of Mercker & Wiedemann (1996) for open jet wind tunnels. See Section 2.2 for a detailed description of this technique.



**Figure 2.7.7** - Team formation on rig in wind tunnel test section (displaying Sequence 1 in descending size order)

During athlete testing the mean experimental uncertainty in  $C_D A$  for athlete tests was 0.6% ( $0.0007 \text{ m}^2$ ) for a given test configuration. This is primarily due to human factors arising from athlete subjects and the complications in repeating and maintaining constant body position and posture. This stated uncertainty does not factor in the ability of an athlete to reproduce a posture each time a change is required. To monitor athlete positioning images were recorded for each test configuration from a fixed perspective to allow detection of any errors or shifts in body position between tests. An indication of reproducibility was evaluated by considering the change in baseline drag for a given sequence as a team baseline was taken to begin and end each sequence of tests. Overall all athletes and sequences the mean variation was 1.6%. This is relatively high, but not entirely unsurprising given the complications inherent with four separate athletes and that postures were being changed as a part of the test program. However, it should be noted that this is slightly distorted as the drag of the

trailing riders is considerably less than the leader's and so the same shift in  $C_{dA}$  is a larger percentage. Furthermore, it was noted that the variation in baseline drag in positions 3 and 4 was considerably greater than the first or second positions. This may be a combined product of the system. Slight changes to the upstream cyclists will compound for those further downstream resulting in larger variations in drag. The mean variation in baseline drag for the lead position across all 4 athletes was 0.4%. All tests were conducted at  $18 \text{ m}\cdot\text{s}^{-1}$  ( $65 \text{ km}\cdot\text{h}^{-1}$ ), which is the approximate steady state speed of an elite men's pursuit team maintained after the initial acceleration phase. The single test velocity was selected based on practical application and is in the flattest region of the Reynolds number-drag curve.

Three generalised riding postures were identified that could be applied to any cyclist. These were; head raised, head lowered and tucked and finally; elbows together. Each of these was referenced from athletes' existing riding posture which was taken as the baseline case. An example of the positioning can be seen in Figure 2.7.8 below for one of the athletes. Whilst variation between athletes means that each posture will have a unique effect on drag, they represent a generalised physical change that provides practical insight into geometric changes due to body position. As an indication the chin was raised or lowered approximately 75mm and elbows brought together from the baseline case where elbows were positioned at approximately hip width (of the order of 300mm depending on the athlete).



**Figure 2.7.8** - Body positions used during testing; (L-R) baseline, head raised, head lowered, elbows together

Tests were conducted with each individual rider consecutively adopting each position whilst the other athletes in the team remained in their baseline reference position. In addition, tests were conducted with the whole team in the same position. Only a single order of riders was tested but all four possible sequences were tested so that each of the four riders occupied the lead position. This order was selected with the riders arranged in descending size order for the first sequence. In addition to team tests, reference tests were conducted for each rider individually in each of the four postures.

Riders were allowed to dictate their own cadence during tests as this allowed them to maintain the most consistent body position and limit fatigue as well as ensuring that cadence was repeatable over the course of a long test program. Riders maintained a cadence in the range of 90 - 100 RPM through all tests and pedalling synchronisation was not monitored.

### 2.7.5 Full Scale Flow Visualisations

Full scale flow visualisations were conducted as a preliminary investigation of the flow field around two cyclists. Tests were conducted in the Monash University Wind Tunnel using the Multi-Rider Cycling Rig. Two experienced cyclists were used as test subjects for the experiments (Athletes A & G). Athletes were riding their own road specification time trial bicycles. As such the bicycles differed but were similar in overall shape and setup to accommodate each athletes riding posture. Athletes wore identical skin suits and helmets.

Two tandem formations were tested to investigate the influence of separation distance on the flow field. The first was minimum practical separation, equating to 120mm between wheels. The second was a bicycle length distance downstream. These positions utilised the second and third rider mounts of the multi rider rig. The minimum separation case is depicted in Figure 2.7.9 below.



**Figure 2.7.9** - Athletes mounted on Multi-Rider Cycling Rig at minimum separation

A smoke generator (Aerolab) with wand was used to seed the flow with smoke at various locations around the cyclists. Vapour droplet size can vary depending on the element heat and oil flow rate. Droplets are of slightly greater density than air. Over small distances, where the smoke is visible, this method provides a good trace of the flow. As this is a qualitative technique it is sufficient to position the smoke injection point by hand, controlled by the operator. This enables the injection point to be dynamically modified to accommodate multiple injection sites in a short period and tune the injection location for optimum imaging. Images of the flow field were captured using high resolution digital SLR still cameras and video camera. Smoke flow images were captured with cyclists pedalling.

Near surface flow was visualized using wool tufts. To create a more structured view of the surface flow conditions wool tufts were sewn into two identical skin suits worn by the athletes. Tufts were sewn in a regular grid over the back, legs and hips to capture the separation from the hips as this is the origin of the dominant wake vortices for a single cyclist (as identified by Crouch et al. 2014). Video was captured to observe the dynamic response of the flow with pedalling legs. However, only static snapshots are presented in this report. Static images were taken with legs at  $15^{\circ}$  and  $75^{\circ}$  crank angles as these are representative of the symmetric and asymmetric flow regimes respectively. This allowed the comparison of separation pattern over the lead and trailing rider.

To allow for introduction of smoke and capture and imaging of the flow, wind speed was lower than 65 km/h as used in most other experiments described in this report. This is a safety requirement for unsecured individuals operating within the working section of the tunnel. Wind speed was consequently limited to 40 km/h. This is slower than a typical team pursuit, however is still in the region of common cycling speeds.

These visualisation techniques provide only basic qualitative insight into the flow behaviour around tandem cyclists. However, given the knowledge of the single rider flow field, it is possible to use this understanding to better interpret these visualisations. These methods were expected as a precursor to further studies by providing an insight of full scale athlete interactions.

### 2.7.6 Scale Model Flow Measurements

To characterise the flow field around two cyclists in detail and to investigate how the flow field varies from the single rider case, scale models were constructed for use in the Monash University FLAIR water channel. 1/7<sup>th</sup> scale models of mounted cyclists were constructed based on the geometry of the full size Monash anthropomorphic cycling mannequin. In turn, the mannequin was constructed based on athlete dimensions to provide a generalised cyclist body shape. Each scale model was a rigid solid body with fixed leg position. To test the effect of leg position, three separate models were constructed; two at 15° crank angle and one at 75°. These were the two extreme cases identified by Crouch et al. (2014). As previous studies have suggested that the key wake flow structures are primarily generated by the athlete geometry, a simplified bicycle model was sufficient. Thus, bicycles were based on a simplified geometry using circular cross section tubes without handlebars or saddles and simple disks as wheels (Figure 2.7.10). Each bicycle had two pairs of struts fixed to the rear wheel axle and a single supporting pair attached to the front to hold the model firmly in place. Models were mounted on an artificial ground plane suspended in the centre of the test section to minimise wall and free surface interference (Figure 2.7.11).



**Figure 2.7.10** – Cyclist models mounted on ground plane and suspended in the water channel. Shown at minimum separation distance (Spacing 1).

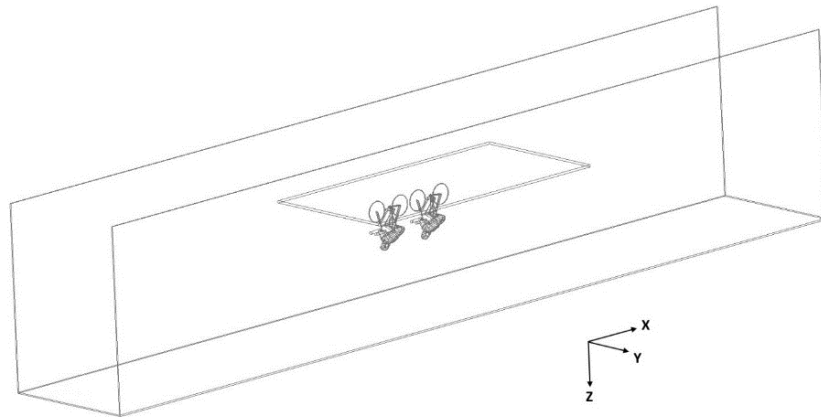


**Figure 2.7.11** – Depiction of model setup in FLAIR water channel test section. Models shown at Spacing 1 (minimum separation).

Particle Image Velocimetry (PIV) using a single camera setup was used to capture two dimensional in-plane velocity components in cross sectional planes. To characterise the near-wake structures, mean velocity fields were obtained in three cross section planes;  $0.25C$ ,  $0.5C$  and  $1.0C$  downstream, measured from the rear of the rider torso, either the single or trailing cyclist (Figure 2.7.12). Here chord length ( $C$ ) is equivalent to the torso length of the cyclist ( $0.086\text{m}$ ), and this is also the characteristic length used to define the Reynolds number. PIV images in the wake cross section ( $YZ$  plane) collected spanwise ( $V$ ) and vertical velocity ( $W$ ) components and allowed calculation of streamwise vorticity. As this method could only capture two dimensional velocity components no streamwise velocity data could be collected from the cross section planes. However, to examine streamwise velocity the  $XZ$  plane was used that cuts through the centreline of the cyclist(s), thus allowing the capture of streamwise ( $U$ ) and vertical ( $W$ ) velocity components. To maintain spatial resolution, multiple image frames were stitched together to generate velocity profiles over an extended whole streamwise domain.

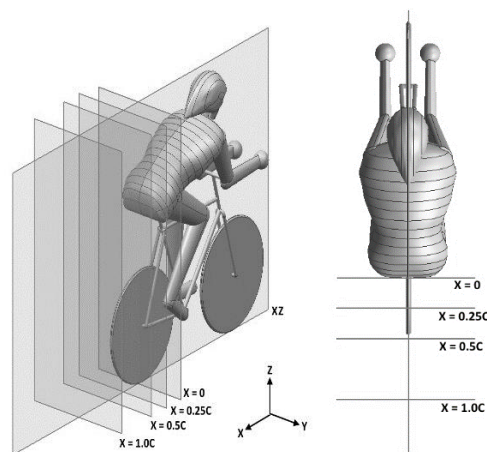


**Figure 2.7.12** – Planes indicate PIV imaging planes. Two dimensional in-plane velocity components were captured at each plane.

Single rider data was collected for both the 15° and 75° leg positions for all planes to provide a reference state and for direct comparison against the full scale experimental results of Crouch et al. (2014) and the numerical simulations of Griffith et al. (2014). For the two rider tandem formation, measurements were taken for two separation distances for the trailing rider. The first configuration corresponded to the minimum practical spacing; which equates to 150mm for a full scale cyclist measured from the trailing edge of lead rider rear wheel to the leading edge of the trailing rider front wheel (Spacing 1). This is representative of the minimum distance that athletes can safely maintain in events such as a team pursuit. The second configuration corresponded to one full bicycle length between the lead and trailing riders (Spacing 2). For both cases, three combinations were tested: both riders at 15° crank angle (symmetric-symmetric), the lead rider at 75° and the trailing rider at 15° (asymmetric-symmetric) and with the lead rider at 15° and trailing rider at 75° (symmetric-asymmetric). This permitted the influence of leg position and upstream flow conditions on the trailing rider to be studied.

To investigate the flow conditions between the lead and trailing riders a composite technique was required as the presence of the riders obscures part of the imaging plane from the camera. To resolve this issue a series of XZ planes were captured at 10 mm intervals laterally from the centre line. These were focussed on the region between the two cyclists. The streamwise velocity data from these nine slices were then interpolated in the lateral direction to generate cross sections of the flow field. This provided streamwise velocity data in cross sections between the lead and trailing riders and provided the additional information missing from the other imaging planes. The location of these planes is depicted in Figure 2.7.13 below.

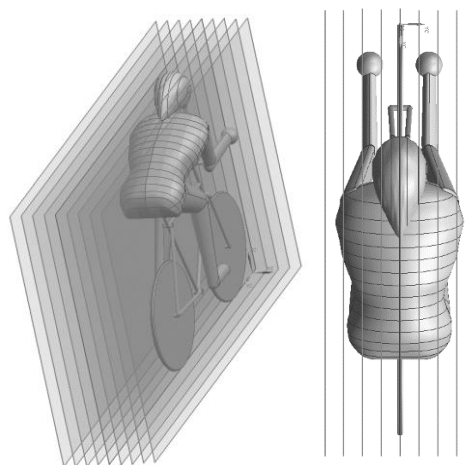


**Figure 2.7.13** - Series of XZ cross section planes. This data was interpolated to capture flow information in the gap between two cyclists.

The chord-based Reynolds number of the cyclists in the water channel was 33,000. This is of the order of 15 times less than a typical full scale Reynolds number of a cyclist travelling at 50km/h. The Reynolds number of these tests was limited by the maximum size and operating speed of the water channel. Whilst previous wind tunnel investigations of cycling have been conducted at Monash University using full scale cyclists at real world Reynolds numbers, that facility does not currently have the capability for high spatial resolution, non-intrusive planar flow mapping such as PIV. The use of scale models in the water channel has this capability and, while the reduced Reynolds numbers of scale models is a

clear limitation, it represents a compromise in pursuit of a greater understanding of the detailed flow field interactions between cyclists.

The lower Reynolds number has potential to generate differing flow behaviour to that of full scale cyclists. However, the existing body of work by Crouch et al. (2014) and simulations by Griffith et al. (2014) provide a basis for comparison with the flow field of a single scale cyclist. The first stage of this investigation was to validate the approach by comparing the single rider scale results with the full scale results. This showed that despite the lower Reynolds number, the scale model wake flow structures did not differ significantly from those around a full scale cyclist, suggesting at least some degree of Reynolds number independence over this range. This comparison will follow in Section 5.4.2.

### **2.7.7 Cyclist Forward Interference Field**

Whilst the wake analysis provides a good insight into the flow field around tandem cyclists, it is also necessary to consider the upstream effect that a trailing cyclist has on the leader. To investigate the upstream interference field produced by a cyclist, a cobra probe was used to measure the flow conditions ahead of the mannequin. Testing was conducted in the Monash University Wind Tunnel with the mannequin was mounted to the Single Rider Cycle Rig. The mannequin was static for all tests with legs positioned at  $15^{\circ}$  crank angle with upper legs level.

A cobra probe (TFI Cobra) was used to characterise the pressure and velocity field upstream of a single cyclist. A single probe was mounted on a fixed slender stand positioned ahead of the cyclist. The probe was positioned in line with athlete's nose (1160mm above ground) as the head is the primary stagnation point for the rider's torso and body. The probe was then translated upstream to measure change in pressure and velocity ahead of the cyclist. Zero axial distance refers to the probe being in line with the bicycle leading edge; level with the front tyre. The probe was then moved forward up to 900 mm in front of the leading edge. Sweeps were conducted along rider centreline and three lateral planes; 100, 200 and 300 mm.

A pitot static tube was used to measure the freestream dynamic pressure and velocity of the flow. The probe was positioned 2m upstream of the cyclist leading edge and off centre to ensure minimal interference on the probe. Dynamic pressure was corrected to the leading edge of the cyclist to normalise the results. Pressure data from the Pitot tube was measured through a digital pressure measurement system (TFI DPMS 1335). This output both total and static pressures from the Pitot tube. Both cobra probe and pressure measurement system were run through the same data acquisition setup to synchronise data sampling. The cobra probe requires a different interface and does not output pressures directly. Each data point was sampled for 30 sec at an output rate of 1000 Hz.

Probe data upstream of the mannequin was normalised by freestream conditions for the empty tunnel at the cyclist leading edge. These reference measurements were taken with the probe in identical setup at the leading edge but with the bicycle and mannequin removed from the setup.

As the static pressure varies longitudinally in the wind tunnel test section, the static pressure results were corrected for the gradient in the tunnel over the interrogation region. This required superimposing a longitudinal gradient over the data to correct for the small change.

### **2.7.8 Dynamic Athlete Wake Traverse**

To extend the realism of the scale model results, the wake of a full scale dynamic cyclist was measured in the wind tunnel. This provides a key link between the scale results and the real world scenario by increasing Reynolds number and using real athlete and bicycle geometries. It also introduces the dynamic component due to the moving legs. The wake of a pedalling athlete was characterised in a single rider formation and in a tandem pair.

A four-hole cobra probe (TFI Cobra) was used to measure pressure and three components of velocity in the cyclist(s) wake. The probe was positioned at one torso chord length downstream of the rear of the single or trailing rider (600 mm). A two-axis automated traverse system was used to move and position the probe in the wake. The probe was mounted on extension tube such that it was positioned 500 mm upstream of the traverse. This minimises forward interference effects from the traverse structure on the wake measurements. Samples were recorded at 1000 Hz.

An elite level athlete was used as the single and rear cyclist in the tandem pair (Athlete B). The bicycle and setup remained fixed in place for all tests. For tandem testing the mannequin was used as the second rider as they were providing interference only. The mannequin was positioned ahead of the athlete with 120mm wheel gap between the two, representing a minimum practical separation for elite track racing (Figure 2.7.14). Mannequin legs were positioned at 15° crank angle (upper legs level). In the single rider case this angle was identified to have a symmetric wake structure with weak vortices. The symmetry was anticipated to best replicate the time averaged nature of a periodic wake and also minimises asymmetric flow across the trailing rider. It will also be shown that the leg position of the leading rider does not have a large effect on the dominant vortices in the trailing cyclist wake.

Wake traverses were conducted in vertical segments behind the dynamic athlete using a two-axis automated traverse system. A course grid with resolution of 80 mm was required so as to minimise time required for sampling when using a human participant in the wind tunnel. As test duration increases athlete's fatigue, they become more prone to movement on the bicycle which will alter their body position and subsequently the flow field. Scale model results from higher resolution PIV data showed that 80mm is sufficiently fine to capture the large scale structures found in the wake of a cyclist. The grid was also cropped to be behind the rider torso and upper legs, rather than extending all the way to the ground plane. Crouch et al. previously showed that this is the primary area of interest as it contains the dominant flow structures. The interrogation region was from 700 to 1660 mm above the ground plane and +/- 400mm either side of centreline. The interrogation region is depicted in Figure 2.7.15 below. For reference the wheel diameter for a standard road bicycle is 700 mm. The rider saddle height was 1050 mm above the ground and the top of the helmet was at 1500 mm. As

the sampling grid of data is relatively coarse, the profiles presented in results are linear interpolations of the sampled data.



**Figure 2.7.14** - Tandem setup in wind tunnel depicting mannequin and athlete with traverse and probe arrangement downstream of the athlete

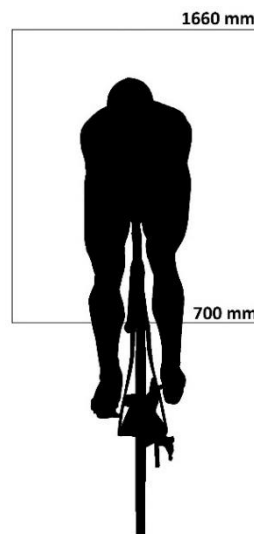


**Figure 2.7.15** - Interrogation region of wake traverse behind the dynamic athlete. Vertical range from 700 mm above ground plane to 1660 mm. Width of 400mm either side of bicycle centreline. Rider shown here with cranks level. Note that rider was pedalling during testing.

A second, identical pressure probe (TFI, Cobra) was used as a reference to measure the freestream conditions during traverses. This was positioned 1m above ground plane height and 1.15 m offset from the tunnel centreline to avoid interference from the cyclists in both single and tandem formations. This probe collected synchronised freestream data used to normalise the wake data.

The limitations of this technique arise through the use of a human athlete as the participant. This imposes limits on the duration of continuous test runs and overall experiment length. As cycling aerodynamics are dominated by the posture of the body it is imperative that the athlete maintain a constant body position for all test runs. Varying body position will alter the wake for each successive wake traverse sweep and will distort the final profile construction (Barry et al. 2014). It is therefore important that individual test runs, and total test time, are not over stretched so that the athlete is fatiguing. Once an athlete fatigues they can lose form and their position on the bicycle changes. To accommodate this only a limited number of data points can be collected in order to maintain sufficient spatial resolution over the cyclist wake region. This limits the spatial resolution possible within the given wake interrogation window. However, the use of athletes for such testing provides full dynamics and realism associated with real world cycling. This was desirable to provide a link between the scale model results and those of real cyclists.

The restrictions on sample time for the tests meant that analysis of the dynamic behaviour was initially thought to be limited due to the small number of cycles sampled at each location. However, further analysis of the data revealed that it was possible to phase average the data with crank angle and achieve convergence to a stable mean. The crank cycle was divided into segments and phase averaging performed over each segment to observe variations in the wake structure with leg position. Review of the mean values showed that the average converged after approximately 30 pedal cycles. A sample is presented in Figure 2.7.16 below.

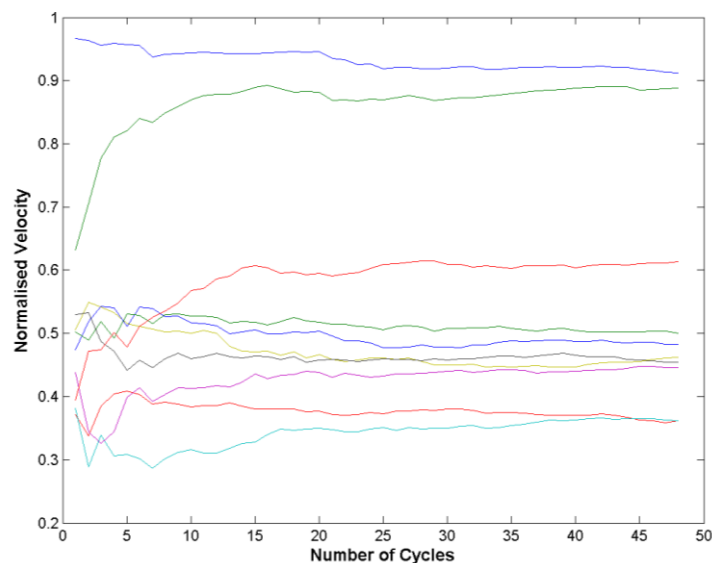


**Figure 2.7.16** - Sample of mean value for phase averaged bin as a function of number of crank cycles. Example shown for streamwise velocity for tandem trailing rider

A magnetic rotational velocity sensor was fitted to bicycle to measure crank velocity. A magnet was secured to the inside of the crank arm such that the sensor receives one pulse per crank revolution. Therefore the sensor only measures average rotational velocity for each crank cycle. The single pulse enabled the identification of the start of each new crank cycle. From this, each pedal cycle was synchronised and phase averaging was performed over discrete angular segments of the crank cycle. For phase averaging, the crank cycle was modelled with constant angular velocity so that each

segment is of equal length in time. For comparison with the static results and to ensure significant number of points per bin, 12 x 30° bins were used in the first round analysis.

Kitawaki & Oka (2013) showed that the crank velocity is not constant during pedalling. For an expert cyclist at a cadence of 100 RPM, the variation in angular velocity is 2% from the mean crank velocity. This showed a peak velocity close to the horizontal position and reduced velocity at the top and bottom of the stroke. This arises due to the muscle recruitment and efficiency at these points. In terms of this analysis, this variation equates to a maximum error of only 2° in crank angle position. Given the large size of the phase segments and the associated error with the leg position ( $\pm 1^\circ$ ) it was reasonable to segment the crank cycle assuming a constant rate of rotation. Furthermore, the flow regimes were not previously observed to change on such rapid scales. Also differences between the athlete dimensions and that of the mannequin used by Crouch et al. & Giriffith et al. could easily distort the precise points of the symmetric and asymmetric flow regimes by a similar order of angular displacement.

The dominant energy containing frequencies of the wake were identified by analysing the power spectral density. Fourier transforms were performed on the time variant pressure signals for each of the 143 sample locations in the in the wake traverse plane to calculate the power spectra. These transforms were performed on the full time signal for the dynamic cyclist wakes, not on the segmented data from phase averaging.

Breaking the crank cycle into 12 segments for phase averaging resulted in a small number of data points in each bin. This was sufficient for phase averaging as mean values were being examined and it was possible to average results across each crank cycle. However, performing a Fourier transform over such small data segments does not produce reliable frequency space data. At the sample rate of 1000 Hz and a pedalling rate of the order of 1.5 Hz the number of samples per segment is only of the order of 50 points. This is not enough for a usable Fourier transform within the crank segments.

### ***Wake Pressure Mapping***

Conducting wake surveys with multi-hole pressure probes is a useful technique, however, point measurements require long sample times and test durations. This is especially true for a body such as a cyclist where geometry is varying with time due to the pedalling of the legs. To further the dynamic analysis of a pedalling cyclists wake and validate the discreet probe measurements it was necessary to be able to sample data using multiple simultaneous channels.

A grid of forward facing pressure tubes was constructed to position in the wake of the cyclist(s) (Figure 2.7.17). As these tubes are pressure taps, not pitot static tubes, they measure the streamwise component of total pressure. That is the static pressure plus the streamwise dynamic pressure. Whilst this is not a typical aerodynamic quantity, it will be shown that this correlates closely with streamwise velocity. By using the total pressure component only, rather than a pitot static, it effectively doubles the number of grid points possible for the same number of data channels. This was important given the large size of the wake interrogation region and a limited number of pressure channels in the pressure measurement units.



**Figure 2.7.17** – (L) Single rider setup with pressure grid 600mm downstream of athlete. (R) Depiction of the interrogation window in the cyclist wake.

The test rig comprised a frame with a regular grid of 121 pressure tubes covering an interrogation region of 0.8 m x 0.8 m. This region extended +/- 0.4 m either side of the athlete centreline and from 1.5 m (the top of the athlete’s helmet) down to 0.7 m (the top of the wheel). This region is similar to the wake traverse testing described earlier, but with a reduction in height due to a limitation on the maximum number of pressure channels that could be sampled. This grid size and resolution was the compromise between size of region and spatial resolution given the number of available sampling channels on the pressure transducers. Analysis of PIV planes from the scale model work showed that this grid size is sufficient to identify the large scale structures in the wake of a cyclist. Pressures were sampled at 1400 Hz using two dynamic pressure measurement systems of 64 channels each (2x TFI DPMS). Each dynamic test run was sampled for 5 minutes (continuous).

Pressure results are presented as a pressure coefficient. This is defined as the streamwise component of total pressure ( $P_{T,x}$ ) normalised by the freestream dynamic pressure.

$$C_P = \frac{P_{T,x}}{\frac{1}{2}\rho U_\infty^2} \quad \mathbf{2.7.1}$$

The pressure measurement systems measure differential pressure. All channels from both units are referenced to the static pressure in the wind tunnel plenum. As the total pressure term is already a differential from the reference there is no need for a reference static pressure, as is typical in presentation of a pressure coefficient. Dynamic pressure was measured using the wind tunnel in-built 6 Pitot tube array. This is mounted upstream of the final contraction and nozzle exit so as to be free from interference from the model. Upstream dynamic pressure was correlated to freestream conditions at the cycling rig to determine freestream conditions at the cyclist.

The pressure grid was positioned 600 mm downstream of the cyclist’s saddle. This corresponds to one torso chord length and is consistent with previous experiments for scale models, wake traverses and the work by Crouch et al. (2012, 2014). Crank position and cadence were measured using the same previously described setup with a magnetic sensor on the crank arm.



**Figure 2.7.18** - Two rider tandem setup with dynamic athlete in trailing position

In addition to the dynamic data sets with the athlete pedalling, the wake of the athlete was also captured for a range of static positions. These profiles provide a reference data set for comparison against the phase averaged results. Previous work by Crouch et al. has covered the wake of a static cyclist in significant detail. Static results will be compared with literature to ensure that the unique approach to this testing is consistent with established understanding. The static tests will provide a direct comparison of the data obtained using this technique with the given athlete. The athlete was positioned on the bicycle with legs static. Wake pressure was sampled at  $30^{\circ}$  crank angle increments around the full crank cycle. Static tests were sampled at 1400 Hz for 30 sec per test. Results show the mean of three back to back samples recorded for each static position. Wake profiles generated for the dynamic cases are the mean of two continuous 5 minute runs with pressure sampled at 1400 Hz simultaneously across the grid. Spatial distribution of pressure values were then linearly interpolated to generate the profiles shown in the results.

Due to the multi-dimensional nature of the data, Proper Orthogonal Decomposition (POD) was utilised to simplify the identification of dominant features in the dynamic wake. Proper Orthogonal Decomposition, or Principal Component Analysis, involves breaking a time variant data set of potentially correlated values into a set of linearly uncorrelated variables. This method defines the transformation in such a way that the first component, or mode, has the maximum possible variance with each successive mode being the next most significant mode. POD is essentially the solving of the eigenvalues of the data set. By calculating for the eigenvectors for the time variant signal at each spatial location it is possible to reconstruct the spatial grid with successive eigenvalues to display the orthogonal modes. For an example of the method see Kerschen et al. 2005.

As there is simultaneous spectral data at each probe location, there is a large volume of dynamic data. POD allows the compression of that data volume into wake profiles representing the dominant features of the fluctuating wake. POD is useful to represent the time variant response across the wake surface but it is also advantageous as it achieves optimality. That is that the modes are ranked and weighted such that each successive mode is less dominant than the previous. As such a reconstruction of 'x' modes will be the optimum representation of the system from 'x' possible modes.



## Chapter 3

### The Effect of Leg Dynamics

#### **3.1 Static vs Dynamic Drag for a Single Cyclist**

The consideration of cycling dynamics is important to an investigation of aerodynamics. It has been shown that leg position affects flow behaviour and subsequently drag. However, it has not been shown how the drag of a cyclist with static legs differs from the drag of a pedalling cyclist. Using an athlete for testing allowed for both static and dynamic measurements to be conducted on the same cyclist geometry. Static results could then be compared with the previous results of Crouch et al. (2014).

Drag of Athlete E was measured at  $15^\circ$  increments for the half crank cycle. Symmetry was assumed for the second half of the cycle. It was seen that the drag of the athlete was at a minimum at the start and mid-point of the crank cycle ( $0^\circ$  and  $180^\circ$ ) when the cranks were horizontal and upper legs close to the level position. Drag reached a maximum between  $60^\circ$  and  $105^\circ$ , corresponding to the left leg raised and close to the torso and the right leg extended (see Figure 3.1.1). This behaviour is consistent with the mannequin results of Crouch et al. (2014). However, as individual cyclist geometry strongly influences drag magnitude it is not reasonable to directly compare the athlete and mannequin drag directly. To enable comparison, the change in drag was determined, referenced to the  $0^\circ$  crank position. The resulting drag difference shows the variation in drag due to leg position and eliminates the differences due to athlete size. The athlete results align with the mannequin results with a mean deviation of 1.7% (see Figure 3.1.1). It was expected that there would be some differences between the two curves caused by geometric differences in the basic human form and functional shape and position of the cyclists. Whilst the primary flow mechanisms are dominated by the position of the legs and this would have the major impact on drag; differences in size and geometry were expected to have a subtle influence on the results and cause variation between athletes. Mean uncertainty for the drag of Athlete E was 0.9% ( $0.0024 \text{ m}^2$ ) and 0.7% ( $0.0018 \text{ m}^2$ ) for static and dynamic measurements respectively.

The drag averaged over the half crank cycle was found to differ from the dynamic drag averaged over time for a pedalling cyclist. The static drag measurements were integrated over the half crank cycle using a trapezoidal method to fit to the data points. From this the mean drag from  $0^\circ$  to  $180^\circ$  of static measurements was calculated. Figure 3.1.1 shows that the time averaged drag of a pedalling cyclist is higher than the integral average of the static measurements around the crank cycle. The difference is greater than the uncertainty for both the static and dynamic results, showing that the two values are significantly different. This indicates that there is some additional flow complexity present in the aerodynamics of a pedalling cyclist, which cannot be fully explained by static measurements.

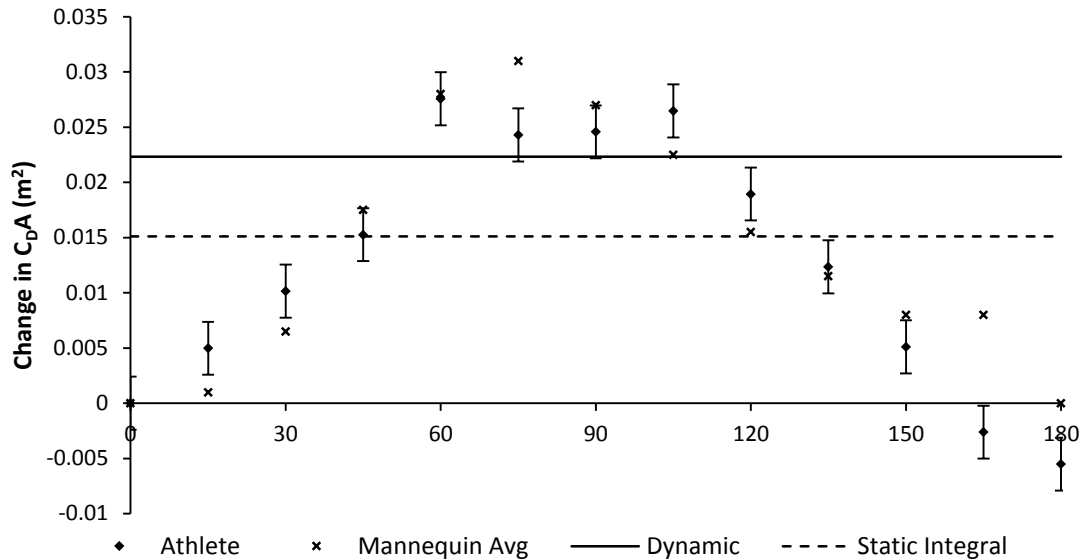


**Figure 3.1.1** – Change in  $C_D A$  referenced to  $0^\circ$  crank position for athlete and mannequin (Crouch et al. 2012), including the time averaged dynamic and the result of integration across the static crank results. (Mannequin values averaged for the first and second halves of crank cycle)

From this result it can be reasoned that the use of a static cyclist for aerodynamic evaluation, rather than a dynamic pedalling athlete, could result in a significant error, depending on the leg position used. Most existing literature has conducted measurements using static cyclists with horizontal cranks. Results presented here show that such an approach will significantly under predict the actual drag of a cyclist when they are pedalling in a real world scenario.

A difference between the normalised  $C_D A$  was observed between the two end points at  $0^\circ$  and  $180^\circ$  crank angles for the athlete. From symmetry of the body these two points should be the same. This shift could be due to the asymmetry of the bicycle driveline but is most likely caused by a change in the athlete’s riding position between tests. This is an inherent limitation of athlete testing, but was necessary to allow comparison of static and dynamic drag.

The results for the static leg positions confirm the more extensive investigation by Crouch et al. (2012, 2014) for an athlete subject. The drag of a cyclist varies with the position of the legs, resulting from changes to the surrounding flow field.

During cycling the pedalling motion of the legs forces the flow to continuously transition between the different flow regimes. As a result, the drag of a dynamic cyclist will oscillate with the leg rotation. This periodic drag response can be observed in the time histories of force measurements for a pedalling cyclist. It has been shown that the instantaneous rotational velocity varies as a function of crank position (Kitawaki & Oka 2013). As a result, a cyclist’s legs will be transitioning through different regions of the crank cycle at different rates. This in turn implies that the time spent at each of the flow regimes is unequal. It was observed that the slowest rates of rotation are when the cranks are near vertical ( $90^\circ$ ), which corresponds to the strongly asymmetric and high drag flow regimes in the wake. This results in a greater period of the pedal cycle being spent in the high drag regime. The higher value

of the dynamic drag compared to the crank angle average of static results is likely caused by this uneven weighting of the high drag flow regimes.

The difference between the static average and the dynamic drag can also be linked to the motion of the legs relative to the freestream. This may be inducing a change in local velocity over the legs that is not present in static tests. This will result in a local increase in drag. Furthermore, the motion of the legs may cause a pumping of the air between the torso and leg. This would then force the flow out over the hips with higher momentum than is seen in the static case, altering the separation points and increasing the pressure drag generated by the wake. More detailed investigation of the dynamic flow field would be necessary to fully determine the mechanism behind this effect. It is also noted that force measurements in the wind tunnel can not differentiate the aerodynamic drag component from potential inertial forces of the moving legs of a pedalling cyclist. These inertial forces may also contribute to the difference between static and dynamic drag.

Changes to the orientation of joints at static positions compared to the activated pedalling motion may lead to subtle differences in geometry between the static and dynamic cases. This may alter frontal area, and hence  $C_D A$ . However, it was shown by Crouch et al. (2014) that the variation in frontal area over the whole crank cycle is less than 2%. Therefore, subtle variations in joint angle will not account for the magnitude of change observed in these results.

Results have shown that static drag varies as a function of leg position. However, given a sufficient time average, drag of a pedalling athlete will be a constant. As such, it is possible to test a static athlete at a leg position that will result in the same drag as would be measured for pedalling legs. From Figure 3.1.1, this would occur between  $45^\circ$  and  $60^\circ$  and again between  $105^\circ$  and  $120^\circ$ . The specific value is likely to vary with individual athlete geometry. Whilst the measured drag may be equal for the two cases, the flow fields will differ. The wake studies of Crouch et al. shows that the minimum drag case corresponds to a symmetrical flow regime, whereas higher drag corresponds to an asymmetric wake. Therefore, a static leg position that has equal drag to dynamic drag will correspond to an asymmetric wake flow regime. By contrast, the periodic nature of a pedalling athlete is expected to result in a symmetric mean wake profile.

Whilst variations in body shape and size are expected to result in differences in the drag between different athletes, these differences will be secondary compared to the more dominant effect arising from the state and position of the legs.

### 3.2 The Effect of Leg Dynamics in Two Cyclist Formations

The drag of a cyclist with static legs has been shown to differ from the drag of that cyclist with pedalling legs. It follows that the drag of cyclists in a two rider formation will also be affected by the dynamics and position of the cyclists' legs. Two athletes were tested in tandem and transverse formations with dynamic legs as well as two static positions; 15° and 75° equating to the two key characteristic flow regimes, as identified by Crouch et al. (2014)

#### 3.2.1 Tandem Formation

Drag was measured for two athletes in a tandem formation. The drag of lead and trailing cyclists was found to vary depending on the state and position of the legs. For the practical case of two dynamic riders a 44% reduction in drag was observed for the trailing athlete, which is consistent with literature (Kyle 1979, Zdravkovich et al. 1996, Broker et al. 1999, Blocken et al. 2013).

Tests with combinations of static and dynamic cases for the lead and trailing cyclist showed that the drag of the trailing rider is influenced by the dynamics and static positions of the leader's legs (Figure 3.2.1). With the lead rider static at 15° crank angle the difference from the dynamic case is small (1%). However, with the lead rider at 75° there is a 4% increase in measured drag for the trailing rider. Crouch et al. showed that a single rider at 75° crank angle generates a highly asymmetric wake. Results indicate that the steady asymmetric wake from a leading rider at 75° crank position results in significantly difference flow conditions to the time varying wake of a pedalling cyclist.

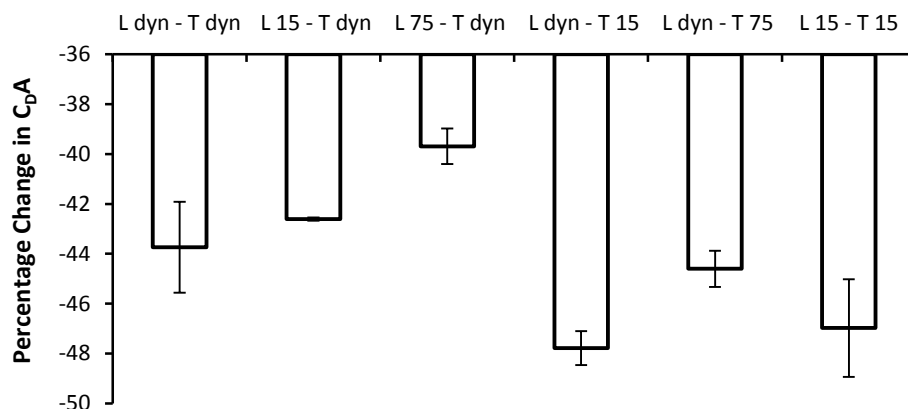


**Figure 3.2.1** – Percentage change in  $C_{dA}$  of the trailing rider in a tandem pair compared to the rider in isolation. Legend; L = lead, T = trail (referring to each rider in the tandem pair), dyn = dynamic legs

Changing the leg position of the trailing rider also influenced the drag of that rider. This was expected from the single rider static results, which showed drag to vary with leg position. With the trailing rider static at  $15^{\circ}$  the drag of that rider is 4% below the drag of the practical case with two dynamic riders. Referring to the earlier static results (Figure 3.1.1), it was seen that at  $15^{\circ}$  a rider's drag was lower than the drag for the dynamic case. Therefore, it can be concluded that the geometry effects of static legs are having a similar influence for a rider when trailing in a two rider formation. A similar explanation can be applied to the  $75^{\circ}$  case. A static single rider at  $75^{\circ}$  crank angle recorded drag greater than the dynamic result. Here, it is seen that the trailing rider with legs static at  $75^{\circ}$  has drag that is slightly greater than the dynamic case. This indicates that it is the individual rider's leg position that is dominating the results; the change in drag is mostly due to changes in the trailing riders flow field, rather than an interaction with the leader. With both riders' legs static at  $15^{\circ}$  there is a 3% decrease for the trailing rider from the dynamic case. This appears to be a summed effect for the cases of each individual rider being static at the  $15^{\circ}$  crank position. A common practice in literature to date has utilised two static riders at a crank angle close to  $0^{\circ}$  (Zdravkovich et al. 1996, Blocken et al. 2013). These results suggest that such test conditions will over predict the drag reduction experienced by the trailing cyclist compared to the practical case with pedalling athletes.

The drag of the lead rider was also seen to vary with leg position. Sample tests were conducted with the instrumented rider in the lead position. In this formation the lead rider experiences nearly a 4% reduction in drag due to interference from the trailing rider when both are pedalling. Computational simulations (Blocken et al. 2013) have previously reported a drag reduction for the leading rider in a tandem formation. With the leading rider static with legs at  $15^{\circ}$  the observed drag was reduced by a further 6% below the dynamic case. Lower drag for the instrumented rider at  $15^{\circ}$  is similar to the trailing rider case, indicating that the leg position of the instrumented cyclist has a greater effect than of the secondary rider.

### **3.2.2 Transverse Formation**

The drag of cyclists in a transverse formation (side-by-side) also varies as a result of aerodynamic interactions between the riders. For the real world case of two dynamic riders there is a 7% increase in drag (Figure 3.2.2). This result has not been previously reported for cyclists. An increase in drag at this position has the potential to significantly impact on cycling tactics, especially in mass start and bunch events. Clearly it is detrimental to the performance of both riders to be riding side-by-side.

The drag of cyclists travelling side-by-side was seen to vary with the motion and position of the legs of both riders. With the secondary, interfering rider static at  $15^{\circ}$  and  $75^{\circ}$ , there is only a small deviation in the instrumented riders drag; a maximum of 2% from the dynamic result. However, with the primary instrumented rider static there are more significant changes in drag. At  $15^{\circ}$  the drag of the instrumented rider is below the drag of the cyclist in isolation. As seen previously for the tandem formation, this is likely the result of the changes to the flow field caused by the legs being static at the  $15^{\circ}$  position as this was seen to have significantly lower drag in single rider tests (Section 3.1). Conversely, the static  $75^{\circ}$  case shows nearly a 3% increase in drag above the dynamic result. This is

consistent with the single rider results which exhibited higher drag for the static 75° case compared to the dynamic pedalling case. With both riders static at 15° there is a significant reduction in drag for the instrumented rider (6%) and the result is close to the single rider baseline result. Similar to previous cases, this result is heavily influenced by the effect of the instrumented rider being static at 15°, an angle at which a single rider has significantly lower drag than in the dynamic case.

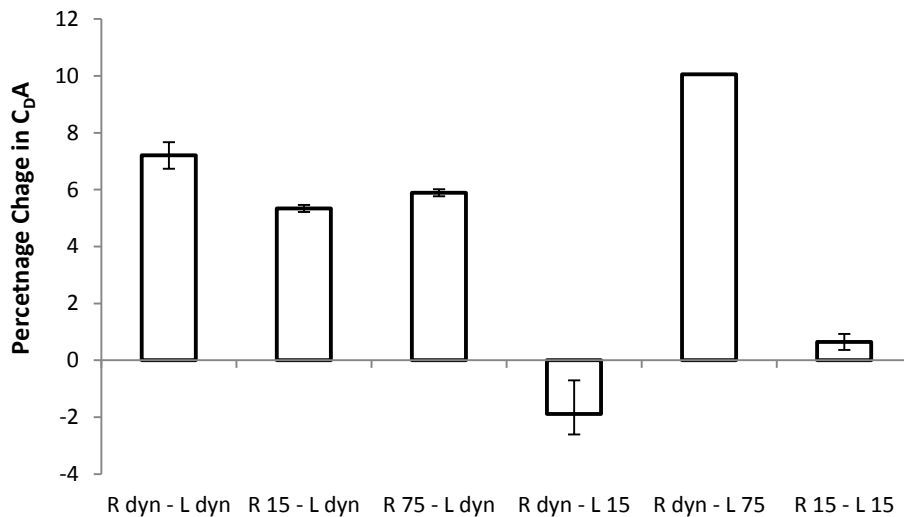


**Figure 3.2.2** – Percentage change in  $C_D A$  for the left rider in a side-by-side (transverse) formation compared to the dynamic cyclist in isolation. Legend; L = rider on left, R = ride on right; 15 = crank angle of 15°, dyn = dynamic legs

This testing contains some bias as the 75° crank position corresponds to the left leg raised; in this case the leg closest to the second rider (right leg) is down. It is possible that the results may vary for the opposite leg raised (255°) as flow will have opposite horizontal velocity component. However, this is expected to have a greater influence on side force than drag.

These results show that it is the leg position of the instrumented rider that has the largest influence on drag in two rider formations. Therefore, it can be recommended that a dynamic cyclist be used for cycling investigations to obtain the closest representation of real world cycling performance. For investigation of two rider formations the use of a static cyclist at 15° for the secondary rider is a reasonable approximation as it translates to only a small error in the measured drag for the instrumented rider in both tandem and transverse formations.

## Chapter 4

### Force Interactions Between Multiple Cyclists

#### **4.1 Drafting**

Riding in the wake of another cyclist or a vehicle has been known, from practice, to significantly reduce aerodynamic drag. Several authors have investigated this effect but the results are inconclusive due to differences in method. This investigation aimed to conduct a detailed wind tunnel study to conclusively identify the influence that spatial distance has on the drag of both the lead and trailing rider in a two rider formation. Drag force was measured for riders travelling in a drafting formation; this is when the riders are in a tandem formation i.e. the riders are in line and parallel to the flow. In addition to the inline formation staggered positions were tested with the trailing rider at a lateral offset from the leader's centreline. Drag was measured for both the lead and trailing riders separately and compared to the rider's standalone drag value.

Two separate test protocols were used in this study. The first had a limited axial range due to the fixed location of the force balance in the wind tunnel. To overcome this limitation on the distance between riders and to hence extend the domain of the study a second phase was run using a different force balance. The two sets of results are presented below.

##### **4.1.1 Phase 1**

In the first iteration of the testing the range was limited by the fixed location of the force balance within the wind tunnel (refer to Section 2.3.1). The resulting drag saving for the lead and trailing rider in a two rider formation are presented in Figures 4.1.1 and 4.1.2 below.

It can be seen that the drag of cyclist varies significantly with proximity and location of a second rider. This result is consistent with existing literature for bluff bodies, vehicles and cyclists. Results showed that other loads are negligible at zero yaw conditions. These results are provided in Appendix D. In addition to the expected drag reduction for the trailing rider, a reduction was also observed for the lead rider. This has not been widely observed in previous experimental studies. The maximum drag reductions were found to be 5.5 and 49% for lead and trailing riders respectively. In both cases this occurred for cyclists being inline and at minimum axial separation.

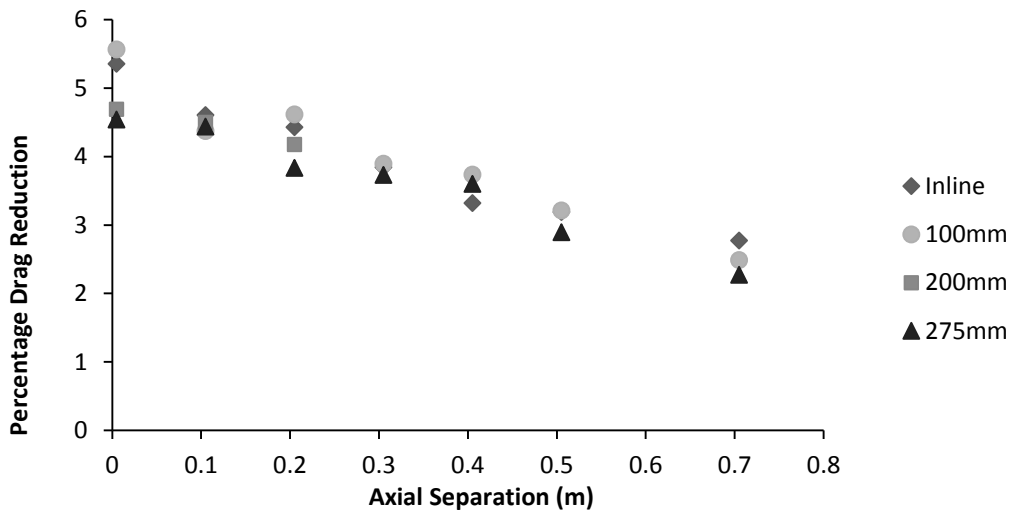


**Figure 4.1.1** - Drag reduction for the lead cyclist in a tandem pair. Series refer to lateral offset of the trailing cyclist from the leading bicycle centreline.

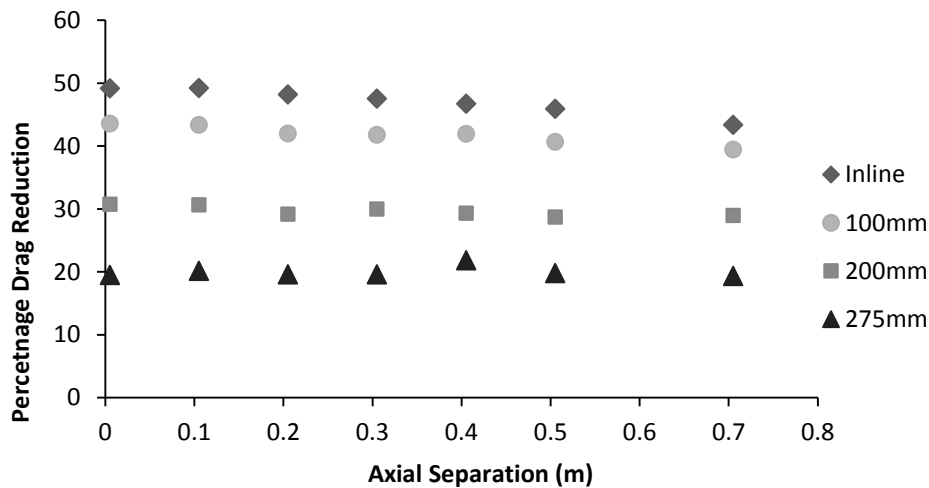


**Figure 4.2.2** - Drag reduction for the trailing cyclist in a tandem pair. Series refer to lateral offset of the trailing cyclist from the leading bicycle centreline

The drag reduction for the lead rider was seen to strongly depend on the axial separation, whilst lateral separation had a minor influence. The reverse is seen for the trailing rider with drag being a stronger function of the lateral displacement from the centreline than distance downstream. In both cases the limit of interactions was not reached as both lead and trailing cyclists were still experiencing a drag reduction at the limit of the test range. Given the mean uncertainty of 0.1% and 0.3% for the lead and trailing rider respectively, even the minimum reduction observed for the lead rider (2.5%) is a significant result in terms of elite competition. To extend the range of spatial positions a second phase of testing was conducted.

It can be seen in Figure 4.1.1 that the drag reduction at 100 mm lateral offset between the lead and trailing cyclists is greater than the inline formation at some points. However, as the difference between results is of the order of the uncertainty in the drag measurements, there is no significant

difference between the curves. It can be stated that over the lateral range tested in these experiments, the lateral offset between lead and trailing did not significantly influence the drag reduction of the leader.

It was previously identified (Section 3.1) that the drag of a static rider will be lower than that of a pedalling cyclist. This was also found to occur for cyclists in a two rider formation. This suggests that the use of a static mannequin for this testing would result in a greater drag reduction than for two dynamic riders. However, because these results are based on differences and the reduction is referenced to the static mannequin in isolation, the observed change in drag will not result in the same magnitude error than that seen when comparing a dynamic and static cyclist in tandem (see Section 3.2). The static mannequin was used as the instrumented rider in this initial phase to minimise variability in results as human test subjects typically have difficulty obtaining high levels of repeatability.

For a single cyclist in a steady state at zero yaw the drag is the only significant load acting on the system. In a tandem formation the same situation applies; there are no significant lateral forces or moments induced on the cyclists. As a consequence only drag is presented in these results. Results for side force, lift and moments for cyclists in a tandem formation can be found in Appendix D.

#### **4.1.2 Phase 2**

A second phase of drafting force testing was conducted to extend the range of the study. To facilitate this, testing was performed using the multi rider air bearing rig (see Section 2.3.2). This allowed the instrumented rider to be positioned far downstream for trailing rider measurements. Similar to the first phase, only one rider was instrumented at a time, with the other acting as interference only. However, positions were reversed with the dynamic athlete now acting as the instrumented rider and the static mannequin as the interference. This was done to maximise the realism of the test scenario by measuring drag of a dynamic athlete. This decision was only made after establishing suitable repeatability from the athlete.

It was shown in Section 3.2 that using a static rider to act as interference in a two rider tandem formation, coupled with a dynamic instrumented rider, results in only a small error compared to the case of two dynamic cyclists. Furthermore, results are presented as a difference from the baseline state to minimise errors associated with the use of the static mannequin as the secondary cyclist. It was previously stated that a mannequin was used in Phase 1 to ensure high repeatability of testing. However, further athlete testing showed that adequately low uncertainty can be achieved using a pedalling athlete. In these tests the mean uncertainty in drag measurements was 0.4%. A maximum separation between the riders of 5 m could be achieved using this new setup. Results for lead and trailing rider are displayed in Figures 4.1.3 and 4.1.4 below.

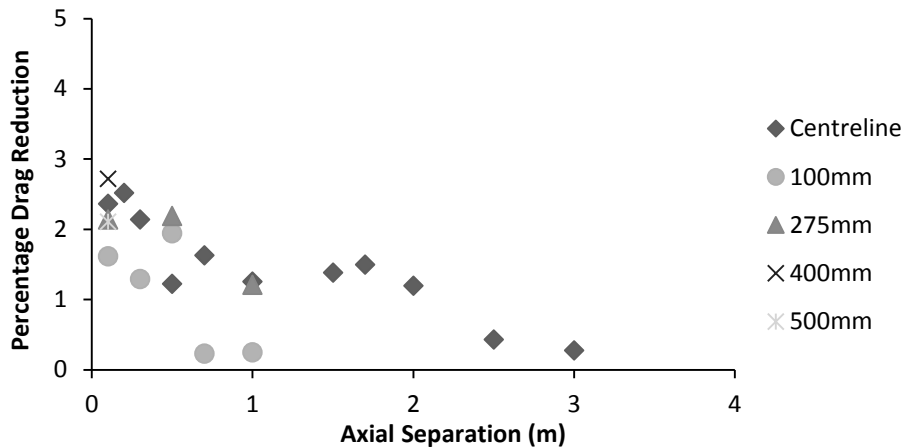


**Figure 4.1.3** - Drag reduction for the leading cyclist in a tandem pair. Measurements are for a pedalling athlete. Series refer to lateral displacement of the trailing cyclist from the bicycle centreline.

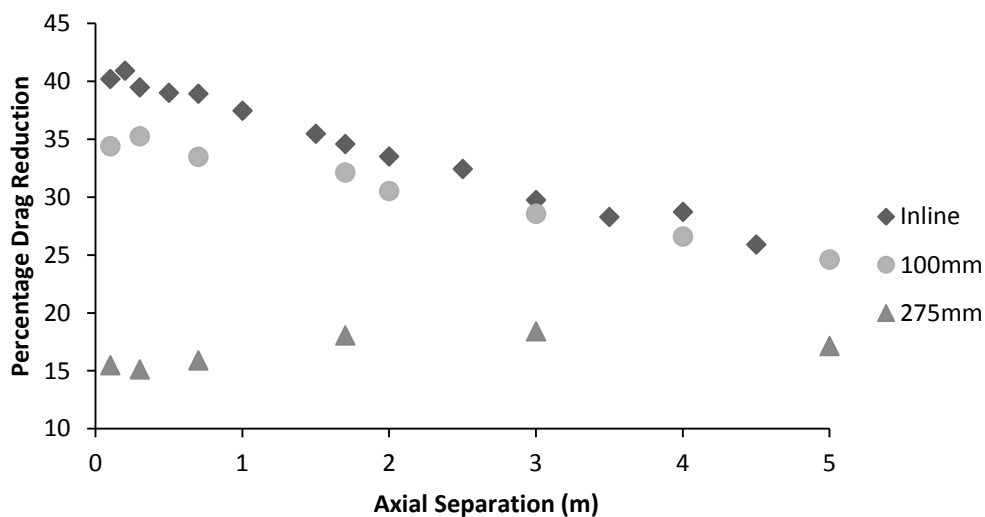


**Figure 4.1.4** - Drag reduction for the trailing cyclist in a tandem pair. Measurements are for a pedalling athlete. Series refer to lateral displacement of the lead cyclist from the bicycle centreline.

Drag results confirm the Phase 1 finding of a drag reduction for the lead rider. Over a short range (up to 0.7 m) the trend in the leading rider drag reduction is similar to the Phase 1 results, with lateral separation having a greater effect on drag than the axial separation. However, beyond 1 m axial separation between cyclists, there is only a significant drag reduction when the lead and trail and inline. Once axial separation exceeds 2 m there is a negligible change in drag for the leader as results approach the measurement uncertainty (0.4%). Therefore, it can be stated that 2 m is the limit of interaction effects for the lead cyclist.

Trailing rider results are consistent with those of Phase 1. Up to 0.7 m axial separation the lateral displacement has a greater effect on drag than axial separation. However, it can be seen that the curves for the inline and 100 mm cases converge as axial distance increases and join at around 3m separation. The curve for 275 mm lateral separation also appears to converge, though it does not meet the other two by the maximum separation distance reached (5 m) in these tests. This means

that the drag reduction for the trailing rider at 275 mm actually slightly increases for greater distances downstream. For all cases of lateral displacement, the limit of interactions for the trailing rider was not reached, despite the large increase in separation distance tested. It is noted that the wind tunnel presents idealised conditions. As such, in real world conditions with atmospheric wind and high turbulence these effects may be degraded. Furthermore, these results have not considered the effect of yaw angles on the drag of the cyclists.

For both the lead and trailing rider the magnitude of drag reduction is decreased compared to Phase 1 results. This is probably caused by the switch in the cyclists. In this case the instrumented rider is the athlete, rather than the mannequin. Due to a size differential between the athlete and mannequin the larger athlete would be expected to have a larger effect on the smaller mannequin (note that athletes used in each phase had similar dimensions). The larger size and area of the athlete is expected to have a slightly greater interference effect when acting as both the lead and trailing rider. This resulted in slightly higher drag reductions for the mannequin in Phase 1 results. In these results for Phase 2, where the mannequin is acting as interference on the athlete, the interaction effect is slightly reduced. This equates to a smaller drag reduction for the athlete when acting as both lead and trail. This theory has been described by Edwards & Byrnes (2007) who showed that athletes with larger standalone drag will provide greater sheltering when acting as the lead rider in a tandem pair. This effect is a natural part of real world cycling as differences in body size and will equate to slightly different interactions for any given pair. However, it is important to note that the trends observed in both sets of results are consistent and the 41% drag reduction for the trailing rider still equates to a very significant effect on performance. Even the 2-3% saving observed for the lead rider, whilst small, is still significant in elite competitions.

### ***Practical Significance***

These results have shown that even with 5 m between cyclists there is still as much as a 25% decrease in drag for the trailing rider. This is of special importance to mass start time trial events, such as amateur (age-group) triathlon racing. The International Triathlon Union (ITU) rules state that for age group events, where drafting is not permitted, athletes must maintain a draft zone of 7 m in length from the front wheel of one rider to the front wheel of the next. Taking a standard bike length to be of the order of 1.7 m this equates to 5.3 m from the rear wheel of one bike to the front wheel of the next. Given that this study found a drag saving as large as 25% for the trailing rider at 5 m it seems clear that there is in fact an advantage for the trailing rider, even when abiding by the ITU rules. Such a conclusion suggests that the ITU may wish to consider whether the rules for non-drafting triathlons should be revised, and the drafting zone increased to a greater distance, if they are to limit the benefit gained by the trailing rider under such situations.

### 4.1.3 Comparison with Literature

The effect of spatial separation on the drag of a drafting cyclist has been previously investigated by several authors; most notably Zdravkovich et al. (1996), Kyle (1979) and Blocken et al. (2011). However, limitations in the methods used have led to inconsistencies in these results.

Kyle conducted coast down tests in the field. Coast down tests, particularly outdoors, are notoriously difficult to control due to environmental conditions, which leads to high uncertainty. This was stated by Kyle in the original paper.

Zdravkovich et al. performed similar experiments to the present results in a closed section wind tunnel. This should provide more controlled conditions. However, the small cross section used in these experiments resulted in high blockage. No details were provided of any blockage correction. It was reported that at 900mm (the limit of the study) the drag saving for the trailing rider was negligible. This is a much more rapid decay in the interference effect between the two riders than reported by all other published work. It also contrasts with anecdotal reports from athletes, which suggest a significant drag reduction beyond 1 m. Zdravkovich et al. also reported that one of the athletes experienced an increase in drag above their standalone value at large separation. Such a result contradicts the findings of all other documented work relating to drafting cyclists.

Blocken et al. conducted computational simulations on two cyclists in drafting formations using suspended rider geometries; i.e. without bicycles. This study reported drag reductions that were considerably lower (maximum of 14%) than other literature and lower than observed in practice from power meter data. Whilst the magnitude of drag reduction reported was very low, the gradient was more similar to that found by Kyle and also the results found here. This suggests that interaction benefits exist for the trailing rider at large axial separation values. Blocken et al. also reported a small drag reduction (2.6%) for the lead rider, which had not been previously shown in experimental studies. This is of a similar order to the results of this work.

Compared to key literature the results presented here show an interaction effect for the trailing rider that extends far downstream. When the cyclists were separated by 5 m, the limit of interaction effects was still not reached for the trailing cyclist. This gradient of decay is consistent with Blocken et al. and Kyle, as well as anecdotal evidence. Similarly the large drag reduction is of equal magnitude as that seen in several other studies (McCole et al. 1990, Broker 1999, Edwards & Byrnes 2007, in addition to Zdravkovich et al., Kyle and Blocken et al.), which have considered drafting only at small separations. Given that the current studies employed dynamic athletes, a proven, reliable force balance and a large wind tunnel test section, it is suggested that the results of this work could provide more reliable indications of cyclist drag as a function of spatial position than any previously published data.

## 4.2 Overtaking

Tandem formations only describe some of the interactions experienced by cyclists in competition. During mass start and team events cyclists will spend time travelling side-by-side with other riders, for example when overtaking. Figure 4.2.1 describes the drag reduction experienced by a cyclist who is being overtaken. Spatial positions refer to the location of second, interfering cyclist relative to the instrumented reference cyclist. The zero point refers to the front wheels of the two cyclists being level with 500 mm lateral offset between bicycle centrelines (see Section 2.7.3). Figure 4.2.2 shows a visual representation of the drag saving as a spatial map.

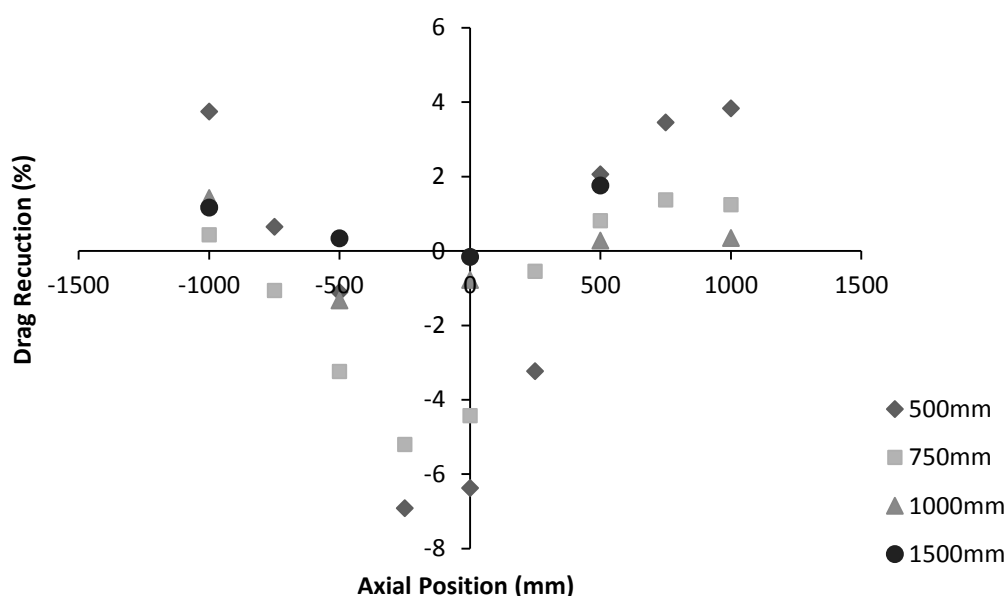


**Figure 4.2.1** - Drag reduction for a cyclist with a second, interfering cyclist overtaking. Spatial positions refer to the location of the secondary cyclist's front wheel. Positive axial position indicates secondary rider is ahead of the instrumented rider. Negative drag reduction indicates an increase in drag for the cyclist being overtaken.

The sequence of drag changes as a rider (primary) positioned on the left is being overtaken by a rider (secondary) on their right can be described as follows. The passing rider is initially downstream and is reducing their drag by drafting the lead rider, who also experiences a small drag reduction. As the passing rider moves forward the primary rider's drag increases. At the point of being side-by-side both riders experience drag that is above their standalone value. As the passing rider continues forward the riders' drag begins to decrease. As the riders begin to conform to a drafting formation the drag again drops below the standalone value. At such point the primary cyclist is now in the trailing position, hence the observed drag saving being greater for positive axial positions. As lateral distance is increased between the two riders the influence of the second rider is reduced and by 1500mm the interference is negligible. This can be seen in Figure 4.2.1 (above) and is depicted as a spatial contour in Figure 4.2.2 below.

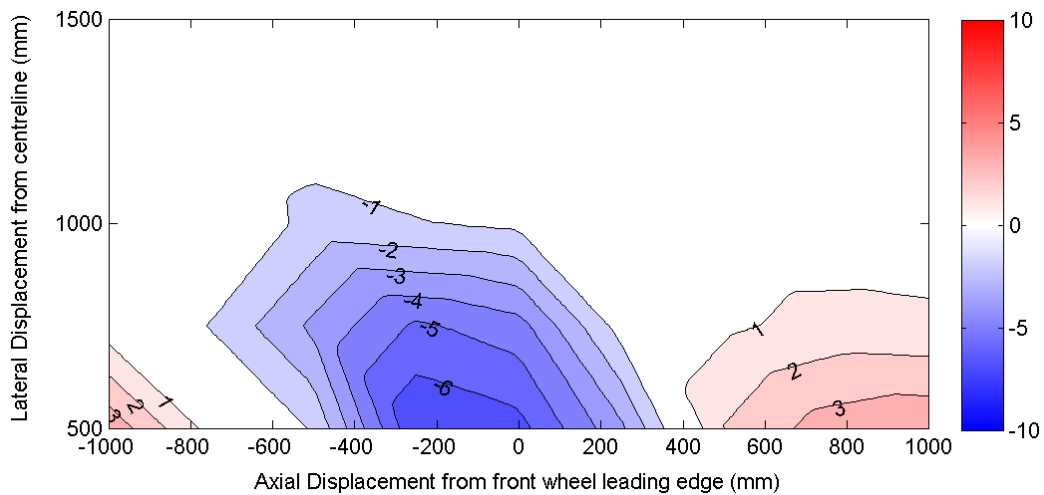


**Figure 4.2.2** – Spatial contour map of drag reduction (%) for a cyclist with a second, interfering cyclist overtaking. Spatial positions refer to the location of the secondary cyclist’s front wheel. Positive axial position indicates secondary rider is ahead of the instrumented rider. Negative drag reduction indicates an increase in drag for the cyclist being overtaken.

In contrast to what is seen for inline formations, drag is not the only significant load acting on cyclists travelling side-by-side. Due to the complex flow interactions side force, roll and yaw moments are induced on both riders. These loads are, however, lower in magnitude than the drag. Side force, roll moment and yaw moment all vary as a function of both axial and lateral position of the interfering rider. The behaviour of these loads is similar to that of drag, with the maximum influence occurring at minimum lateral separation and close to or just behind level axially. As side force, yaw and roll moments are negligible for a single rider the results are expressed as coefficient area products rather than a percentage of the single rider value. These results are shown in Figures 4.2.4, 4.2.5 and 4.2.6 below. Side force was found to peak at approximately 25% of drag force. This occurs when the overtaking rider’s axial position is just behind that of the reference rider. Side force is measured as positive for the cyclist on the left, which equates to a repulsive force. Roll and yaw moments are both outwards from the centre of the two riders.

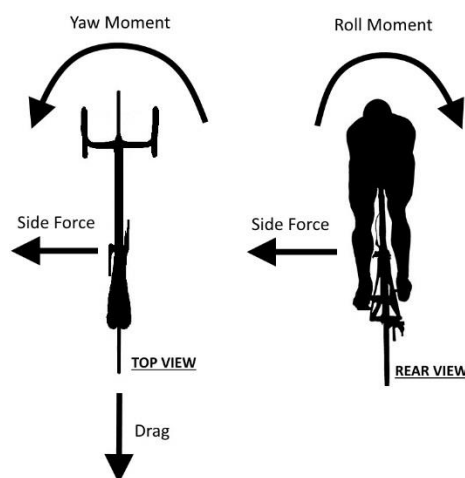


**Figure 4.2.3** – Aerodynamic load and moment direction definitions shown (positive direction).

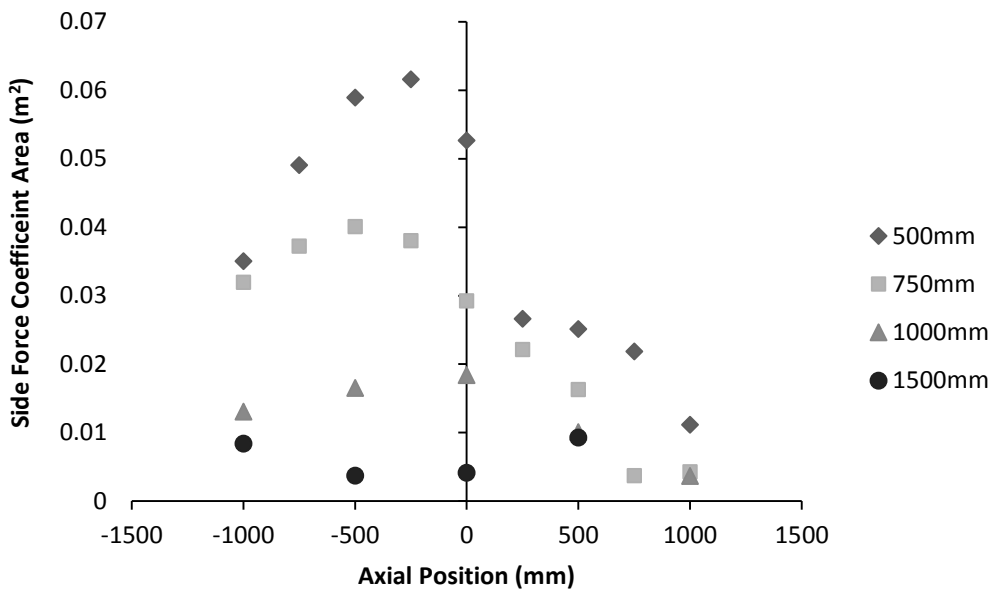


**Figure 4.2.4** - Side force ( $C_{sA}$ ) for a cyclist with a second interfering cyclist overtaking. Spatial positions refer to the location of the secondary cyclist's front wheel. Positive axial position indicates secondary rider is ahead of the instrumented rider.

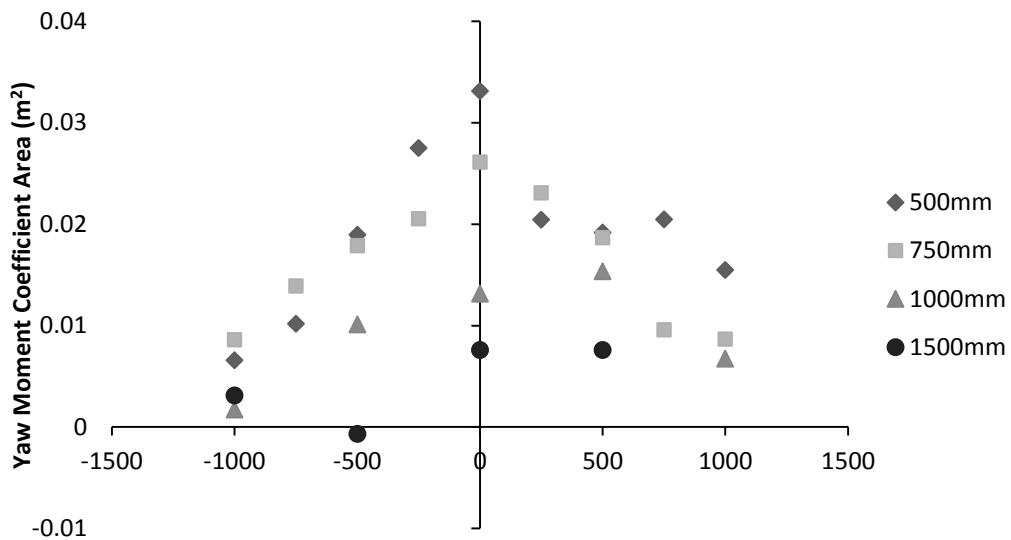


**Figure 4.2.5** - Yaw moment ( $C_{mzA}$ ) for a cyclist with a second interfering cyclist overtaking. Spatial positions refer to the location of the secondary cyclist's front wheel. Positive axial position indicates secondary rider is ahead of the instrumented rider.

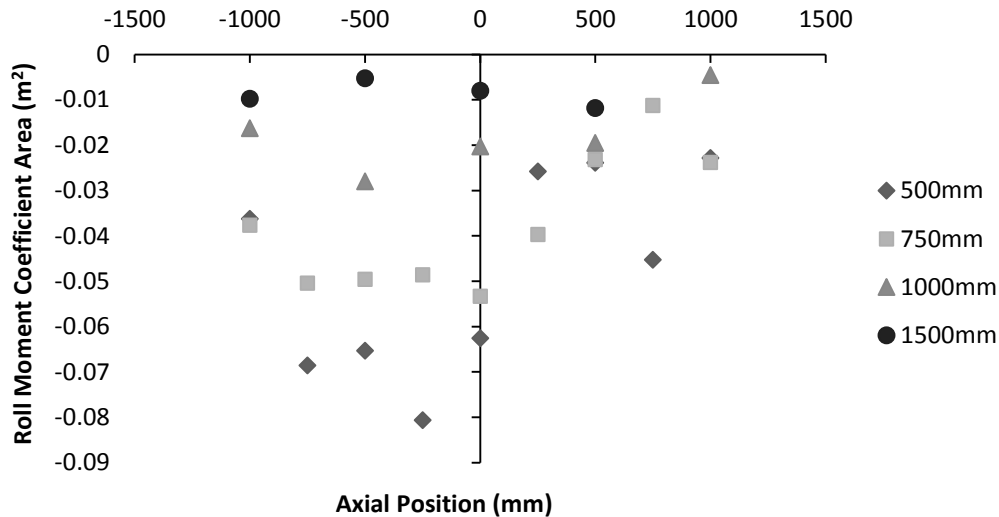


**Figure 4.2.6** - Roll moment ( $C_{MxA}$ ) for a cyclist with a second interfering cyclist overtaking. Spatial positions refer to the location of the secondary cyclist's front wheel. Positive axial position indicates secondary rider is ahead of the instrumented rider.

These results are consistent with trends observed in literature for circular cylinders, which have been shown to have drag above the single cylinder configuration when positioned side-by-side (Biermann and Herrnstein 1933, Zdravkovich 1977, Hori 1959). A repulsive side force was also observed between two cylinders at small separation. Results also agree with the findings by Romberg et al. (1971), who performed similar experiments on scale model stock cars. The region of interference for the stock cars was similar to that of the cyclists, with the maximum drag increase occurring when the overtaking car was slightly downstream of being level with the front car. The drag was found to increase by 37% when the passing car was half a length downstream and there were 0.478 car lengths between the cars' centrelines. The side force was also significant, with a maximum occurring when the overtaking car was 0.5-0.85 lengths downstream. As with the cyclists, the side force was repulsive.

One key difference between a cyclist and other bluff bodies is that majority of the bluff part of the combined cyclist and bicycle system is far shorter than the total bicycle length. The rider contributes far greater area to the total than the bicycle and Crouch et al. (2014) showed that the primary separation occurs behind the torso of a cyclist. However, the wheels of a bicycle extend well ahead and downstream of the rider's body. If the rider's chord (~600mm) is used to normalise the positions, it can be seen that axial position of maximum interference (250mm) corresponds to a normalised length of 0.42, compared with 0.5 for the stock cars.

### ***Practical Significance***

This finding has significant practical significance as it shows that cyclists travelling side-by-side in close proximity will induce a drag increase for both. This contradicts current cycling practice which typically advises cyclists to ride at minimum axial separation when working together. Results presented here show that this is in fact detrimental to performance. For riders looking to maximise speed, for example in a breakaway group, it would be best to rotate turns whilst maintaining 1.5m between their centrelines to minimise any potential interference and induced drag.

This result is also of importance to sprinters and highlights the importance of athletes being mindful of their proximity to other riders. When coming out of a slipstream it is best to increase lateral distance to avoid the drag increase zone. For match sprinting on a track this effect has little influence on overall performance as the drag increase will be equal for both riders so they effectively slow each other. However, when considering more than two riders tactics need to factor in interference between cyclists.

It is important to note that these findings are specifically for zero yaw conditions. A group of cyclists exposed to strong cross winds will experience an effective yaw angle for the incoming air velocity vector. For such wind conditions there will be a balance between the lateral shelter and the interference effect. However, given the high speeds of elite competition, environmental winds typically do not induce a relative wind vector greater than  $20^{\circ}$ - $30^{\circ}$ . As such the shelter from the side wind will only become significant when the passing rider is nearly ahead. At the point of maximum drag increase, downstream of level, the potential shelter would be minimal, thus keeping some lateral separation would still be beneficial to maximising speed.

### 4.3 The Effect of Geometry on Drag Interactions

Sections 4.1 and 4.2 covered the variation of cyclist drag as a function of spatial position with a constant body posture for the athletes. Literature covering interactions between bluff bodies has shown that aerodynamic interactions can also be influenced by the geometry of the bodies. In the case of cycling this is analogous to each athlete's individual riding posture, which, along with their physical dimensions and equipment, will influence the flow field around cyclists in close proximity. To investigate the effect of geometric changes on interactions a four rider pursuit team was studied in the wind tunnel.

#### 4.3.1 Drag in a Team Pursuit

Drag measurements were recorded for each athlete at each position in the team for the four possible sequences. Each athlete's drag was also measured in isolation. This made it possible to determine the drag saving at each position in the team. The drag reduction for each athlete at each position in the team is presented in Figure 4.3.1 (below). Results are for the baseline riding position only. Only data from riders in their baseline posture is included in this set. The mean drag savings measured in positions 1, 2, 3 and 4 of the team were 5%, 45%, 55% and 57% respectively.

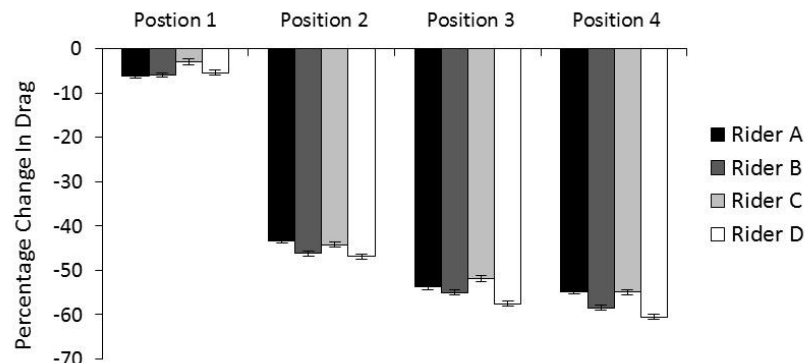


**Figure 4.3.1** – Mean drag saving at each position in a pursuit team compared to cyclist in isolation (baseline position only)

Whilst the drag reduction is broadly similar for each of the athletes there were noticeable differences between them at each position in the team. This is consistent with the findings of Edwards and Byrnes (2007). The variation arises because of size and body shape differences between the athletes, which induce complex interactions in the flow structures. The flow field around a cyclist is dominated by the general human form, and the nature of the flow over the torso and legs, but will have subtle variations due to differences between athletes such as limb length and diameter, torso shape, diameter and position, hip angle, muscle definition and size etc. When these are combined with the interaction effects in a team it is unsurprising that the drag for each athlete differs at each position in the team. The mean deviation between the values of drag saving for each rider at each position was found to be

1.6%. For elite team pursuit racing this change represents a significant margin. This variation between athletes suggests that specific team testing may be necessary to properly optimise the performance of a pursuit team, rather than relying on general values.

Team pursuit aerodynamics has been previously investigated by Broker et al. (1999). In addition to data from track tests with on-board power meters they also reported on wind tunnel results. Defraeye et al. (2013) have also published results from a computational simulation of a four rider pursuit team. Broker et al.’s results were all presented as a percentage of the lead rider’s power output, as power is the conventional form of data output from the track tests. Whilst this is not a precise indicator of an individual’s actual drag reduction, the results from the present study are presented in this format here for comparison (Figure 4.3.2). The results presented are for the drag at each rider’s baseline riding position. The drag measurements from the wind tunnel were expressed as power required (P) using a simplified equation of motion for cycling; based on the work of Martin et al. (1998). Three sources of resistance are modelled for the cyclist; rolling resistance ( $\mu [m_1+m_2] g$ ), bearing resistance ( $F_B$ ) and aerodynamic drag ( $D$ ):

$$P = [(\mu \cdot (m_1 + m_2) \cdot g + F_B) + D] \cdot V \quad \text{4.3.1}$$

This simplified model assumes constant speed, zero gradient and no environmental wind (values for rolling resistance were taken from Kyle & Burke (1984) and Kyle (1986) and the bearing resistance was taken from Wilson (2004). The  $C_D A$  results from Defraeye et al. were converted in an identical manner. The values used in the model are shown in Table 4.3.1.

**Table 4.3.1** Values used in power equation (4.3.1) to model changes in drag as cycling power required

Athlete Mass	$m_1$	70 kg
Bicycle Mass	$m_2$	6.8 kg
Coefficient of Rolling Resistance	$\mu$	0.005
Bearing Friction (per wheel)	$F_B$	0.2N
Cyclist Velocity	$V$	18 m/s

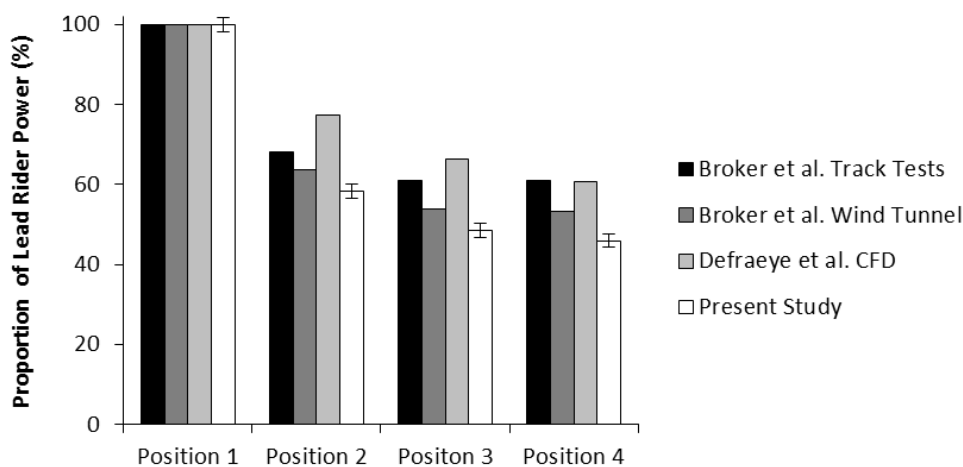


**Figure 4.3.2** - Power required in a cycling team as percentage of leader. Comparison with Broker et al. (1999) and Defraeye et al. (2014)

Comparing the four data sets, the track tests of Broker et al. are higher than both sets of wind tunnel results. This was expected as the track tests have less control over relative spatial position and it has been previously shown for cyclists that tandem drag is a strong function of proximity. Due to variation in positioning during the track tests the drag for the trailing rider is likely to increase, resulting in higher measured power. Whilst this technique may be considered to represent a more practical performance guide it is not as accurate a method for determining drag interactions. The differences between the present wind tunnel studies and those of Broker et al. may be caused by variations in athlete geometry or methodology. Broker et al. provide limited details of their experimental procedure for the wind tunnel data. Hence, corrections, setup, equipment selection and leg dynamics could all have influenced the results. They also did not provide details of the power model used to calculate the power values from force measurements. This could also affect the final values. The computational results of Defraeye et al. are significantly higher than both the wind tunnel and track results. However, their model did not include bicycles, consisting only of suspended rider geometries. As a result, the reported  $C_{DA}$  values are significantly lower than the experimental results for the full system. It seems reasonable to assume that the experimental results more closely reflect the realistic drag of a pursuit team.

#### **4.3.2 Influence of the Team Environment on Individual Rider Drag**

Changing the posture and body position of a cyclist will affect their aerodynamic drag. This has been investigated for an isolated cyclist extensively (Kyle & Burke 1984, Grappe et al. 1997, Zdravkovich et al. 1996, Gibertini et al. 2008, García-López et al. 2008, Defraeye et al. 2010, Underwood et al. 2011, Oggiano et al. 2008, Barry et al. 2014). However, when a rider is then placed in a team and subject to the interactions occurring with other riders the same changes in the drag force might not be observed.

Each rider was tested for the four body positions in single rider reference tests as well as for the full range of team combinations. From this data it was possible to compare the change in drag ( $\Delta C_{DA}$ ) observed for a given body position for a solo rider test and at each position in the team. The team  $\Delta C_{DA}$  is defined as the change in drag for a given rider in formation referenced to the drag of that athlete at their baseline position in the given sequence (with all cyclists in their baseline position). Therefore, two sets of  $\Delta C_{DA}$  values are obtained. One from the single rider tests, for each athlete at each body position, relative to baseline;  $\Delta C_{DA_{Solo}}$ , and the second from the equivalent body position change in the team formation, referenced to the baseline position drag in the team formation ( $\Delta C_{DA_{Team}}$ ). The difference between these two values indicates the influence of interaction effects on drag.

The difference between the  $\Delta C_{DA}$  values for the team and solo tests was calculated for each configuration by subtracting the solo rider difference ( $\Delta C_{DA_{Solo}}$ ) from the difference recorded in the team test ( $\Delta C_{DA_{Team}}$ ). For consistency, this is then presented as a percentage of each individual rider's solo baseline drag. When referenced to the drag in situ the proportions will be distorted given the much lower reference drag of riders in a trailing position compared to the leader. The percentage change in  $\Delta C_{DA}$  ( $\Delta$ ) was calculated for each rider, at each body position, in each team sequence:

$$\Delta = \frac{\Delta C_{DA_{Team}} - \Delta C_{DA_{Solo}}}{C_{DA_{Solo, Baseline}}} \quad \mathbf{4.3.2}$$

For the head raised position, which increased drag in all solo tests, a negative value of  $\Delta$  indicates a smaller difference in the team testing i.e. lower drag. For the head tucked and the elbows in, which generally decreased drag in solo tests, a negative indicates that the team difference ( $\Delta C_{DA_{Team}}$ ) is greater than for solo tests i.e. lower drag. Therefore, negative values represent a beneficial result for that rider as their drag is lower at that body position compared to what it would be if tested as an isolated single rider. The results are presented in Figure 4.3.3 below. As an example, a value of negative 2% indicates that the drag is 2% lower in the team formation than it was in the solo rider tests, as referenced to the solo baseline drag.

Each column in Figure 4.3.3 represents the mean of the four cyclists tested in each position to show the overall effect, irrespective of individual rider characteristics or performance. The labels "Head Up", "Head Down" and "Elbows In" refer to the single rider adopting the given position while the others remain in the baseline position. The "Team" labels refer to the case when all four riders in the team adopted that position. For example; "Team Up" describes the case where all four athletes in the team adopted the "Head Up" posture. In all cases it is seen that the difference value is negative, and thus of benefit to the athlete(s). This indicates that interactions within the team generally have a favourable influence (from a performance perspective) on the athletes'  $\Delta C_{DA}$ . In other words, similar body position changes lead to better drag performance in the team, compared to when the athletes are riding solo.

To understand Figure 4.3.3, consider first the four data points plotted in the first segment; "Head Up". Each of the series represents the average value of  $\Delta$  (change in  $\Delta C_{DA}$ ) from the four athletes in the stated position in the team., The first point (Position 1) with a value of -0.1% is the mean value of  $\Delta$  for the four athletes when riding in position 1, the lead position of the team, in the "Head Up" posture. Thus, the plotted value of  $\Delta$  is averaged across the 4 sequences such that the mean is taken for each athlete at the same position within the four rider team. The other three series in this segment refer to the equivalent case for the trailing positions; 2 to 4.

The error bars shown in Figure 4.3.3 are greater than the 0.6% uncertainty stated for the measured drag of an athlete. This error is a result of averaging the change in  $\Delta C_{DA}$  across the four athletes at each position in the team. A mean variation of 1.6% was observed in the values of  $\Delta$  for the four cyclist subjects (each column in Figure 4.3.3). This is caused by variations in rider geometry and the consequent influence on the interactions. Given the magnitude of  $\Delta$  (maximum of 4%) this highlights just how sensitive cyclist drag is to an individual rider's geometry and the complex interactions that are present between cyclists in a team. Note that this variation translates to some values of  $\Delta$  being positive for individual athlete cases. Figure 4.3.3 presents the mean values across all four athletes.

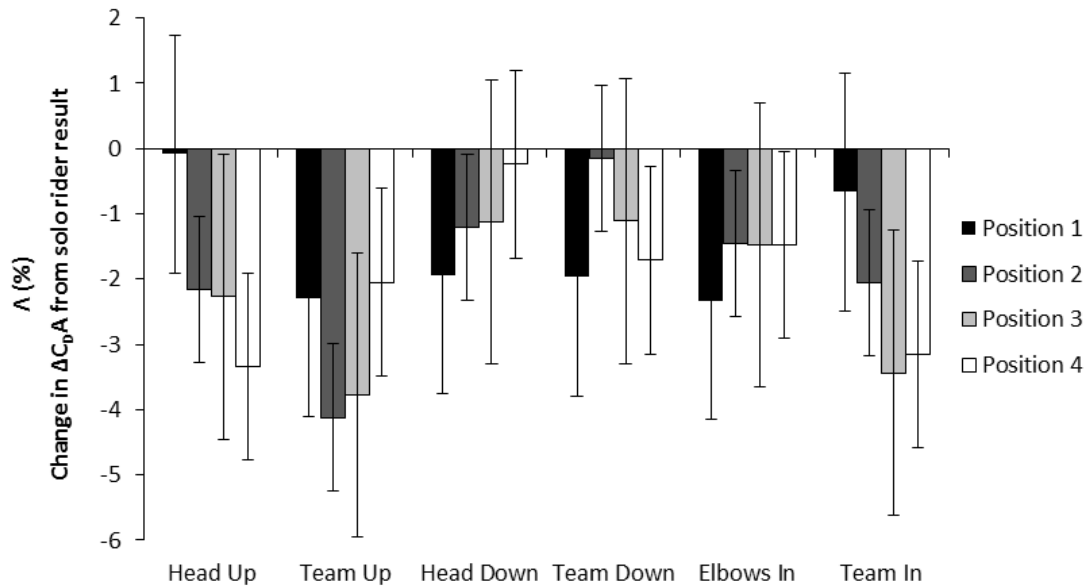


**Figure 4.3.3** - Change in  $\Delta C_{DA}$  ( $\Lambda$ ) from solo to team as percentage of rider solo baseline drag. See Equation 4.3.2.

Whilst some of the results are small, they still represent significant changes in the drag of the athletes. For example, in the solo rider tests the drag of subjects B and D did not change significantly with elbow position. So whilst the result of -1.5% for elbows in is relatively small, it represents a clear interaction effect. As a reference, the change in drag from the solo rider tests is given in Table 4.3.2 below.

**Table 4.3.2** - Percentage change in drag from solo rider tests at each body position for each athlete referenced to the baseline position

	Rider A	Rider B	Rider C	Rider D
Head Raised	6.7%	5.9%	9.3%	6.0%
Head Down	-5.0%	-1.5%	-0.2%	-1.5%
Elbows Together	-2.4%	0.1%	2.1%	-0.4%

It is important to be clear that a value of 0% in Figure 4.3.3 indicates that the change in drag for that rider in the team test is equal to their change as seen in solo tests, not that the rider's drag is unchanged. It can, therefore, be stated that a change in drag observed from the testing of an isolated single rider is likely to translate into the team environment. This means that a posture that increases drag for a solo rider test will have the same effect in a team, though the magnitude of that increase is likely to be smaller. Similarly, a posture that decreases drag in solo rider tests is likely to have the same effect when riding in a team but with a greater drag reduction. These results are consistent and general, despite the large variations between athletes, as exhibited by the size of the error bars.

### 4.3.3 Drag Interplay Between Riders in a Team Pursuit

Riding in a team has been shown to change the magnitude of the change in drag induced by changes in body position for an individual rider. In addition to influencing their own drag, a rider changing their body position will also influence the flow around the other athletes in the team, and hence the drag of team mates.

The simultaneous drag measurements of all four athletes allowed the interference effects between the riders to be tracked. It was seen that, under certain conditions, changing the body position of one rider could influence the drag of another team member. Results showed that there were significant interactions occurring between members of the team, however, few common trends were identified from the results (see Table 4.3.3). This is due to the complex nature of the flow interactions between the individuals arising from subtle differences in the athletes' body shape.

One common result observed was that each time the lead rider lowered their head, the drag of the rider immediately behind increased. This was as expected, given that the trailing rider becomes more exposed to the oncoming flow. However, this trend does not directly translate to other positions in the team. For example, with the athlete in Position 2 adopting the head down posture, the drag of the rider in Position 3 does not necessarily increase. In fact, there were cases of both the rider behind and ahead being influenced, with both positive and negative drag changes occurring. This is due to the complex and compounding effects of multiple athletes on the flow field.

Edwards and Byrnes (2007) showed that a cyclist will experience a greater drag reduction if drafting behind a rider with a higher  $C_D A$ . In this study it was hypothesised that a rider raising their head, thus increasing their drag, would induce a greater drag reduction for the rider(s) downstream. However, this effect was not universally seen. In certain cases, the drag of riders further downstream was seen to increase and sometimes an upstream effect was observed when the change was applied to one of the trailing riders. Edwards and Byrnes conducted road tests, which have far less control over the spatial positioning of the riders than wind tunnel tests. This has been shown to potentially have a large influence on drag. Their test method could have compromised the accuracy with which sensitive variations in drag could be measured. Also, the more complex case of interactions between four riders may be introducing additional effects.

In addition to a single rider changing their body position, tests were also run with all four cyclists adopting the same posture. In this case, it was observed that the final rider always experienced a greater shift in drag than when the three lead riders were in the baseline position. This applied to all three postures tested and both positive and negative changes in drag.

It is clear that there are interactions that affect cyclist drag in a four rider team, but riders are highly coupled by mechanisms that are more intricate than the basic geometry and position identified here. A more comprehensive understanding of these interactions could lead to performance benefits in competition. However, the differences between the athletes' body position, riding style and geometry mean that without direct testing of the intended subjects these trends will be difficult to predict. There seems little doubt that flow interactions influencing cyclist drag are very much athlete specific.

The stated repeatability of 0.6% applies to back-to-back tests. However, subjects can still vary their position between different configurations. Image tracking revealed that with Rider C leading in Sequence 3, their head position was slightly higher than the baseline case when the riders in positions 2 – 4 had were in the head up posture (see Table 4.3.3). This contributed to a higher drag and is not due to forward interference effects from downstream.

The drag interactions in a cycling team can also be considered as a combined effect from the summation of the drag for each of the individual riders in the team. Figure 4.3.4 shows the percentage change in the sum team drag for each of the four sequences tested. For every case there is a consistent result in the compounding effect of the cyclists in the team. When the whole team adopts a given posture the resultant change to the sum team drag is significantly greater than the change for any one rider. It can also be seen that there is no direct correlation between the rider in the team changing their posture and the resulting team drag. The team drag is not more closely linked to any one of the positions in the team. Results also show the direction of the drag change to be consistent with the single rider tests. An athlete raising their head will increase the sum drag of the team. Similarly, an athlete lowering their head or drawing elbows in will lower the sum team drag. It is noted however there are certain cases where the change is slightly opposite, though the magnitude is so small in these cases to be below the uncertainty interval of the test.

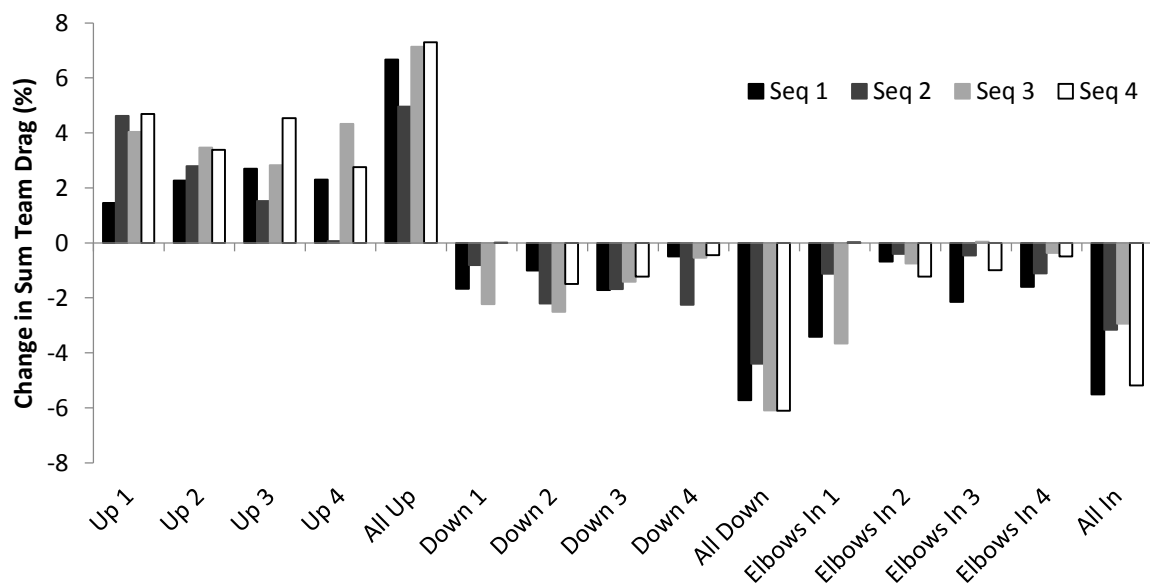


Figure 4.3.4 – Percentage change in the sum drag of the 4 riders in the team for each of the 4 sequences (Seq).

**Table 4.3.3** - Percentage change in drag for each rider (change in  $C_{dA}$  in  $m^2$ ), at each position in each sequence, referenced to baseline position in a given sequence (not as standalone rider). “Team” rows describe results when all 4 riders adopted the same position. All other tests indicate 1 athlete out of the 4 at a given position whilst others remained in their baseline position. eg. Head Up 1 refers to the first rider in that sequence raising their head whilst all other riders remain in their baseline position.

	Sequence 1				Sequence 2				Sequence 3				Sequence 4			
	A	B	C	D	B	C	D	A	C	D	A	B	D	A	B	C
<b>Head Up 1</b>	4.72	-5.42	0.58	3.23	8.97	-0.44	1.16	4.87	7.49	0.35	3.73	0.79	7.93	2.64	2.98	2.81
	(0.011)	(-0.007)	(0.001)	(0.003)	(0.019)	(-0.001)	(0.001)	(0.006)	(0.016)	(0.000)	(0.004)	(0.001)	(0.016)	(0.004)	(0.003)	(0.003)
<b>Head Up 2</b>	-1.04	9.40	0.29	3.89	-0.18	10.18	-0.02	2.41	3.27	5.50	4.15	0.58	0.21	10.01	0.60	3.18
	(-0.002)	(0.011)	(0.000)	(0.003)	(0.000)	(0.013)	(0.000)	(0.003)	(0.007)	(0.006)	(0.005)	(0.001)	(0.000)	(0.014)	(0.001)	(0.003)
<b>Head Up 3</b>	0.26	0.53	10.28	2.87	0.54	1.31	4.79	0.96	3.39	-2.35	9.94	-1.07	0.27	1.73	16.30	5.31
	(0.001)	(0.001)	(0.011)	(0.002)	(0.001)	(0.002)	(0.004)	(0.001)	(0.007)	(-0.003)	(0.012)	(-0.001)	(0.001)	(0.002)	(0.016)	(0.005)
<b>Head Up 4</b>	0.94	0.35	2.94	8.12	-0.08	-0.88	-2.45	3.37	4.76	0.19	1.61	11.77	-1.20	2.93	2.08	11.07
	(0.002)	(0.000)	(0.003)	(0.007)	(0.000)	(-0.001)	(-0.002)	(0.004)	(0.010)	(0.000)	(0.002)	(0.011)	(-0.002)	(0.004)	(0.002)	(0.011)
<b>Team Up</b>	5.80	3.21	8.09	12.20	4.63	7.02	0.18	7.07	5.81	2.22	10.20	12.36	1.84	8.27	9.32	14.79
	(0.014)	(0.004)	(0.009)	(0.010)	(0.010)	(0.009)	(0.000)	(0.008)	(0.013)	(0.003)	(0.012)	(0.012)	(0.004)	(0.012)	(0.009)	(0.015)
<b>Head Down 1</b>	-4.91	1.45	1.30	-0.82	-3.21	3.12	0.46	-1.67	-6.43	2.51	0.25	-1.23	-2.18	2.36	0.80	0.29
	(-0.012)	(0.002)	(0.001)	(-0.001)	(-0.007)	(0.004)	(0.000)	(-0.002)	(-0.014)	(0.003)	(0.000)	(-0.001)	(-0.004)	(0.003)	(0.001)	(0.000)
<b>Head Down 2</b>	0.07	-5.77	0.15	1.30	0.00	-5.44	-1.84	-3.02	-2.53	-5.93	-0.65	-0.64	-1.22	-6.55	5.63	-2.05
	(0.000)	(-0.007)	(0.000)	(0.001)	(0.000)	(-0.007)	(-0.002)	(-0.003)	(-0.006)	(-0.007)	(-0.001)	(-0.001)	(-0.002)	(-0.009)	(0.006)	(-0.002)
<b>Head Down 3</b>	0.39	-1.54	-9.01	1.51	-0.03	-1.84	-5.91	-1.20	-1.22	1.70	-5.47	-0.57	-0.92	1.50	-7.33	0.43
	(0.001)	(-0.002)	(-0.010)	(0.001)	(0.000)	(-0.002)	(-0.005)	(-0.001)	(-0.003)	(0.002)	(-0.006)	(-0.001)	(-0.002)	(0.002)	(-0.007)	(0.000)
<b>Head Down 4</b>	0.25	0.16	-0.11	-4.01	0.55	-2.44	-4.05	-5.82	1.51	-0.88	0.92	-6.75	-0.31	1.59	0.70	-4.72
	(0.001)	(0.000)	(0.000)	(-0.003)	(0.001)	(-0.003)	(-0.004)	(-0.007)	(0.003)	(-0.001)	(0.001)	(-0.006)	(-0.001)	(0.002)	(0.001)	(-0.005)
<b>Team Down</b>	-5.63	-2.12	-10.53	-4.92	-2.29	-3.98	-4.12	-8.96	-6.60	-1.97	-6.51	-9.41	-2.30	-7.69	-6.20	-11.37
	(-0.013)	(-0.003)	(-0.011)	(-0.004)	(-0.005)	(-0.005)	(-0.004)	(-0.010)	(-0.014)	(-0.002)	(-0.008)	(-0.009)	(-0.005)	(-0.011)	(-0.006)	(-0.012)
<b>Elbows In 1</b>	-3.59	-3.40	-4.89	-1.06	-0.83	-1.16	-0.59	-2.04	-4.61	-1.41	-4.29	-3.40	-1.38	1.36	0.79	0.12
	(-0.008)	(-0.004)	(-0.005)	(-0.001)	(-0.002)	(-0.001)	(-0.001)	(-0.002)	(-0.010)	(-0.002)	(-0.005)	(-0.003)	(-0.003)	(0.002)	(0.001)	(0.000)
<b>Elbows In 2</b>	-0.61	-3.24	-1.68	4.05	1.56	-2.23	-0.31	-2.12	-0.62	-2.58	0.78	-0.70	0.73	-3.67	-1.02	-1.87
	(-0.001)	(-0.004)	(-0.002)	(0.003)	(0.003)	(-0.003)	(0.000)	(-0.002)	(-0.001)	(-0.003)	(0.001)	(-0.001)	(0.001)	(-0.005)	(-0.001)	(-0.002)
<b>Elbows In 3</b>	0.37	-0.92	-8.73	-2.50	2.15	-1.37	-5.67	-0.12	0.38	1.74	-0.60	-2.02	-0.24	-2.17	0.79	-2.60
	(0.001)	(-0.001)	(-0.009)	(-0.002)	(0.005)	(-0.002)	(-0.005)	(0.000)	(0.001)	(0.002)	(-0.001)	(-0.002)	(0.000)	(-0.003)	(0.001)	(-0.003)
<b>Elbows In 4</b>	0.13	-1.03	-4.62	-3.43	1.56	-1.30	-0.57	-6.27	1.51	-0.60	-0.72	-4.04	0.02	-1.10	0.40	-1.56
	(0.000)	(-0.001)	(-0.005)	(-0.003)	(0.003)	(-0.002)	(-0.001)	(-0.007)	(0.003)	(-0.001)	(-0.001)	(-0.004)	(0.000)	(-0.002)	(0.000)	(-0.002)
<b>Team In</b>	-2.58	-3.46	-14.26	-5.41	1.87	-4.16	-5.61	-9.43	-1.53	-3.17	-4.25	-4.30	-1.21	-5.21	-7.04	-11.22
	(-0.006)	(-0.004)	(-0.015)	(-0.005)	(0.004)	(-0.005)	(-0.005)	(-0.011)	(-0.003)	(-0.004)	(-0.005)	(-0.004)	(-0.002)	(-0.007)	(-0.007)	(-0.011)

### 4.3.4 Statistical Correlation of Drag Interaction Between Riders

To test the inter-dependence of the drag of the riders, correlation coefficients were calculated using the corrected  $C_{dA}$  values for each sequence (see Figure 4.3.5 below). The correlation coefficient is defined as the sample covariance between two samples, in this case the drag of two of the riders -  $s_{xy}$ , normalised by the product of the standard deviation for each of the two individual variables ( $s_x s_y$ ):

Correlation Coefficient: 
$$r_{x,y} = \frac{s_{xy}}{s_x s_y} \quad \mathbf{4.3.3}$$

An analysis was performed on the full data set, not the mean values. The correlation was calculated for all runs, using data from all postures. Using the correlation coefficient provides a quantitative measure of the strength of the interaction. Here, values greater than 0.5 can be considered a strong correlation, given the relatively high uncertainty resulting from the use of human test subjects.

Considering the data by position in the team, irrespective of the athlete, it is seen that only positions 3 and 4 have a consistently high correlation. If the results are studied from an athlete perspective, ignoring the position in the team, riders A and C are seen to have a strong correlation for all sequences. The other combinations have mixed results that depend on their position in the team.

This variation lends further weight to the hypothesis that results are specific to a given team and hence testing needs to be team specific, given the dependence of interaction effect on athlete geometry. The variability in the magnitudes seen across the results further suggests that optimisation of the aerodynamic interactions in an elite team requires in situ testing, using specific athletes.

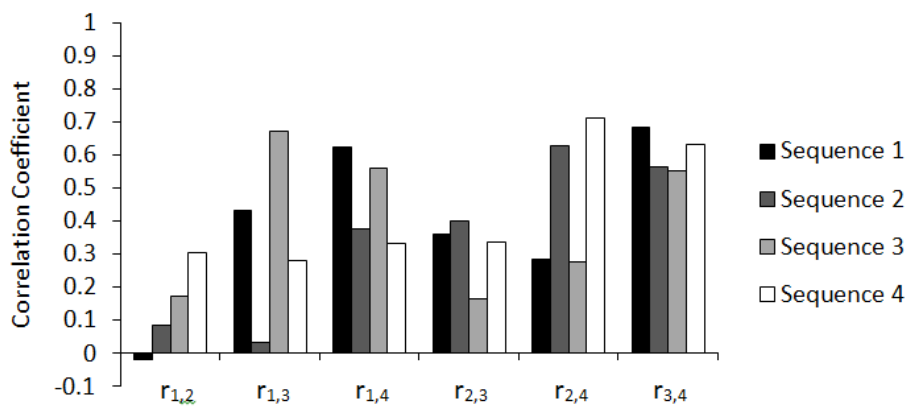


**Figure 4.3.5** - Correlation coefficient for the drag between each position in the four cyclist team ( $r_{1,2}$  = correlation coefficient between positions 1 and 2 in the rider pursuit team)

## **Summary**

When considering the aerodynamic interactions of a cycling team it is important to consider how any new found knowledge can be used in the pursuit of improved performance. Contrary to perceptions, the sum drag of a team of cyclists (the sum of the drag for each of the four cyclists) is not the primary indicator of team performance in events such as track team pursuit or team sprint. Taking the team pursuit as an example, the team performance is measured by the finishing time, which is closely linked to the average speed that can be maintained over the 4000m event. There is also a transient period of the race when the riders are accelerating. During the steady state phase the speed of the team is dictated by the leader, with each athlete sharing pace setting duties at the front. As the speed of the team is dictated by the pace of the leader, the teams speed will only increase with the leader. Given a fixed power output from the athlete, lowering the leader's resistance will in turn will increase the speed of the team. In this way reducing the sum drag of the team by lowering the drag of the trailing three riders will not directly increase the team's velocity. Obviously there are also physiological factors that need to be considered when translating aerodynamic knowledge into performance improvement. For example, the recovery of athletes in the trailing position and the influence on their output when leading. The ideal outcome, aerodynamically, would be to manipulate interactions such that the drag of the lead rider is reduced by redistributing drag over the trailing three.

Such a situation was observed for some of the test configurations investigated here. However, these reductions were small and were not seen for all test subjects. It is clear that such an effect will be athlete specific. This is especially important given that negative interference effects were also seen when changes to the posture of the rider in Position 2 caused an increase in the lead rider's drag. This further highlights how sensitive interactions between cyclists can be and the importance of better understanding these effects.

A more robust finding from the research was that lowering the head and bringing the elbows together generally resulted in a lower drag for the lead rider. This corresponds with the results of solo tests, where these changes had the same effect. In fact, the drag reduction for cyclists in a team scenario is generally greater than that observed in solo tests. Therefore, any change that can be made to lower an athlete's drag in individual tests is likely to lower their drag when in the lead position and so benefit the performance of the team.

These results show that it is possible for trailing riders to influence the drag of riders upstream. However, both positive and negative influences were observed. This again suggests specificity is needed in athlete testing for aerodynamic optimisation. The drag response of the athletes in a team is linked through complex flow mechanisms that extend beyond the basic postural changes investigated here. More detailed characterisation is needed to identify additional factors that can influence the aerodynamic interactions within a team.

For elite performance, this research suggests that it is currently necessary to test desired athletes in their team because consistent trends in the interplay effects between riders could not be identified from postural changes to the cyclists alone. Results indicate that it is possible for pursuit teams to optimise team aerodynamics by careful consideration of the dynamic posture of individual team members. In such an approach each rider might adopt a different posture depending on the team's current sequence.

The findings from Section 4.3 have been published in Sports Engineering (Barry et al. 2015).

## Chapter 5

### Flow Topology of Two Cyclist Tandem Formations

The first phase of this project focussed on the changes in aerodynamic forces, particularly drag, that occurs as a result of aerodynamic interactions between cyclists in close proximity. This chapter covers the results of investigations aimed at characterising the flow field around a pair of cyclists in tandem and examines how the flow differs from that seen for a cyclist in isolation. This provides the understanding and insight to identify the mechanisms responsible for the changes in drag observed in a two rider formation.

Due to the complexity of imaging and characterising the flow surrounding cyclists in a tandem formation, a range of different techniques were utilised to compile a comprehensive understanding of the flow field. This section begins with visualisations of the full scale flow field around athletes, using smoke injection and surface wool tufts. To extract greater detail of the flow field, particle image velocimetry was used with scale model cyclists to capture high resolution cross sections of the flow around two riders in a tandem formation. The flow characterisation was then linked to the full-scale results by capturing wake profiles for a dynamic athlete in both single and tandem formations.

## **5.1 Full Scale Flow Visualisation of Two Cyclists in Tandem**

A series of full scale flow visualisations were conducted on two riders in a tandem formation in the wind tunnel to capture the key flow features.

### ***Smoke Injection***

Smoke was injected into the flow around the riders to capture the bulk flow motion away from the rider's bodies. A narrow wand was used to inject the smoke at a variety of points around the two cyclists at minimum separation and when the two were separated by one bicycle length. In general, clean attached flow can be identified by a tightly confined smoke stream, since smooth laminar flow has low turbulence and consequently less mixing. In contrast, separated flow is observed in regions where the smoke particles are more dispersed, as they diffuse more rapidly with the higher turbulence.

Figure 5.1.1 shows smoke injected upstream of the lead rider's head. Flow impacts on the helmet stagnation point and remains attached around sides of the helmet. Flow separating from the rear edge of the helmet appears to cleanly reattach on to the upper back. The flow remains attached down the rider's back before separating at their waist. After separating the flow retains a downwards component of velocity such that it impacts on the head and torso of the trailing rider rather than only impacting the head and helmet of the trailing cyclist. The separating streamline is low enough such that the flow stagnates on the front of the trailing cyclist. However, the dispersion of the smoke indicates there is significantly higher turbulence than in the freestream flow. This suggests there is a reduction in the streamwise momentum in the flow approaching the trailing cyclist.



**Figure 5.1.1** - Smoke injected immediately upstream of the lead cyclist's helmet. Athletes in a tandem formation at minimum separation distance (120mm).

Some cases of bluff bodies and smooth vehicles have exhibited a clean reattachment and a shifted stagnation point on the trailing body at small separation (Ishigai et al 1972, Zdravkovich 1977, Rajamani 2006, Watkins & Viro 2008, Pagliarella 2009). This shift in the stagnation point appears to reduce the frontal pressure on the body and results in a significant drag reduction. Given that the cyclists' body lengths are shorter than the total length of the bicycle, even when the separation is minimal, there is considerable separation between the two riders. Since the drag is primarily experienced by the riders' body, the separation between torsos' is of important consideration when comparing against other bluff body flows. In terms of the torso chord length (shoulder to rear of hip), at minimum bicycle separation the gap from the rear of the leader to the head of the trailing cyclist is of the order of 1.5 times the chord length (see Figure 5.1.2).



**Figure 5.1.2** - Smoke injected immediately upstream of separation point on the lead cyclist. Riders positioned at minimum separation. Both athletes pedalling during test.

Figure 5.1.2 shows smoke injected over the back of the lead rider, rather than upstream. As this is immediately upstream of the separation point from the back, the smoke is dispersed rapidly. This suggests that the flow impacting on the trailing rider has lost significant momentum compared to freestream and to the attached flow over the lead rider.

Figure 5.1.3 shows smoke injected immediately behind the lead rider. The rapid dispersion indicates mixing and is indicative of a separated region of the wake and high turbulence. This was known from existing literature (Crouch et al. 2012, 2014) and shows that a large portion of the flow observed by the trailing cyclist will be highly turbulent. The turbulent flow reflects a transfer of energy from the streamwise component of the flow into fluctuating in-plane components in the separated flow region. This results in a reduced component of streamwise pressure and velocity imparted on the front of the trailing rider compared to freestream. From the momentum equation we can deduce that this will decrease the drag acting on the trailing cyclist (Munson et al. 2006).



**Figure 5.1.3** - Smoke injected at the hip of the leading cyclist in a tandem formation. Still snapshot taken during athlete pedalling.

Figure 5.1.4 shows a comparison of the flow over the lead (left) and trailing (right) riders in a tandem formation. Smoke particles over the lead rider are much more constrained ahead of the helmet and diffusion is small over the upper back and increasing down the back towards the separation point at the hips/waist. In comparison the flow over the trailing rider shows much greater dispersion of the smoke, indicating higher turbulence levels. This is caused by the disturbed flow from the lead rider's wake. Figure 5.1.4b also indicates that separation is occurring slightly higher on the back of the rear rider. This is likely due to reduced energy in the flow over the back, resulting from inlet conditions, and thus less able to overcome the adverse pressure gradient. However, it must be noted that the separation point will also be influenced by individual rider geometry. Although the two athletes are adopting different head positions, it is observed that the flow appears to reattach onto the upper back immediately downstream of the helmet in both cases. Furthermore, the upstream flow conditions provide evidence of the differing inflow for the riders. In the trailing rider case there is greater dispersion upstream of the rider. This dispersion of smoke continues downstream, indicating reduced streamwise energy in the flow.



**Figure 5.1.4** - Left; flow over lead cyclist in tandem pair. Right; flow over trailing cyclist with bicycle length separation between riders

Figure 5.1.5 shows the trailing rider at a bicycle length downstream of the leader. Smoke was injected at three heights upstream to highlight the disturbed flow region ahead of the trailing rider. The left image (Figure 5.1.5a) shows the freestream conditions outside the wake region from the leader. The smoke dissipation evident results from the natural turbulence levels in the tunnel. The second image shows smoke injected at helmet height for the trailing rider. At this height the effect of the lead rider's wake becomes more evident with much greater turbulence compared to freestream. The third frame (Figure 5.1.5c) shows the injection point lowered further to be at the height of the trailing cyclist's chin. At this height the flow is highly turbulent, compared to the freestream conditions (Figure 5.1.5a). This is indicative of a reduction in streamwise momentum, compared to the freestream flow seen by a single or leading rider. This reduction in streamwise momentum will contribute to the drag reduction previously determined for a trailing cyclist at this separation distance.



**Figure 5.1.5** - Flow profile ahead of the trailing cyclist at a bicycle length downstream of the lead rider. Three injection points shown, indicated by wand location, highlighting the difference in flow profile with vertical height

Observation of the flow dynamics with the cyclists pedalling revealed more detail than is visible in the above snapshots. With smoke injected under the rider's torso the smoke ejected over the riders hips was seen to oscillate with the same periodicity as that of the pedalling legs. This was caused by, one leg closing towards the chest and restricting the flow out over the hip. Conversely, on the opposite side the hip was open allowing flow to pass over the hip and torso, resulting in the earlier separation, as seen previously in static results. This is an indication that the fundamental flow regimes observed in static cases by Crouch et al. translate to the dynamic case of a pedalling cyclist. This behaviour was evident for both the lead and trailing cyclists.

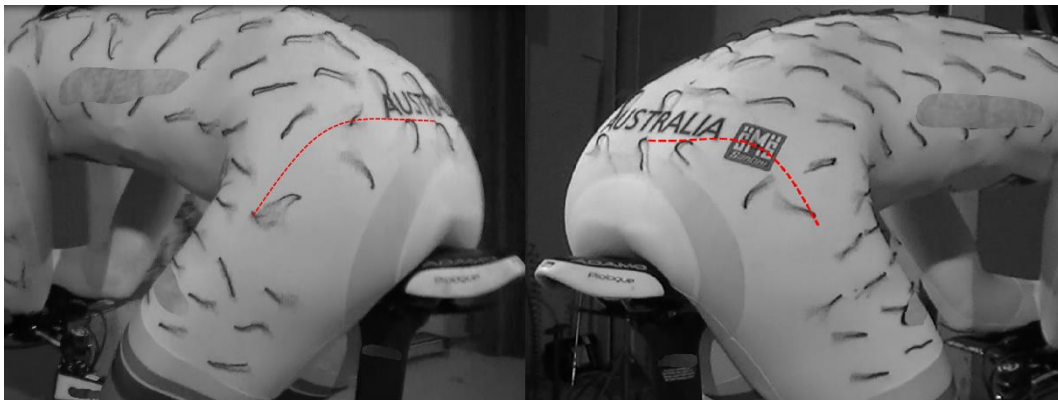
### **Wool Tufts**

Wool tufts were sewn in a regular grid into the skin suits of each cyclist. Whilst this is a very coarse technique, the use of wool tufts allowed the observation and identification of some general flow behaviour. By comparing with the detailed characterisation of a single rider flow field (Crouch et al.) it is possible to use wool tufts to identify the primary flow behaviour of cyclists in a two rider formation.

Wool tufts show the flow behaviour on the surface of the cyclist. In this way they can be used to identify attached and separated flow regions over the cyclist. In the following still images, where tufts are clearly defined (not blurred) the tuft is fairly stable and its position does not vary significantly with time. This indicates that flow is attached on the surface of the cyclist. Where tufts are unclear or

blurred indicates the presence of fluctuations in the tufts position and that the flow has separated from the body of the rider. Tufts pointing upstream indicate reversed flow at the surface and are evidence of a separated region. For clarity the separation lines observed in the tests have been superimposed onto the snapshots.

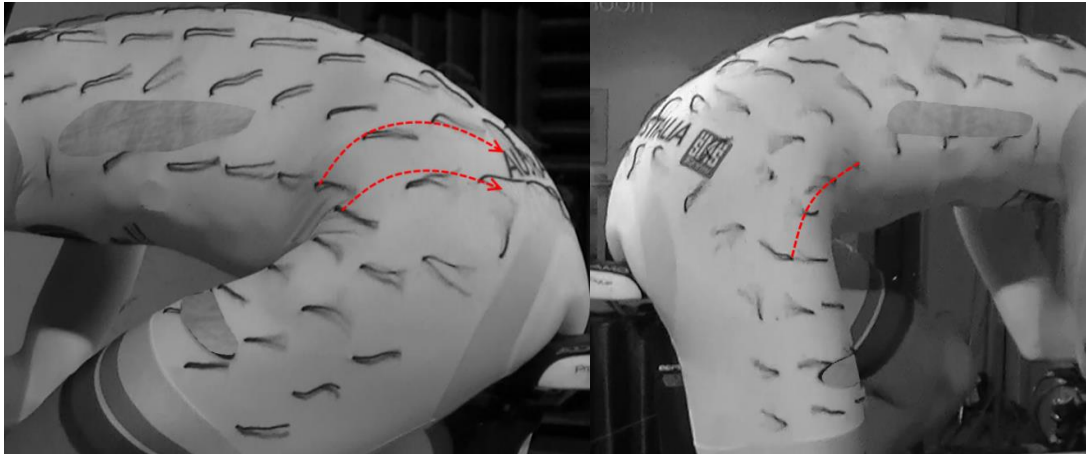
Figure 5.1.6 shows snapshots from video recordings of the lead rider with legs positioned at  $15^{\circ}$  crank angle. It can be seen that the flow separates from the cyclists' hips at the same location on both sides. Separation lines (red) are symmetrical for both sides of the body, indicating a symmetric wake and is consistent with skin friction contours and wake profile suggested by Crouch et al. The presence of symmetric separation and resulting wake structure was identified previously as one of the key flow regimes for a cyclist, occurring when the upper legs are level.



**Figure 5.1.6** - Lead cyclist, with legs at  $15^{\circ}$  crank angle, in tandem formation wearing wool tuft suit showing left and right hips respectively. Red line indicates separation point on hips.

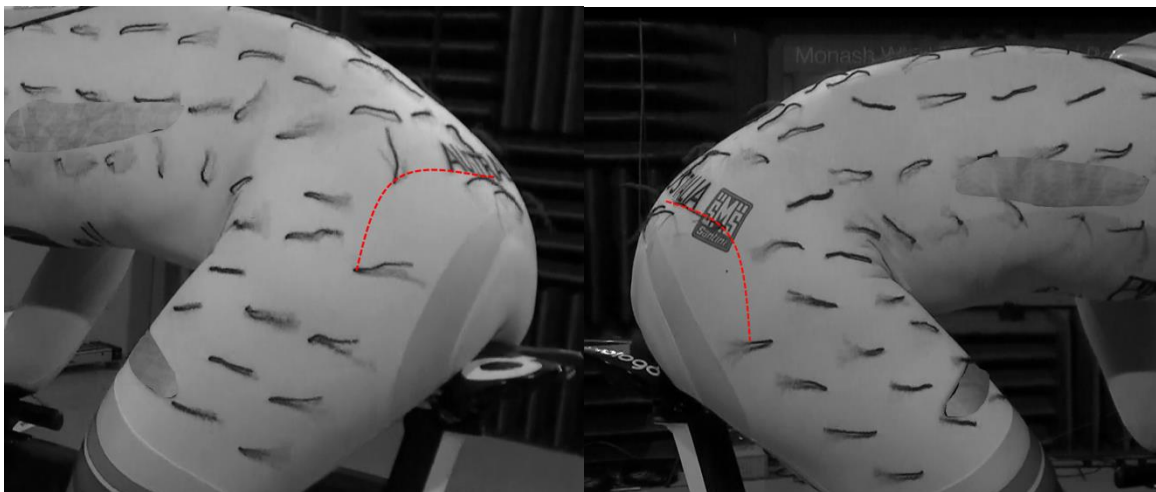
Figure 5.1.7 shows snapshots of the same lead rider with legs now positioned at  $75^{\circ}$  with left leg at maximum position and right leg at maximum extension. With the legs in this position the flow over the riders back can be seen to be highly asymmetric. On the left side, with the leg raised, the flow wraps over the hips and backside of the cyclist and separates much further down the rear of the cyclist. This introduces strong downwash and cross flow over the back of the rider. This is shown by the dotted red lines indicating the direction of the flow over the closed hip. In contrast, the right side shows much earlier separation at the side of the hip. This asymmetric behaviour is consistent with the surface flow and wake structures observed by Crouch et al. for this leg position.

The identification of these two key flow regimes indicates that the leading rider in a tandem pair maintains the dominant flow features previously described for a single cyclist by Crouch et al. and the presence of the trailing rider has not significantly disrupted the flow behaviour.



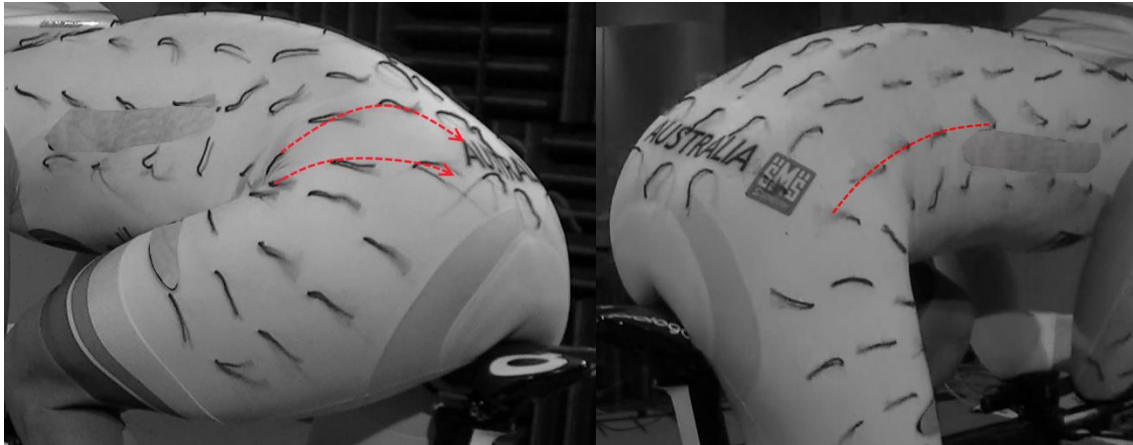
**Figure 5.1.7** - Lead cyclist, with legs at  $75^{\circ}$  crank angle, in tandem formation wearing wool tuft suit showing left and right hips respectively. This position relates to the minimum hip angle on the left side. Red line indicates separation point on right hip. Arrows indicate flow direction as it wraps over the closed left hip.

Figure 5.1.8 shows snapshots of the flow over the trailing rider positioned statically at  $15^{\circ}$  crank angle. The separation lines (in red) show that separation occurs at the same point on both hips. This indicates the formation of a symmetric wake structure. This flow behaviour is similar to that observed for the leading cyclist and is consistent with previous results for a single cyclist in isolation.



**Figure 5.1.8** - Trailing cyclist, with legs at  $15^{\circ}$  crank angle, in tandem formation wearing wool tuft suit showing left and right hips respectively. Red line indicates separation point on hips.

Figure 5.1.9 shows that with trailing rider positioned with static legs at a crank angle of  $75^{\circ}$ , the flow over each hip differs greatly. On the left side, with the hip joint closed, the flow wraps over the hips and down onto the backside. This delays separation and causes a strong downwash and cross flow over the rear of the rider and in the wake. On the right side, with the hip open, the flow separates early at the hip joint. This asymmetric flow behaviour is consistent with the lead rider case and with literature for a single isolated cyclist. It appears that travelling in the wake of another cyclist does not disrupt the formation of the primary hip vortices for a trailing cyclist.



**Figure 5.1.9** - Trailing cyclist, with legs at  $75^{\circ}$  crank angle, in tandem formation wearing wool tuft suit showing left and right hips respectively. This position relates to the minimum hip angle on the left side. Red line indicates separation point on the right hip. Arrows show flow wrapping over closed left hip.

In addition to the static snapshots shown above, the cyclists were observed during dynamic pedalling. Whilst pedalling, wool tufts exhibited oscillatory motion as the legs rotated around the crank cycles. It was possible to discern the transitioning between the asymmetric flow regimes as each leg was raised or lowered respectively. This shows that the flow fields identified for a static rider remain dominant features in the wake even with the addition of pedalling dynamics. This was observable in the wake of both the leading and trailing cyclist.

### **Summary**

The use of flow visualisation techniques has provided new, albeit qualitative, insight into the flow behaviour around two cyclists in a tandem formation. Smoke injection showed that the separating streamline from the rear of the leading rider stagnates on the front of the trailing rider, even at small separation. However, the bulk of the flow seen by the trailing cyclist is significantly more turbulent than the freestream conditions seen by a single or leading rider, due to the wake of the leading cyclist. This is indicative of a loss of streamwise momentum, thus reducing the inlet energy on the trailing cyclist. This will contribute to the reduction in drag seen for a trailing cyclist.

Wool tufts revealed that the flow over both the lead and trailing riders maintains similar flow behaviour to the topology of an isolated cyclist (Crouch et al.). This was observed statically for the two primary flow regimes, characterised at  $15^{\circ}$  and  $75^{\circ}$  crank angles. At  $15^{\circ}$  separation was symmetrical over both cyclist's hips, while at  $75^{\circ}$  there was a large asymmetry evident. Observation of pedalling athletes showed that the same flow regimes are still evident, with oscillation between left and right asymmetric regimes with the motion of the legs around the crank cycle.

These methods provide a basic insight into the flow field surrounding two cyclists in a tandem formation; however, much greater detail is needed in order to make assessments of the changes from a single rider and the mechanisms responsible for the drag reduction observed by both cyclists.

## 5.2 Velocity Fields of Scale Tandem Cyclists

Reduced scale model cyclists (1/7<sup>th</sup>) were constructed for experiments in the FLAIR water channel. Particle Image Velocimetry was used to capture high resolution flow field data around two cyclists in a tandem formation. At this reduced scale the Reynolds number was less than that of a full scale cyclist. To evaluate the validity of the technique, results for a single rider were compared against the full scale wind tunnel results of Crouch et al. (2012, 2014).

### 5.2.1 Validation of Scale Model Technique

Crouch et al. (2012, 2014) identified that at a crank angle of 15<sup>o</sup>, with a cyclist's upper legs level (symmetric case), the wake is largely symmetric with weak trailing vortices. These streamwise vorticity fields ( $s^{-1}$ ) in the Y-Z plane at  $x = 0.5C$  and  $1C$  are shown in Figure 5.2.1 alongside those obtained in this study at  $x = 0.25C$ ,  $0.5C$  and  $1C$ . In each case the vortex boundaries have been identified using the swirling strength criterion, which identifies vortex boundaries from the eigenvalues of the velocity gradient tensor (Zhou et al. 1999). Both sets of results have a symmetric vorticity distribution about the centreline ( $y = 0$ ). The upper hip vortex pair and inner thigh vortex pair are evident in the near body planes ( $x = 0.25C$  and  $0.5C$ ). However, at the  $x = 1C$  plane the coherent structures evident in the wake as concentrated regions of vorticity have diffused. The scale results show the individual vortices diffusing more rapidly as they convect downstream. It is suggested that this greater rate of decay is the result of higher diffusion of vorticity due to the relatively higher viscous effects in the lower Reynolds number flow (Morton 1984). Results from this study are presented at  $x = 0.25C$  (not available at full-scale) as this cross-section is most similar to full-scale results at  $0.5C$ , further supporting the more rapid diffusion at the lower Reynolds number. At  $x = 1C$  downstream the vorticity distributions are similar, with both showing a broad regions of counter-rotating vorticity.

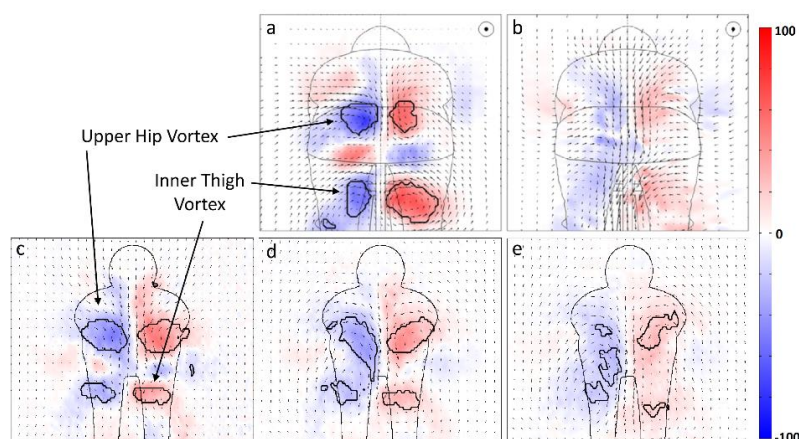


**Figure 5.2.1** – (a) Wind tunnel results of Crouch et al. [29] showing streamwise vorticity ( $s^{-1}$ ) in the wake of a full-scale cycling mannequin at 15<sup>o</sup> crank angle at 0.5C downstream of rear of rider and (b) 1.0c downstream. (c) Vorticity in the wake of scale model cyclist at 15<sup>o</sup> crank angle at 0.25C downstream of the rear of the rider, (d) 0.5C downstream and (e) 1.0C downstream. Contours of swirling strength criterion identify vortex boundaries as used by Crouch et al.

At a crank angle of  $75^{\circ}$  (asymmetric case) the scale-model results exhibit a clear asymmetry in the left and right hip vortices (see Figure 5.2.2), similar to the full-scale mannequin results of Crouch et al.. However, the strong diagonal flow from the top left of the cyclist to the lower right is less pronounced in downstream planes. This appears a result of the left hip vortex being higher and further from the centre which reduces the interaction with the right hip vortex. The position of this vortex is likely influenced by slight geometric nuances between the two cyclist models changing the interaction between the flow over the hip and back. It may also be linked to the difference in Reynolds number changing the flow separation over the left hip. The smaller knee vortex is also evident at  $x = 0.25C$ , positioned wide of the left hip vortex, but diffuses further downstream. Differences in the position of the flow structures may be associated with the Reynolds number difference, but also may indicate a sensitivity of cyclists' wakes to geometric differences of the cyclist geometry. There are also potential secondary effects due to the differences in bicycle geometry.

As found in the  $15^{\circ}$  crank angle case, the structures diffuse at a higher rate in the scale experiment. At  $x = 1C$  the full-scale results continue to exhibit a high degree of asymmetry, whereas the scale model results begin to lose the cross flow component behind the hips at  $x = 0.5C$ . By  $x = 1C$  the asymmetry between the counter-rotating hip vortices is further degraded and the asymmetry in the wake structure no longer prominent. Whilst the relative position of the left and right vortex may influence this result, it is suspected that there is a Reynolds number effect.

The dominant flow structures, in particular the hip vortices, for both symmetric and asymmetric wakes identified in the work of Crouch et al. are also present in these lower Reynolds number experiments. It follows then, that with appropriate regard to the higher diffusion rate, studying the wake of a trailing cyclist at this Reynolds number will provide insight into whether the main flow structures are similar or distinct from those of a single cyclist. Of concern is the higher rate of diffusion of these structures at the lower Reynolds number. The interaction between the flow structures in the wake of the lead cyclist and the body of the trailing cyclist will likely be less in these experiments than in full-scale suggesting these results are more indicative of greater spacing at full-scale.

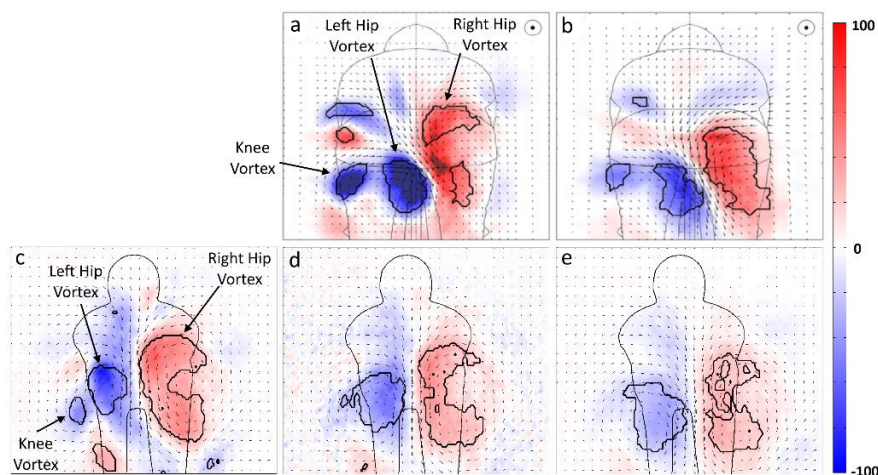


**Figure 5.2.2** – (a) Wind tunnel results of Crouch et al. [29] showing streamwise vorticity ( $s^{-1}$ ) in the wake of a full-scale cycling mannequin at  $75^{\circ}$  crank angle at  $0.5C$  downstream of rear of rider and (b)  $1.0C$  downstream. (c) Vorticity in the wake of scale model cyclist at  $75^{\circ}$  crank angle at  $0.25C$  downstream of the rear of the rider, (d)  $0.5C$  downstream and (e)  $1.0C$  downstream. Contours of swirling strength criterion identify vortex boundaries, as used by Crouch et al.

## 5.2.2 Streamwise Vorticity in the Wake of Tandem Cyclists

### *Two Tandem Riders at 15° Crank Angle (Symmetric-Symmetric)*

Figure 5.2.3 shows contours of streamwise vorticity for the single-rider symmetric case (15° crank angle), behind the trailing rider at Spacing 1 and Spacing 2 in the symmetric-symmetric case at downstream planes of  $x = 0.25C$ ,  $0.5C$  and  $1.0C$ . All vorticity results are non-dimensional: calculated from non-dimensional velocity and position (normalised by rider torso chord length). Profiles of in-plane velocity components are provided in Appendix E.

At Spacing 1 the pair of upper hip vortices, seen for a single cyclist, remain the dominant feature in the wake, although vorticity is decreased. Peak vorticity is reduced by 26% and 28% in the left and right hip respectively. A broad reduction in vorticity is observed across the wake region; the result of the reduced energy in the inlet flow seen by the trailing rider. The inner thigh vortices have reduced in vorticity magnitude and shifted downwards and outwards from the cyclist centreline compared to the single rider result. There is a localised change in spanwise velocity immediately below the cyclist's hips compared to a single cyclist. This indicates a change in the local in-plane velocity gradient, which is why the vortices are seen lower and wider in the wake. This change in velocity is likely due to the flow coming through the trailing cyclist's legs. Thigh vortices are formed from the inside of the rider's legs and so their formation will be affected by the changed flow conditions due to the lead rider wake. In the trailing rider case the flow between the legs will contain vorticity and cross flow velocity components as well as reduction in streamwise velocity due to the presence of the leading cyclist. The combined effect of these flow changes on the formation and evolution of the thigh vortices will contribute to the changes observed in the inner thigh vortices. Secondary features in the lower part of the wake are consistent with the single rider profile but with a reduction in vorticity evident.

For Spacing 2 (Figure 5.2.3 right) the wake profile of the trailing rider exhibits close similarity with the single rider result. The profile of three stacked pairs of counter-rotating vortices behind the torso is clearly evident in the trailing rider wake. The upper hip vortices and inner thigh vortices occur in the same relative position as seen for a single rider, although magnitude of vorticity is slightly reduced. No combining of vorticity regions across the centreline is evident, as was seen for Spacing 1. Secondary features in the lower region of the wake are consistent with the single rider profile and a decrease in vorticity is evident across the wake. However, with downstream planes the thigh vortices can be seen to diffuse rather than combine with the hip vortices.

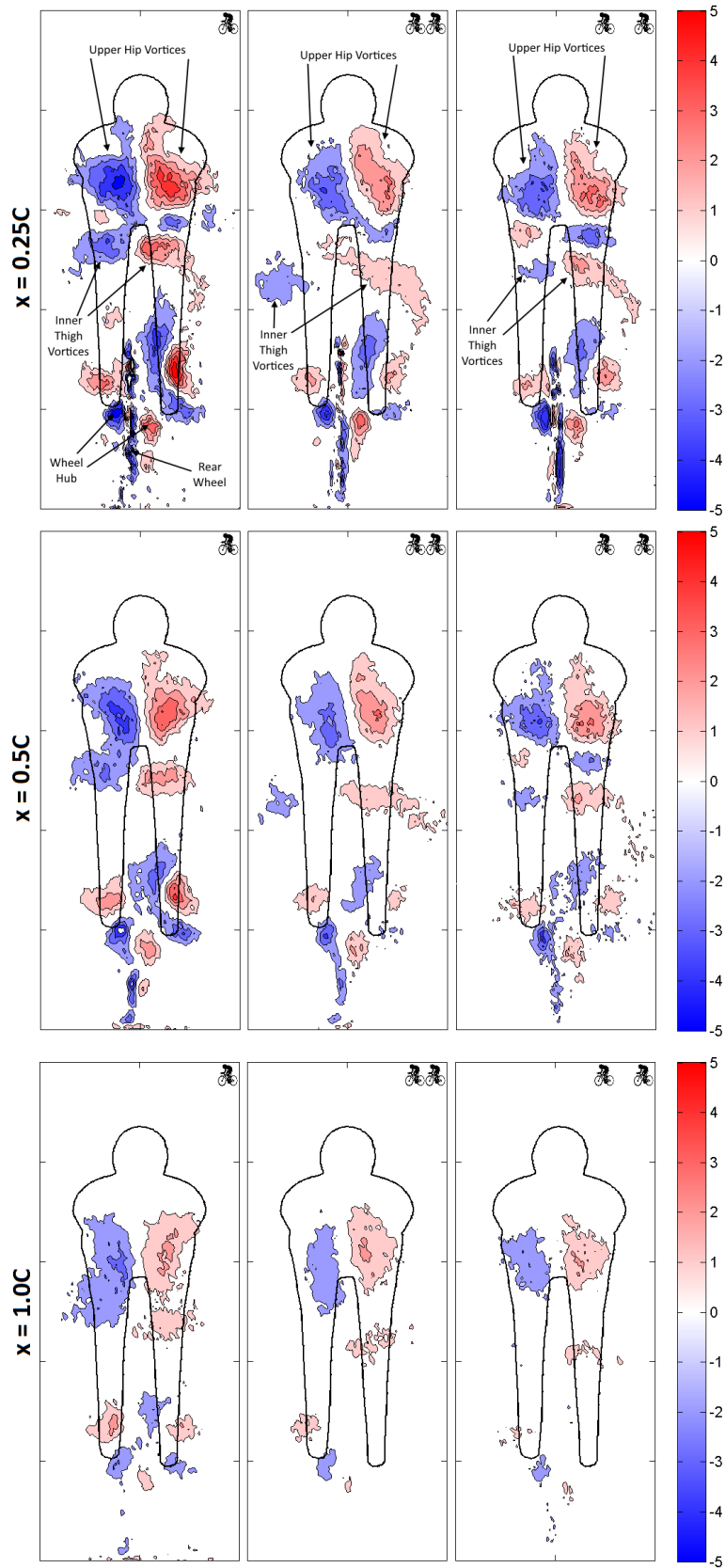


**Figure 5.2.3** – Streamwise vorticity (non-dimensional) at a  $x = 0.25C, 0.5C, 1.0C$  downstream of (left) a single rider at  $15^\circ$  crank angle, (middle) the trailing rider at Spacing 1 with both at  $15^\circ$  crank angle, (right) the trailing rider at Spacing 2 with both riders at  $15^\circ$  crank angle.

### Lead Cyclist 75° Crank Angle – Trailing Cyclist 15° Crank Angle (Asymmetric-Symmetric)

Figure 5.2.4 shows the in-plane velocity vectors and vorticity field ( $x = 0.25C$ ) for the single cyclist at 75° and 15° (a, b) and the symmetric trailing cyclists for Spacing 1 (c) and Spacing 2 (d). This case provides insight into the effect of an upstream asymmetric wake on the wake of the more symmetric body. Profiles of streamwise vorticity at  $x = 0.5C$  and  $1.0C$  can be found in Appendix F. The asymmetric (75°) case is provided as a reference for the leader wake.

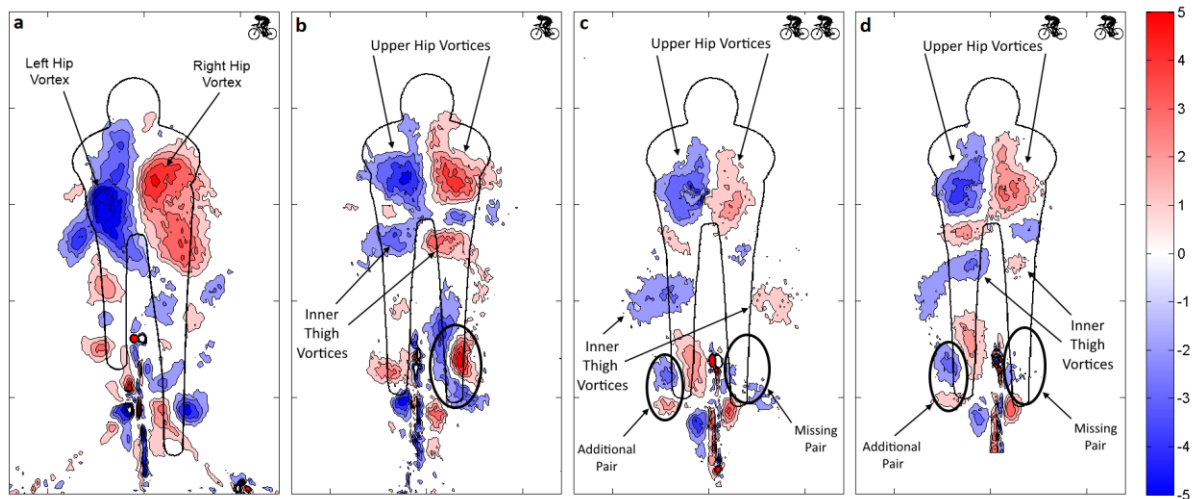


**Figure 5.2.4** – Streamwise vorticity (non-dimensional) at  $x = 0.25C$  downstream of (a) a single rider at 75° crank angle, (b) a single rider at 15° crank angle, (c) a trailing rider at Spacing 1 at 15° with the leader at 75° and (d) a trailing rider at Spacing 2 at 15° with the leader at 75°.

In Spacing 1 (Figure 5.2.4c) the three stacked pairs of trailing vortices are apparent and the upper hip vortices are the dominant feature of the wake as was seen for single and symmetric-symmetric cases. However, as with the previous case, peak vorticity is reduced; 23% and 36% for left and right hips respectively. The bias to the left is likely due to the leader wake which has significantly higher vorticity in the left hip vortex compared to the right (-8 and 5.5 respectively). Some persistence of this vorticity into the trailing wake appears to bias the negative vorticity in the left hip vortex. The asymmetric wake has higher peak vorticity and vortices persist further downstream compared to the symmetric case, thus potentially greater influence from the leader wake. The inner thigh vortices are displaced significantly downwards and outwards from the rear of the rider, similar to the symmetric-symmetric case. However, in difference, there is no combining of vortices across the centreline. The slight bias to the left side inner thigh vortex is likely the result of vorticity persisting from the leader wake.

Figure 5.2.4b shows a strong counter-rotating vortex pair behind the right foot/lower leg for the single rider case. However, the pair are absent from the trailing rider profiles. These were visible in the symmetric-symmetric case, indicating some dependence on the leader wake profile. Considering the single cyclist asymmetric profile (75° crank angle), there is a distinct negative vortex on the outside of the right lower leg/foot, whereas in the symmetric case (15°) at the corresponding location the vortex is of positive sign. The positive vorticity generated at the wheel hub also differs in the asymmetric case. It seems then that the vorticity generated from the leading rider is impacting on the trailing rider right

leg with vorticity annihilating through cross-diffusion to eliminate that positive vortex. This is disrupting the formation of that counter-rotating pair observed in the single rider symmetric case.

On the left side, there is a small additional counter-rotating vortex pair in the trailing rider profiles (shown in Figure 5.2.4). These were not evident in the single rider wake. Whilst they do not appear to correlate directly with structures in the single asymmetric wake, that region of the wake is characterised by small pockets of vorticity, rather than strong coherent structures. Therefore, it is believed that the interaction of this flow on the right leg of the trailing rider is altering the flow separation conditions, resulting in the small additional counter rotating pair.

In Spacing 2, the three paired vorticity regions in the upper wake are clearly visible, as seen for the previous symmetric-symmetric case. The upper hip vortices remain the dominant feature of the wake but with a reduction in peak vorticity; 12% left, 21% right. This bias appears to be linked to the bias in vorticity in the leading rider wake, as described above, despite the separation distance. The inner thigh vortices remain close to the cyclist centreline compared to Spacing 1, similar to the symmetric-symmetric case. These vortices also show significantly lower vorticity compared to the single rider case. The vortex pair on the lower right that was missing in the Spacing 1 wake, is also absent at Spacing 2. The additional vortex pair on the lower left is again evident. This was not so in the symmetric-symmetric case, indicating that this pair has its origins in the leading rider's wake. Despite the increase in separation distance, the wake of the leader evidently still has an impact on the flow from the lower legs of the trailing rider.

The distribution of the thigh vortices of the asymmetric-symmetric case at Spacing 2 appear to be a mirror of the behaviour seen in the symmetric-symmetric case with the region of vorticity at the left thigh wrapping down into the lower wake. In the symmetric-symmetric case the region of vorticity at the right thigh extends down towards the right foot. This behaviour is due to the change in the vortices at the feet. In the symmetric-symmetric case there is a strong positive vortex on the outside of the right foot. This results in a broad region of vorticity banding between the thigh and foot. However, in the asymmetric-symmetric case that positive right heel vortex is absent. In contrast, there is the additional negative vortex at the left foot and a band of vorticity is observed between the thigh and heel.

### ***Lead Cyclist 15° Crank Angle – Trailing Cyclist 75° Crank Angle (Symmetric-Asymmetric)***

To investigate potential changes to the asymmetric regime of a trailing cyclist, the asymmetric cyclist model was positioned behind a leader at the symmetric (15°) position. Figure 5.2.5 shows the in-plane velocity vectors and vorticity field ( $x = 0.25C$ ) for the single cyclist at 15° and 75° (a, b) and the trailing cyclists for Spacing 1 (c) and Spacing 2 (d). Profiles of streamwise vorticity at  $x = 0.5C$  and  $1.0C$  can be found in Appendix F.

As was with the case with the symmetric trailing rider case, the trailing asymmetric wake maintains a strong degree of similarity to the case of the single rider at 75° crank angle. However, compared to the single rider profile, the primary hip vortex pair is reduced in size and vorticity, but remains the dominant feature of the wake for both Spacing 1 and Spacing 2.

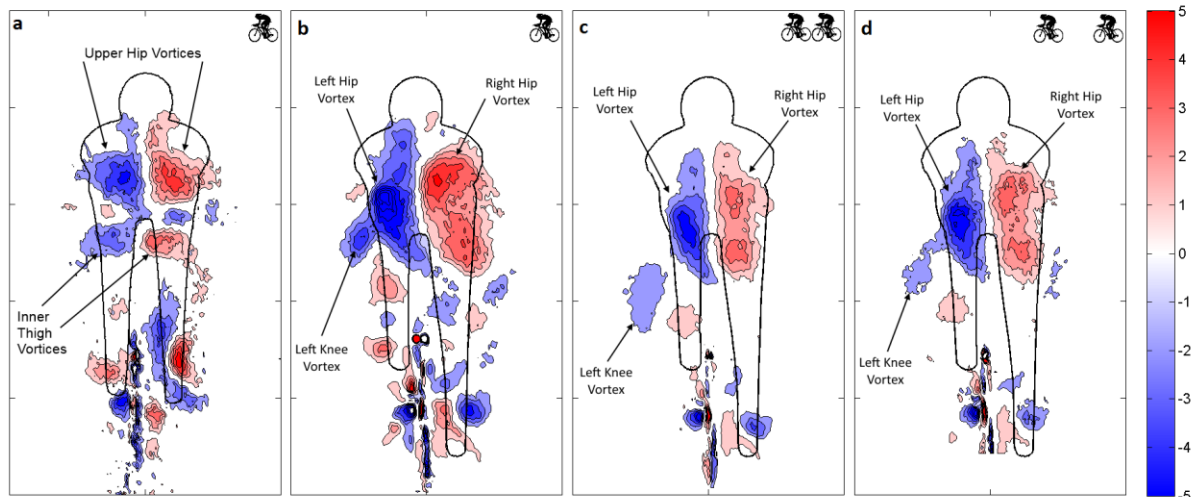


**Figure 5.2.5** – Streamwise vorticity (non-dimensional) at  $x = 0.25C$  downstream of (a) a single rider at  $15^\circ$  crank angle, (b) a single rider at  $75^\circ$  crank angle, (c) the trailing rider at Spacing 1 at  $75^\circ$  with the leader at  $15^\circ$  and (d) the trailing rider at Spacing 2 at  $75^\circ$  with the leader at  $15^\circ$

At Spacing 1 the peak vorticity of the hip vortices is reduced by 41% and 27% respectively. The degree of cross flow between the two hip vortices is also reduced compared to the single rider case. The knee vortex has diffused and has moved lower and wider in the wake, with a 52% and 60% reduction in peak vorticity compared to single rider case. This behaviour is similar to the movement of the thigh vortices seen in the symmetric wake cases at Spacing 1 and likely due to the reduced energy inflow conditions and cross flow components and vorticity in the inflow affecting formation and evolution in the trailing wake. The small features in the lower region of the wake are not evident in the trailing rider wake. This is likely due to disruption to their formation from upstream flow and cross-annihilation with vorticity from the leading cyclist's wake. A negative vortex shed from the right foot is still evident as is a small positive region behind the left foot.

The increased distance between the leading and the trailing riders in Spacing 2 has little effect on the global structure of the wake (see Figure 5.2.5d). The primary counter-rotating hip vortex pair are similar to that for Spacing 1 and of reduced strength compared with the single-rider result. Peak vorticity is reduced by 32% and 26% compared to the single rider result, which represents a small recovery compared to Spacing 1. The lower section of the wake is also similar to Spacing 1, with small structures from the single rider case no longer evident, showing greater diffusion potentially cross-diffusive annihilation from mixing with flow from the leader.

## 5.2.3 Centreline Streamwise Velocity Profiles In Tandem Formations

### *Effect of Leg Position on the Wake of a Single Cyclist*

To investigate the effect of interactions on streamwise velocity, an orthogonal plane coinciding with the rider centre line was also investigated. From this a streamwise cross section of the flow could be captured to display contours of streamwise velocity.

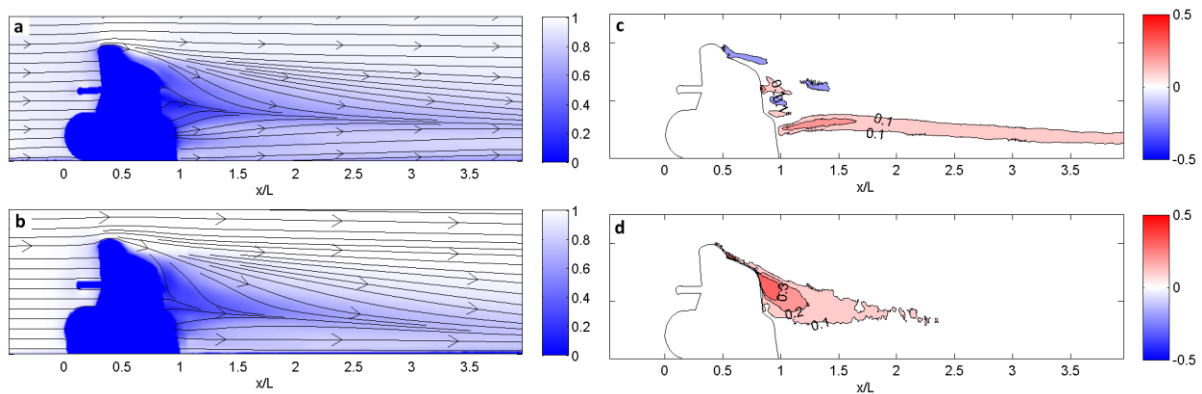


**Figure 5.2.6** – (a) Centre plane normalised streamwise velocity contours for a single rider at  $15^\circ$  crank angle and (b)  $75^\circ$  crank angle. (c) Streamwise velocity difference fields by subtracting the single rider  $75^\circ$  field from that of a single rider at  $15^\circ$ , (d) vertical velocity difference.

Before analysing the results for two-rider formations, it is necessary to consider the velocity profile of a single rider and the influence of the leg position. Figure 5.2.6 shows the streamwise velocity profiles for a single rider at  $15^\circ$  (symmetric) and  $75^\circ$  (asymmetric) leg positions. Contours show velocity normalised by the freestream flow velocity. Although subtle, there are small differences evident in the flow as a result of the different leg positions. To provide a better comparison, the velocity field of the  $75^\circ$  rider was subtracted from the  $15^\circ$  field to generate a velocity-difference field. These results are plotted in Figure 5.2.6c & d above. Positive regions indicate higher streamwise velocity of the cyclist at  $15^\circ$ . It is seen that the largest difference occurs in a narrow region extending downstream approximately centred vertically at the height of the wheel. Over this part of the wake the  $15^\circ$  crank angle position (symmetric leg position) results in higher streamwise velocity than the  $75^\circ$  position. This seems likely to be due to the  $75^\circ$  (asymmetric) position having greater downwash and extending further down below the rider's hips, compared to the symmetric case. There are some additional small regions of localised differences, but the bulk of the centre plane flow is similar between leg positions. However, if the vertical velocity component is compared, a much more distinct difference is apparent between the fields (see Figure 5.2.6d). In the  $75^\circ$  case, there is a clear increase in downwash evident immediately behind the rider torso; note that as the velocity was negative in both profiles, the positive region indicates greater velocity downwards. This is consistent with the flow described by Crouch et al.. It should also be noted that the centre plane velocity is only showing a slice of the streamwise flow and so the full wake flow behaviour is not being captured.

### ***Two Tandem Riders at 15° Crank Angle (Symmetric-Symmetric)***

The single-rider results, presented above, provide a reference point for the tandem-rider streamwise velocity comparison. Results for tandem riders at minimum separation (Spacing 1) and with one bicycle length gap (Spacing 2) are presented in Figure 5.2.7 below. Rows 1 and 2 relate to the symmetric-symmetric case (sym-sym) with both cyclists at 15° crank angle. Rows 3 and 4 relate to the asymmetric-symmetric case (asym-sym) with the leader at 75° and the trailing cyclist at 15° crank angle. Rows 5 and 6 relate to the symmetric-asymmetric case (sym-asym) with the leading cyclist at 15° and the trailing cyclist at 75° crank angle. In all cases streamwise velocity is plotted at the cyclists' centre plane, with the field normalised by the freestream velocity. The single rider velocity fields can be seen in Figure 5.2.6 (above).

The results show that the wake behind a trailing rider appears similar to that of a single rider. The similarity in the magnitude of velocity is not unexpected, given the similarities observed in the vorticity fields in cross-sectional planes. As before, to highlight the differences in the wake, the velocity field from the single rider case was subtracted from that of the trailing rider for both Spacing 1 and 2 to better highlight the difference in velocity distributions. The results are shown in Figure 5.2.7c & d. Negative regions indicate a velocity deficit in the trailing rider wake compared with that of a single cyclist.

As evident in the velocity profiles, there is a large deficit immediately upstream of the trailing rider for both formations due to the leading rider's wake. This deficit is significantly larger in size and magnitude for Spacing 1 with a smaller distance from the leading rider than for Spacing 2. This is expected as the increased distance between leading and trailing riders allows greater energy recovery in the wake from freestream.

Compared with the wake of a single rider, the lower region of the wake, below the height of the wheel, has a reduced velocity for both trailing-rider formations; this is of the order of 10% lower than for the single-rider wake. However, Spacing 2 exhibits a slight recovery compared to Spacing 1. Analysis of this frame reveals that there is only a small difference in velocity in the lower region but below the minimum contour threshold in Spacing 2. In the upper wake, above wheel height, there are some small areas of positive velocity difference close to the rider's back. However, most of the upper wake region shows velocity to be negligibly different from the single-rider case, despite a significant velocity reduction upstream of the riders. This indicates that the wake of a trailing rider is not greatly influenced by the distance downstream.

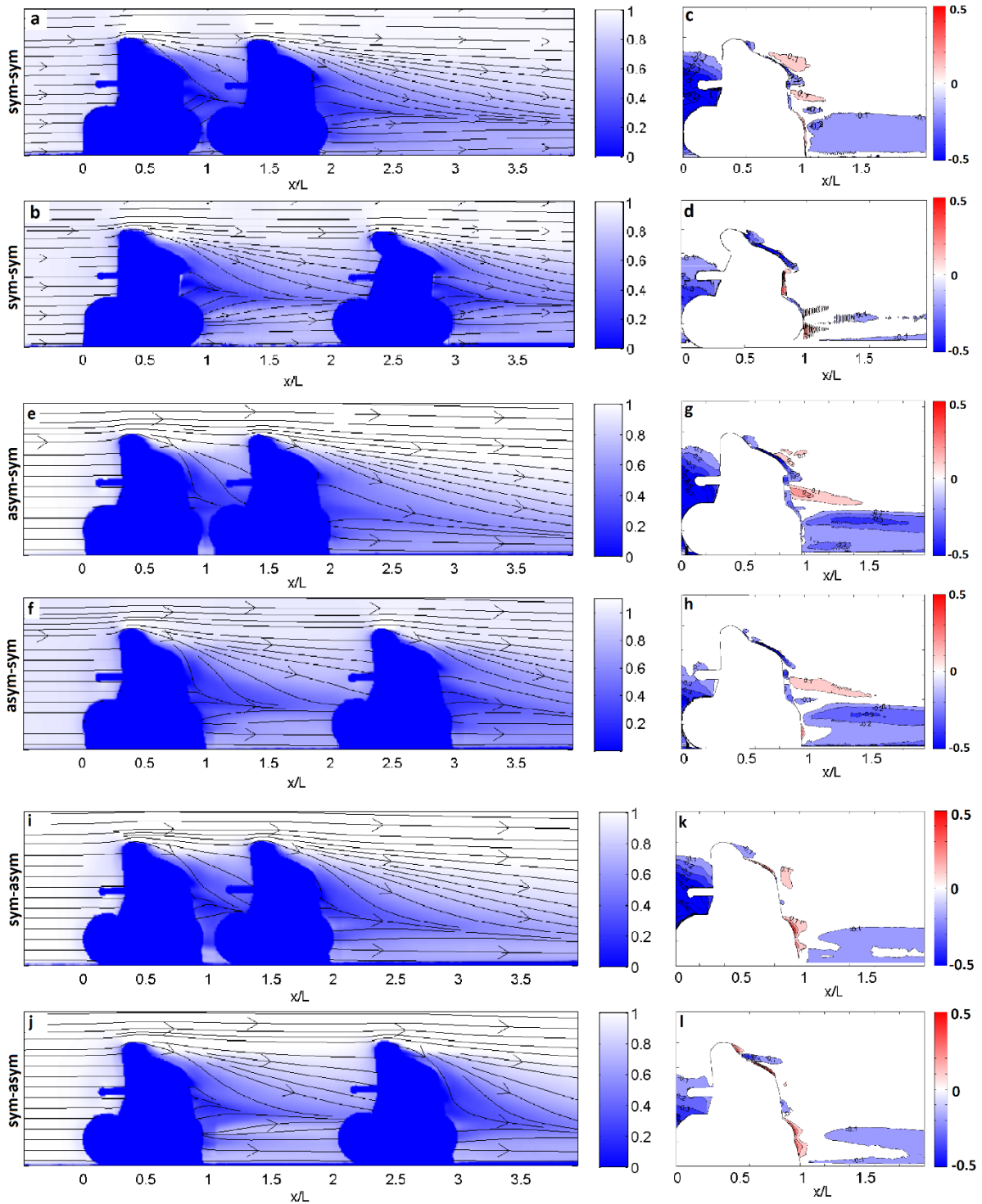


**Figure 5.2.7** – Normalised centreline streamwise velocity profile for the symmetric-symmetric case at (a) Spacing 1 and (b) Spacing 2. (c) Difference in wake velocity of the trailing rider from the single rider symmetric profile at Spacing 1 and (d) at Spacing 2.

Normalised centreline streamwise velocity profile for the asymmetric-symmetric case at (e) Spacing 1 and (f) Spacing 2. (g) Difference in wake velocity of the trailing rider from the single rider symmetric profile at Spacing 1 and (h) at Spacing 2.

Normalised centreline streamwise velocity profile for the asymmetric-symmetric case at (i) Spacing 1 and (j) Spacing 2. (k) Difference in wake velocity of the trailing rider from the single rider symmetric profile at Spacing 1 and (l) at Spacing 2.

Figure 5.2.8 shows that the wake of the leading rider in Spacing 2 is similar to that of the single rider wake. Performing a similar wake comparison as described above reveals that the two flow fields have negligible difference in velocity. This shows that the forward influence of the trailing rider is small and that the wake of the leading rider develops in a similar manner to that of a single rider at that separation distance.

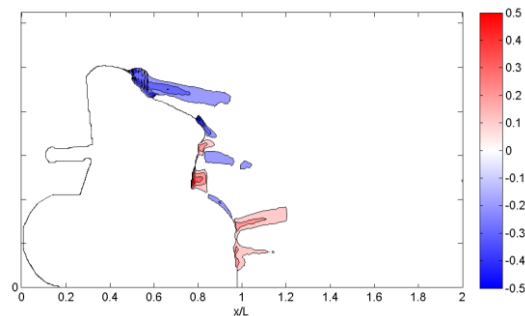


**Figure 5.2.8** – Streamwise velocity difference generated by subtracting the single rider at  $15^\circ$  streamwise velocity profile from that of the leading rider in Spacing 2 (trailing cyclist at a bicycle length downstream).

#### ***Lead Cyclist at $75^\circ$ Crank Angle – Trailing Cyclist at $15^\circ$ Crank Angle (Asymmetric-Symmetric)***

To investigate the influence of the upstream cyclist, the crank angle of the leading rider in the tandem pair was then set to the  $75^\circ$  leg position, with the trailing rider remaining at the  $15^\circ$  leg position. The velocity profiles for the trailing rider at minimum separation (Spacing 1) and at one bicycle length downstream (Spacing 2) are shown in Figure 5.2.7 e-h (Rows 3 & 4).

The single-rider streamwise velocity profiles show only minor differences with leg position and similar small changes are evident in the wake of the leading rider at  $75^\circ$  leg position (see Figure 5.2.6). These become most apparent with a bicycle length separation between the two, as the wake evolution is more evident. The trailing rider, at  $15^\circ$  crank angle, has a wake field very similar to the previous result for both riders at  $15^\circ$  crank angle. Given that the cross-sectional wake fields show that the leg position of the upstream rider has only small effect on the trailing rider wake, it is expected that the streamwise velocity would not show significant changes for the trailing rider. As before, to better identify these small differences, these fields have been subtracted from that for the single rider at  $15^\circ$ , for the trailing rider in the two different downstream positions.

The velocity-difference fields for the trailing rider in both Spacing 1 and 2 are similar, showing a general deficit in the lower wake region (again below one wheel height). This is similar to that seen with both the leading and trailing riders at the  $15^\circ$  leg position (see Figure 5.2.7a-d). However, in this case with the leading rider at  $75^\circ$  crank position there is a contained region of greater velocity deficit compared to the leader at  $15^\circ$  crank position. From the single rider results it was observed that the  $75^\circ$  crank position resulted in a localised pocket near the top of the wheel which had lower velocity than the  $15^\circ$  case (see Figure 5.2.6). This greater velocity deficit observed in Figure 5.2.7g,h is therefore the result of lower inflow resulting from the lead cyclist's leg position. The small areas of increased velocity just below seat height are also consistent with the previous results with both riders at the same phase of the crank cycle, though slightly more pronounced. From this it is concluded that the leg position of the leading rider does not have a large influence on the streamwise velocity in the primary

wake region of the trailing rider, though some changes are present in the lower wake. Given that the  $15^\circ$  and  $75^\circ$  positions are the two extremes in terms of both drag and wake structure, it is suggested that the instantaneous leg position of a pedalling cyclist will not significantly influence the trailing rider's primary wake structure behind the torso and upper legs. The wake of the trailing rider is dominated by that rider's individual geometry and position.

#### ***Lead Cyclist at $15^\circ$ Crank Angle – Trailing Cyclist at $75^\circ$ Crank Angle (Symmetric-Asymmetric)***

To look at the effects on the flow around a cyclist at the asymmetric ( $75^\circ$ ) position, the order of the cyclists was then reversed so that the trailing rider was at  $75^\circ$  crank angle and leader at  $15^\circ$ . The streamwise velocity fields are shown in Figure 5.2.7 i-l (Rows 5 & 6) with contours normalised by the freestream.

Subtracting the velocity profile of a single rider at  $75^\circ$  crank position from the two tandem fields leads to a velocity difference similar to that which was seen previously. These fields show the same trends as the previous two cases. Ahead of the trailing rider there is a large velocity deficit. This is significantly greater for the rider at minimum distance downstream. There is minimal difference between the two wakes corresponding to the trailing riders at the two downstream positions. Again, the main difference from the wake of a single rider is the increased velocity deficit near the ground extending up to wheel height. This is of the order of 10% of the freestream velocity, the same as both cyclists at  $15^\circ$ .

Streamwise velocity cross sections have shown that the trailing rider has a greater streamwise velocity deficit in the lower part of the wake up to the height of the wheel. This was consistent across all cases of leg position. However, the bulk of the wake field above wheel height for the trailing rider had broadly the same velocity profile as for a single rider for both Spacing 1 and 2. This shows that the distance downstream, over this range, does not have a significant effect on streamwise velocity component in the trailing rider wake. Given that the cross-stream vorticity fields also exhibited similar profiles, it is concluded that the wake structure of a trailing cyclist is not substantially different from that of a single rider. Therefore, the mechanism responsible for the large drag reduction cannot be solely attributed to a change to the dominant vortex structures or a decrease in wake velocity deficit. The key point of difference between the flow fields around the trailing riders was the increased velocity deficit ahead of the rider caused by the leading rider. It follows then that the reduction in upstream velocity and the decrease in oncoming kinetic energy is having a large effect on the drag reduction for a trailing rider.

## 5.2.4 Flow Between Two Tandem Cyclists

The wake cross sections and streamwise centre plane data showed that there are only small changes to the wake structure of a trailing rider due to an upstream cyclist, compared to an isolated single cyclist. The primary longitudinal vortex structures are not significantly altered and the centre plane streamwise velocity showed similar fields for trailing riders at both Spacings, particularly in the upper wake. The only significant difference from the single rider case was the slight increase in velocity deficit in the near ground region. Indeed, these changes do not appear sufficient to fully explain the significant drag reduction observed for a trailing rider, being of the order of 40% at minimum separation and still up to 35% with a bicycle length gap (Spacing 2). Therefore, this drag reduction must be the result of an additional mechanism upstream of the rider. To investigate this, flow cross sections were generated in the region between the leading and trailing riders for both Spacing 1 and 2. In all cases discussed in this section the cyclists were at 15° crank angle. Figure 5.2.9 shows the normalised streamwise velocity contours immediately downstream of the leading rider's trailing edge for each of the three cases. Due to the presence of the trailing rider, any cross sections viewed further downstream would cut through the trailing cyclist model and therefore include physical blockage and shadowing. For the minimum separation case there is only a very narrow region where the image is not obscured and a full cross section can be viewed.

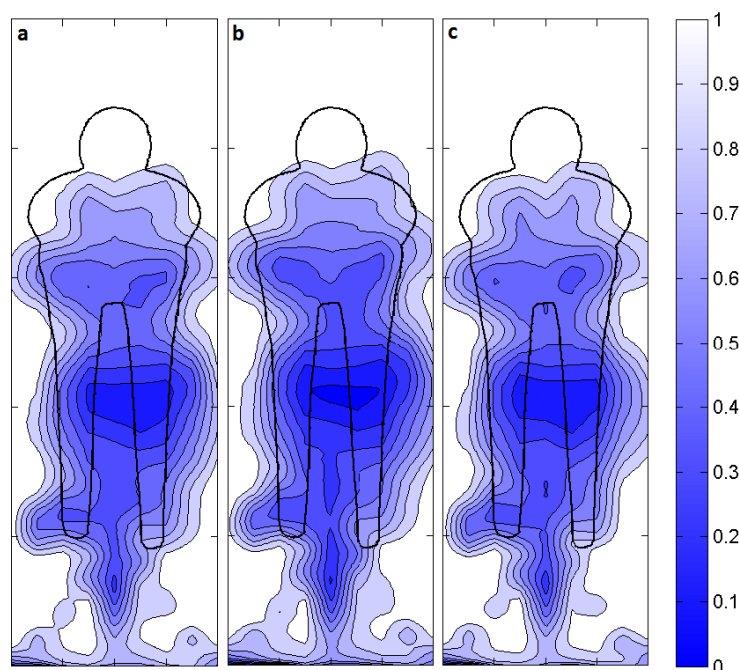


**Figure 5.2.9** – Streamwise velocity contours immediately downstream of: (a) a single rider, (b) the leading rider in Spacing 1 (with the trailing rider at minimum separation), (c) leading rider in Spacing 2 (with the trailing rider at one bicycle length downstream). In all cases both cyclists with legs positioned at 15° crank angle.

It can be seen that the three fields are all very similar in shape and magnitude. Considering Figure 5.2.9a and 5.2.9c, corresponding to the single rider and to Spacing 2, respectively; the two streamwise velocity fields exhibit negligible difference. This indicates that the trailing rider has negligible forward influence on the leading rider at this separation distance. This is consistent with previous observations

in drag that show negligible change in force for the leading rider with a second rider at one bicycle length separation (Section 4.1). Figure 5.2.9b shows the velocity behind the tandem leader at minimum separation and shows a slight difference from the other two fields. There is an increase in the velocity deficit, predominantly in the centre of the wake, compared to the single or Spacing 2 cases.

These velocity effects can be quantified by averaging the velocity over the whole field. Normalised velocity for the single rider, tandem riders at Spacing 1 and Spacing 2 were 0.76, 0.73 and 0.76 respectively. This confirms that the overall velocity difference between the single rider and the leader at Spacing 2 is negligible. However, at minimum separation (Spacing 1) the velocity deficit across the leader is greater than for a single rider despite having lower drag.

Velocity difference for Spacing 2 is consistent with force results, which have reported negligible drag reduction for the lead rider at separation distance of one bicycle length, indicating that the lead rider is beyond the range of forward interference effects from the trail. However, at minimum separation distance a drag reduction of the order of 2.5 - 5% has been reported for the lead rider. The mean velocity cross section results show a decrease in velocity which indicates greater energy loss compared to the single rider, suggesting an increase in drag. However, this assumption neglects three dimensional effects resulting from distortions to the lead rider wake vortices. In fact, the reduced velocity is likely to be a result of forward interference from the trailing rider, as this plane is immediately upstream of the trailing rider leading edge. Numerical simulations by Blocken et al. (2013) showed that the presence of the trailing rider acted to increase the pressure on the rear surface of the leading cyclist and it is this effect that is responsible for the leading cyclist drag reduction. However, PIV results do not provide pressure data so this cannot be confirmed from these results.

### ***Wake Behind a Trailing Cyclist at Minimum Separation***

The imaging planes used to assemble the streamwise velocity fields in cross-sectional planes did not cover the entire downstream length captured for the centre plane velocity comparison discussed previously. However, the near wake of the trailing rider was captured. Figure 5.2.12a shows the wake behind the trailing rider at minimum separation in a tandem formation. (For the single rider wake see Figure 5.2.9a). This corresponds to the same streamwise position as Figure 5.2.12, immediately downstream of the rear-wheel trailing edge. Figure 5.2.10b shows the difference in velocity; the result of subtracting the single rider field (5.2.9a) from the tandem trailing rider field (5.2.10a). This is presented to highlight the regions of difference between the two fields.

Figure 5.2.10b clearly highlights the differences between the two profiles of the single rider and the trailing rider. Despite being further downstream, the centre region of the trailing rider wake is actually at a higher velocity than the single rider. However, the wake is wider and less confined. The increase in width of the wake is likely to be associated with the changed inflow conditions seen by the trailing rider, which have an already reduced streamwise component. As the flow passes over the trailing rider there is further energy loss, resulting in a larger overall velocity deficit across the wake. Compared to the single rider wake (Figure 5.2.9a), Figure 5.2.10a shows that the large central region of low velocity is lower in the wake. This results in the positive region seen in the centre of Figure 5.2.10b. It was shown previously that at small separation, the lower pair of hip vortices are weaker and less cohesive than found for a single rider (see 5.2.3). The greater diffusion of these structures, combined with

disturbed inflow conditions containing significant in-plane velocity components cause the wake to be less structured and allow for greater mixing across the wake, facilitating the region of higher velocity. However, it should be noted that the mean streamwise velocity over the whole wake is lower than the single cyclist case.

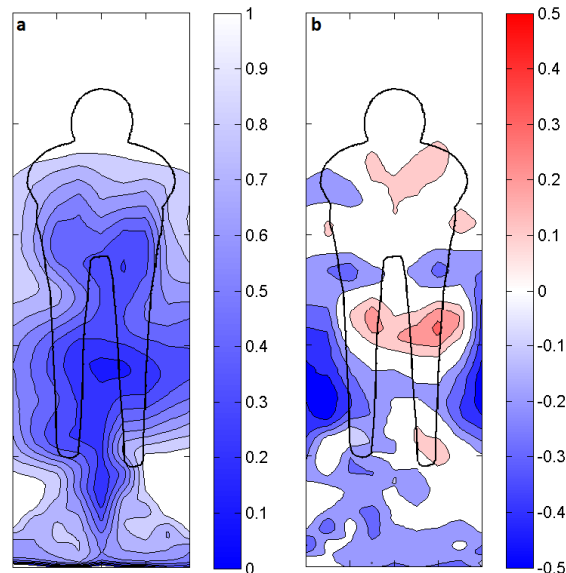


**Figure 5.2.10** – (a) Streamwise velocity cross-sections immediately downstream of a trailing rider in a tandem pair for Spacing 1 with both riders at  $15^\circ$  leg position, (b) streamwise velocity difference generated by subtracting the single rider field from that of the trailing rider.

### ***Trailing Rider Inflow Conditions***

From the above discussion, it is suggested that the primary mechanism for drag reduction for a trailing rider immediately behind the leading rider is due to large changes in inflow velocity, rather than significant disruption to the wake. Figure 5.2.11 shows the streamwise velocity profiles immediately ahead of the trailing rider for the two tandem formations.

Inflow conditions for the two cases differ significantly, as would be expected given the significant change in separation distance. With the trailing rider positioned further downstream at Spacing 2 (Figure 5.2.11b) there is capacity for greater mixing and energy recovery in the wake. This is evident from the higher streamwise velocity across the field. Whilst there is still a large region where velocity is well below freestream conditions, the upper wake region shows substantial recovery approaching freestream conditions.

A slight asymmetry can be seen in the inlet conditions for the rider at Spacing 2 (Figure 5.2.11b). This bias in wake deficit was not evident in near wake of the leading cyclist. Analysis of cross sections in the gap region between riders shows that this asymmetry evolves as the flow moves downstream from the leader. This is likely the result of a small asymmetry in the lead cyclist model affecting the downstream evolution of the wake and recovery from freestream.

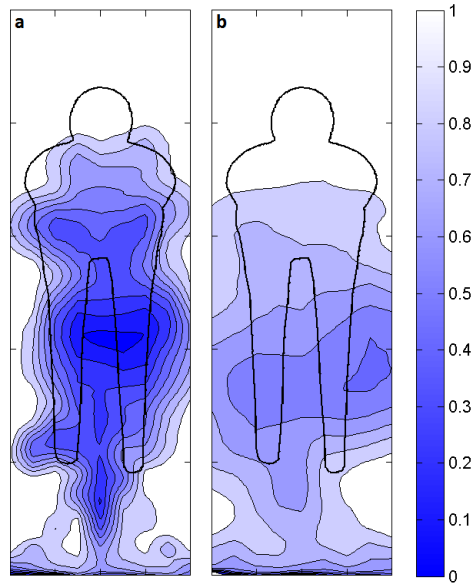


**Figure 5.2.11** – (a) Streamwise velocity immediately upstream of the trailing rider for Spacing 1, (b) streamwise velocity profile immediately upstream of the trailing rider for Spacing 2. Legs of both leading and trailing riders at the 15° crank position.

To quantitatively compare the state of the flow at the inlet and outlet for each configuration, the streamwise velocity component was averaged over the full cross-sectional planes at the leading and trailing edges for each bicycle. The cross-sectional region used for averaging will affect the computed averages, so this only represents an attempt to isolate the local flow conditions experienced by a cyclist. However, it does provide a method for direct comparison between the three cases as the region is of equal area. The square of the mean velocity is tabulated as it provides an indication of the dynamic pressure at inlet and outlet for each case (Table 5.2.1). Drag reduction for tandem cyclists from the wind tunnel is also presented for reference (see Section 4.1).

**Table 5.2.1** – Square of the mean normalised streamwise velocity averaged over flow cross sections.

\*Trailing rider wake at bicycle length separation outside interrogation region - modelled as worst case.

		Mean Inflow	Mean Outflow	Velocity Deficit	Reduction Inflow	Drag Reduction
<b>Single Rider</b>		<b>1.00</b>	<b>0.60</b>	<b>0.40</b>	<b>0</b>	0
<b>Minimum Separation</b>	Lead	1.00	0.55	0.45	0	2.5 – 5 %
	Trail	0.55	0.52	0.03	45%	40 – 49 %
<b>Bicycle Length Separation</b>	Lead	1.00	0.59	0.41	0	0
	Trail	0.67	0.52 – 0.60*	0.15 – 0.07*	33%	35%

Note that the trailing cyclist outflow for one bicycle length separation was outside the interrogation region. Given the strong similarity of the trailing rider wake at Spacing 2 to the single rider case (see Figure 5.2.3) it is estimated in Table 5.2.1 to lie between that of a single rider and the trailing outflow result for the minimum separation case. The trailing rider at minimum separation had the lowest mean velocity outflow so this represents a conservative case in terms of local velocity deficit over the rider

at Spacing 2. However, it is seen that the resulting deficit is still significantly lower than that seen for the leading or single rider cases due to the reduction in inflow velocity.

It can be seen that the inflow conditions vary far greater than those at outflow. This is unsurprising given the similarity observed in the vorticity cross sections of the wake, and as previously discussed. The area-averaged inflow for the trailing riders at minimum separation (Spacing 1) and one bicycle length separation (Spacing 2) were 0.55 and 0.67 respectively. For comparison the leading rider outflow in Spacing 2 was 0.59; close to that of a single rider in isolation. This shows that at greater downstream distance the flow recovers some energy from the freestream. This is consistent with drag results from wind tunnel tests (see Section 4.1), which have shown that drag reduction for the trailing rider decreases with distance downstream.

At minimum separation, the trailing cyclist has a lower mean outflow (0.52) than that for a single rider (0.60). However, the trailing rider has been previously shown to experience a large drag reduction. This indicates that it is not a recovery of streamwise energy in the wake that is responsible for the large drag reduction, but rather an upstream effect, as the trailing rider inflow velocity is significantly below freestream. This results in a significant change in the velocity deficit over the cyclist. This supports the contention that it is the reduction in inflow velocity that is the primary contributor to the trailing rider drag reduction.

Results in Table 5.2.1 show that the percentage reduction in inflow squared velocity is of similar order to the drag saving observed for trailing cyclists in the wind tunnel. This provides quantitative evidence that the drag of the trailing cyclist is dominated by the reduction in inflow energy, rather than a downstream effect. It is noted that the trailing rider was observed to have lower mean velocity in the wake than a single rider, suggesting that drag reduction will not be directly proportional to reduction in inlet dynamic pressure. Furthermore, vorticity results showed lower magnitude of streamwise vorticity in the trailing rider wake. However, these effects appear to be secondary contributors to the trailing rider drag saving behind the reduction in inlet momentum.

### ***Normalised Streamwise Vorticity***

To investigate the influence of inflow energy on the wake structure of the trailing rider, the trailing rider velocity fields were corrected for a lower inlet velocity. The mean value of streamwise velocity was calculated from the streamwise cross section fields ahead of the trailing rider (as shown in Figure 5.2.11 & Table 5.2.1). Velocity fields were then normalised by these local values, rather than freestream velocity and streamwise vorticity recalculated from the new velocity fields. To quantitatively compare the magnitude of vorticity between the cases the peak (positive and negative) and mean vorticity was calculated for each of the identified hip and thigh vortices in both the symmetric and asymmetric wake cases. Peak and mean values were calculated within the vortex boundary area identified using the swirling strength criterion.

The resulting values of maximum and mean streamwise vorticity for the hip and thigh vortices for the single symmetric, symmetric-symmetric and asymmetric-symmetric cases are plotted in Figure 5.2.12. The asymmetric values are shown in Figure 5.2.13. Only hip vortices are plotted in the asymmetric case as thigh vortices are no longer distinct at that leg position. As the inlet velocity for the trailing

rider was only measured for the symmetric-symmetric case, the same value of inlet was used for all cases. This is an approximation, however, velocity values will be of the correct order and so provides a reasonable model for indicative trends in the vorticity.

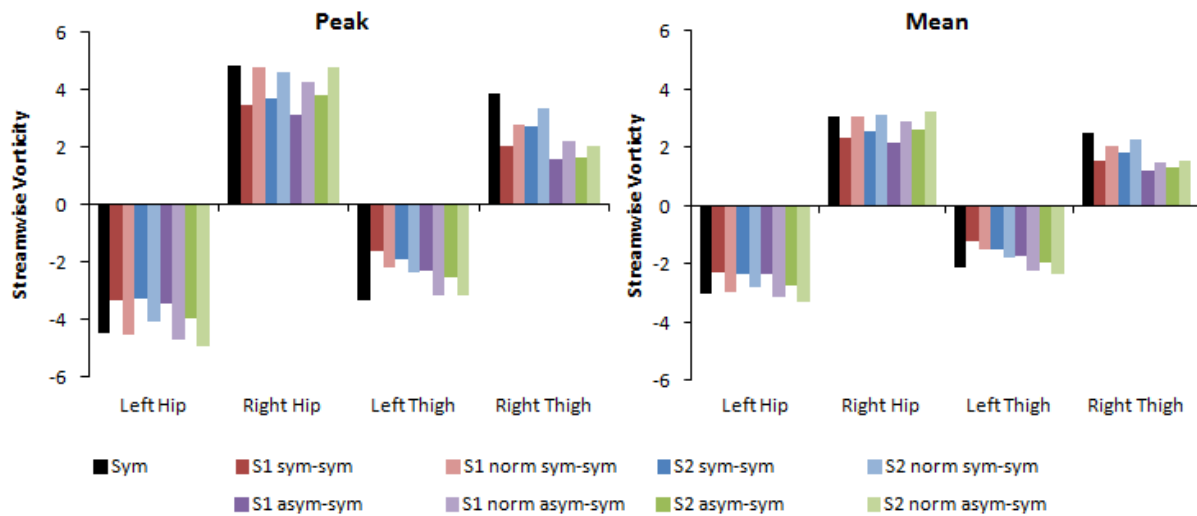


**Figure 5.2.12** – Peak (left) and Mean (right) vorticity magnitude in the primary vortices in the wake of a symmetric cyclist (at 15° crank angle). Values taken within vortex boundaries identified from swirling strength criterion. ‘norm’ refers to normalised vorticity, calculated from in-plane velocity fields normalised by trailing rider inlet velocity rather than freestream. S1 = Spacing 1, sym = symmetric, asym = asymmetric

In the symmetric cases, it can be seen that for the four identified vortices (Left & Right, Hip & Thigh), normalising the vorticity has resulted in an increase in both peak and mean vorticity. In the case of the hip vortices, normalising the inlet velocity has corrected the vorticity to be of the same order as the single rider result, on both the left and right. This suggests that the reduction in inlet streamwise velocity for the trailing cyclist accounts for a large portion of the loss in vorticity identified in the trailing rider hip vortices. However, in the case of the thigh vortices, the maximum and mean vorticity does not recover to the same level as the single rider wake. This indicates that there are other factors influencing the vorticity in addition to the reduction in streamwise velocity.

Results have shown that the flow approaching the trailing riders legs is not only reduced in streamwise velocity but also contains vorticity and in plane velocity components from the leader wake. Given that the inner thigh vortices are formed from flow separating on the inside of the legs, the combined effect of these changes will alter the formation and evolution of the thigh vortices which results in the complex changes observed in vorticity profiles; noting that spatial distribution of the thigh vortices varies as well as peak and mean vorticity. By comparison, the hip vortices result from interaction between flow over the hip and flow down the back. XZ centreline planes have shown that the flow down the back of the trailing cyclist is not significantly different from the single rider case. This results in smaller disruption to the hip vortices. The fact that vorticity calculated from locally normalised velocity fields is of similar order to the single rider wake shows that the streamwise losses are the main mechanism responsible for the reduced vorticity in the dominant hip vortices in the trailing cyclist wake. Tabulated values can be found in Appendix G.

In the asymmetric cases the large vortices are essentially the combining of the hip and thigh vortices. As such only the left and right hip vortices are identified in this analysis. Normalising vorticity shows a recovery in both peak and mean vorticity in the left vortices. However, a full recovery is not evident at either Spacing 1 or 2. This indicates that the reduction in streamwise velocity alone can not account for the losses in the wake and there is some influence from the disturbances in the inflow due to the lead rider. In contrast, the right hip vortex shows recovery of normalised vorticity closer to the single cyclist values, indicating that inlet energy accounts for much of the losses observed in the trailing cyclist wake.

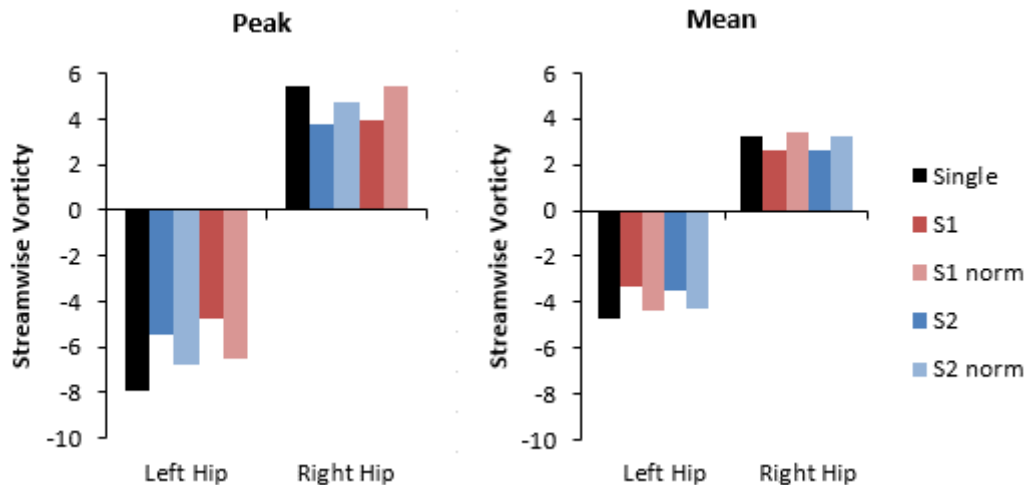


**Figure 5.2.13** – Peak (left) and Mean (right) vorticity magnitude in the dominant hip in the wake of an asymmetric cyclist (at 75° crank angle). Values taken within vortex boundaries identified from swirling strength criterion. ‘norm’ refers to normalised vorticity, calculated from in-plane velocity fields normalised by trailing rider inflow velocity rather than freestream. S1 = Spacing 1, sym = symmetric, asym = asymmetric

The normalisation of velocity fields by local inlet velocity is approximate as a constant mean reduction was used and consideration of in plane velocity components was not considered. However, the significant recovery of vorticity in the dominant hip vortices, shows that a large portion of the reduction in vorticity seen in the trailing rider wake is attributable to the reduction in inlet energy for the trailing cyclist in a tandem pair.

### Summary

The Reynolds number at which experiments were conducted was an order of magnitude lower than experienced by a real world cyclist. However, comparison with full-scale results show that the primary flow topology is not significantly affected, however a higher rate of diffusion of longitudinal vortex structures as they convect downstream is evident. It was concluded that this approach provides a valid representation of the flow field around a full-scale cyclist.

Profiles of streamwise vorticity in the wake of tandem cyclists have shown that the wake structure of a trailing rider in a tandem pair maintains similarity with that observed for a single cyclist. For both key flow regimes, at 15° and 75° crank angles, the hip vortices remain dominant in the wake of the

trailing cyclist. However, the magnitude of vorticity is reduced compared to the single rider case. By calculating vorticity from in-plane velocity fields normalised by local inlet velocity, rather than freestream, a significant recovery of peak and mean vorticity was observed in the hip and thigh vortices. This indicates that the reduction in the streamwise inlet velocity for the trailing cyclist is a major contributor to the observed reduction in vorticity in the wake.

For the trailing rider at  $15^\circ$  the hip vortices maintain similarity with the single rider profile. At small separation the inner thigh vortices were displaced downwards and away from the centreline due to the changes in the flow between the trailing rider's legs. With cyclist separated by 1 bicycle length (Spacing 2) the wake structure becomes increasingly similar to that seen for a single rider. This situation was expected as proximity to the leading rider will cause the inflow onto the second rider to contain greater vorticity and include greater cross-plane and fluctuating velocity components. At a bicycle length downstream, vortices from the leading rider wake lose coherence as vorticity diffuses and vorticity of opposite sign annihilates through cross diffusion. Increased separation also allows for greater streamwise energy recovery from the freestream, thus reducing impact on the trailing rider flow field.

Changing the leading rider leg position was found to not significantly alter the general wake profile of the trailing cyclist. The upper hip vortices remain the dominant feature of the wake; similar to the wake of a single cyclist. Thigh vortices exhibit a significant reduction in vorticity and at Spacing 1, are displaced away from the centreline. This is consistent with the symmetric-symmetric case. However, in the lower region of the wake there are some changes evident. A counter-rotating pair seen behind the right foot in the single rider case is absent. This appears to be due to cross-annihilation from vorticity formed on the leading rider extended leg. On the left side there is an additional counter-rotating vortex pair formed from interactions with flow from the leader wake. The changes to these vortices at the feet were seen to influence the interaction with the thigh vortices.

Crouch et al. showed that the dominant hip vortices are the result of large-scale separation from the torso and are a significant contributor to a cyclist's drag. The decrease in streamwise vorticity magnitude seen in the wake for a trailing rider may contribute to a reduction in the drag contribution associated with the formation of these trailing vortices. However, the primary trailing vortex structures, and even most of the secondary structures in the lower wake, are still present. Given this similarity to the single rider case it suggests that the drag reduction seen for a trailing cyclist is not solely attributable to a reduction in energy losses associated with these longitudinal vortex structures. Analysis of the streamwise velocity at inlet and outlet of each cyclist has shown that the velocity deficit over the trailing cyclist is significantly smaller than a single or leading cyclist. It is concluded that the reduction in streamwise momentum at the inlet is the major contributor to the drag reduction observed for a trailing cyclist. As distance between the leader and trailing cyclist increases, energy is recovered from the freestream, increasing the effective inflow velocity for the trailing rider and thus the drag saving is diminished.

### 5.3 Forward Interference Field of a Cyclist

The effect of a single cyclist on the upstream flow distribution was measured using a four-hole cobra probe and the mannequin. Figure 5.3.1 shows the variation of the velocity distribution ahead of the front wheel at a height level with the cyclist's nose (1160mm). Velocity values are normalised by the streamwise velocity of the empty tunnel at the bicycle leading edge ( $x=0$ ). Results show that beyond 500 mm the dynamic pressure returns to within 1.5% of the freestream value. The variation of dynamic pressure is also presented as a dynamic pressure coefficient referenced to the empty tunnel dynamic pressure and normalised by freestream dynamic pressure. A decrease in dynamic pressure was observed immediately upstream of the cyclist with velocity below freestream conditions, which will cause a corresponding increase in static pressure. The dynamic pressure reduction was highest at the centreline and reduced as the lateral offset was increased.

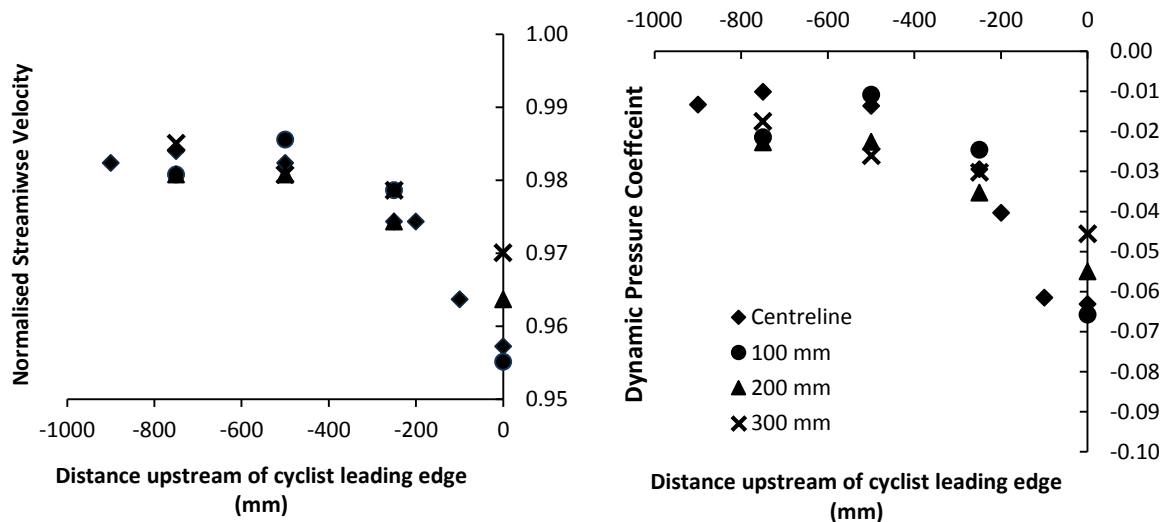


**Figure 5.3.1** – (left) Normalised streamwise velocity distribution ahead of a cyclist measured from the leading edge of the front wheel. Series refer to lateral offset from centreline. Measurements taken at nose height of mannequin (1160mm above ground).

The static pressure field upstream of the cyclist reflects the interference pattern seen for dynamic pressure. Immediately upstream of the cyclist there is a local increase in the static pressure coefficient above freestream conditions (see Figure 5.3.2). Pressure coefficient is referenced to the static pressure in the empty tunnel at the cyclist leading edge, and normalised by freestream dynamic pressure. Static pressure coefficient decreases and asymptotes as distance upstream of the cyclist is increased. Similar to the dynamic pressure, the static pressure coefficient approaches an asymptote beyond 500 mm ahead of the cyclist. Results show that total pressure ahead of the cyclist remains constant (within 1%). At 100 mm lateral displacement from the rider centreline there is minimal change from the centreline profile. However, at 200 and 300 mm there is a reduction in static pressure, indicating reduced interference from the cyclist.

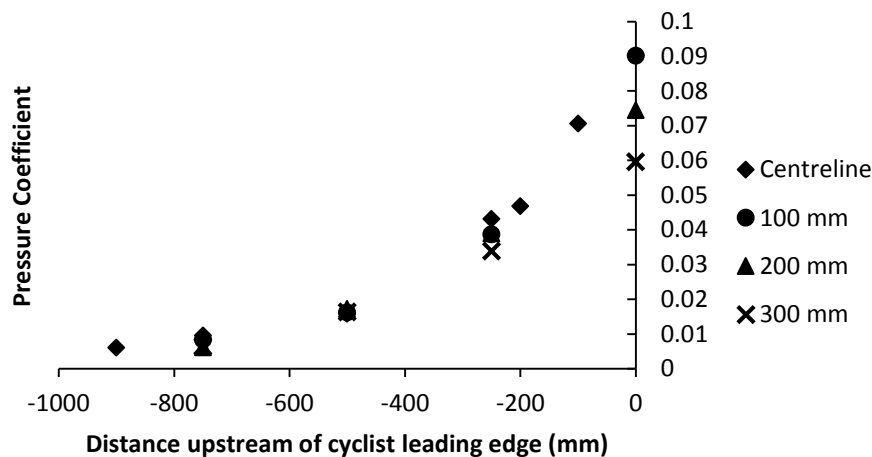


**Figure 5.3.1** – Pressure coefficient ahead of a cyclist measured from the leading edge of the front wheel. Series refer to lateral offset from centreline.

The streamwise velocity and pressure results show that a cyclist has an interference field that extends a small distance upstream. Within 500mm of the front wheel leading edge there is a decrease in velocity and an increase in static pressure. Beyond 500mm in front of the wheel leading edge this effect is negligible, with streamwise velocity recovering to within 1.5% of freestream.

Applied to a tandem formation the static pressure increase will impact on the rear of the leader, causing an increase in base pressure. This will effectively decrease the static pressure gradient over the lead rider, resulting in lower drag. This is analogous to the corrections necessary to account of longitudinal pressure gradients in the wind tunnel, as described in Section 2.2. Applying the maximum change in pressure coefficient (0.09) to the pressure gradient acting over the cyclist can be estimated to induce a change in the cyclist  $C_{DA}$  by approximately  $0.01 \text{ m}^2$ . This value was calculated using the method for horizontal buoyancy corrections outlined in Section 2.2. This change in  $C_{DA}$  is equivalent to a 5% reduction in drag for the mannequin, which is consistent with drag measurements in the wind tunnel (Section 4.1) reporting a lead rider drag reduction of 2.5 - 5%.

Velocity contours from scale model testing showed that there was a decrease in streamwise velocity behind the lead rider in a tandem pair compared to the single rider wake. This was of the order of 3% of the freestream velocity. Considering the results in Figure 5.3.1 above, velocity upstream of the isolated cyclist also decreased of the order of 3% of freestream. Given this behaviour for the full scale cyclist it can be concluded that the velocity deficit seen in the wake of the lead cyclist in a tandem pair is due to upstream interference from the trailing rider. It is noted that the scale model flow was measured using PIV and so pressure data could not be collected.

## **5.4 Wake Topology of Dynamic Athletes**

This section presents the results of wake analysis of a dynamic cyclist in single and tandem formations. This provides an important comparison to the reduced Reynolds number studies presented in 5.2 above. Not only does it test athletes as full scale Reynolds numbers, but also introduces the dynamic leg motion, inherent in all practical cycling cases. Whilst it has been suggested that the wake flow of a cyclist can be adequately modelled using a quasi-static approach, there remains little investigation of the full dynamic problem. Furthermore, the reduced Reynolds number results only cover the two characteristic flow regimes and not a full crank cycle of leg angles. To investigate with full realism it is therefore necessary to test pedalling athletes. Due to the limited investigations of aerodynamics of a dynamic cyclist, the single case was first investigated to provide a reference case for the tandem formation.

### **5.4.1 Time Average Wake Profiles**

A four-hole pressure probe was used to characterise the wake of a dynamic cyclist in isolation and in a tandem formation with minimum practical separation (100 mm) between riders. Flow field results for the scale model cyclists (Section 5.2) showed that as separation distance increases, the trailing rider wake more closely resembles the single rider wake profile. Given that the maximum drag reduction and greatest change in the wake flow occurs at the minimum separation distance, this is the critical case, as it will exhibit greatest change from the single rider. Scale results showed that the primary hip vortices in the trailing rider wake are not greatly influenced by changes in the lead rider wake profile resulting from leg position. It was therefore reasonable to use the mannequin as the lead cyclist (static at 15° crank angle) and a dynamic athlete as the trailing cyclist for the tandem formation.

Time averaged results were collected to investigate the effects of interactions on the wake of a pedalling athlete. The streamwise velocity profiles for the single rider and the trailing rider in the tandem pair are shown in Figure 5.4.1 below. Wake profiles are generated by linearly interpolating from the probe measurement points.

The single rider result shows that the time averaged wake of a cyclist is symmetric. Given the periodic nature of the leg motion when pedalling, this result is not unexpected. The tandem wake is also largely symmetric. However, there is an asymmetry observable around hip height ( $z = 1.2$  m). The most likely reason for this asymmetry is that testing is being conducted on a human subject and so some degree of asymmetry is to be expected. Given that the effect is more pronounced in the trailing rider result than the single rider case, it appears that the rider being in the wake of the leader is magnifying the asymmetry. It will be shown in subsequent results that this asymmetry is only prominent in the streamwise component of velocity. Therefore this asymmetry does not significantly detract from conclusions drawn from this data.

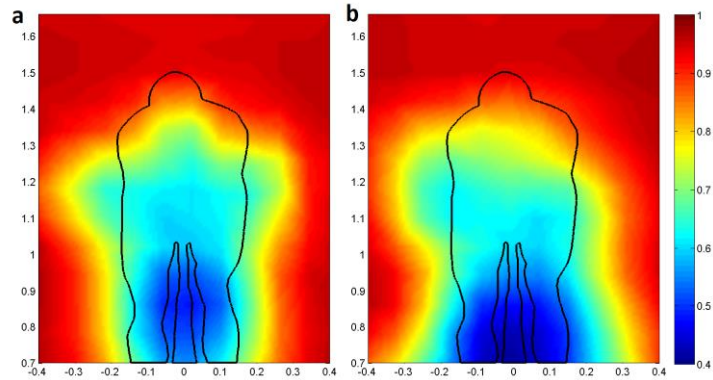


**Figure 5.4.1** - Time averaged normalised streamwise velocity in the wake of (a) a single pedalling cyclist, (b) a tandem pair with dynamic athlete in trailing position

Figure 5.4.2 shows the streamwise velocity profiles in the wake of the scale models previously presented in Section 5.2. These results also show that there are some differences between the single and tandem wakes. Overall the two profiles remain largely symmetric; however, the distribution is different. This symmetry confirms that the interactions are not inducing an asymmetry in the trailing rider wake. The tandem wake shows a smaller peak velocity deficit but an increase in width in the lower region of the window compared to the single rider. The dynamic athlete results also show that the velocity deficit in the lower region of the tandem wake is wider compared to the single rider case. However, in the dynamic case the trailing rider has greater peak velocity deficit, differing from the static model case. This can be explained from an understanding of the difference in the flow structure for the static and dynamic leg cases. With legs static at  $15^\circ$  the velocity deficit in the wake is at a minimum, compared to other positions around the crank cycle. By introducing dynamics, the legs will now pass through all angles, thus including the asymmetric regimes, which have been shown to have greater losses in streamwise velocity (Crouch et al. 2012, 2014). Therefore, time averaging the dynamic wake can be expected to result in a lower mean velocity compared to the result for static cyclists at  $15^\circ$  crank angle.

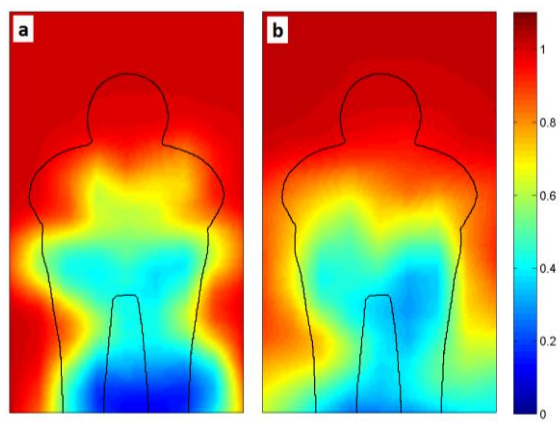


**Figure 5.4.2** - Normalised streamwise velocity in the wake of a single (left) and tandem trailing cyclist (right). Results are for a static model cyclist at a crank angle of  $15^\circ$  taken from previous scale model results (Section 5.2.4)

The time averaged streamwise velocity results indicate that there is not a significant difference in streamwise velocity deficit behind the hips (above  $z = 1.0$  m), where the dominant vortices have been shown to occur. This is consistent with the quasi-static assumption of Crouch et al., who showed that the streamwise velocity behind the hips and back does not vary greatly with leg position. As described above, the greater velocity deficit in the lower wake is consistent with static profiles when considering the full crank cycle, as the asymmetric regimes result in greater deficit in the lower wake.

Mean streamwise velocity in the wake was calculated and is presented in Table 5.4.1. This process is dependent on the averaging area and so provides a comparison between single and tandem cases, rather than a true representation of the wake profile. Calculating the mean velocity component over a common interrogation window for both data sets returns values of 0.76 and 0.71 for the pedalling athlete wake traverse in single and tandem formations respectively and 0.79 and 0.76 from the scale model in single rider and tandem formations. The trailing rider wake was found to have a reduction in mean streamwise velocity compared to the single rider case in both dynamic athlete and static scale model tests. As previously discussed this is contributed by the large reduction in inlet velocity upstream of the trailing rider. The lower velocity in the wake is not indicative of total energy losses as the deficit over the rider is far smaller than the single rider case. However, it does confirm the trends of the scale model tests.

**Table 5.4.1** - Mean streamwise velocity in the wake of a cyclist. Comparison between static scale model results and wake traverse of a pedalling athlete taken over a common interrogation window.

	<i>Mean Velocity</i>	
	<b>Athlete</b>	<b>Scale Model</b>
Single Rider	0.76	0.79
Tandem Trailing Rider	0.71	0.76

The mean velocity for both pedalling cases is lower than that of the static scale models. This is the result of the differences in the leg dynamics, with the scale models being static at  $15^\circ$  crank angle. As discussed earlier (Section 3.1), the drag of a dynamic cyclist is greater than for a static cyclist at  $15^\circ$ . This is linked to the fact that the dynamic drag encompasses the large portion of the crank cycles where legs are positioned asymmetrically and have high drag. The asymmetric leg positions which correspond to high drag also correspond to a greater deficit in streamwise velocity. A time averaged dynamic wake should therefore have lower streamwise velocity than a static case with the rider's legs at  $15^\circ$ .

The difference between single and tandem mean velocity also differs between the two cases. This is likely a function of both the leg dynamics and the differences in the geometry of the two sets. However, the results show the same trend and confirm that mean velocity in the trailing rider wake is lower than the single rider case. This indicates that drag reduction for the trailing cyclist is not the result of a disruption to the trailing rider wake that facilitates streamwise energy recovery in the wake.

During these test runs drag measurements were also recorded for both athletes using the multi-rider air bearing rig. This reported a 5% drag reduction for the lead rider and 40% for the trailing rider. These values are of equivalent order to those reported previously in Section 4.1. The fact that the tandem wake had the lower mean wake velocity confirms that the drag reduction experienced by the trailing

rider is not due to a recovery of energy in the cyclist wake but is dominated by the upstream sheltering effect.

Profiles of streamwise vorticity in the wake of a single and trailing tandem cyclist are shown in Figure 5.4.3 below. It is important to note that because the vorticity is calculated from the time averaged wake of a pedalling cyclist, they will not resemble the wake profiles presented previously for static cyclists. As such it is unsurprising that coherent vortices are absent from the wake. Peak vorticity in the single case was 0.70 and -0.50 for positive and negative vorticity and 0.83 and -0.58 in the tandem wake. This is greatly reduced compared to that previously seen in the scale model results. In the symmetric case ( $15^\circ$  crank angle) peak vorticity in the single rider wake was 4.86 and -4.48 for positive and negative vorticity respectively, and 3.49 and -3.33 in the trailing case. This highlights the lack of coherent structures when averaging the wake over the full crank cycle. However, the results show that the streamwise vorticity profiles in the wake of the single and tandem trailing riders is similar. Both exhibit a symmetric profile about the centreline with a negative region extending over a large region of the left side of the centreline and a mirror on the right side with positive vorticity. The sign and location of these concentrations of vorticity are consistent with previously observed flow structures for static cyclists. Negative vorticity is generated from the left hip vortex and positive from the right. Given the much lower peak vorticity in the time averaged dynamic wake profiles, the small difference between the single and tandem cases are not significant.

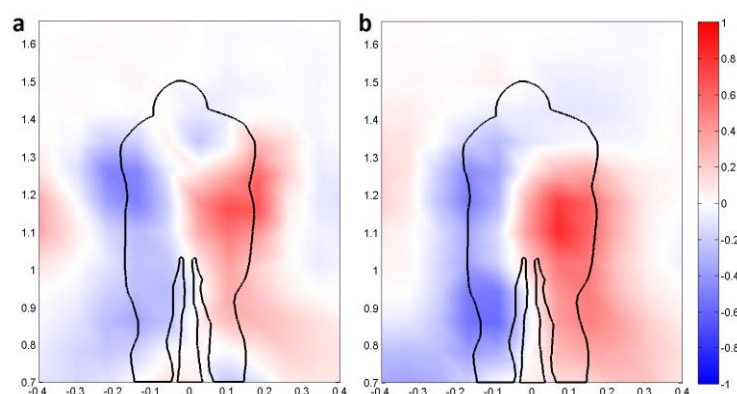


**Figure 5.4.3** – Non-dimensional streamwise vorticity in the time averaged wake of a single pedalling cyclist (a) and a trailing pedalling cyclist in a tandem formation (b)

The wake of a pedalling cyclist oscillates between the two opposing asymmetric flow regimes as each leg is raised and lowered respectively while passing through the symmetric profiles every half cycle. The time averaged wake is not expected to show a distinct vortices, but will show regions where vorticity is present in the wake as an average for all leg positions. From static results it is observed that the sign of vorticity for each hip vortex is constant around the crank cycle, however the position changes. The two hip vortices will oscillate up and down behind the hips. As reference the two most asymmetric profiles identified by Crouch et al. (2014) for the mannequin are presented in Figure 5.4.4 below. The time averaged vorticity profiles in Figure 5.4.3 (above) follow this logic, as they show regions of vorticity of opposite sign either side of the centreline. Importantly the profiles are both symmetric due to the periodic nature of the changes in the wake.

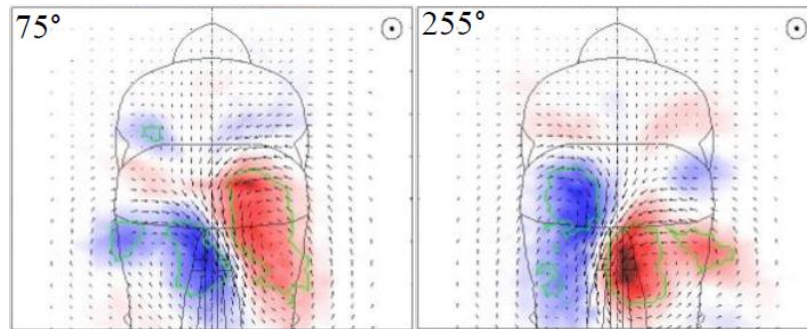


**Figure 5.4.4** - Streamwise vorticity in the wake of the Monash anthropomorphic cycling mannequin at crank angle positions of 75° (left) and 255° (right). (Crouch et al. 2012)

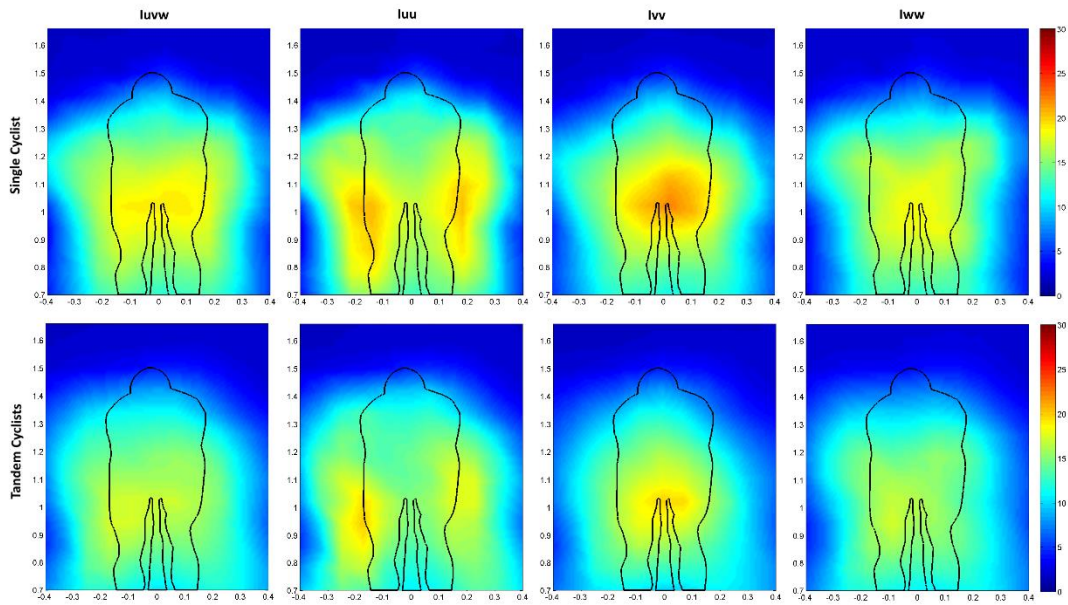
The symmetry in the vorticity profiles is consistent with expectation as any change in the wake structure should be symmetric due to the periodic nature of the changing wake structure. This confirms that the relatively small asymmetry observed in the streamwise velocity profiles (Figure 5.4.1) is not a dominant feature and is not a physical mechanism induced by the interaction effects. As vorticity is a stronger indicator of the coherent vortex structures in the wake, this provides good confirmation that the single and tandem wakes maintain similarity. This is consistent with the outcomes of the scale model testing, thus indicating that scale model testing can provide useful insight for full scale cyclist applications.

Figure 5.4.5 shows the turbulence intensity ( $I_{UW}$ ,  $I_{UU}$ ,  $I_{VV}$ ,  $I_{WW}$ ) in the wake of the single and trailing rider(s), where fluctuations have been normalised by freestream rather than the local mean component. Figure 5.4.6 then shows the same series of figures but with fluctuations normalised by the local mean velocity. Normalising fluctuations by the local flow component results in higher turbulence intensity for all cases due to the velocity deficit in the rider wake. Comparison of the sets for the single and tandem wakes reveals a general similarity in the distribution of turbulence and with symmetry about the cyclist centreline. It is seen that fluctuations for each component of the velocity are of similar magnitude, with no one component dominating. However, a difference in distribution is evident. In the streamwise component ( $I_{UU}$ ) the maximum turbulence intensity is concentrated towards the side of the rider at the hips. The spanwise component ( $I_{VV}$ ), meanwhile, is concentrated in the centre of the wake behind the rear of the rider. The vertical component ( $I_{WW}$ ) shows turbulence centred behind the rider and extending up to the top of the hips.

Comparing the freestream normalised profiles (Figure 5.4.6), it is seen that there is a slight decrease in the turbulence intensity in the tandem wake. Maximum and mean values for each profile in Figure 5.4.5 and 5.4.6 are shown in Table 5.4.2 below. This is counter-intuitive given that the trailing cyclist is exposed to inlet conditions with much higher turbulence compared to a single or lead rider that encounters freestream conditions. With turbulence intensity based on the local velocities, this scenario is reversed, with the tandem wake exhibiting slightly higher turbulence. However, this is due to the lower velocity observed in the trailing cyclist wake. From this it can be concluded that the loss in energy at the inlet for the trailing rider results in smaller fluctuating components downstream in the wake and thus the lower turbulence intensity.

**Table 5.4.2** – Maximum and mean values of Turbulence Intensity in the wake of single and tandem cyclists showing values based on freestream and local mean velocities.

		Freestream Normalised				Local Normalised			
		luvw	luu	lvv	lww	luvw	luu	lvv	lww
Single	Maximum	19.2	20.5	22.1	18.3	30.7	30.6	33.6	31.2
	Mean	9.6	10.3	9.4	9.0	12.8	13.6	12.6	12.0
Tandem	Maximum	17.4	20.0	19.7	17.4	31.7	30.4	33.6	31.9
	Mean	9.1	9.9	8.6	8.6	13.2	14.2	12.6	12.5



**Figure 5.4.5** - Turbulence intensity (%) in the wake of a single pedalling cyclist (top), and a tandem pair (bottom) with pedalling rear athlete. Turbulence intensity corrected to freestream flow velocity.

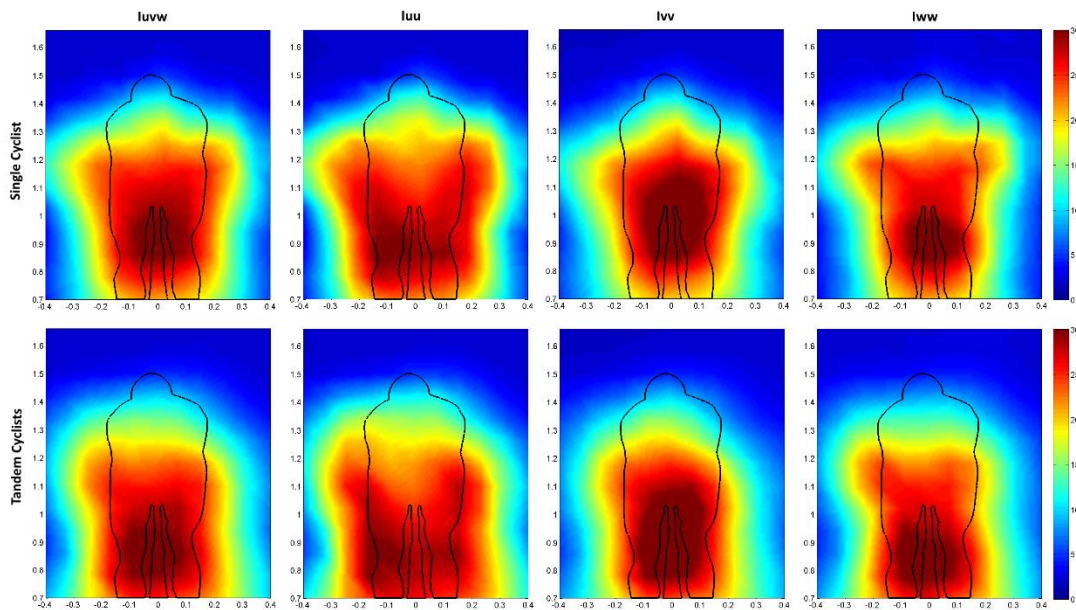


**Figure 5.4.6** - Turbulence intensity (%) calculated from local flow velocity in the wake of a single pedalling cyclist (top), and a tandem pair (bottom) with pedalling rear athlete. Turbulence intensity corrected to freestream flow velocity.

The spanwise velocity component ( $V$ ) also exhibits strong similarity in distribution between the single and tandem cases (see Figure 5.4.7). Positive values indicate flow from left to right of the plane. Despite the periodic nature of the pedalling cyclist there is a distinct cross flow component present in the time averaged wake of both cases. Though there is an apparent division down the centreline of the athlete there is a slight bias with the positive region of velocity on the left side of the profile being slightly larger than that on the right. It is noted that the scale on these profiles is only 10% of the freestream velocity and so the difference from right to left side of the wake is small; being of the order of 2% of the freestream. This is within the expected range for testing with an athlete. The small magnitude of the time averaged results is expected given the wake profiles seen for a static cyclist (Crouch et al.). This showed that as the legs move away from level there is a large cross stream component of velocity introduced in the wake. As these results are time averaged, the cross flow induced as each leg is raised will be oscillate about the zero point. As such, it is unsurprising that the mean cross flow component for both the single and trailing cyclists is of a small magnitude. A slight increase in the magnitude of spanwise velocity (of both signs) is evident across the tandem profile. This increase in cross flow is likely the result of the higher cross stream velocity components at the inlet for the trailing rider and this persisting downstream of the rider.

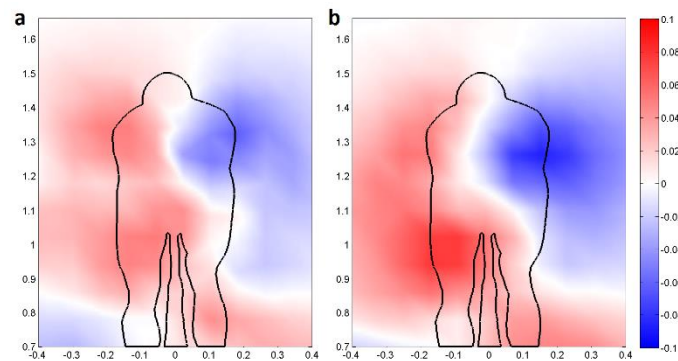


**Figure 5.4.7** - Time averaged normalised spanwise velocity component in the wake of (a) a single pedalling cyclist, (b) a tandem pair with pedalling rear athlete

Figure 5.4.8 shows profiles of the vertical component of velocity ( $W$ ) in the wake of a single and tandem cyclist formation. Negative values (blue) indicate downwards direction of flow. For both the single and tandem cases a strong downwash dominates the centre of the wake region, with wake being symmetric about the centreline. The presence of a strong downwash in the dynamic wake is consistent with the quasi-static assumption applied to cyclists at static leg positions. At all leg positions there is a flow component down the back of the rider that separates from the hips and induces a downwash in the wake. As alternate legs are raised there is an oscillation in the flow from left to right. However, the vertical component is constant, regardless of which leg is raised. This results in a strong vertical component of velocity present throughout the majority of the crank cycle and therefore strongly present in the time averaged results.

The tandem wake exhibits an increase in the downwash component; both strength and size of the region compared to the single rider wake. This is likely the result of the inflow conditions for the trailing cyclist. From the single rider profile it can be concluded that travelling in the wake of another cyclist will result in the observed inflow conditions having a strong vertical velocity component. The

persistence of this downwash in the flow downstream into the wake of the trailing rider is the likely reason for this increase. The presence of a strong vertical component ahead of the trailing rider was also previously observed in scale model tests (Section 5.2).

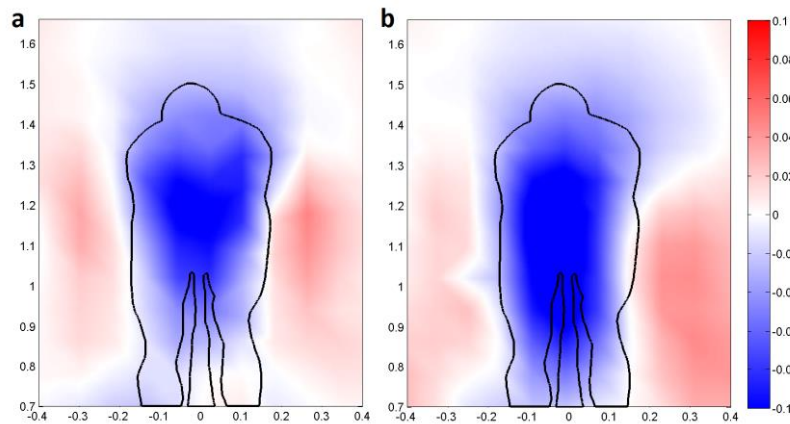


**Figure 5.4.8** - Time averaged normalised vertical velocity component in the wake of (a) a single pedalling cyclist, (b) a tandem pair with pedalling rear athlete. Negative (blue) indicates downwards

The drag of a model can be calculated from quantitative wake survey data through application of the integral momentum equation over a control volume. This technique is based on the work of Betz (1924) and Maskell (1972) and has been further refined by numerous authors since, such as Brune (1994) and Kusunose (1997). Applying the momentum integral equation to a control volume over a model in the wind tunnel, the drag can be calculated by considering the stagnation pressure deficit, streamwise kinetic energy deficit and the transfer of energy to the cross flow components;

#### 5.4.1

$$D = \iint_{Wake} (P_{T\infty} - P_T) ds + \frac{\rho}{2} \iint_S (U_\infty^2 - U^2) ds + \frac{\rho}{2} \iint_S (V^2 + W^2) ds$$

In this integral the stagnation pressure integral is calculated only in the wake of the model, as stagnation pressure is constant outside the wake. However, the velocity integrals are evaluated over the entire control surface, which in this case is the wind tunnel cross section, and not only the measurement region behind the model.

This equation can be modified to only consider the streamwise velocity within the wake region by introducing the term  $U^*$ ;

$$U^{*2} = U^2 + \frac{2}{\rho}(P_{T\infty} - P_T)$$

The drag of a model is now rewritten in terms of  $U^*$ :

$$D = \iint_{Wake} (P_{T\infty} - P_T) ds + \frac{\rho}{2} \iint_{Wake} (U^* - U)(U^* + U - 2U_\infty) ds + \iint_S (V^2 + W^2 - u'^2) \quad 5.4.2$$

Where  $u'$  is the perturbation velocity;  $u' = U^* - U_\infty$

In this case the final term is called the induced drag or vortex drag term but is calculated over the full cross section, not only the wake region. Given that this is the drag due to the cross flow components

induced by the model, it is assumed that the contribution to model drag from outside the wake interrogation region is small. As such this integral was calculated over only the wake region where values were surveyed, and not over the full tunnel cross section. By normalising Equation 5.4.2 by the freestream dynamic pressure this equation can be used to determine the drag coefficient area ( $C_{DA}$ ). These values are presented in Table 5.4.3 below.

**Table 5.4.3** - Output from wake integral approach (Equation 5.4.2) including contribution from each term. Tandem\* modified integral; trailing rider inlet modelled as the single rider wake.

	<b>Force Balance</b>	<b>Wake Integral</b>	<b>Pressure Term</b>	<b>Streamwise Velocity Term</b>	<b>Induced Drag Term</b>
Single Rider	0.231	0.1731	0.2181	-0.0468	0.0018
Tandem	0.139	0.1996	0.2634	-0.0671	0.0033
Tandem*	0.139	0.0321	0.0326	-0.0043	0.0038

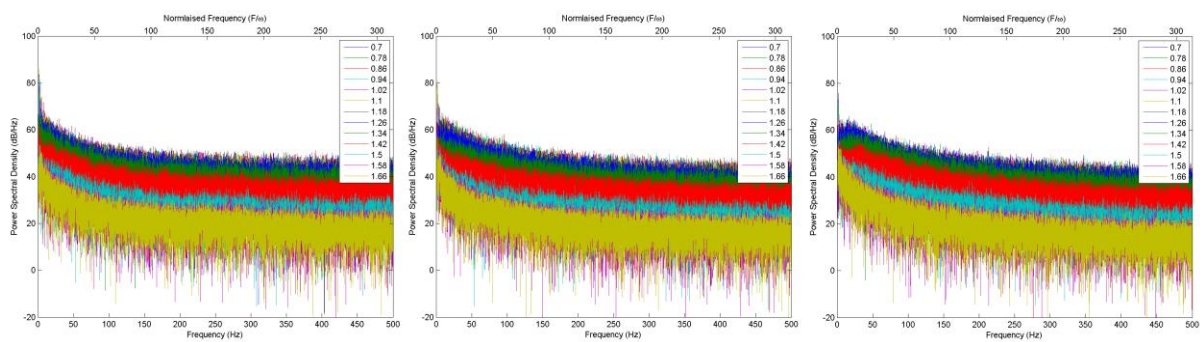
Table 5.4.3 shows that the wake integral significantly under predicts the drag acting on a single cyclist. This is unsurprising given that the interrogation region does not capture the full wake region of the cyclist. It is also noted that the induced drag term contributes very little to the total drag acting on the cyclist; the majority is due to the stagnation pressure defect. Given the previously identified large scale vortex structures in the wake of a cyclist it could be expected that there would be a significant induced drag component. However, as this integral has been applied to only the time averaged wake the oscillating nature of the wake structures observed in quasi-static investigation means that vorticity is less concentrated than for planes behind a static cyclist or instantaneous snapshots for a dynamic cyclist.

Despite the simplifications of this technique, it was anticipated that it could still be used for relative comparison with the trailing cyclist wake. However, results in Table 5.4.3 suggest that the drag of the trailing cyclist is actually greater than the single cyclist. This is due to the nature of the development of the integral, which assumes freestream inlet conditions. As shown previously, the streamwise velocity ahead of the trailing cyclist is significantly lower than freestream. As such, the momentum drop over the trailing rider is smaller resulting in decreased drag. To approximate the change in inlet conditions for the trailing rider, the integral was modified with the freestream terms replaced with the values from the single rider wake. Previous results with the scale model cyclist showed that the wake of the leader in a tandem pair at this spacing is not identical to the single rider case. However, the difference between the two is relatively small and represents a far smaller error than using freestream conditions as inlet for the trailing cyclist. The Tandem\* value in Table 5.4.3 represents the outcome of the integral using the single rider wake as inlet conditions. It is seen that the modified integral significantly under predicts the trailing cyclist drag. This is consistent with the single rider results and follows the same limitations of a truncated wake capture region and the time averaged nature of the field. However, it shows that changing the inlet conditions for the trailing rider do significantly reduce the drag calculated. Considering the change in drag between the single and trailing riders, the integral value is of the same order to the difference measured using the force balance. This shows the significance of the change in inflow conditions to the trailing cyclist drag. This is further evidence that it is the change to the inlet conditions, particularly reduction in streamwise momentum that is the dominant mechanism responsible for the trailing rider drag reduction.

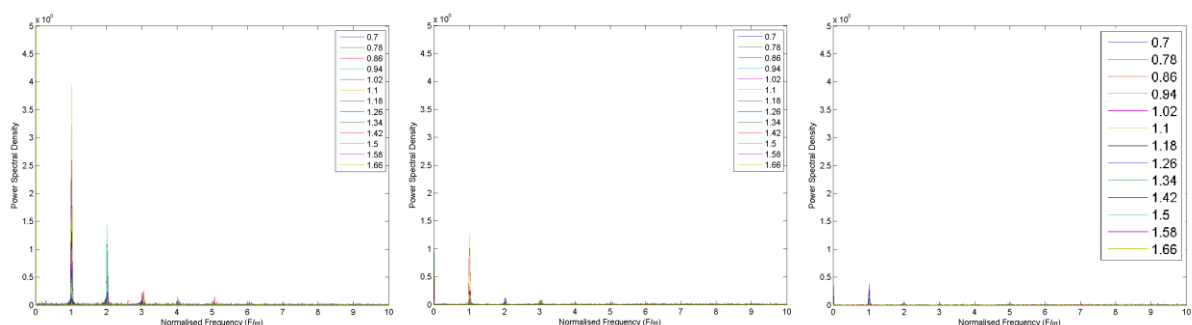
The fact that the trailing rider drag calculated using the standard equation is greater than the single rider result shows that streamwise momentum in the trailing rider wake is lower than the single rider case. It has been shown that this is erroneous as a representation of drag, as the trailing rider has significant lower upstream momentum compared to the single rider case. However, this does quantitatively show that the drag reduction for the trailing rider is not linked to energy recovery in the trailing cyclist wake. This further confirms the contention that drag reduction is dominated by upstream effects.

## 5.4.2 Spectral Analysis of the Dynamic Wake

As the geometry of a pedalling cyclist is dynamic it is of interest to also consider the time varying behaviour of the wake flow. For each sample point in the interrogation window the frequency content of the flow was analysed by computing the power spectrum. Figure 5.4.9 shows a sample of the full power spectrum for a series of points in the wake of a single cyclist in each of the three velocity components (normalised by freestream). Each series represents a single measurement point in the wake. This group of 13 individual spectra represent a vertical line in the wake taken at  $y = -0.16$  m; behind the cyclist's hip. Each point is separated in the vertical by 0.08 m from  $z = 0.7$  m. At this scale there are no clear concentrations of power in the spectrum evident. However, when looking at the lower end of the frequency spectrum there are distinct concentrations of power visible (see Figure 5.4.10). These peaks are observed at the same frequencies in each of the three components of velocity, although they are greatest in the streamwise component (U). In Figure 5.4.10 the frequency has been normalised by the cyclist cadence ( $\omega$ ); where  $\omega = 1.59$  Hz and 1.54 Hz for the single and tandem tests respectively. Cadence was averaged over the full sample period.



**Figure 5.4.9** – Sample power spectral density for the three components of velocity (L-R: U, V, W). Each figure shows a vertical series of sample points at  $y = -0.16$  m from  $z = 0.7 - 1.66$  m.



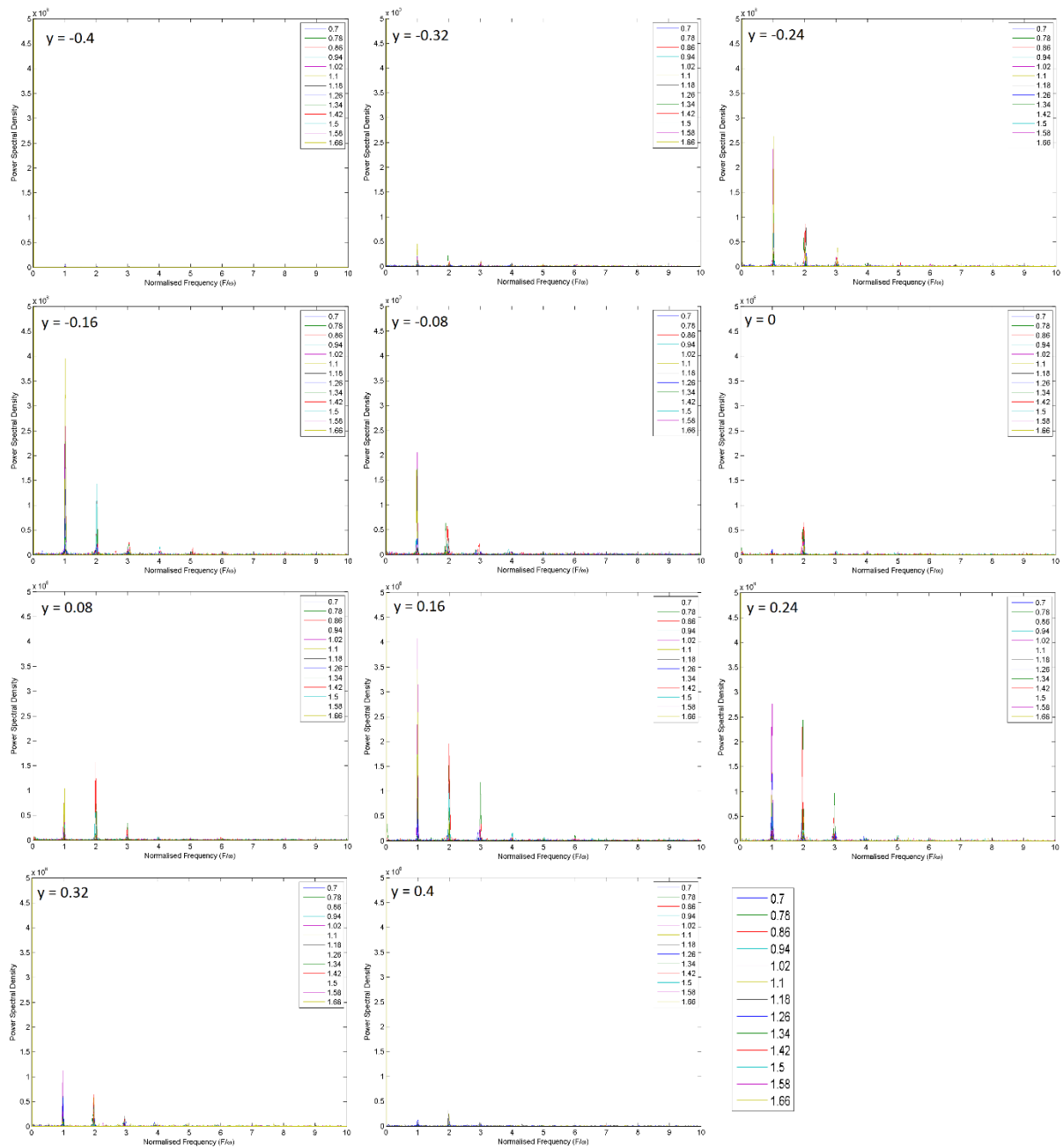
**Figure 5.4.10** – Sample power spectra for the three components of velocity (L-R: U, V, W) showing only the low end of the frequency spectrum. Frequency normalised by pedalling cadence ( $\omega$ ). Each figure shows a vertical series of sample points at  $y = -0.16$  m from  $z = 0.7 - 1.66$  m.

Figure 5.4.11 shows the complete set of power spectra for the streamwise (U) velocity component in the wake of a single cyclist, with the tandem spectra in Figure 5.4.12. Each figure shows 13 individual spectra that form a vertical line in the cyclist wake. As such, each individual figure represents a lateral step across the wake. The V and W velocity power spectra are provided in Appendix H.

The same frequency components emerge from many of the measurement locations in the wake. The lowest frequency is dominant across many of the points in the cyclist wake spectra with a peak occurring at the pedalling cadence ( $F = \omega$ ). Two additional peaks in the power spectrum are also consistently evident at two higher frequencies;  $2\omega$  and  $3\omega$ . These correspond to higher order harmonics above the fundamental frequency of the cyclist's cadence. Given that the large scale structures observed in the wake of a cyclist have been shown to vary with crank angle, it is not surprising to see that the fluctuating energy is dominated by the cadence of the cyclist.

It can be seen that the same spectral distribution is common to both the single and tandem rider wakes. Whilst pedalling cadence varied slightly between the tests, it is observed that the peaks in the power spectrum occur at the same normalised frequency correlating to the first three modes of the cyclist cadence. Static results showed the significance of the leg position in formation of the primary hip vortices. Scale model tests (Section 5.2) have confirmed that these structures persist in the wake of a trailing cyclist. It follows then that both the single and tandem cases exhibit the same dominant frequency components corresponding to the pedalling cadence. Whilst the frequency components are consistent in both the single and tandem wakes, the tandem wake has a reduction in amplitude at each of the key frequencies identified. This indicates a reduction in the fluctuating energy. This reduction is likely the combined result of the reduced streamwise energy seen by the trailing cyclist in addition to greater turbulence. This will reduce the energy in the flow and result in a broader distribution of energy in the trailing wake. This is consistent with static scale model wake profiles (Section 5.2) which showed some reduction in vorticity in the primary hip vortices for a trailing cyclist, particularly at minimum separation.

It is observed that the frequency spectra are not equal for at all points in the wake. To highlight the spatial distribution of the fluctuating energy the maximum amplitude was plotted for each of the three dominant frequencies observed in the individual spectra. For each sample point in the interrogation window the maximum amplitude was identified at  $1\omega$ ,  $2\omega$  and  $3\omega$  for the single and tandem cases. From this a spatial contour could be generated to highlight the spatial distribution of fluctuating energy in the wake. The distribution of maximum fluctuating energy for each of the three identified frequencies in the wake of a single and tandem cyclist(s) are shown in Figure 5.4.13, 5.4.14 and 5.4.15 for the streamwise (U), spanwise (V) and vertical (W) components of velocity respectively.



**Figure 5.4.11** – Power spectral density of the streamwise component of velocity (U) for each point in the interrogation window in the wake of a single pedalling cyclist. Data recorded with a cobra probe from discrete points in a wake survey. Series refer to vertical position with  $z = 0.7 - 1.66$  m.

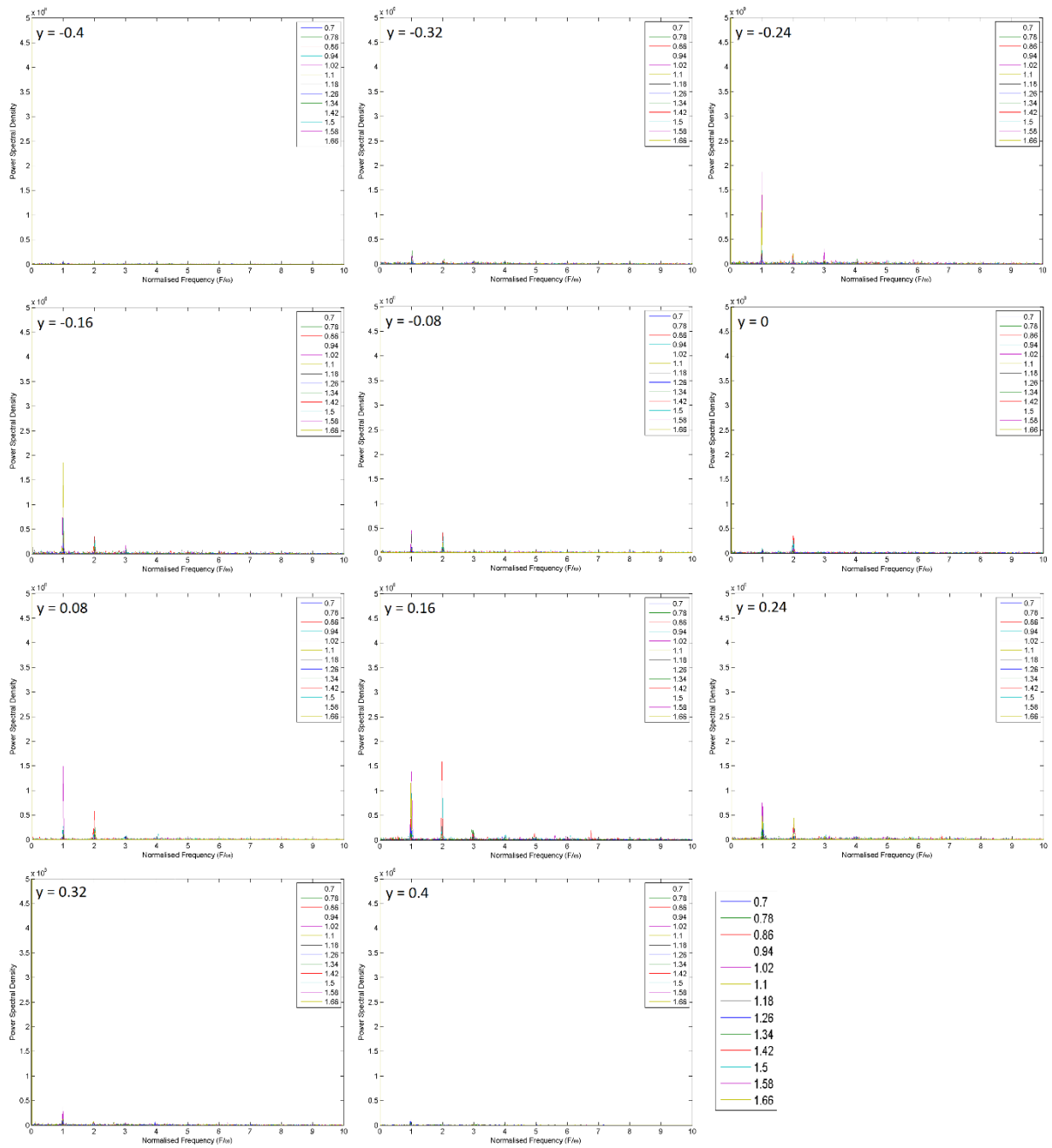


**Figure 5.4.12** – Power spectral density of the streamwise component of velocity (U) for each point in the interrogation window in the wake of a trailing pedalling cyclist in a tandem formation at minimum separation. Data recorded with a cobra probe from discreet points in a wake survey. Series refer to vertical position with  $z = 0.7 - 1.66$  m.

The distribution of fluctuating energy in the streamwise component of velocity in the wake of single and tandem cyclist(s) is shown in Figure 5.4.13. At the pedalling cadence ( $\omega$ ) the profile is symmetric about the centreline with two high energy regions located behind either hip of the rider. This is due to the movement of the dominant hip vortices, whose size and location have been shown to vary as the legs cycle around the crank. It is therefore unsurprising that the highest energy content for any of the velocity components or frequencies corresponds with the cadence frequency. Not surprisingly this distribution is similar in shape to that seen for the turbulence intensity in the streamwise component ( $I_{UU}$ ) with concentrations behind the hips. At  $2\omega$  the profile is also symmetric but the highest energy regions are lower down in the wake behind the upper leg/knee. The change in the distribution suggests that these peaks are linked to different phenomenon. Given the physiology of a cyclist and the location, it is suggested that this energy is associated with the changing direction of the leg, as this process is occurring twice each crank revolution. A small bias is evident to the lower left region. This is most likely the result of a slight asymmetry in the athletes positioning and pedalling style. The high energy content behind the hips is no longer a dominant feature, further indication of a different process. At  $3\omega$  the magnitude of fluctuating energy is greatly reduced and regions are far less pronounced. However, fluctuating energy is still evident in the region behind each hip and leg resulting from pedalling motion of the legs. Despite the less distinct energy concentrations in this profile, the individual power spectra show that this frequency, at certain points in the wake, still contains fluctuating energy that is above background levels, although nearly an order of magnitude lower than peak energy at  $F = \omega$ . Given the gross nature of the leg motion it is unsurprising that the cadence frequency is dominant.

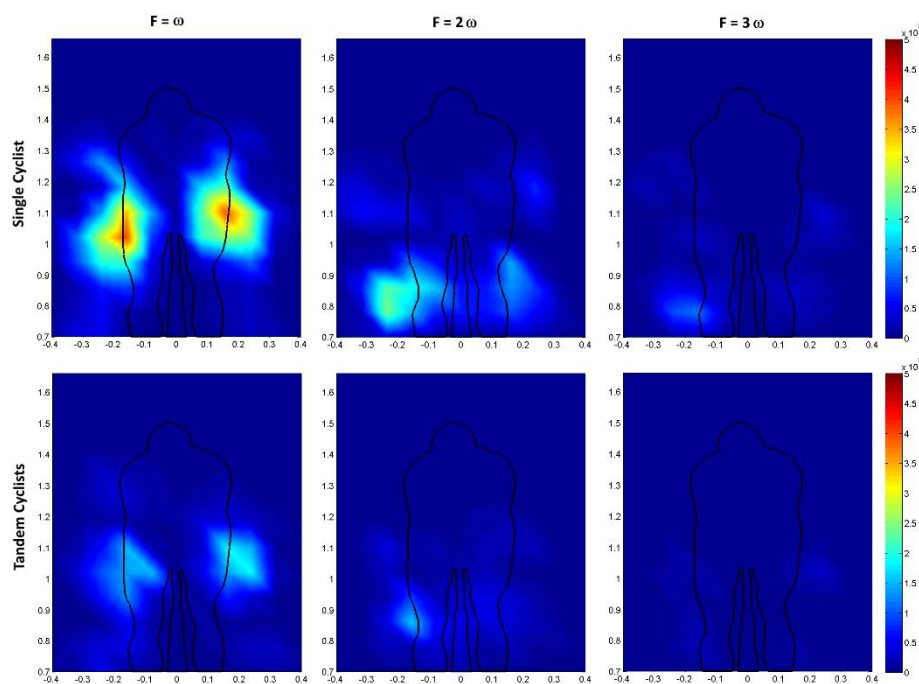


**Figure 5.4.13** - Distribution of peak energy content in streamwise velocity (U) for the single and tandem wake cases at each of the first three modes of the cyclist cadence ( $\omega$ )

Distribution of fluctuating energy in the wake of the trailing tandem cyclist exhibits a similar distribution to that seen for the single rider case. However, peak energy is reduced across all profiles at each frequency. In the streamwise velocity case, at the pedalling frequency the same two high energy regions are evident behind the cyclist's hips, correlating with the location of the hip vortices that dominate the wake of a cyclist. The profile is generally symmetric about the centreline and is similar in distribution to the single rider profile, however, peak energy is reduced. Power spectra are plotted for velocity components normalised by freestream with the same reference for the single and tandem cases. As such the power reduction is due to lower peak power rather than an increase in background noise. At  $2\omega$  the profile is similar to the single rider case, but amplitude is again, reduced. Similar to the single rider case there is a bias to the lower left due to the athlete. At  $3\omega$  there is minimal fluctuating energy evident as power is of an order of magnitude lower than the peak in the single cyclist maximum.

The distribution of the spanwise component of velocity ( $V$ ) exhibits a notably different distribution of energy (Figure 5.4.14). At the pedalling cadence, there is one high energy region concentrated in the centre of the wake, rather than two separate regions behind the hips, as seen in the streamwise component. This is similar to the distribution observed in the spanwise turbulence intensity ( $I_{wV}$ ). This corresponds with the oscillating nature of cross flow. Applying a quasi-steady approach, the cross flow seen in asymmetric profiles will oscillate from left to right each leg is raised and lowered respectively. As the spanwise flow reverses every half cycle in this central region a concentration in fluctuating energy is evident. At the higher harmonics ( $2\omega$  and  $3\omega$ ) energy content in the flow is not significantly above background levels, unlike the streamwise component. The trailing rider wake profiles exhibit the same behaviour as that seen for the single cyclist. Fluctuating energy is concentrated centrally behind the rear of the cyclist at the cyclist cadence frequency; however, peak power is reduced compared to the single rider. At the higher harmonics there is negligible fluctuating energy evident.

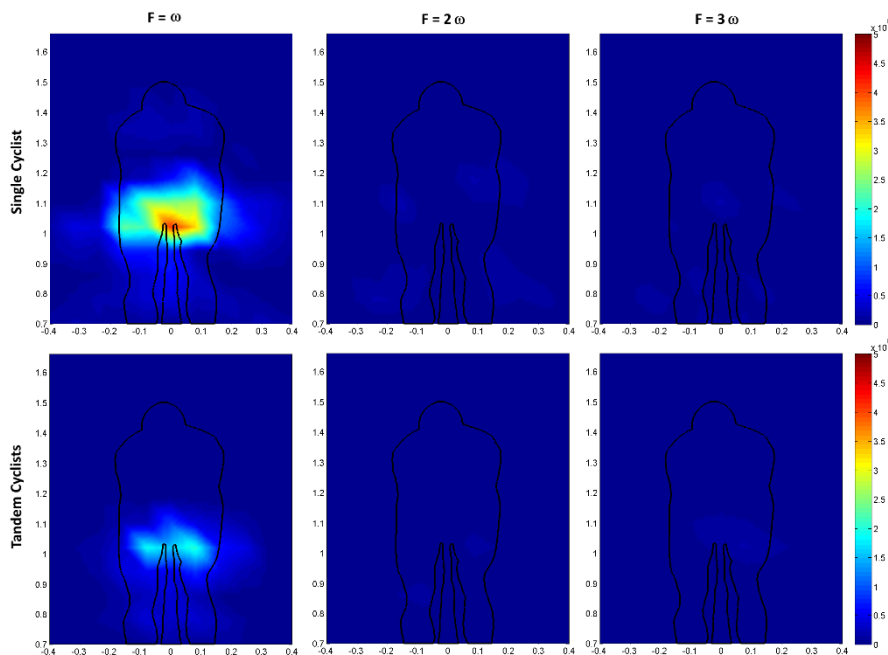


**Figure 5.4.14** - Distribution of peak energy content in the spanwise velocity component ( $V$ ) for the single and tandem wake cases at each of the first three modes of the cyclist cadence ( $\omega$ )

The vertical velocity component profiles (Figure 5.4.15) show broad regions of fluctuating energy at the pedalling cadence, though the magnitude is greatly reduced compared to the streamwise and spanwise components of velocity. There is a broad distribution of small magnitude either side of the centreline behind the rider's hips and legs. Similar to the spanwise component, the higher order harmonics do not exhibit significant fluctuating energy. With lower power in the tandem case, there are no significant regions of concentrated fluctuating energy across the wake as they are an order of magnitude smaller than the peak in the streamwise component. Although, it is possible to identify peaks at the key frequencies, above background levels, from the individual power spectra (see Appendix H).

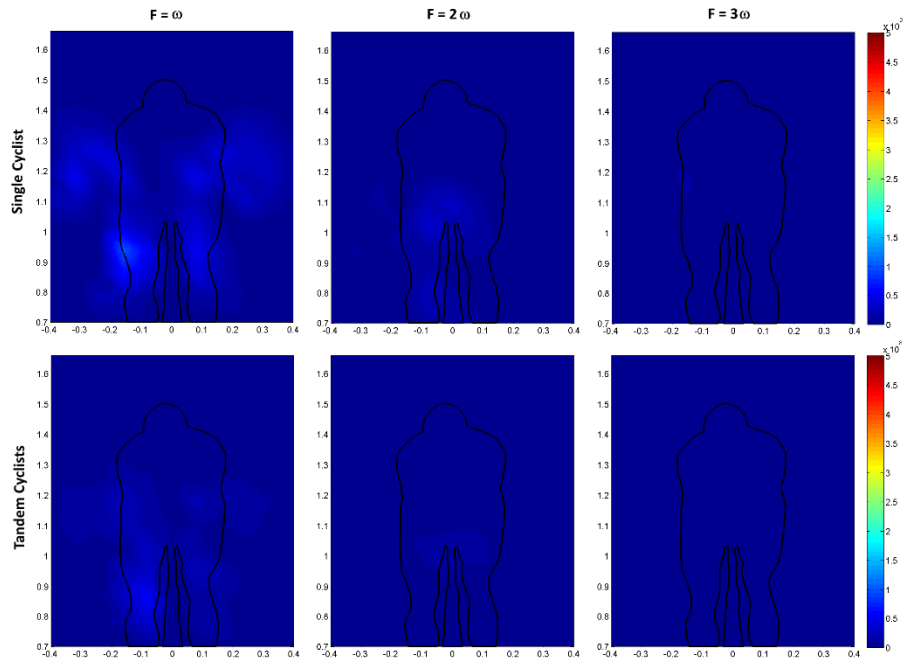


**Figure 5.4.15** - Distribution of peak energy content in the vertical velocity component ( $W$ ) for the single and tandem wake cases at each of the first three modes of the cyclist cadence ( $\omega$ )

### 5.4.3 Phase Averaged Wake Profiles

Using a magnetic sensor to identify each crank cycle, it was possible to dissect the time varying wake of a pedalling cyclist in isolation and tandem formation. The crank cycle was divided into 12 equal segments and data averaged over that section of the crank cycle. This phase averaging approach allowed the variation of the wake structure with the position of the legs to be analysed. This is a relatively coarse dissection, but maintains sufficient data points in each segment to obtain a stable average. Also it will be shown that this is sufficient to identify the transition between the asymmetric flow regimes for each half of the crank cycle. Figures 5.4.16 and 5.4.17 show the phase averaged streamwise velocity for the single and tandem cases respectively. Phase averaged profiles of spanwise and vertical velocity are plotted in Appendix J.

The streamwise velocity results show that there is a clear oscillation occurring in the wake. It is also evident that wake profile switches across the centreline every  $180^\circ$ . This corresponds to a half crank cycle where the leg position reverses and the opposite leg is raised. Previous work by Crouch et al. (2014) identified that there is higher velocity behind the raised leg as the flow remains attached longer and wraps down over the rear of the cyclist. By comparison, on the open hip, there is separation from the side of the hip and torso resulting in a low velocity region in the wake. For a pedalling cyclist, as the legs move around the crank cycle each leg is raised and lowered alternatively which results in a periodic switching observable in the streamwise velocity profiles. However, these profiles are still dominated by the large velocity deficit centred behind the hips and legs of the athlete. To highlight the regions of fluctuating streamwise velocity, the time averaged mean streamwise velocity profile was subtracted from each phase averaged field. The resulting profiles of change in streamwise velocity for the single and tandem cyclist cases are presented in Figures 5.4.18 and 5.4.19 below.

After subtracting the mean component from each profile the fluctuating component of the streamwise velocity is more clearly evident. Both the single and tandem results exhibit the same basic structure. The profiles are dominated by two regions behind the cyclist's hips, each being of equivalent magnitude but opposite sign. As the legs move around the crank cycle the regions shift, and after a transitional period are observed to switch sides of the cyclist's centreline. A mirror image profile is then observed for the second half of the crank cycle. Take the first frame ( $0^\circ - 30^\circ$  segment), the wake is dominated by a large negative region on the left and positive region on the right. This clearly indicates an asymmetric flow profile with greater deficit on the left. This general profile is maintained over the next few frames until  $90^\circ - 120^\circ$  where the structure is observed to change. As crank angle is increased beyond  $150^\circ$  the reverse profile begins to emerge with a positive region on the left and negative on the right. This reversal indicates that the legs have transitioned through the level position and the opposite leg is then being raised. This corresponds to the opposite asymmetric flow regime. The transitional period between the two correlates to the legs being level. In static tests this resulted in a symmetric wake profile. A symmetric wake profile is not clearly evident in the phase averaged wake profiles; however, the transitional behaviour as the positive and negative regions switch sides is observable. It is possible that the symmetric regime does occur in the time evolving wake of a cyclist but the coarse nature of the measurement grid and the large crank angle segments of this technique are not capable of discerning that flow regime. As the symmetric profile was observed to only exist for a range of approximately  $15^\circ$  either side of the position where upper legs were level, the resolution of these measurements limits the ability to distinguish such a regime. Furthermore, as the wake

structure is a dynamically evolving process the movement of the streamwise vortices with the changing leg position will not be discrete and so it is possible that a clearly defined symmetrical profile will not be observable for a pedalling athlete. This characteristic behaviour is applicable to both the single rider case and the tandem case. However, where the two sets differ is in the magnitude of fluctuating velocity. The magnitude of the change in velocity in the tandem wake is reduced compared to that of the single rider case. This indicates that whilst the flow behaviour is similar, the fluctuating component in the wake is reduced. This is consistent with the frequency analysis presented above (Section 5.4.2). It also follows from the scale model results (Section 5.2) which showed reduction in the magnitude of vorticity in the hip vortices of the trailing cyclist in a tandem pair.

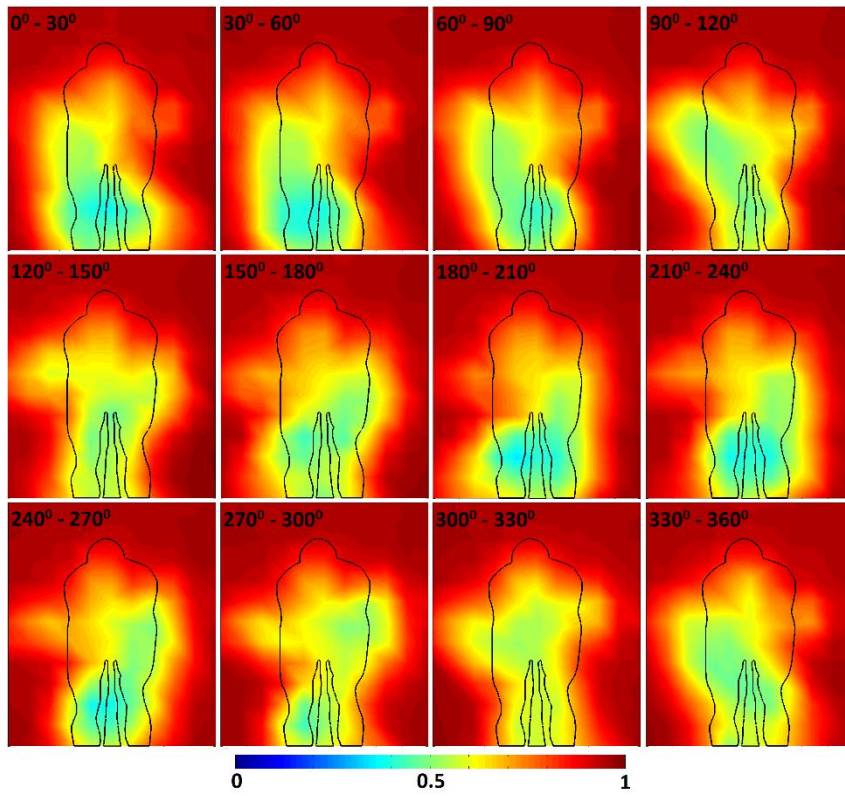


**Figure 5.4.16** - Streamwise velocity in the wake of a single pedalling cyclist, phase averaged over 30° segments of the crank cycle

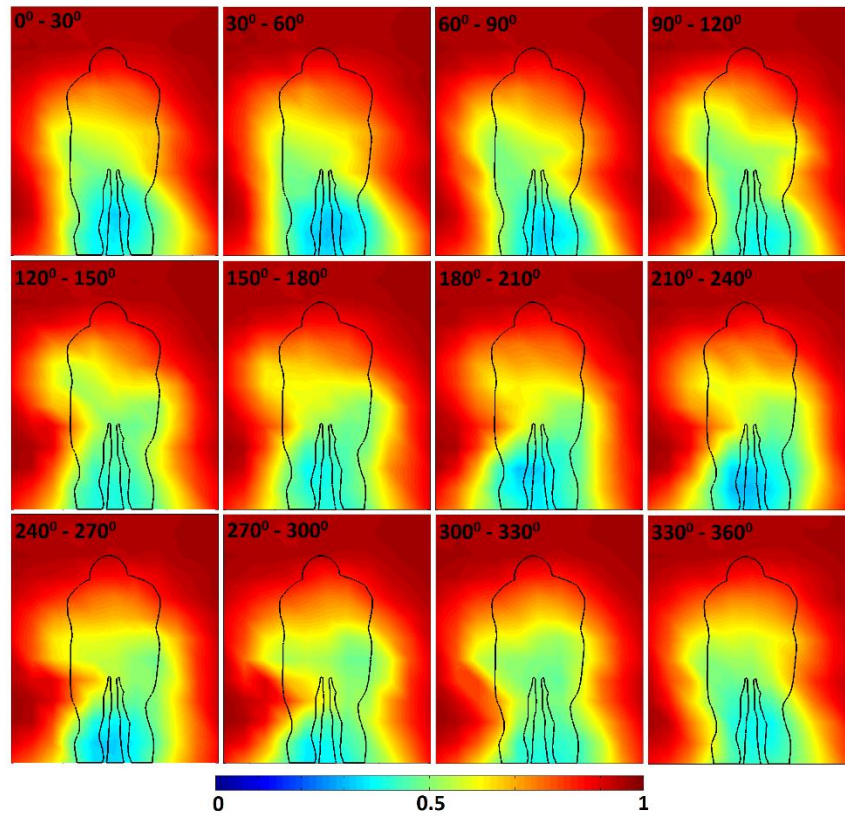


**Figure 5.4.17** - Streamwise velocity in the wake of a trailing pedalling cyclist in a tandem formation, phase averaged over 30° segments of the crank cycle

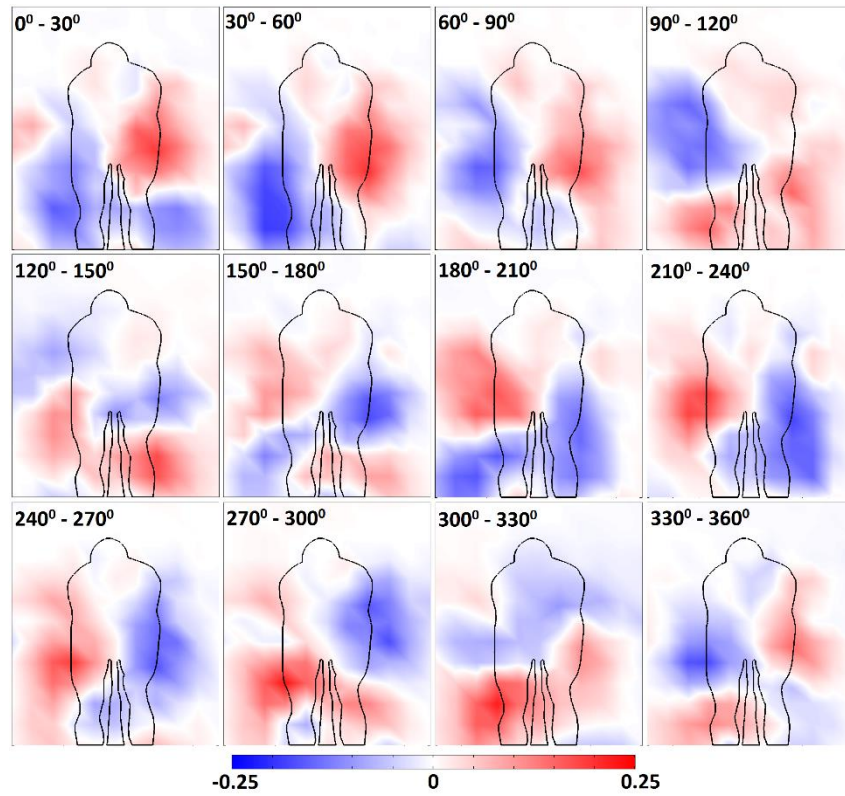


**Figure 5.4.18** - Difference in streamwise velocity from the time averaged flow in the wake of a single pedalling cyclist, phase averaged over  $30^\circ$  segments of the crank cycle.

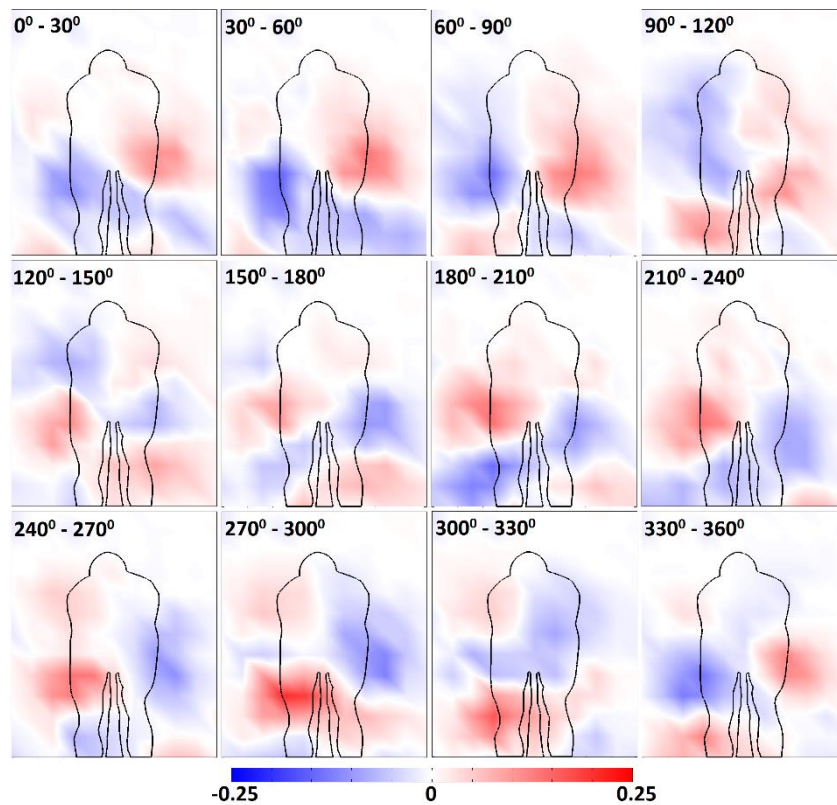


**Figure 5.4.19** - Difference in streamwise velocity from the time averaged flow in the wake of a trailing pedalling cyclist in a tandem formation, phase averaged over  $30^\circ$  segments of the crank cycle.

### ***Streamwise Vorticity***

Changes in the streamwise velocity have indicated that there are large scale changes in the wake of a cyclist; however, streamwise vorticity shows the presence and changes to coherent structures in the wake. Figures 5.4.20 and 5.4.21 show the phase averaged streamwise vorticity for the single and tandem rider wakes respectively. The coarse sampling grid and the phase averaging of a time evolving process means that the profiles are not as cleanly defined as was previously observed for static cyclists (see Section 5.2). However, the dominant streamwise vortices that form from the cyclist's hips are clearly evident in the centre of the each profile. For the majority of the crank cycle, the upper legs are not level, thus the characteristic asymmetric profile is evident across the majority of profiles. It was previously described by Crouch et al. (2012, 2014) that when a leg is raised and closes off the hip angle the flow wraps over that hip and the rear of the rider and the resulting hip vortex occurs lower in the wake. By contrast, the open hip results in higher separation and the resulting vortex is seen to sit higher in the wake. This was also seen for scale model cyclists in Section 5.2. However, it is noted that the sign of the vortices from each hip is constant around the crank cycle. It is only the position of the vortices that changes. This behaviour, previously observed for the static cases, is evident in the phase averaged dynamic profiles. In the first 4 frames the negative left hip vortex is seen to sit up higher in the wake with the positive right hip vortex sitting lower. As the legs move around the crank cycle a transition point occurs where the profile shape reverses and the left and right hip vortices switch. This can be seen to occur between  $90^{\circ}$  and  $150^{\circ}$ . Beyond this point the right positive vortex sits higher than the negative left vortex. This shows that the primary hip vortices identified in static wake profiles persist in the wake of dynamic cyclist. Due to the spatial resolution of measurements and the noise associated with the dynamic evolution of the wake it is not possible to identify the smaller scale structures that are evident in static profiles. However, the primary hip vortices, which are the dominant feature in the cyclist wake, are distinguishable in the dynamic wake of a cyclist.

Comparing the single and tandem rider cases, the same periodic behaviour is observed in both sets of profiles. Furthermore, the streamwise vorticity is not significantly lower in the tandem wake when compared to the single rider case. This is different to the streamwise velocity, which showed a reduction in the tandem rider case. This shows that the formation of the hip vortices over a rider in a tandem formation is not significantly disrupted by the presence of an upstream rider. It appears that whilst there is a reduction in the fluctuating streamwise velocity component, the strength of the dominant wake vortices is not significantly different. Scale model results indicated some reduction in vorticity of the hip vortices for static cases. It appears that with the addition of dynamics, the difference in strength between the single and tandem cases is less significant. The persistent presence of these primary vortices in the tandem cyclist wake further supports the hypothesis that the drag reduction experienced by a trailing cyclist is dominated by the upstream flow changes, rather than a disruption to the characteristic wake structures. It is noted that the magnitude of vorticity observed in the dynamic wake is significantly reduced compared to the static results. This suggests that the dynamic evolution does weaken the formation and sustained vorticity of those hip vortices.

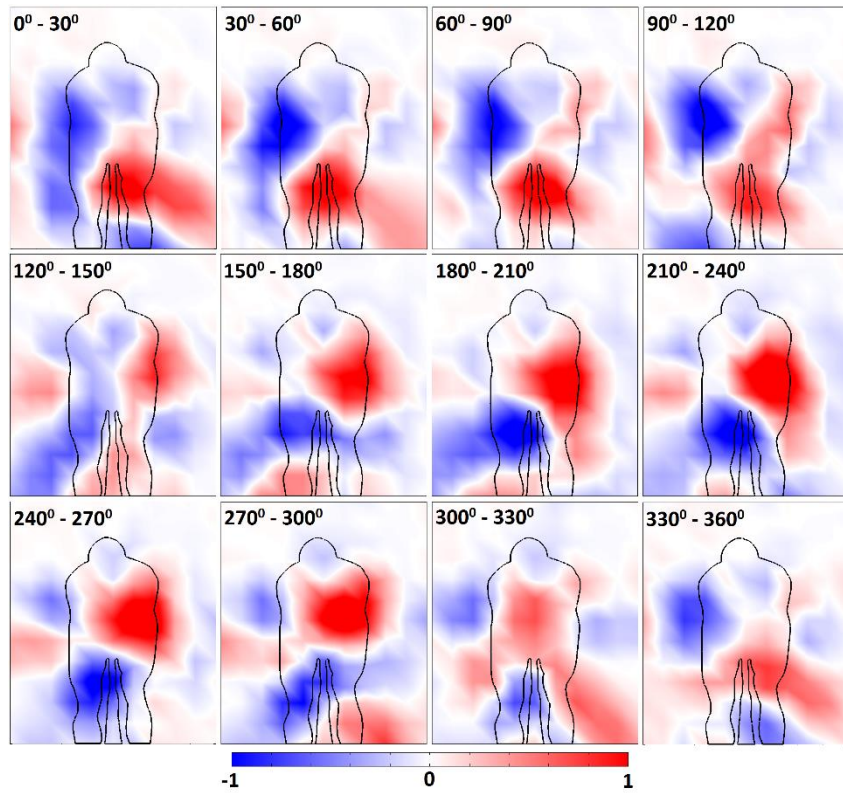


**Figure 5.4.20** - Streamwise vorticity in the wake of a single pedalling cyclist, phase averaged over  $30^\circ$  segments of the crank cycle

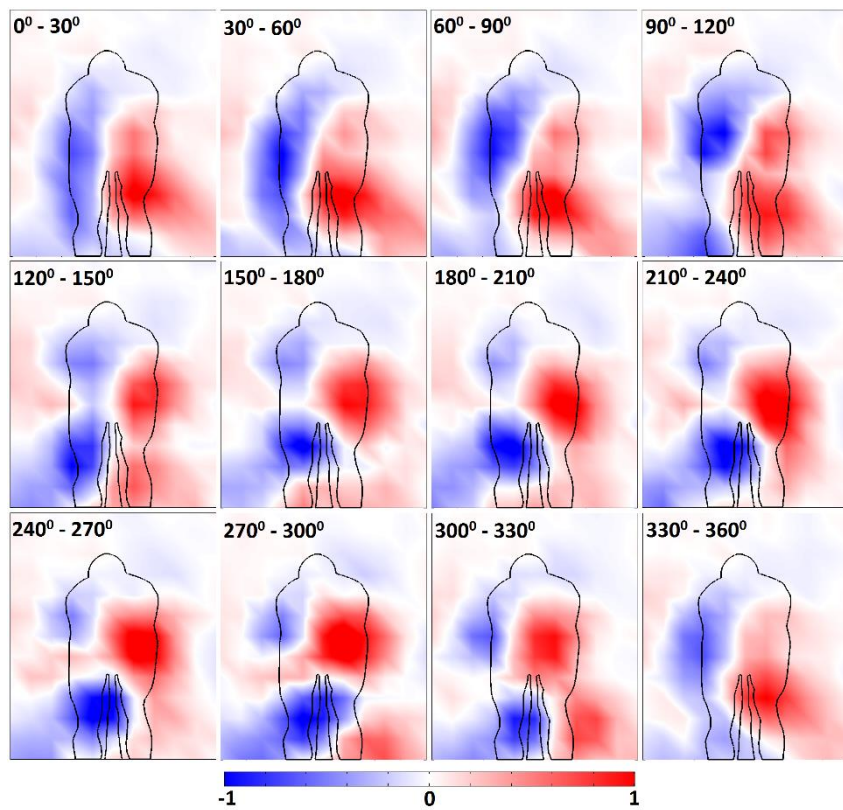


**Figure 5.4.21** - Streamwise vorticity in the wake of a trailing pedalling cyclist in a tandem formation, phase averaged over  $30^\circ$  segments of the crank cycle

From the vorticity results the streamwise velocity fluctuations can be correlated to the leg position and flow regime. It is important to distinguish that the vorticity profiles indicate the location of the hip vortices. As the direction of rotation of these structures is a result of the cyclist geometry, the sign of vorticity behind each hip is constant across all crank angles. It is the location of the vortices that changes with leg position. By comparison, the streamwise velocity profiles show a reversal in positive and negative velocity difference every half crank cycle. Comparing the two data sets it can be determined that the positive region of streamwise velocity difference correlates with the lower hip vortex. From the static profiles we know that this corresponds to the leg on that side being raised, closing the hip angle and allowing flow to wrap over the hip and separate later, resulting in the vortex sitting lower in the wake. The negative regions of streamwise velocity difference coincide with the higher of the hip vortices. This corresponds to the extended leg with the open hip angle that causes separation to occur higher on the hips.

### ***Convection Velocity***

It is evident from the phase averaged streamwise velocity and vorticity that the  $0^{\circ}$  -  $30^{\circ}$  crank angle position does not coincide with the symmetric flow regime, as was identified in static results. Similarly the second symmetry/transition point does not occur at  $195^{\circ}$ . The reason for this is that the wake profiles are indexed to the current position of the cranks. As the wake is being measured downstream of the athlete there is convection time for the flow to travel downstream from the athlete to the point of measurement. During this time the cranks continue to rotate. As such, the crank angle index applied to the phase averaged results does not line up with the static leg position at which that regime would be expected. This creates an effective phase shift between the wake profiles of the dynamic cyclist and those seen for a cyclist at a static leg position.

The phase shift in the results can be estimated by modelling a wake convection velocity. Given the velocity gradients across the wake, different regions of the wake will convect at different rates. And as structures in the wake change around the crank angle, velocity in the wake at a given location will not be a constant. As an approximation a mean wake velocity was determined and used to model the convection velocity (Wu, Sheridan et al. 1996). This was calculated from the time averaged mean velocity results for the single and tandem cases respectively. To exclude the freestream conditions at the edges of the interrogation region, the flow was averaged over a window which closely enclosed the athlete dimensions. This was taken as 400mm wide, based on the athletes shoulder width and up to a height of 1500mm, the top of the athlete's helmet. Within this region the mean normalised streamwise velocity was calculated to be 0.75 and 0.70 for the single and tandem cases respectively. These values were then used to model a wake convection velocity. As a reference the minimum velocity of the time averaged wake was 0.38 for the tandem case. The measurement plane was 600 mm downstream of the rear of the saddle. However, the dominant flow structures in the wake are formed from the hips of the cyclist. For calculation of convection velocity the convection length was defined to the athlete's hip joint, further upstream of the saddle. Convection length was therefore defined as 750 mm. Given an average cadence of 95.5 RPM and 92.7 RPM it was possible to determine a phase shift of  $31^{\circ}$  and  $32^{\circ}$  for the single and tandem wakes, respectively.

A visual comparison of the profiles in Figures 5.4.18 to 5.4.21 suggests that the phase shift is actually far greater than the calculated values of  $31^\circ$  and  $32^\circ$ . By inspection, the transition region is first evident at the  $90^\circ - 120^\circ$  segment. As the width of the phase averaging segments is large, it is difficult to identify small changes in the flow. Also, the coarseness of the grid does not clearly define small scale structures. This was an acknowledged limitation of this technique, however, the coarse grid was necessary to analyse the wake of a dynamic athlete. This method remains valid as the primary wake vortices are identifiable and the periodic nature of the wake is evident. The transition region corresponds to the point where the cyclist's upper legs are passing through the level position as the profiles appear to become less biased in their asymmetries as the legs approach the symmetry condition before switching.

Due to the specific geometry of this athlete the thigh level position actually occurred later than  $15^\circ$  as previously identified for the mannequin. Due to the nature of the ankle joint, Athlete B's upper legs were level at a crank angle of  $23^\circ$ . From this it can be stated that the effective phase shift for a pedalling cyclist is actually of the order of  $67^\circ$ , if the transition point is taken as  $90^\circ$  from the profiles. This equates to a convection velocity of 0.34, which is below the minimum velocity measured in the wake. Despite the limitations of this technique, it can be concluded that there is some additional mechanism associated with the generation and transport of the dominant wake structures in the wake of a cyclist causing the effective lag. This appears to be linked to the process of evolution of the wake structures and formation from a moving leg differing to that observed from the time averaged wake of a static cyclist at a fixed leg position.

To refine the calculation of convection velocity, the mean velocity behind the hips of the cyclist was used for the single and tandem cases. This was selected as the primary vortices are generated at the hips of the cyclist. This point is also closer to the centre of the wake where velocity is considerably slower and so likely provides a better approximation of the convection velocity of the hip vortices. This resulted in a convection velocity of 0.62 and 0.58 for the single and tandem cases respectively. Following the same process, this equates to an effective phase shift of  $36^\circ$  and  $37^\circ$  respectively. This is still well below the shift physically observed in wake profiles. Given this difference it can be concluded that the leg dynamics introduce an additional mechanism associated with the effective phase lag between the leg position and the measured flow downstream that is not accounted for in a quasi-steady assumption.

Velocity measurements in the wake of a cyclist enabled the identification and tracking of the evolution of the dominant wake structures. It can be seen that the single and tandem wakes did not exhibit a significant phase shift relative to one another. As such, the two wakes will have a crank angle phase shift of similar order. Given that the tandem wake has a slightly lower mean velocity, it is expected that the phase offset will be slightly greater than the single case. However, this will be small given that the difference in mean velocity is of the order of a few percent. In the context of these results it is not possible to resolve differences of that scale. It is, therefore, reasonable to model phase shift on the same order for the single and tandem wakes in this case, as is evident from the profiles, which show that the two data sets are aligned.

### Quantitative Wake Analysis

Applying the control surface wake integral (Equation 5.4.2) to the time averaged results under predicted the drag of the athlete(s) in all cases. This was as expected given that only a section of the wake region was captured. However, it was also proposed that the induced drag contribution from vorticity in the wake would not be representative as the time averaged flow masks the moving coherent vortices forming from the hips. As seen in the profiles of streamwise vorticity, the segmented phase averaging approach captures the size and location of the hips vortices as they shift with the rotation of the legs. Therefore, applying the wake integral to each segment individually may give a better representation of drag of a cyclist as it better captures the changing nature of the wake. This approach also has the potential to capture the variance in the drag with leg rotation. The quasi-static investigations of Crouch et al. (2012, 2014) previously showed that drag varies with leg position with minima at the symmetric leg positions and peaks at the asymmetric positions. Using the phase averaged segments it was possible to calculate the drag at each leg position by integrating Equation 5.4.2 as described previously. The results are plotted in Figure 5.4.22 below as a function of the median crank angle for each segment (eg. the value of  $C_{DA}$  for the  $0^\circ - 30^\circ$  segment is plotted at  $15^\circ$ ).

It can be seen in Figure 5.4.22 that  $C_{DA}$  for both the single and tandem cases does not vary significantly with leg position. The maximum range of  $C_{DA}$  values is of the order of  $0.01 \text{ m}^2$  in all three cases. By comparison, the range of quasi-static results by Crouch et al. (2012) was of the order of 3 times greater. Furthermore, no regular periodic pattern is evident as was observed in quasi-static results.

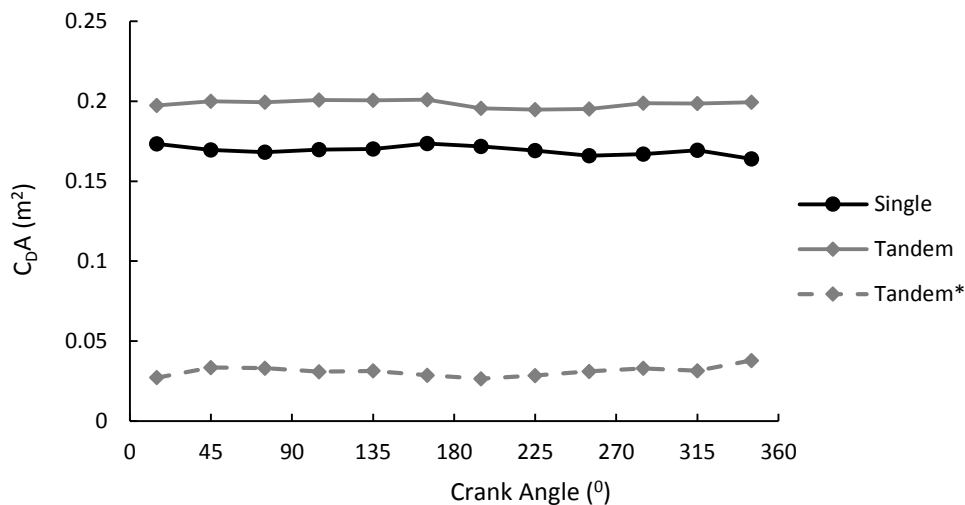


**Figure 5.4.22** –  $C_{DA}$  calculated from wake integral of phase averaged profiles (Equation 5.4.2). Tandem\* represents the modified integral using single cyclist wake values as inlet.

Figure 5.4.22 also shows that the phase averaged application of Equation 5.4.2 still under predicts the drag acting on a cyclist. However, mean results are consistent with the results from the time averaged wake fields which were found to be 0.173, 0.200 and 0.032 for the single, tandem and modified tandem cases respectively. Drag being lower than the measured force results is unsurprising given that only a section of the wake is captured. However, the mean of the phase averaged drag exhibits negligible difference from the previous results for the time averaged field. This suggests the induced drag term does not contribute significantly to the drag of the cyclist.

Figure 5.4.23 shows the relative contributions of each term in the single rider case, with the induced drag term (vortex drag) plotted on a different scale. It can be seen that the induced drag term provides only a small contribution to the total drag, with the stagnation pressure deficit dominating. In addition, the variation of the induced drag term with leg position is very small. However, the observed variation does correlate with the observed wake profiles. Consider the change in streamwise velocity or streamwise vorticity profiles. Whilst a symmetric regime is not distinct, the wake structure is observed to transition between the two asymmetric regimes in the  $120^{\circ}$  -  $150^{\circ}$  and  $300^{\circ}$  -  $330^{\circ}$  frames. And it is at these angles that the induced drag term is a minimum. Quasi-static results showed that the vortex drag term accounts for the variation in  $C_{D,A}$  with leg position and that due to the low vorticity in the symmetric wake profiles, the drag is a minimum. Whilst the variation in induced drag is of a much smaller magnitude, it does indicate that the changes in the wake are being reflected in the calculation of drag. This is consistent with previous quasi-static results. The small magnitude of induced drag is likely linked to the small peak vorticity in the phase averaged profiles compared to that measured with the static scale model (1.5 compared to 7 in normalised vorticity; athlete and scale respectively). This suggests that whilst the same structures identified in a static wake profile are present in the dynamic wake, the strength is reduced and this is reflected in the relatively small contribution of the induced drag term. It is noted that the low spatial resolution of samples in the wake survey and the broad crank angle segments used in this technique will limit the resolution of a piecewise wake integral. This will have an impact on the sensitivity of the piecewise integral but is not expected to affect peak values significantly, and hence the peaks the drag curve.

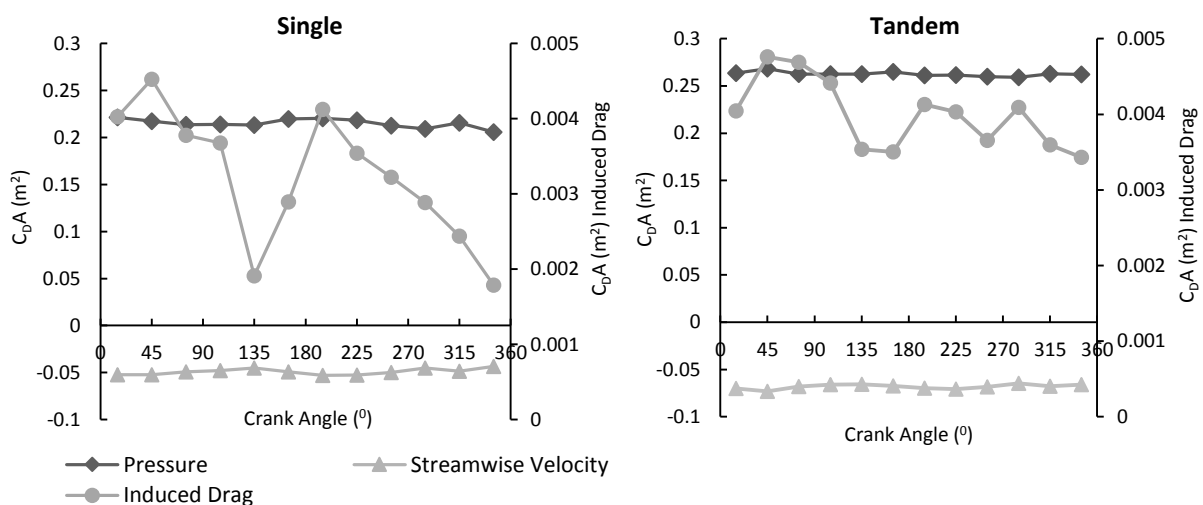


**Figure 5.4.23** – Contributions of each term in Equation 5.4.2 to the total  $C_{D,A}$  of a single cyclist (left) and tandem cyclist (right). Induced drag term plotted on right vertical axis to highlight variation with crank angle.

Figure 5.4.24 shows the individual induced drag terms from each of the three cases (including the modified tandem). This shows that the contribution in each of the three cases is generally of the same order; being significantly smaller than the contribution from stagnation pressure deficit. Like the single case, the tandem case does exhibit variation with crank angle. In this sense the maxima and minima generally align between the cases; although the range in  $C_{D,A}$  is small. The reduced range of the tandem cases is not surprising given the reduced peak vorticity and coherence of structures previously identified in the wake of a trailing cyclist. This will result in a smaller induced drag component and so

reduce the change in drag with leg position. The fact that the mean of the tandem cases is above the single is linked to the fact that the induced drag term also includes the perturbation velocity in addition to the in-plane components of velocity (see Section 5.4.1).

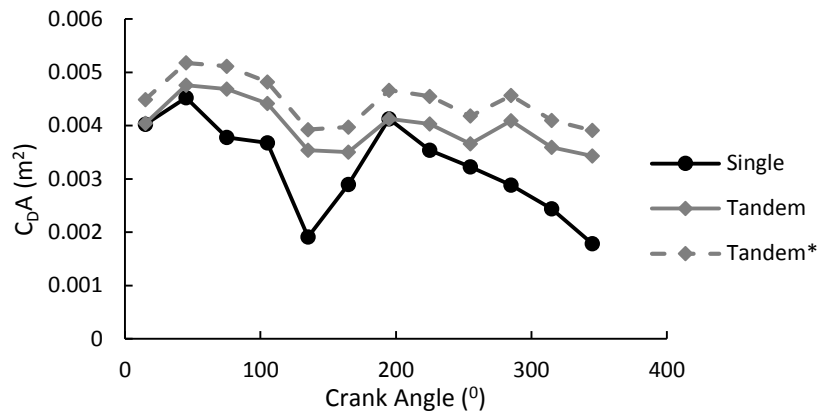


**Figure 5.4.24** – Induced drag (vortex drag) term for the single and tandem cases. Tandem\* represents the modified integral using single cyclist wake values as inlet.

### Summary

The wake of a dynamic pedalling cyclist was investigated by traversing a cobra probe in the wake. This was performed for a single athlete in isolation as well as the same athlete acting in a trailing position in a tandem pair, immediately behind the leading rider. Time averaged results show that there is a general similarity between the single and tandem wakes. Streamwise velocity showed a greater deficit in the lower region of the trailing rider wake. However, in the upper region behind the cyclist’s hips, where the dominant vortices have been shown to occur, there is only a small difference in streamwise velocity. Vorticity and in-plane velocity components show strong similarity between the single and tandem cases. Applying the momentum equation over the wake interrogation region showed that momentum deficit in the wake of the trailing tandem cyclist are in fact greater than the single rider case; indicating that there is no energy recovery in the trailing rider wake. The combined results show that the introduction of an additional cyclist upstream has only small impact on the time averaged wake of the trailing cyclist. This supports the findings of the scale model tests.

Analysis of the time varying components in the wake showed that the pedalling frequency contains the highest energy fluctuations in the wake of a pedalling cyclist. In addition there are also energy concentrations at the next two higher order harmonics. In the streamwise case the distribution at  $2\omega$  differs from the fundamental mode case. This indicates a different mechanism is acting at this frequency. Given the nature of the motion and geometry it is suggested that this is linked to the changing direction of the knee, which occurs twice per cycle at top and bottom of each stroke. The same three modes of the cadence are evident in all three components of velocity but is strongest in the streamwise component. Given the large scale motion of the legs and the associated flow changes observed in static profiles previously, it is unsurprising that the fluctuations are dominated by the pedalling frequency. Frequencies and spatial distribution of fluctuating energy in the wake are consistent for the single and tandem cases. However, the wake of the tandem cyclists exhibits a

reduction in peak energy fluctuations compared to the single rider case. This is consistent across all frequencies and velocity components.

Phase averaged wake profiles showed that the wake of a pedalling cyclist transitions through the two asymmetric flow regimes identified for static cyclists; corresponding to each leg being raised and lowered respectively. From profiles of vorticity it was possible to distinguish the flow regimes observed in static cyclist wakes at sections within the crank cycle. These characteristic regimes oscillate periodically such that the wake profile reverses every half crank cycle. Results showed that the trailing rider wake maintains close similarity with structure and behaviour of the single rider. There is minimal change in the phase averaged structure of the wake indicating that dynamic behaviour is largely unchanged. A difference was observed in the fluctuating component of streamwise velocity, with the tandem wake exhibiting smaller magnitude compared to the single rider. However, the distribution and structure of the wake remains similar. This is consistent with the frequency spectra which showed a reduction in peak fluctuating energy in the tandem wake. However, it is noted that streamwise vorticity does not differ significantly. This indicates that the same dominant vortex structures are present in the time evolving dynamic wake of a cyclist and remain so for a trailing cyclist.

These results show that the same dominant flow structures observed in the wake of a single cyclist prevail in the wake of a tandem cyclist. This follows on from similar findings from static wake profiles of scale model cyclists which showed a similar outcome. This indicates that results from scale model tests provide a useful representation of the full scale cyclist wake behaviour despite the lower Reynolds number. Furthermore, the characteristic flow regimes seen for a static cyclist are evident in the wake of a pedalling cyclist and these are consistent for both single and tandem cases. These combined findings further support the hypothesis that the large drag reduction observed for the trailing rider is not due to a major disruption to the wake of a the trailing cyclist. This provides further evidence that the drag saving is dominated by an upstream change. Furthermore, given the persistent presence of strong hip vortices in the wake of a tandem cyclist, as seen in both athlete and scale model tests, it can be concluded that the formation of these vortices is so strongly defined by the cyclist geometry that their presence in the wake is largely independent of the inflow conditions.

## 5.5 Pressure Distribution in the Wake of a Dynamic Cyclist

### 5.5.1 Time Averaged Results

A grid of 121 forward facing pressure taps was used to map the time resolved pressure changes in the wake of a pedalling cyclist. The time averaged streamwise components of total pressure coefficient in the wakes of a single cyclist and two cyclists in tandem are shown in Figure 5.5.1. By comparing this data to the time-averaged streamwise velocity profiles taken by traversing a single 4-hole probe across the wake it can be seen that the distributions are similar. Figure 5.5.2 plots the streamwise component of total pressure, normalised by freestream dynamic pressure for comparison against the total pressure grid results.

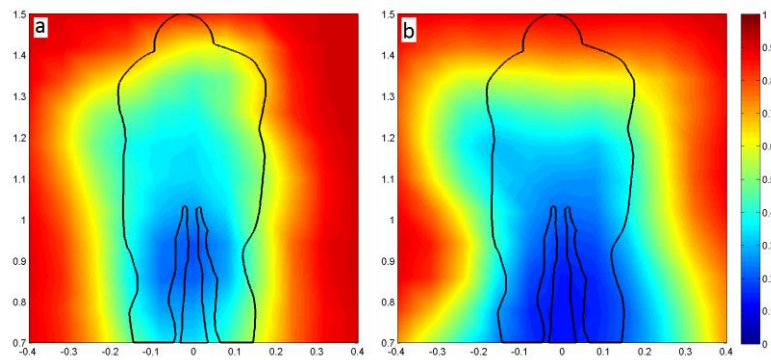


**Figure 5.5.1** - Time averaged streamwise total pressure coefficient measured using grid of forward facing pressure probes, in the wake of (a) a single pedalling athlete and, (b) a tandem pair

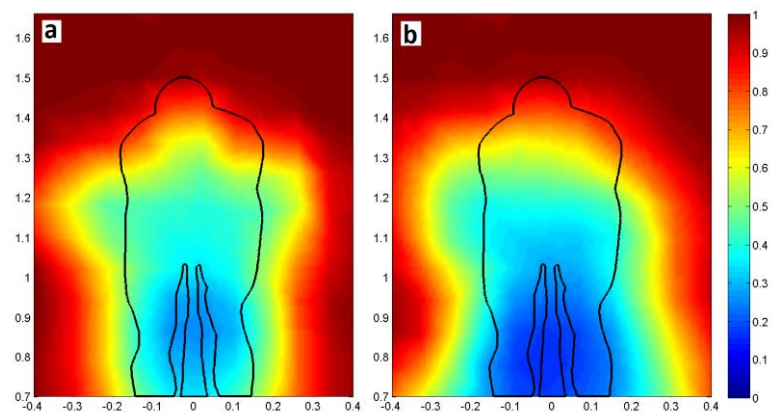


**Figure 5.5.2** - Time averaged, streamwise total pressure from point measurements with a cobra probe, in the wake of (a) a single pedalling athlete and, (b) a tandem pair

The wake profiles collected with the pressure grid exhibit a general similarity with those from point measurements with the cobra probe. Like the probe results, the total pressure wake profiles are not symmetric, but this is unsurprising given the use of an athlete. The single rider profile is largely symmetric but with a wake region slightly narrower than the probe results. The tandem wake

measured with the pressure grid exhibits a distinct asymmetry, with lower pressure on the left of the cyclist. However, this distribution matches closely with that observed with point measurements from the pressure probe. This confirms that the total pressure grid provides a strong correlation with the streamwise velocity in the wake of a cyclist. Given that streamwise velocity in the wake of cyclist has been shown to vary strongly with leg position, this technique will prove a useful tool for a simultaneous investigation of the dynamic behaviour of a pedalling cyclist's wake.

The asymmetry observed in the tandem wake is consistent with the streamwise velocity results collected with the multi-hole pressure probe. As this is common for both experiments it shows that the pressure profile is repeatable. As previously stated, it appears that this feature of the wake is due to a slight asymmetry in the athlete and bicycle system being magnified by the interactions between the riders. As with the streamwise velocity wake measurements, the upper half of the interrogation region exhibits similarity between the single and tandem cases. In the lower half of the window, below the cyclist's hips, the tandem wake exhibits a lower pressure and larger region compared to the single rider case. The simultaneous samples of pressure using the pressure grid will be used to confirm the time varying behaviour of the cyclist wake across the wake region.

### 5.5.2 Spectral Analysis of the Dynamic Wake

The power spectra were computed for each of the pressure taps in the wake of the cyclist using Fast Fourier Transforms of the time varying pressure signals. Samples of the full spectra for the single and tandem rider wakes are shown in Figure 5.5.3. Each graph shows a series of spectra in a vertical slice at  $y = -0.16$  m from  $z = 0.7$  m to  $1.5$  m at  $0.08$  m intervals. At this scale there are no significant power concentrations evident in the spectrum. However, when considering only the low end of the frequency band, several key frequencies emerge. The full collection of power spectra showing the low end of the frequency band are plotted in Figure 5.5.4 and 5.5.5 for the single and tandem wakes respectively. Spectra are plotted against frequency normalised by pedalling cadence ( $\omega$ ). Mean cadence for the single and trailing tandem cyclist cases was  $92.42$  RPM and  $92.37$  RPM. Each spectrum was filtered for background wind tunnel noise by normalising each by the spectrum recorded for the empty wind tunnel with no cyclists present.

A common set of frequencies can be observed to dominate the spectra across many of the probe locations in the wake of a dynamic cyclist. The most dominant peak occurs at the pedalling cadence ( $\omega$ ) with secondary peaks occurring at the next two higher order modes at  $2\omega$  and  $3\omega$ . Given the large scale structures observed in the wake of a cyclist that vary with leg position it is not surprising to see that the pedalling frequency is the most dominant energy content in the wake of a dynamic cyclist. This is consistent with previous wake traverse results with the cobra probe.

The same frequencies dominate the spectra of the tandem rider wake as those seen in the single rider case. The dominant frequencies in the wake occur at the pedalling cadence and at two higher order harmonics. Compared to the single rider wake, the tandem spectra exhibits a reduction in peak power at each of the key frequencies. It can also be seen that the power peaks in the tandem wake are

broader than seen for the single cyclist. This indicates a spread of energy over the surrounding frequencies. It has been identified that the trailing rider in a tandem pair has greatly reduced inflow energy compared to that of the leader or an isolated cyclist. It follows then that the fluctuating energy in the wake would be of reduced magnitude. The spread in energy will also be linked to the reduced strength of the primary hip vortices in the wake as a result of the low energy and turbulent inlet conditions. It must be noted that the lead rider was static at a crank angle of  $15^\circ$ , rather than dynamic. Whilst inlet conditions were shown previously to not have a large effect on the dominant structures in the wake, it may have an influence on the distribution of energy in the spectrum.

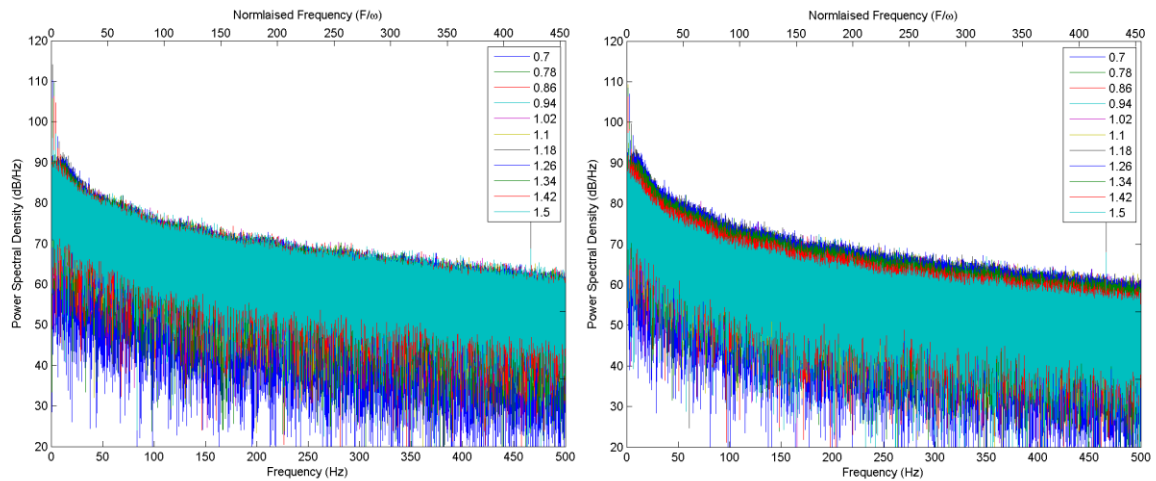


**Figure 5.5.3** – Power spectral density in the wake of a single rider (left) and tandem cyclist wake (right). Samples taken in a vertical line at  $y = -0.16$  m at  $z = 0.7$  to  $1.5$  m at  $0.08$  m intervals.

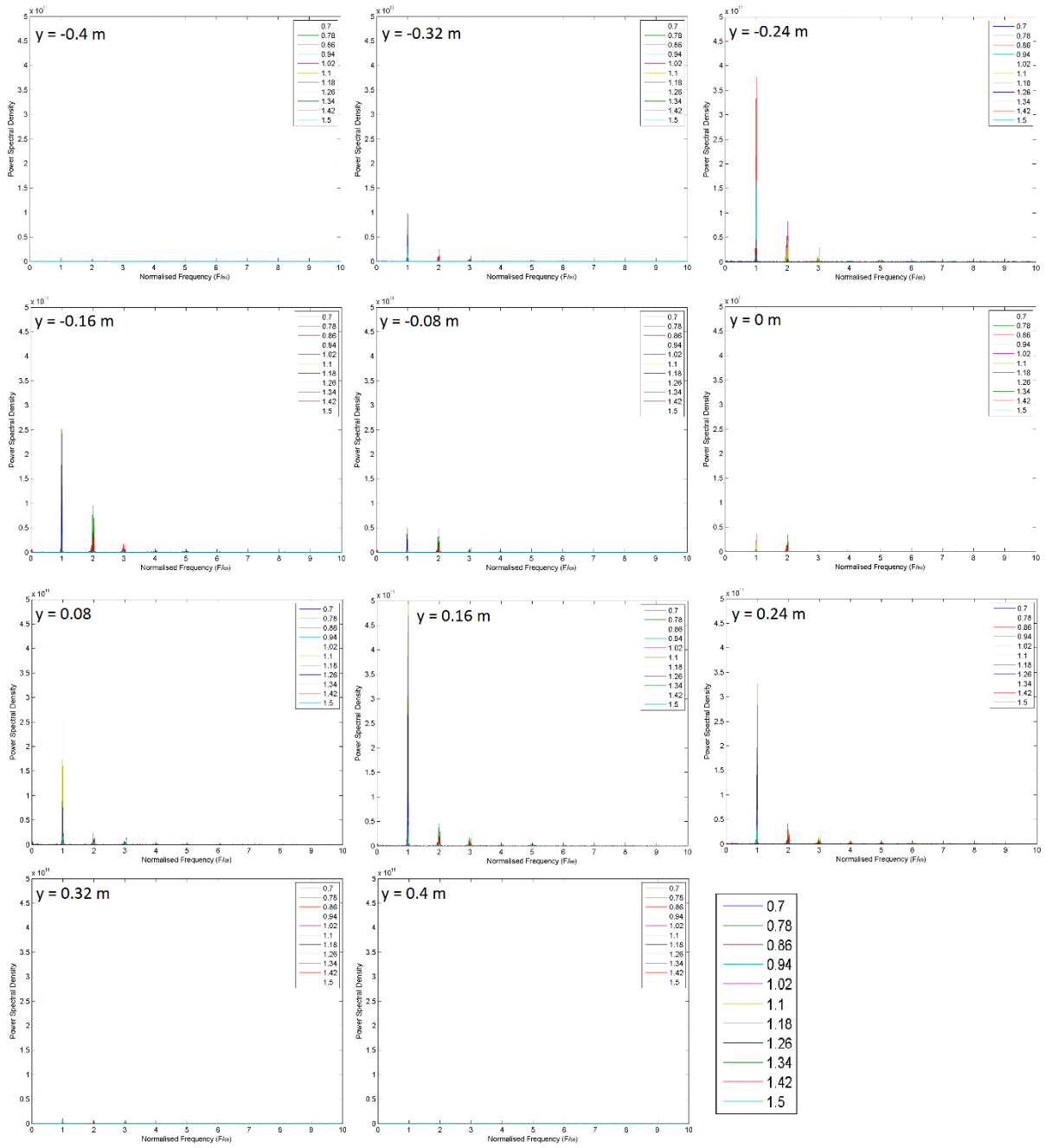


**Figure 5.5.4** – Power spectra for each pressure channel in the wake of a pedalling single cyclist. Each frame shows a vertical slice in the wake with points from  $z = 0.7$  to  $1.5$  at  $0.08$  m intervals. Frequencies have been normalised by the cyclist cadence ( $\omega$ ).

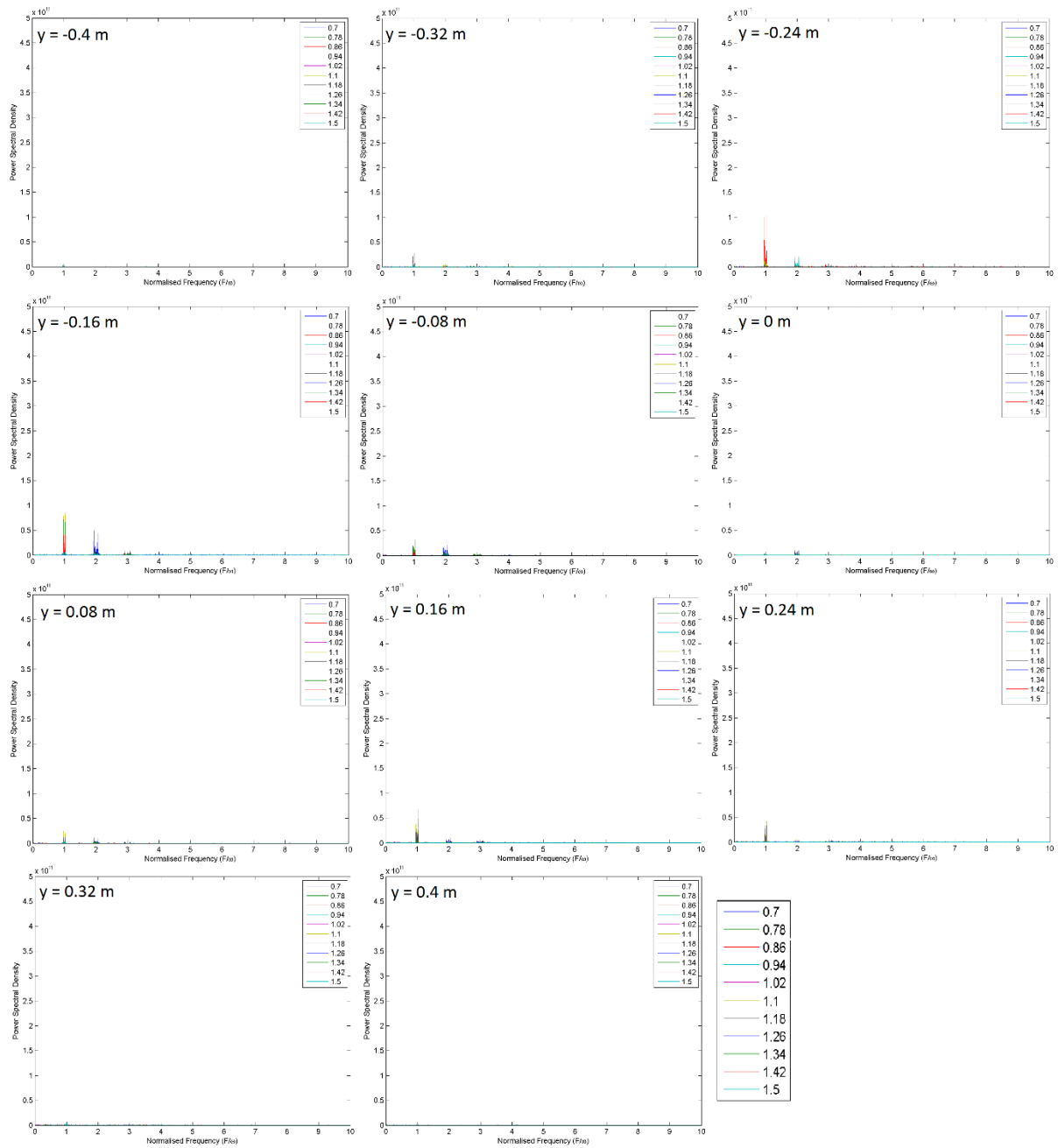


**Figure 5.5.5** - Power spectra for each pressure channel in the wake of a pedalling trailing tandem cyclist. Each frame shows a vertical slice in the wake with points from  $z = 0.7$  to  $1.5$  at  $0.08\text{m}$  intervals. Frequencies have been normalised by the cyclist cadence ( $\omega$ ).

As was seen with the point probe measurements (Section 5.4) the distribution of fluctuating energy varies with position in the wake. To highlight the spatial distribution of fluctuating energy, the peak amplitude at each of the three key frequency bands was identified and plotted as a surface over the sample region. The results for the single and tandem wakes are shown in Figures 5.5.6 below.

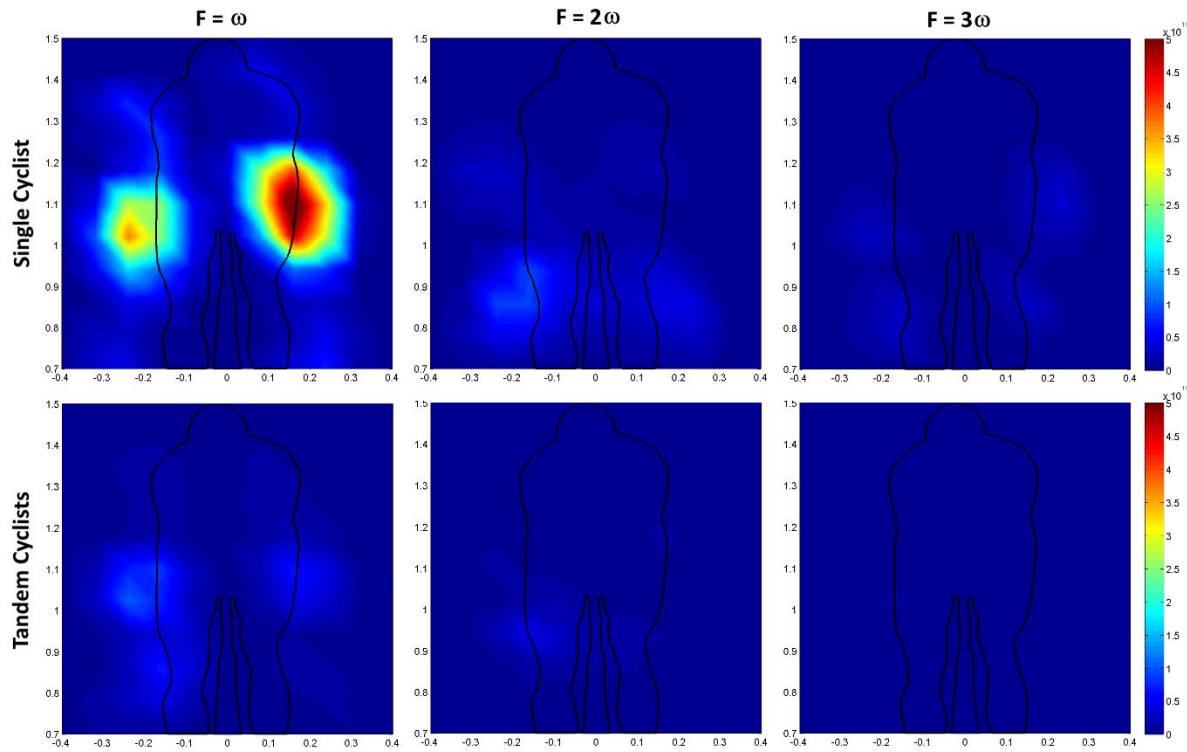


**Figure 5.5.6** - Distribution of peak energy content at (L-R); at the 3 modes of the pedalling cadence ( $\omega$ ) in the wake of a dynamic single cyclist (top row) and trailing tandem cyclist (bottom row)

The profiles for the single rider (Figure 5.5.6 top row) show that the cadence frequency is far more dominant than the higher order modes at  $2\omega$  and  $3\omega$ . This is unsurprising given that it coincides with the cyclist's cadence and subsequently the changes in large scale hip vortices. It also follows that the peak fluctuating energy is concentrated in the region behind the cyclists hips given that the primary streamwise vortices are shed from each hip as the legs cycle. It can be seen that there is a very strong localisation of the peak frequency in these areas and low energy across the rest of the wake. This profile correlates very closely to the streamwise velocity energy profile presented earlier in Section 5.4, although the asymmetry from left to right hips is slightly more pronounced. At the first harmonic ( $2\omega$ ) the profile exhibits a large decrease in energy concentration. However, there is still some fluctuating energy concentrated behind the rider's knees/legs. This distribution is consistent with the previous results for streamwise velocity, although the reduction in energy, compared to the first mode, is greater. Similar to previous results there is a slight bias to the left of the image, most likely due to an asymmetry in the athlete. The second harmonic ( $3\omega$ ) shows relatively small increases in energy compared to the dominant pedalling frequency. However these are symmetric about the centreline and correlate with the distribution previously observed in streamwise velocity.

The tandem wake exhibits a significant reduction in peak energy at each of the three key modes of the cadence frequency, compared to the single rider result. Even at the cadence frequency, peak power in the tandem wake is significantly lower than that seen for the single rider. However, close examination shows that the distribution is similar, with peak power concentrated in regions behind the hips. At the higher modes the peak power is an order of magnitude lower than the maximum seen in the single rider wake.

The reduction in peak power at the higher harmonics is consistent with previous results from streamwise velocity. However, the peak power at the cadence frequency is lower than previously seen in the velocity measurements with the cobra probe. Individual spectra show that there is power concentrated at these key frequency bands, but they are significantly smaller than the maximum observed in the single rider wake.

### 5.5.3 Wake Profiles of a Static Cyclist

To further investigate the correlation between the streamwise total pressure and the streamwise velocity component, a series of measurements were taken in the wake of the cyclist at 12 static leg positions around the crank cycle ( $30^{\circ}$  increments). The time averaged wake results are shown in Figure 5.5.7 below. These static measurements also provide a reference point for comparison of the dynamic results when extracting phase averaged profiles.

Results clearly show a periodic oscillation in the wake with the low velocity region switching sides at the midpoint of the crank cycle ( $180^{\circ}$ ). This is consistent with the detailed static results presented by Crouch et al. (2014) which showed the strong relationship between leg position and wake structure. As one leg is raised the flow wraps down over that hip and separates low on the cyclist's rear. This results in a smaller velocity deficit behind the closed hip. Conversely, on the open hip, flow separates early, resulting in a greater velocity deficit. As the legs transition through  $180^{\circ}$  and the opposite leg is raised, the reverse profile is evident. This switching can be seen in Figure 5.4.18 and 5.4.19 above for the streamwise velocity in the wake of a single and trailing rider using point pressure probe measurements.

For the frames from  $45^{\circ}$  through to  $195^{\circ}$  it is possible to distinguish a distinct localised low pressure region on the left of the image. This is due to the flow separating from the left arm and elbow. However, it is noted that the same is not observed for the right arm. This is likely due to the athlete's positioning on the bike, such that the right arm is further inboard of the hips compared to the left. The effects of cyclist posture on drag and wake structure are discussed in a separate investigation in Appendix K. As the measurement of each static profile is separated in time it is also possible that the asymmetry may be due to movement of the athlete between tests. However, the feature is consistent on the left of the wake across half of the crank cycle, suggesting it is due to the athlete's posture, rather than a change occurring between tests. In certain profiles, the low pressure region behind the head is more distinct than in others. This is most likely due to changing interaction with the large scale flow separation occurring over the cyclist's hips and lower back. Though it could also be contributed by slight changes in the athletes head and back position between tests.

As the cyclist wake is dominated by a large region of low pressure consistent across all leg positions, the fluctuating component in the flow is difficult to distinguish. To extract only the fluctuating component from the static profiles the time averaged dynamic wake for the pedalling single rider was subtracted from each static profile. These results are shown in Figure 5.5.8 below.

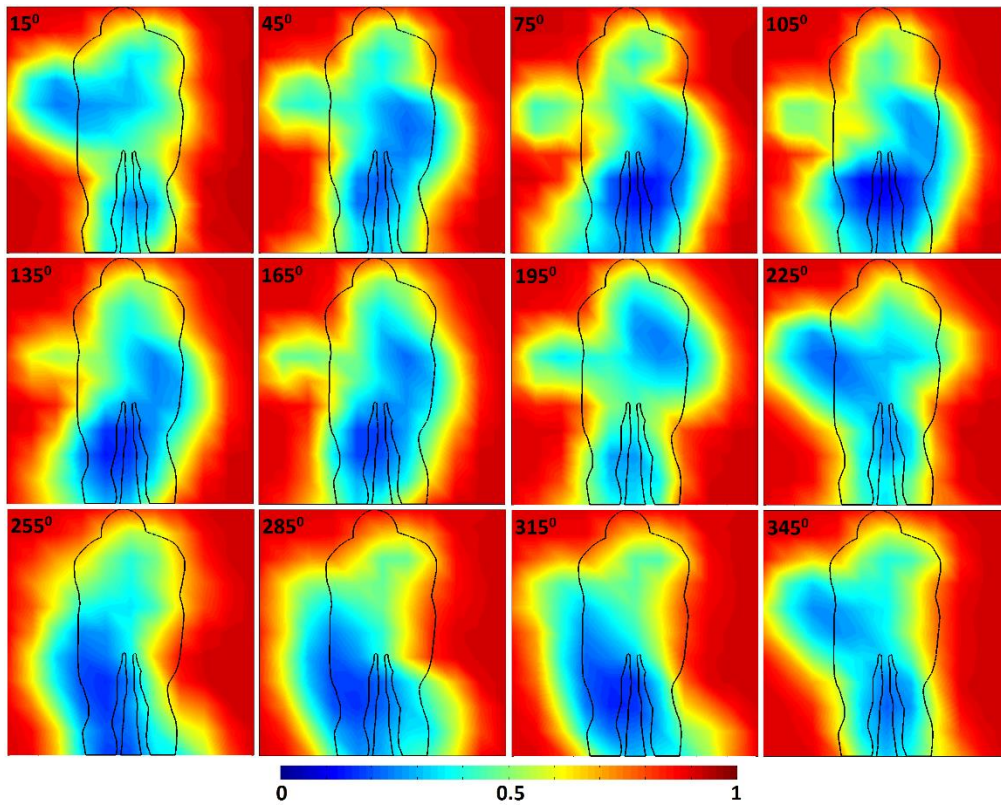


**Figure 5.5.7** - Time averaged streamwise component of total pressure coefficient in the wake of a single static cyclist at the stated leg positons

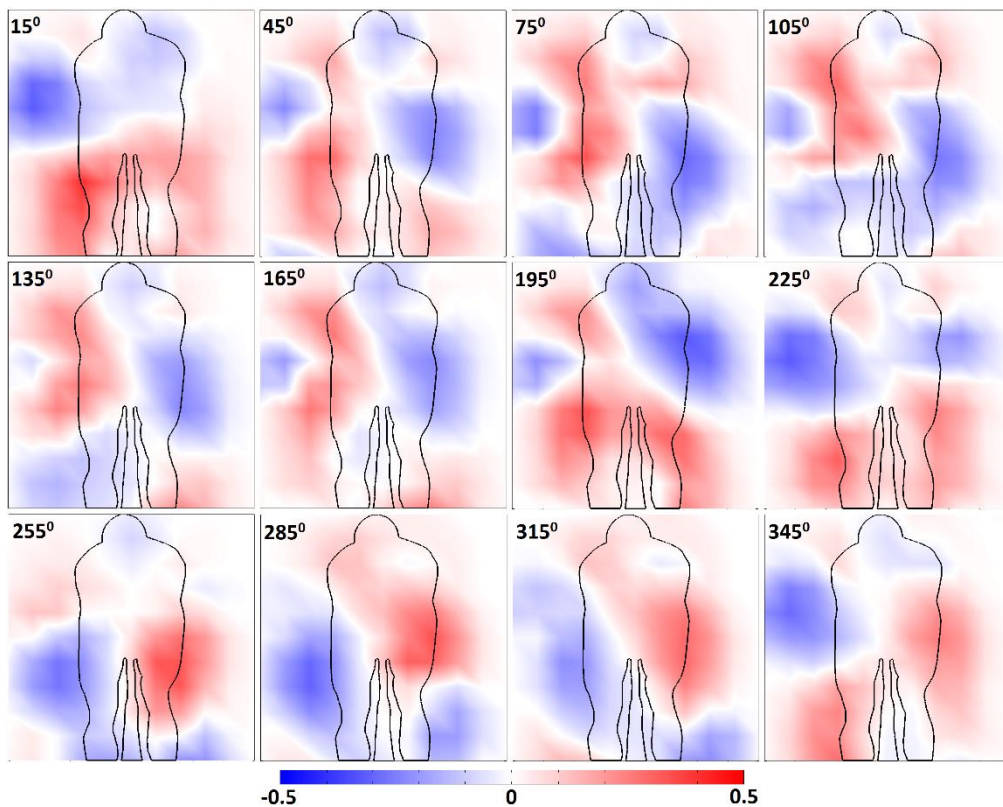


**Figure 5.5.8** - Time averaged streamwise component of total pressure coefficient difference from time averaged dynamic wake of a single static cyclist at the stated leg positons

After subtracting the time averaged wake from the static profiles the fluctuating component can be more clearly identified. At  $15^\circ$  there is a definite symmetry to the wake either side of the centreline. This pattern is expected to then be repeated half a cycle later at  $195^\circ$ . However, it can be seen that the  $195^\circ$  is not fully symmetric. It appears to be transitioning towards the symmetric regime. This is evident as the  $225^\circ$  profile also shows similarity to the  $15^\circ$  profile. The reason for this slight shift in the symmetric regime is that the cyclist's upper legs are not perfectly level at  $15^\circ$ . Crouch et al. (2014) noted in their analysis that the  $15^\circ$  crank angle and subsequent symmetric wake profile coincided with the upper legs being level. In the case of this athlete, the upper legs were aligned slightly later at  $23^\circ$ . This postpones the symmetric regime previously identified. In addition, subtle nuances with the interaction between the athlete's legs and hips, as well as the individual shape of torso and legs, will influence the exact angle that the symmetric regime occurs. It is also noted that the angular range over which that regime occurs is small, with the crank cycle being dominated by the asymmetric regimes for each leg being alternatively raised and lowered. The result of this is that the symmetry point for the athlete is occurring somewhere between  $195^\circ$  and  $225^\circ$ . This is close to that previously proposed in literature and coincides with the position where the athlete's thighs are level.

From the symmetric profile, as crank angle increases the asymmetric nature of the wake becomes clearly apparent with a positive region dominating the left of the wake and a negative region to the right. These two regions are consistently the dominant features of the wake across the first half of the crank cycle ( $45^\circ$ - $165^\circ$ ). Other small regions do appear in different frames but are secondary in nature and are less consistent with crank angle. As the legs transition through the second symmetry point between  $195^\circ$  and  $225^\circ$  a similar but opposite flow regime is observed now with negative on the left and positive on the right of the rider centreline.

Despite the clear similarities between the two halves of the crank cycle, they do not exhibit perfect symmetry with one another. This will be contributed by the fact that testing with an athlete means that it is not a perfectly controlled subject. Subtle variations in the athlete's body position between each static test run are possible as some leg positions are more comfortable than others to maintain statically. In addition there is the coarse spatial grid used for capturing the pressure field. The grid is of sufficient resolution to capture the large features of the wake but small features will not be clearly visible. The  $30^\circ$  increments to crank angle also mean that finer details of the transition between regimes are less clear. Such a step size was necessary to accommodate an athlete test subject as some crank positions are more difficult to maintain statically. This in turn leads to instability in the rider's posture and has subsequent adverse effects on the results. This method made it possible to distinguish key flow features in the wake and thus sufficient indication of the periodic nature of the flow and the changes that occur each half crank cycle as alternate legs are raised.

It has been shown previously that  $75^\circ$  and  $255^\circ$  are characteristic of the two asymmetric profiles (being opposite of one another for alternate legs raised and extended respectively). At  $75^\circ$  a strongly asymmetric pressure profile is observable in the wake. This is dominated by a large positive region on the left side of the frame and a similarly sized negative region on the right of the centreline. With the cyclist at the opposing leg position,  $255^\circ$ , the reverse structure is seen in the pressure profile. A large negative region dominates the left side and opposing positive region on the right.

Although streamwise total pressure in the wake has been shown to correlate with the streamwise component of velocity, pressure coefficient profiles can not identify vortices as there are no rotational flow components measured. However, the established knowledge base for the wake of a cyclist as a function of leg position allows insight to be drawn from the pressure profiles and from this, infer the presence of those streamwise vortices. As these pressure profiles are actually difference from the mean case, the pressure coefficient is showing the changing pressure in the wake. It has been previously described that as the leg of a cyclist is raised, the hip angle is closed which causes flow to wrap over that hip and separate low in the wake. Conversely, on the other side, the leg is extended and flow separates high on the hips/torso which results in a large vortex higher in the wake. From this it can be concluded that the positive region on the left of the  $75^{\circ}$  profile is indicative of the location of the left hip vortex (negative vorticity) as flow on that side remains attached until lower on the rear of the cyclist. The negative region of pressure difference on the right side corresponds with the location of the right side hip vortex which has positive vorticity and separates from high on the rider's hips/torso due to the extended right leg.

#### 5.5.4 Phase Averaged Wake Profiles

Using the cadence sensor to identify each crank cycle from an extended measurement of the wake flow, it was possible to phase average the pressure signal in the wake of the cyclist(s). Initially the crank cycle was divided into 12 segments. This process is analogous to that applied earlier in Section 5.4. The streamwise total pressure coefficient from each point in the wake was then averaged over that segment ( $30^\circ$ ). The mean streamwise total pressure coefficient profiles for a single rider and a tandem pair are shown in Figure 5.5.9 and Figure 5.5.10 respectively.

Phase averaged mean pressure fields exhibit clear changes in the flow occurring in the wake at each segment of the crank cycle. There is also an evident periodicity to the wake flow with a switching occurring approximately every  $180^\circ$  degrees. This is consistent with the static results presented above as well as existing literature. As one leg is raised the flow is channelled over the closed hip and there is a large velocity deficit downstream in the wake, evident here as low pressure. As the alternate leg is raised the field is reversed as flow wraps down over the opposite hip. This generates the periodic flow that is observable in the total pressure coefficient profiles. However, whilst the single and tandem result both exhibit some degree of periodic wake behaviour, the fields are dominated by the large decrease in pressure in the centre of the wake. To highlight the fluctuating regions in the flow, the time averaged mean pressure field was subtracted from each of the phase averaged fields. The resulting profiles of variation in streamwise component of total pressure coefficient are shown in Figure 5.5.11 and 5.5.12 below for the single and tandem formations respectively.

In the static results it was possible to identify the separation from the right arm as occurring distinct from the torso wake. The equivalent feature was not evident on the left side of the wake with the opposite leg raised. Comparing to the phase averaged profiles there is some evidence of this asymmetry with a small region evident at the left arm/shoulder but not so for the left. When considering the wake of the tandem formation, this asymmetry is more pronounced. Across all profiles there is a persistent region of low pressure occurring at the location of the left shoulder. It appears that the addition of the lead rider ahead of the athlete has strengthened the slight asymmetry seen in the single rider results. This is particularly true when considering the time averaged wakes. Whilst the single rider time averaged wake is symmetric, the tandem wake shows an asymmetry. In the tandem case this may be attributed to any slight asymmetry in the mounting of the lead rider ahead of the trail. However, it seems that there is some combination of the effect from the athlete position, as seen for the single tests, and the addition of the mannequin upstream. Significantly, this behaviour is consistent between the static profiles and the time averaged profiles extracted from the dynamic wake. This confirms that these changes are linked to the cyclist geometry rather than the specific result of flow interactions.

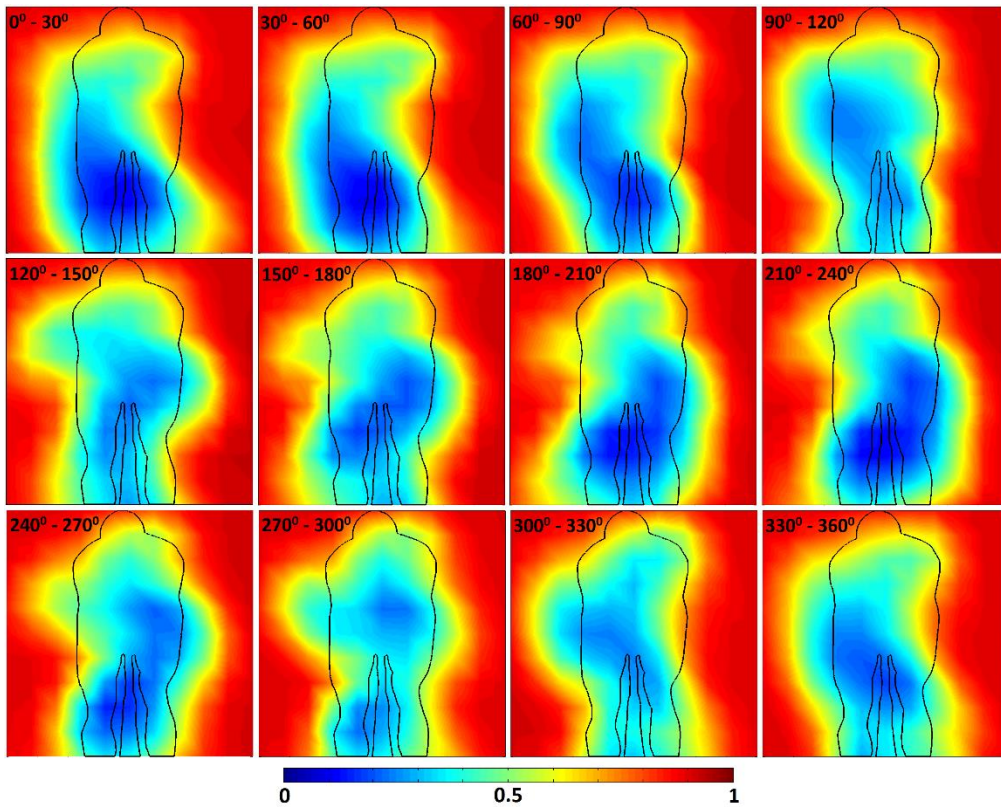


**Figure 5.5.9** - Streamwise component of total pressure coefficient in the wake of a single pedalling cyclist, phase averaged over  $30^\circ$  segments of the crank cycle

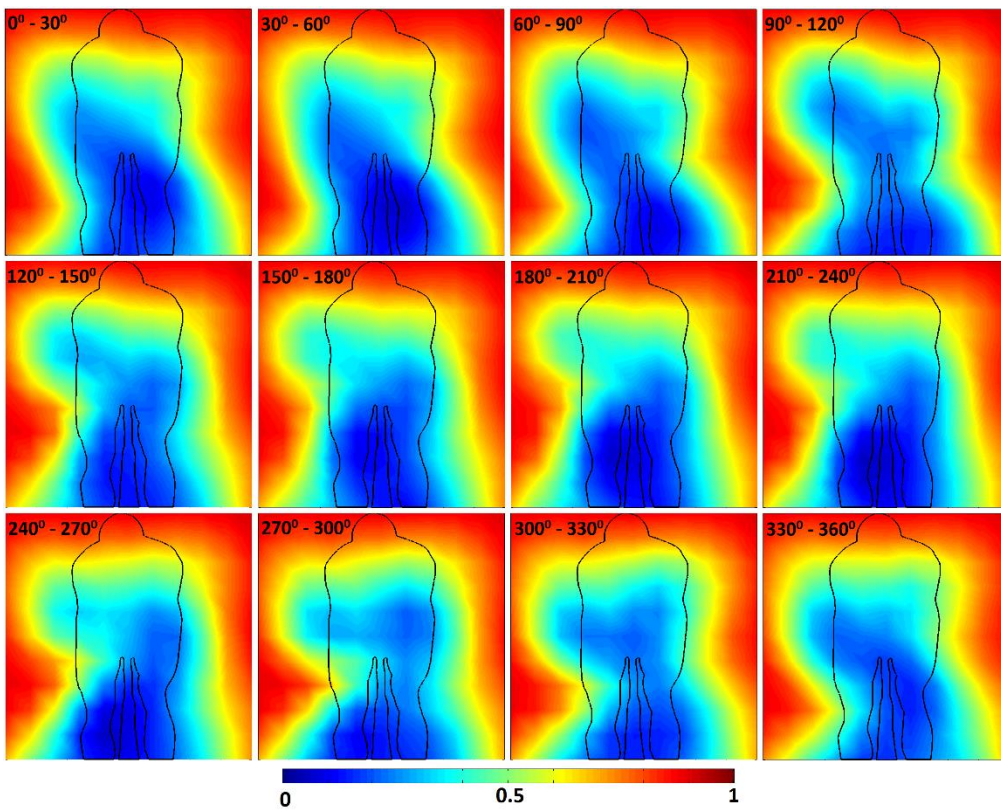


**Figure 5.5.10** - Streamwise component of total pressure coefficient in the wake of two cyclists in a tandem formation with a pedalling trailing cyclist, phase averaged over  $30^\circ$  segments of the crank cycle

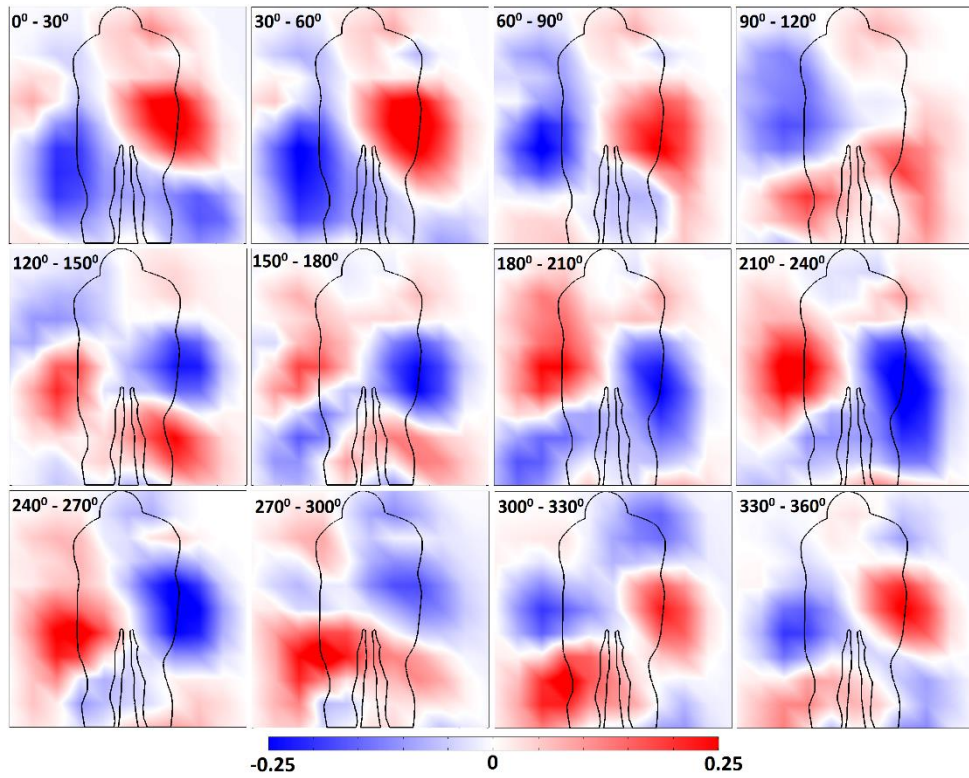


**Figure 5.5.11** - Streamwise component of total pressure coefficient difference from time averaged mean flow for a single pedalling cyclist phase averaged over  $30^\circ$  segments of the crank cycle

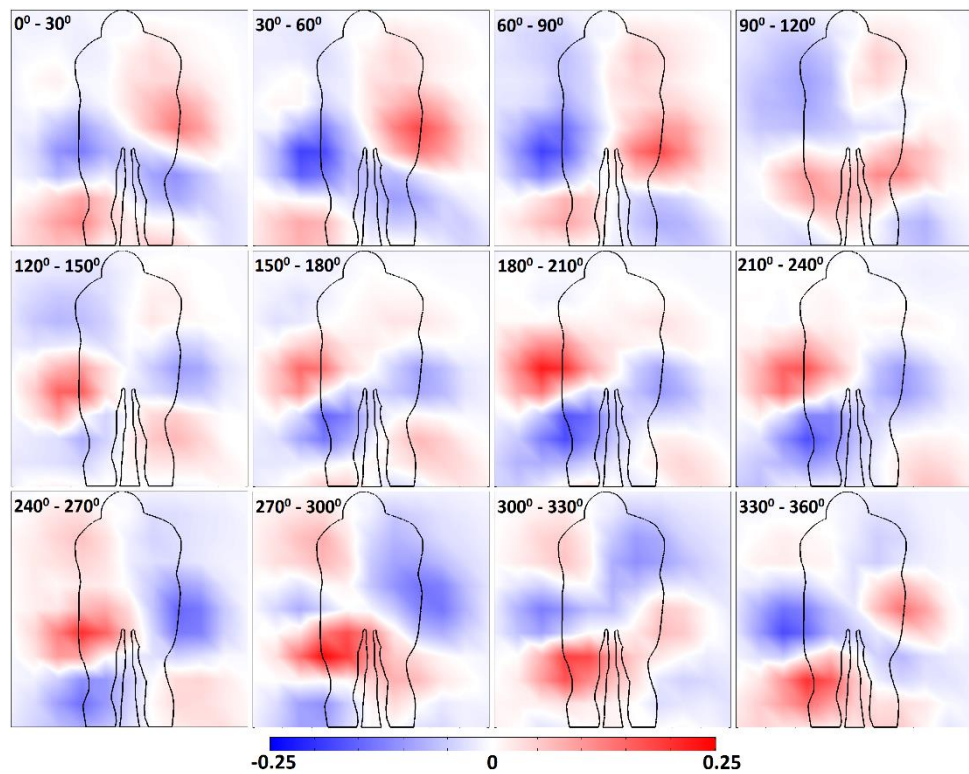


**Figure 5.5.12** - Streamwise component of total pressure coefficient difference from time averaged mean flow for a tandem formation with the trailing cyclist pedalling, phase averaged over  $30^\circ$  segments of the crank cycle

The varying component of total pressure in the wake reveals a strong periodic oscillation evident in both the single rider and tandem wake profiles. This switching coincides with alternate legs being raised and is consistent with previous static results. It can be seen that the wake tends to be dominated by two large and opposite regions either side of the centreline. These reverse sign every  $180^\circ$  in accordance with the opposite leg being raised or lowered respectively. This behaviour correlates closely with fields previously reported from point measurements in the wake. This confirms the correlation between the total pressure component in the wake and streamwise velocity. Comparison with static pressure fields can therefore be used to provide insight into the streamwise velocity behaviour of the dynamic wake of a pedalling cyclist.

Comparing the single and tandem wakes, the two sets exhibit similar distribution for the same respective crank angle. The two opposing regions of change in pressure are clearly evident either side of the centreline in both the single and tandem profiles. However, in the tandem case the maximum pressure difference is reduced compared to the single rider case. This reduction is of the order of 0.1 in total pressure coefficient, which equates to approximately a 10% reduction in freestream magnitude of total pressure. This result is consistent with the results of point measurements using the cobra probe, confirming that the streamwise total pressure component and velocity correlate.

Take the first frame of Figure 5.5.11, averaged over  $0^\circ$  to  $30^\circ$ . The single rider result at this position shows a clear asymmetry with a strong negative region dominating the left of the wake and an equivalent positive region on the right. These two regions are also slightly offset vertically. This coincides with the dominant hip vortices which have previously been shown to be offset. On the left the negative region extends across the centreline beneath the primary positive region. In the case of the tandem wake a very similar structure is observed. Although the overall profile shows lower peak pressure difference, the same features still dominate the wake; a negative region on the left and a positive on the right, sitting slightly higher in the vertical plane. The one distinct difference in the tandem wake profile is the additional positive region in the lower left of the frame; although evidence of this secondary region are evident in the single rider wake. As the crank cycle progresses the two cases follow the same pattern. Up to  $90^\circ$  both single and tandem wakes are dominated by a negative region on the left of centre and positive on the right. The wake profiles then transition through the symmetric region and as crank angle increase further, the asymmetric profile is reversed with a positive region on the left and negative on the right.

In the tandem wake, the second half of the crank cycle exhibits a slight difference compared to the first half. From  $180^\circ$  to  $240^\circ$  there is a bias of pressure fluctuation on the left half of the wake with the two distinct regions (of opposite sign) on the left of the cyclist stronger than their opposites on the right. In the single rider wake profiles between  $180^\circ$  and  $270^\circ$  a negative pressure region is evident on the left side of the wake beneath the primary positive region of pressure difference, however this is weaker than the primary negative region on the right of the cyclist wake. In the tandem wake this secondary region in the lower left of the frame is stronger than the expected 'primary' structure on the left of the centreline. Given that the negative region on the left of the wake is still evident and the relative magnitude of pressure fluctuations in the tandem wake, this difference does not indicate a major change in the composition of the tandem cyclist wake. This asymmetry correlates with the fluctuating energy distribution shown in Figure 5.5.6 above. Previous results from the wake traverse with a cobra probe show that this slight asymmetry is due to the use of athletes in testing and the associated inherent asymmetries.

Pressure profiles from the same athlete in static positions around the crank cycle provide a direct point for comparison for the phase averaged profiles from the dynamic cases. As was the case with the point measurements with the cobra probe, there is an angular offset between the flow regimes identified for a static cyclist and the leg position in phase averaged results. The reason for this discrepancy is that the wake measurements are indexed to the position of the cranks at the point of measurement. As the wake is being measured downstream of the athlete there is convection time for the flow to move downstream from the point of generation on the athlete to the probe location. During such time the cranks continue to rotate. As such, the crank angle index applied to the phase averaged results does not line up with the static leg position at which that regime would be expected. This creates an effective phase shift between the wake profiles of the dynamic cyclist and those for a cyclist at a static leg position. As described earlier, the calculation of a convection velocity results in a phase offset of  $31^\circ$  and  $32^\circ$  for the single and tandem wake respectively. However, inspection of the profiles show that the phase offset is significantly greater than this. In the phase averaged profiles the transition region is observed to begin in the  $90 - 120^\circ$  frame. However, static profiles show the wake is close to symmetric at  $15^\circ$ , which is consistent with previous results. The symmetric wake should coincide with the upper legs of the cyclist being level. In the case of this athlete that point occurs at  $23^\circ$  crank angle. This results in an effective phase shift of the order of  $67^\circ$ ; using  $90^\circ$  as the symmetry point, as observed from wake profiles. This is over twice the offset calculated from a wake convection velocity. However, the offset is consistent with the previous results from the multi-hole pressure probe measurements with the flow transitioning between asymmetric regimes at the same crank angles. Reverse calculation reveals that a  $67^\circ$  shift equates to an effective convection velocity of 0.34 in normalised velocity. This is below the minimum velocity measured in either the single or tandem wakes. It is therefore concluded that there is some additional mechanism associated with the formation and transport of the hip vortices for a dynamic cyclist. Furthermore, both the single and tandem wakes observe a similar phase shift in the results; of the order of  $67^\circ$ . However, given the lower mean velocity for the tandem wake it is expected that the phase shift will be slightly greater. The visual identification from these results does not offer resolution to distinguish any significant difference in the phase shift between the single and tandem cases.

A phase difference of the order of  $67^\circ - 97^\circ$  offsets the static and phase average profiles by 3 frames in Figures 5.5.8, 5.5.11 and 5.5.12. Comparing the two sets at this offset, it can be seen that the primary flow features evident in the static profiles are also evident in the corresponding phase averaged dynamic results. The wake effectively reflects every  $180^\circ$ . With the left leg raised, the left side of the wake exhibits a positive difference in local pressure (from the mean), with a corresponding negative on the right side. These two regions are persistent over half of the crank cycle. In the second half of the cycle this basic structure is reversed. With the right leg raised the left side of the wake exhibits a negative pressure with a corresponding positive on the right side. This direct comparison with the static results is evidence that the primary wake features observed in the wake of a static cyclist are forming and evolving at a sufficient rate to remain prevalent in the wake of a pedalling cyclist. This remains true for the wake of a trailing cyclist in a tandem pair.

Despite the evident transition occurring at the half crank cycle in the phase averaged results, the expected symmetric profile is not clearly observed. One reason for this is the angular size of the segments used in the phase averaging. Whilst the asymmetric regime occurs over a wide range of crank angles, the symmetric regime occurs in a much narrower band. Therefore, the large phase bins result in a loss of resolution in capturing a clean symmetric wake profile. Additionally the dynamic

evolution of the cyclist wake may mean that a distinct symmetric profile, as observed in static tests, is not apparent in instantaneous snapshots. However, even though the symmetric profile may not be distinctly evident, the transition between the two asymmetric flow profiles can be clearly identified. Evidence of this occurring is present from the transitional profiles where flow can be seen moving towards symmetry. By reducing the width of the phase averaging segments it is possible to generate better resolution of the transitional behaviour of the wake flow. The time series pressure data was sufficient to be dissected into smaller segments of the crank cycle. The size of the phase averaged segments was halved to produce 24 individual frames for a full crank cycle. The velocity difference from the mean for the single and tandem cases are plotted in Figures 5.5.13 and 5.5.14.

Increasing the number of phase averaged segments exhibits the same fundamental behaviour in the pressure fluctuations in the wake. The same pattern is evident in terms of oscillating positive and negative pressure regions. However, by increasing the temporal resolution the transition between the two phases of the cycle is more distinguishable. Consider the  $75^{\circ}$  -  $90^{\circ}$  profile; the growth of positive pressure in the lower left of the frame is evident. The following series of frames show the wake pressure profile distorting as the legs transition through the level position and the wake structure reverses. Between  $105^{\circ}$  and  $135^{\circ}$  the two profiles show evidence of the symmetric flow regime observed for static cases where the upper legs were level. Although not perfectly symmetric about the centreline, there are no longer two large regions of opposite pressure either side of the centreline that indicate the presence of the dominant hip vortices. Instead the lower section is positive on both sides of the centreline and the upper section negative. Beyond  $135^{\circ}$  the negative region on the right side grows, followed by the positive pressure region on the left of the centre. This indicates the reversal in the wake structure. Similar behaviour is observed  $180^{\circ}$  later, at  $285^{\circ}$ , for the opposite leg case.

The same description can be applied to the tandem cyclist wake. Similar transitional flow behaviour is observed as the wake transitions from one asymmetric regime to the other. The notable difference with the tandem wake is that in the second half of the cycle ( $>180^{\circ}$ ) the negative pressure region on the left side of the rider, below the primary positive region, is stronger than the expected primary region on the right of the centreline. In the single rider case the right side negative region was dominant but also extended across the centreline and below the left side positive region. The difference with the tandem case is that the centre height right side negative region is relatively weaker. However, the presence of negative pressure in that location is consistent with the single cyclist result as well as the reverse from the first half of the crank cycle.

As noted, the coarseness of the sampling grid contributes to the fact that a clearly symmetric wake is not observed. Furthermore, this technique is looking at wake pressure, not streamwise vorticity, and so changes are only indicative of the presence of vortices that have been previously characterised using other techniques. Most significantly, these results are capturing a dynamic response to the cyclist's geometry, rather than a static cyclist where the wake is able to evolve and stabilise. As such, the dynamic wake was not expected to be as clearly defined as that seen for a static cyclist. Despite this, the conclusions about the influence of pedalling dynamics on flow over a cyclist are consistent. The flow regimes observed for a static cyclist are strongly representative of the flow field for a dynamic pedalling cyclist. Vortex shedding from the hips dominates the wake and evolve at a higher rate than the leg rotation meaning that snap shots from a dynamic cyclist wake are consistent with fields from a static cyclist.

From these results it can be concluded that the wake of a tandem trailing cyclist maintains similar dynamic flow behaviour to that of a single cyclist. This is consistent with previous work which has shown the wake of a tandem pair to be similar to that of single cyclist from both static tests of scale models and the full scale wake traverse. Whilst some small differences are evident between the two sets of results, the primary flow structure from the phase averaged profiles remains the same for both cases. The most significant difference observed in the trailing rider wake was a reduction in the range of maximum total pressure fluctuations. This is consistent with previous results from point measurements with a cobra probe. It can be concluded that the lower energy and disturbed flow conditions seen by the trailing cyclist result in a reduction in fluctuating streamwise velocity in the wake. It has also been shown that the streamwise component of total pressure in the wake correlates closely with the streamwise velocity component. Therefore observed changes in wake pressure can be used to infer the behaviour of streamwise velocity in the wake.

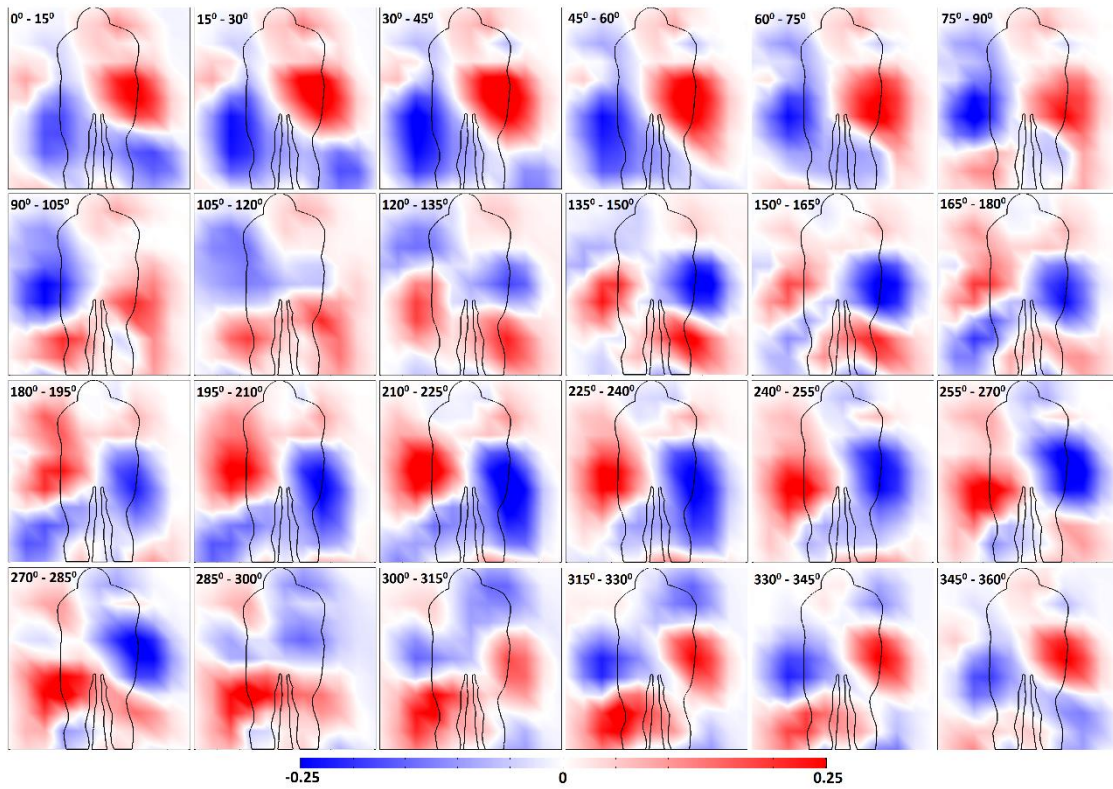


**Figure 5.5.13** - Streamwise component of total pressure coefficient difference from time averaged mean flow for a single pedalling cyclist, phase averaged over 24 segments of the crank cycle

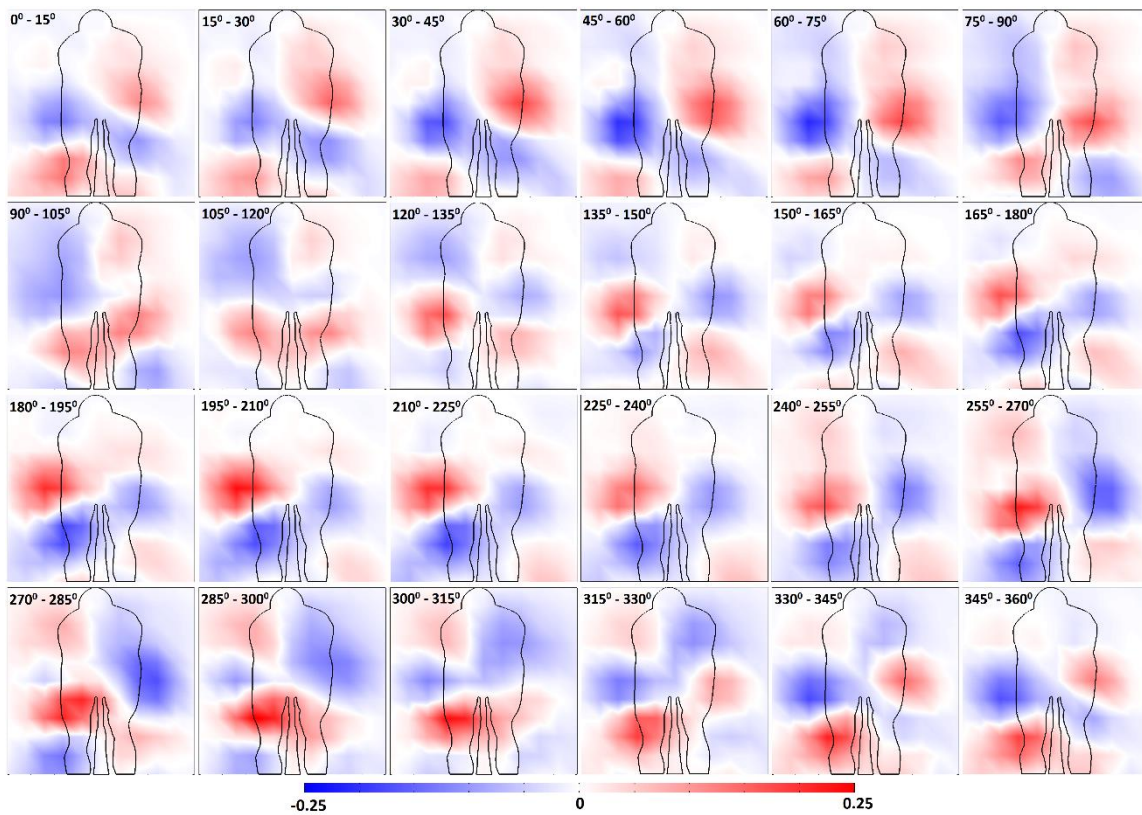


**Figure 5.5.14** - Streamwise component of total pressure coefficient difference from time averaged mean flow for a two rider tandem pair, phase averaged over 24 segments of the crank cycle

### 5.5.5 Modal Decomposition of the Dynamic Cyclist Wake

Proper orthogonal decomposition (POD) was performed on the time resolved pressure results to further investigate the dynamic effects of a pedalling cyclist in both single rider and tandem pair formations. The energy spectrum for the first 10 modes of the single rider wake is shown in Figure 5.5.15 below. Energy is plotted relative to the mean flow energy and then normalised by the first fluctuating mode. It can be seen that the first fluctuating mode contains the majority of the fluctuating energy. However, Mode 1 is only 10% of the mean flow energy (Mode 0). Mode 2 is then less than 40% of Mode 1 and Mode 3 onwards are less than 20% and decreasing. Subsequent modes show a continued gradual decrease in energy and these modes will have small overall contribution to the composition of the wake. In fact even Modes 3 and 4 will have small significance given their energy content is of the order of 2% of the mean flow. Comparison with Figure 5.5.1 shows that, as expected, Mode 0 exhibits the same profile as the mean pressure field for the single cyclist wake.

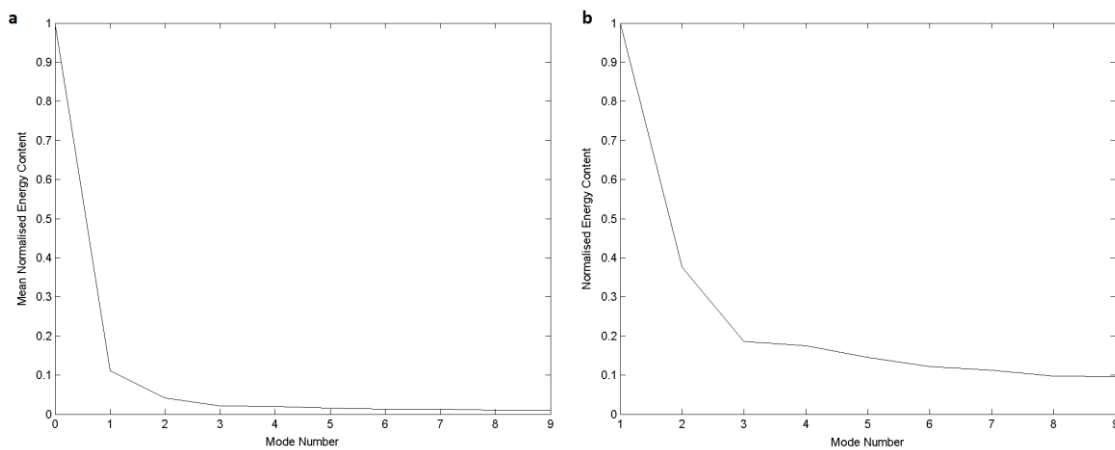


**Figure 5.5.15** - Energy content of each POD mode for the single rider wake. L – Normalised by the mean flow (mode 0) energy, and; R - normalised by the first fluctuating mode (mode 1)

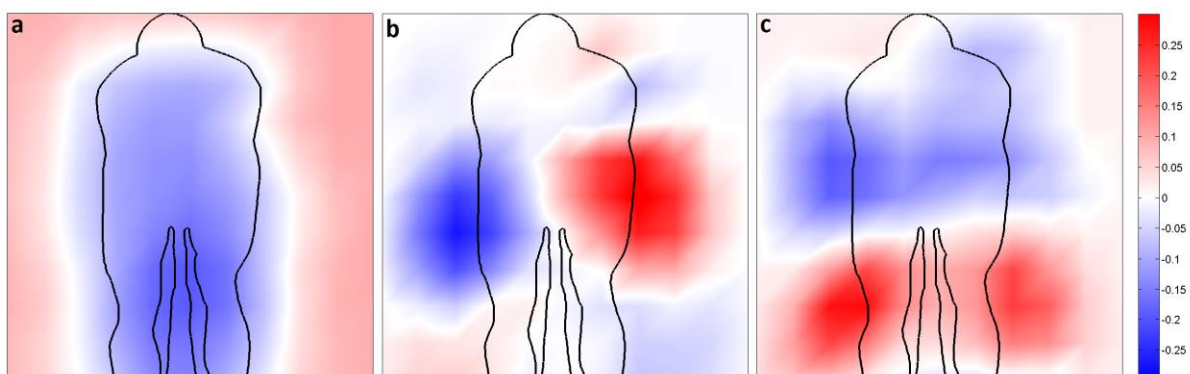


**Figure 5.5.16** - First three modes generated from POD of the total pressure in the wake of a single pedalling cyclist (L-R; Mode 0, 1, 2). Energy content has not been normalised so energy scales are not equivalent – see energy distribution in Figure 5.5.14. Mode 0 represents the mean flow.

Figure 5.5.16 shows the mean flow (Mode 0) and first two fluctuating modes resulting from the proper orthogonal decomposition of the single rider dynamic wake. These profiles are plotted with individual colour scale for clarity. Relative energy content of each mode is depicted in Figure 5.5.14. According to the energy spectrum, the first fluctuating mode contains the majority of the fluctuating energy in the flow. The profile for Mode 1 can be seen to exhibit strong similarity to the asymmetric pressure difference profiles observed in phase averaged wake fields. The interrogation region is dominated by two regions of equal size and strength but opposite sign, positioned adjacent with one another either side of the centreline. Given the persistence of this flow regime in the static and phase averaged difference results it is not surprising to see the primary fluctuating mode to resemble the same profile. The reason for this flow regime, as described earlier, is the periodic nature of the flow over a cyclist. As each leg is alternatively raised and lowered, the wake structure goes through large changes. When one leg is raised the flow wraps around that hip and separates lower on the rear of the cyclist and induces large cross flow and downwash. On the opposite side where the hip is open, flow separates early causing a large separation region. As the cyclist pedals this scenario switches from left to right, generating a large scale oscillation in the wake.

In contrast to the first mode, Mode 2 is symmetric about the rider centreline. The profile contains seemingly 4 regions in each quadrant of the interrogation window. The upper two are of the same sign and conjoin to nearly form a single large region. The lower pair is of similar structure but opposite sign. This wake regime is characteristic of the symmetric flow regime observed in the static results and apparent in the transitional regions of the phase averaged dynamic results. The fact that these two modes contain the majority of the fluctuating energy confirm that the two key flow regimes previously identified from static experiments remain dominant in the wake of a dynamic pedalling cyclist.

The decomposition for the tandem wake shares strong similarity with the single rider result; consistent with the previous findings. The energy spectrum is shown in Figure 5.5.17 below. Figure 5.5.17a shows the mode energy normalised against Mode 0, the mean component. Figure 5.5.17b shows the energy spectrum of the first 9 fluctuating modes normalised by the first fluctuating mode. It can be seen that the fluctuating component is very small compared to the mean flow; with even Mode 1 being less than 5% of the magnitude of the mean flow. This is less, even than the single rider spectrum, which showed the first fluctuating mode to be around 10% of the mean. However, this is consistent with the previous phase averaged difference profiles and frequency spectra which showed that the fluctuating component in the tandem wake was of smaller magnitude than that of the single rider wake. The fluctuating normalised energy spectrum shows that the decay in energy does not appear as rapid as the single rider result. However, given the relatively smaller proportion of energy in the first mode, the significance of higher order modes remains small.

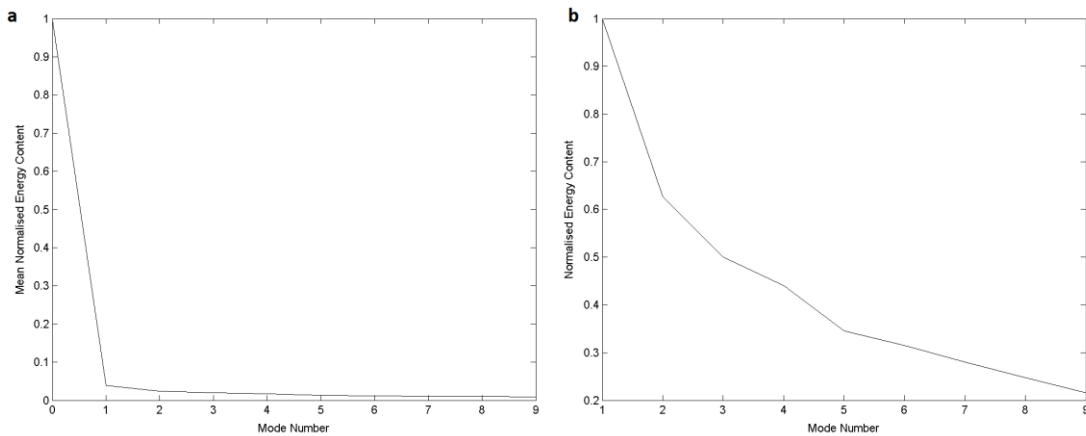


**Figure 5.5.17** - Energy content of each POD mode (a) normalised by the mean flow (Mode 0) and, (b) normalised by the first fluctuating mode (mode 1)

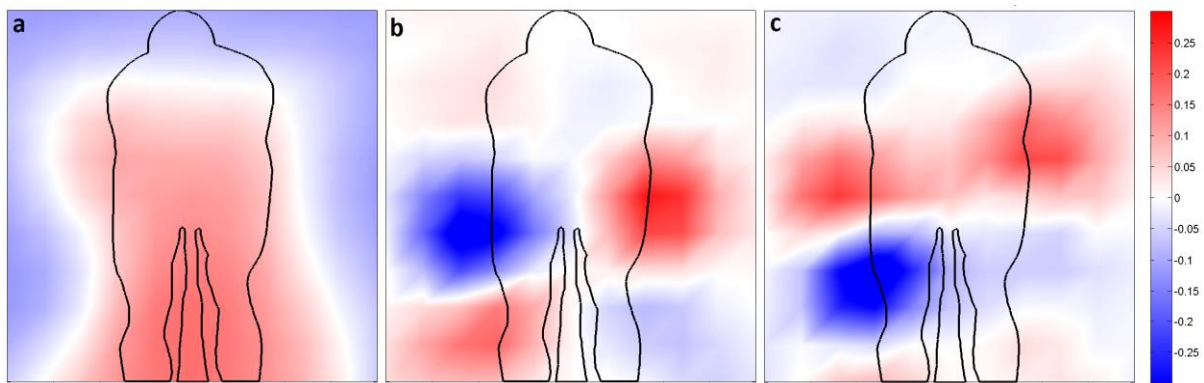


**Figure 5.5.18** - First three modes generated from POD of the total pressure in the wake of a tandem trailing cyclist (L-R; Mode 0, 1, 2). Energy content has not been normalised so energy scales are not equivalent – see energy distribution in Figure 5.5.16. Mode 0 represents the mean flow.

Figure 5.5.18 shows the first 3 modes from the POD of the tandem wake pressure data. Mode 0 shows the expected similarity to the time averaged mean flow results (Figure 5.5.1), including the slight asymmetry in the upper left of the interrogation region. Mode 1 shows the same basic pattern observed for the single rider case. The profile is dominated by two regions of opposite sign situated either side of the centreline. These features are representative of the periodic oscillations in the wake as the legs translate and there is large scale separation from alternate hips. This lateral oscillation of velocity in the wake was observed in the phase averaged results and is captured clearly by the decomposition. It must be noted that the mode profiles have independent scales. As such, the intensity in Mode 1 for the tandem flow appears the same as it is in the single rider case. However, the energy spectra in Figure 5.5.17 show the relative energy content of each mode. The first fluctuating mode in the tandem wake is of the order of half the strength of the single rider result, although the structure of the mode remains similar.

The second fluctuating mode exhibits a more symmetrical structure about the centreline of the frame, similar to the single rider result. However, the left side shows a significantly stronger negative region on the right side compared to the left. The fact that both sides of the centreline exhibit the same sign is similar to the single rider result and is characteristic of the symmetric flow regime observed when

the cyclist's legs are positioned level. The increased energy in the lower left of the frame, beneath the left hip, is consistent with the phase averaged pressure difference and streamwise velocity presented earlier, which exhibited a bias to the lower left. This shows that there is an asymmetric distribution of energy beneath the hips, likely resulting from an asymmetry in the cyclist's pedalling style. Between  $150^{\circ}$  and  $270^{\circ}$  the balanced asymmetric profile, as characterised by Mode 1, also exhibited a distinct negative region in the lower left quadrant of the frame. This was also seen in Mode 2 for the single rider, but was less pronounced. Given the same athlete was used it is suggested that the change to the inlet conditions for the trailing cyclist is acting to magnify an asymmetry inherent in the athlete's geometry and pedalling motion. It is also important to note that the maximum energy in Mode 2, for both single and tandem cases, is significantly lower than the mean flow. In higher order modes the energy contribution is very small and so has minimal contribution to the overall composition of the wake. However, comparison of subsequent modes for the single and tandem wakes shows that the two sets maintain a similar distribution in subsequent modes.

Proper orthogonal decomposition has revealed that there are two primary fluctuating modes prevalent in the wake of a cyclist. The first is characteristic of the periodic oscillations that occur in the wake as the result of shedding from alternate hips as legs translate around the crank cycle. The second exhibits greater symmetry, correlating with the symmetric flow regime identified in static tests when the upper legs are level. These characteristic structures are consistent with the fluctuating phase averaged results. Energy content of each successive mode decreases significantly, such that the first and second modes are the most significant. The structure of the modes for both the single rider wake and the tandem wake exhibited strong similarity over the dominant modes. This is consistent with all previous results and confirms that the flow over a trailing rider is not sufficiently disrupted to cause large differences in flow behaviour to that observed for a single cyclist in isolation.

## **Summary**

A grid of pressure taps was used to map the full field dynamic response of the wake of a cyclist in single and tandem formations. Streamwise component of total pressure, as measured with a forward facing pressure tap, was observed to correlate closely with streamwise velocity in the cyclist wake. Dividing the crank cycle into segments and phase averaging revealed a periodic behaviour that reverses every half crank cycle as the legs are raised and lowered alternatively. As one leg is raised and the other lowered there is a strong asymmetry in the dominant vortices in the wake that form from the hips. It is the oscillation of these structures with each half crank cycle that is evident in the pressure field of the cyclist wake. Spectral analysis showed that the pedalling frequency of the rider contains the majority of the fluctuating energy in the wake, with secondary peaks also observed at the next two higher order harmonics. The spatial distribution of fluctuating energy indicates the primary regions behind the cyclist hips, at the location of the dominant hip vortices.

Analysis of two cyclists in a tandem pair showed that wake structure and dynamic behaviour does not greatly differ from that of a single cyclist. Phase averaged results show that periodic changes in the wake are consistent with the formation and movement of the hip vortices, which dominate the wake as each leg is raised and lowered respectively. Frequency spectra show that the fluctuating energy is concentrated at the pedalling frequency and behind each hip in the wake. However, tandem results exhibit a reduction in the magnitude of fluctuating energy. Phase averaged results exhibit a reduction in magnitude of change in streamwise total pressure coefficient. This aligns with spectral results which showed a reduction in peak amplitude at each key frequency. The wake of a tandem cyclist exhibits the same fundamental flow structure dominated by the streamwise vortices that form over the hips of the cyclist and move in the wake with the position of the legs. Whilst a reduction in the fluctuating energy in the wake may contribute to the drag reduction experienced by the trailing cyclist, the relative change in fluctuating energy components is not sufficient to account for the large change seen in drag measurements. This further confirms that the drag reduction for the trailing cyclist in a tandem pair is not the result of disruption to the dominant wake structures.

The dynamic behaviour and energy distribution in the cyclist wake are consistent with the previous results seen from the independent point measurements with the cobra probe. This confirms that even with relatively short sample time required to accommodate athlete testing, point measurements can still provide useful insight from limited number of cycles. Due to the coarse spatial grid used it is not possible to determine the smaller scale structures from this data. However, results clearly show the location and change of the dominant hip vortices. This confirms that the flow regimes observed for static cyclists do evolve on sufficiently short time scales to be evident in the wake of a dynamic rider.



# Chapter 6

## Conclusions

### **6.1 Major Findings**

#### **6.1.1 Drag variation with relative spatial position**

The drag acting on two cyclists travelling in formation was characterised as a function of spatial position. A tandem formation, representative of a drafting scenario, have been investigated previously in literature, but differences in setup have resulted in no unified model for drag variation as a function of separation distance. This work quantified the drag saving for the lead and trailing cyclist in a two rider tandem team with separation distance, including the effect of lateral offset from centreline. For a dynamic athlete a maximum drag saving was found of 2.5% and 40% in the lead and trailing positions, respectively. Both of these occurred with cyclists inline at minimum separation distance. At the maximum separation of 5 m a drag reduction of 25% was still measured for the trailing cyclist when in line with the leader. Testing with the Monash Anthropomorphic Cycling Mannequin suggest that there is some dependence on relative size of the athletes as shown by Edwards & Byrnes (2007). It was also found that with downstream separation less than 1 m, drag is more sensitive to lateral separation than axial separation.

Additional testing was conducted with cyclists in a range of transverse positions, with riders travelling side-by-side, including lateral and axial displacement from this position. Such formations are representative of an overtaking manoeuvre. It was found that at small lateral distance between cyclists there is a drag increase of up to 6%. In addition, the interactions induce significant repulsive side force, yaw moment and roll moment. However, the interference region is small, and with increasing lateral separation or axial offset of the cyclists, the effects diminish. Beyond 1.5 m lateral separation interactions between cyclists are negligible.

#### **6.1.2 Flow field around two tandem cyclists**

A series of experiments were conducted to provide a detailed characterisation of the flow field around two cyclist in a tandem formation. These included full scale flow visualisation, PIV fields of scale model cyclists and wake surveys of full scale dynamic cyclists. The results of each of these investigations combine to give a more detailed understanding of the flow field.

### ***Full Scale Flow Visualisations***

Full scale visualisation using smoke injection and surface wool tufts provided a fundamental insight into the flow behaviour around two tandem cyclists. Wool tufts indicated that the separation behaviour over the cyclists hips, were similar for both leading and trailing riders in a tandem pair. With upper legs level the flow behaviour over the hips was symmetric. With one leg raised and the other extended there was a distinctly asymmetric flow behaviour and separation from the hips. This is consistent with previous results for a single cyclist. Furthermore, with the introduction of pedalling legs, the flow could be seen to transition from one asymmetric flow regime to the other as each leg was raised or lowered around the crank cycle. This suggested that the primary streamwise vortices shedding from the hips would still be present in the wake of tandem cyclists. Smoke injection showed much greater turbulence ahead of the trailing rider, as a result of travelling in the leaders wake. This indicates a reduction in flow momentum impacting on the trailing rider, which would contribute to the drag reduction measured for a trailing cyclist in a tandem formation.

### ***Flow Field Around Scale Model Cyclists***

PIV was used to capture high resolution velocity planes around static scale model cyclists in single and tandem formations. Limitations on the water channel setup resulted in a Reynolds number that was an order of magnitude below that of a full scale cyclist at racing speeds. However, validation of the single cyclist wake profiles against the full scale work of Crouch et al. (2012, 2014) showed that wake structure maintains a similar profile. Therefore, it is reasonable to assume that investigation of two scale model cyclists will provide insight into the flow field around two cyclists in tandem at full scale Reynolds numbers.

Streamwise vorticity planes in the wake showed that the wake structure of a trailing cyclist in a tandem pair maintains similarity with the single rider wake. The primary hip vortices identified in the single rider wake remain the dominant features of the tandem wake, although the magnitude of vorticity is decreased. It was identified that much of the vorticity reduction in these coherent structures is due to the reduction of streamwise energy at the inlet. In the symmetric wake profile, the thigh vortices in the tandem wake are affected and exhibit a loss of vorticity and translation away from the rear of the rider at small separation. At a bicycle length separation the magnitude of vorticity is not greatly recovered in the tandem wake. However, the distribution of vorticity more closely resembles the single rider wake. In the symmetric wake profile, the location of the thigh vortices is more similar to the single rider case at this distance.

Changes to the lead rider leg position were found to not greatly affect the primary hip vortices of the trailing cyclist. However, some small secondary vortices formed on the lower legs and feet were affected by changes to model leg position. This indicates that the geometry of the cyclist has such powerful influence over the formation of the hip vortices seen in the wake of a cyclist, that their generation is largely independent of inflow conditions.

The most significant difference between the trailing and single rider flow fields was the inflow velocity ahead of the trailing cyclist. Mapping of the flow between the lead and trailing cyclists showed a large reduction in streamwise velocity in the effective inflow for the trailing rider. This is clearly due to the

sheltering from the lead cyclist wake. As separation distance is increased, the flow recovers energy from the freestream such that the trailing cyclist is exposed to higher effective inlet velocity than a rider at smaller separation distance. This suggests that reduction of streamwise momentum at the inlet for the trailing rider is a major contributor to the measured drag reduction.

### ***Full Scale Pedalling Cyclists***

To validate the results of scale model tests for full scale dynamic cyclists, wake surveys were conducted in the wake of a pedalling athlete in single and tandem formations. Time averaged results showed some similarity between the single cyclist and tandem wakes. Streamwise vorticity, spanwise (V) and vertical (W) velocity components and turbulence intensity profiles were all similar between the single and tandem cases. However, the tandem wake showed an increase in the streamwise velocity deficit in lower region of the wake; below the hips. Scale results also showed lower velocity in the lower region of the tandem wake, however, this was below wheel height; closer to the ground plane. This difference arises due to the dynamics of the cyclist in the full scale profiles. Pedalling legs incorporate the asymmetric profiles, as well as symmetric, which have been previously shown to have greater velocity deficit in the lower wake. From the quasi-static model it can be expected that a dynamic cyclist will exhibit greater deficit in the lower wake compared to a static cyclist at the symmetric ( $15^\circ$ ) leg position. Despite this difference, the streamwise velocity behind the cyclist's hips remains similar between the single and tandem cases.

Analysis of a pedalling athlete introduces the additional mechanism of dynamic geometry and considerations of how the wake structure varies in time. Spectral analysis shows a strong concentration of power at the pedalling cadence. This is due to the large scale changes in the wake resulting from the motion of the legs. In addition, there was a concentration of energy observed at the two higher harmonics above the pedalling frequency. This was observed in all three velocity components, though power was greatest in the streamwise velocity. Spatial distribution of the peak frequencies showed that maximum fluctuating energy in the streamwise component is concentrated behind the hips of the cyclist where the dominant streamwise vortices form. This behaviour was consistent between the single and tandem cases. However, the tandem wake exhibited a reduction in fluctuating energy at each dominant frequency. Interestingly, at the first harmonic (twice the cadence) the distribution of power differs from the fundamental case. This indicates there is contribution from a different mechanism. It is suggested that this is due to the changing direction of the knee and leg, which occur twice each crank cycle.

Dividing the crank cycle into segments and phase averaging allowed the dynamic evolution of the wake to be characterised. This revealed that the primary streamwise vortices from the hips observed in the wake of a static cyclist evolve sufficiently rapidly to be evident in the wake of a pedalling cyclist. The flow regime could be seen to reverse every half crank cycle as each leg is raised and lowered alternatively. This causes the wake to oscillate between the two asymmetric flow regimes observed in the wake of a static cyclist and characterised by the wake profiles at  $75^\circ$  and  $255^\circ$  crank angles. Comparison between the single and tandem wakes showed that the same wake structure is observed in both cases. This is consistent with the previous results observed for scale models. The same periodic evolution is seen to occur as the legs rotate and the dominant streamwise vortices are identifiable in both cases. The tandem wake only differed from the single case in the magnitude of the fluctuations

in streamwise velocity, which were reduced. As the legs rotate around the crank cycle, the magnitude of the change in streamwise velocity from the time average profile is smaller than that observed for a single cyclist. This is consistent with the spectral analysis, showing a reduction in fluctuating energy in the tandem wake. However, magnitude of streamwise vorticity did not differ significantly between the single and tandem cases, in difference to scale model results. Although peak vorticity in the dynamic wake was reduced compared to that recorded with the static scale models.

The use of a coarse grid to accommodate the testing of an athlete limited this technique to identifying only large scale flow structures. However, the resolution was sufficient to identify the hip vortices, which are the dominant features in the wake. Identification of these therefore provides a strong indication of overall behaviour of the wake.

Simultaneous sampling of pressure fluctuations in a grid in the wake confirmed the findings from the point measurements with the pressure probe. It was shown that the streamwise component of total pressure correlates with streamwise velocity. From this it was observed that the pressure field behaviour follows that of streamwise velocity and can be used to identify the oscillations in the wake due to the change in separation and resulting location of the dominant streamwise vortices from the hips. This validates the use of a pressure grid to map wake dynamics in complex systems such as a cyclist as it is a much more efficient process than sampling point measurements with a pressure probe.

### ***The Tandem Flow Field***

The combined insight of investigations in this project have provided understanding to characterise the flow field surrounding two cyclists in tandem. Streamwise velocity between the cyclists suggests that the wake of the leader is not significantly disrupted compared to a single rider. At small separation it has been shown that there is a reduction in streamwise velocity and increase in base pressure resulting from the upstream influence of the trailing cyclist. For the trailing cyclist, travelling in the wake of the leader results in a significant change in inflow conditions compared to freestream. There is a significant reduction in streamwise velocity as well as flow being inhomogeneous due to the separated flow from the leading cyclist. However, despite the large change in inlet conditions, the trailing rider wake maintains a generally similar structure to the single rider case. Wake survey data showed that profiles of streamwise vorticity, spanwise velocity and turbulence intensity all are similar between the single and tandem wakes. However, there is a greater deficit in time-averaged streamwise velocity behind the legs, as well as greater downwash, in the tandem wake. Furthermore, analysis of the dynamic wake showed that the fluctuations in streamwise velocity in the trailing rider wake are reduced compared to the single rider case.

### **6.1.3 Mechanisms responsible for drag reduction in a tandem formation**

#### ***Lead Cyclist***

In a tandem formation the leading cyclist has been shown to experience a reduction in drag of the order of 2.5 – 5%. This occurs over a much smaller spatial range compared to the effects experienced by the trailing cyclist. Analysis of the streamwise velocity between the lead and trailing cyclists shows that the wake profile of the tandem leader maintains similarity to that of a single cyclist. This suggests that the major vortices are still present. However, a small decrease in the mean velocity over the region was observed in the scale model results. Analysis of the flow field upstream of a full scale cyclist in the wind tunnel showed that there is a forward interference region that extends a short distance (500 mm) upstream of a cyclist. This results in a local decrease in velocity and increase in static pressure. In a tandem formation, the trailing cyclist imposes this field upon the rear surface of the leader. This results in the slight velocity decrease observed in the scale model results. Meanwhile, the pressure results in a small increase in base pressure for the leading cyclist. This acts to partially counteract the pressure drag and results in a small drag saving for the leading rider. The change in static pressure coefficient ahead of a cyclist was shown to be sufficient to induce a drag reduction on the leader of the order of 5%. Due to the pressure field of the trailing rider extending only a small distance upstream, the drag saving for the leading cyclist is only observed for small separation distances. As separation distance increases the leader quickly loses that benefit, whilst the saving for the trailing cyclist extends far further downstream.

#### ***Trailing Cyclist***

Several experimental techniques have been utilised to characterise the flow around tandem cyclists in direct comparison with a single isolated cyclist. Results have consistently shown that the wake of a trailing cyclist maintains a degree of similarity with that of a single rider. At small separation there is some disruption to the wake structure evident in static results, though the primary hip vortices prevail as the dominant feature in the wake. As distance increases the disruption to the wake is reduced. At a separation distance of one bicycle length the distribution of the trailing rider wake is close to that of a single rider, though the magnitude of streamwise vorticity is reduced. Analysis of the wake of a dynamic athlete showed that there is relatively small difference in magnitude of vorticity compared to a single rider. The main change being a reduction in fluctuations of streamwise velocity. Integrating the flow components measured in the trailing cyclist wake has indicated that losses in the wake of a trailing rider do not indicate significant energy recovery to account for the large drag reduction. Although disruption to the primary streamwise vortices may contribute to the drag saving, it is not the primary mechanism. Therefore, the drag reduction for a trailing rider must be primarily due to an upstream effect.

It has been shown that there is a large reduction in streamwise velocity upstream of a trailing cyclist. Applying the reduced streamwise velocity condition to a control volume integral of the momentum equation shows a large reduction in drag. The relative reduction in drag calculated from wake survey data compared to the single rider result is of similar order to the drag reduction measured using the force balance. From this it is concluded that a large proportion of the drag reduction observed for the

trailing cyclist is due to sheltering from the lead rider. Travelling in the wake of the leader results in a much lower effective inlet velocity and so momentum loss over the trailing cyclist is far smaller than seen for a lead or single cyclist. As distance between the lead and trailing cyclist increases, greater energy is recovered from the freestream flow. This increases the effective inlet velocity for the trailing cyclist and thus the drag saving is reduced.

## **6.2 Secondary Findings**

### **6.2.1 The influence of geometry interactions on cyclist drag**

The influence of cyclist geometry and posture on drag was investigated within the context of a four cyclist team formation. Although geometry and posture were found to have a smaller effect on drag than spatial position, they do result in changes significant to elite performance. Similar to previous two rider tests, a small drag reduction was observed for the lead cyclist and a much larger reduction for the trailing rider(s). Mean drag reduction across the 4 athletes was found to be 5%, 45%, 55% and 57%, respectively. Drag at the second position was lower than that seen for a two rider formation. As stated previously this does vary with relative athlete size. At Position 3, drag is further reduced from Position 2; however effects appear to plateau beyond that with Position 4 drag only slightly lower. Furthermore, the drag reduction at each position was shown to be rider dependent with a variation of the order of  $\pm 2\%$  at each position.

Athletes adopted a series of different postures and were tested at each position in the four rider team in addition to isolated single rider tests. This showed that the drag response for a given posture in single rider tests provides a good indication of changes in the team environment. A posture that increases drag in a single rider test will increase drag in the team environment, however, that increase will be of smaller magnitude. Conversely, postures that lowered drag in a single rider test will also result in a drag reduction in the team scenario. However, the reduction will typically be of greater magnitude.

There was also evidence of complex drag interactions between riders within the team, where changing the posture of one athlete would influence the drag of their teammate(s). Whilst there was evidence of coupling between athletes, these were a more complex function than basic postural changes and position in the team. The only consistent trend observed was that lowering the lead athlete would increase the drag of the rider in Position 2. It was previously suggested that the drag reduction of a trailing cyclist is dependent on the  $C_D A$  of the leader (Edwards & Byrnes). In this study, raising an athlete's head and shoulder position was shown to increase drag in a single rider test. However, in the team environment this change did not consistently generate a drag reduction for the rider immediately behind. Therefore, the interactions must be a more complex function of individual rider geometry and size. This suggests that to fully optimise team performance it is necessary to test actual athletes in situ. It also indicates that further optimisation may be possible through dynamic position of athletes by varying riding posture depending on position within the team. Furthermore, given the sensitivity of trailing rider drag to road position, particularly lateral separation, track testing may be important for validating realistic team performance.

### 6.2.2 Postural effects on the wake of a cyclist

Tests were conducted on a pedalling athlete to investigate the effect of posture on performance. A series of postures were selected to replicate athletes in road cycling and draft-legal triathlon. Time averaged flow measurements were recorded in the wake of the athlete. It was found that relatively small changes to the posture of a cyclist can significantly affect the wake distribution. However, it is possible to alter the wake without significantly affecting the drag of the cyclist if regions are merely redistributed. Results showed that aerodynamic drag is associated with regions of separated flow, low streamwise velocity and high turbulence. To minimise drag, it is important that all areas of cyclist posture are optimised.

Lowering the head and torso was found to reduce the frontal area of the rider and this translated to reduction in the size of the wake region. This, in turn, generally correlated with a reduction in drag. However, the position of the arms was also seen to have a significant impact on the wake topology and subsequently the aerodynamic drag. The use of aerobars to bring the arms of the cyclist inside the line of the hips reduced the width of the high velocity deficit and turbulence intensity region. This correlated with force results, which showed that such postures generally have lower drag than postures with wide arm positions. As a recommendation for cycling positioning, lowering the head and torso will generally translate to a reduction in aerodynamic drag by reducing the area of high velocity deficit and turbulence levels in the wake. However, to fully optimise aerodynamic performance it is necessary to also bring the arms inside the silhouette of the torso and hips.

### **6.3 Recommendations**

Due to the large parameter space surrounding the investigation of cycling, and the further increase when moving to multiple bodies, there are numerous areas of further research necessary to fully understand multiple cyclist aerodynamics. This research serves as a foundation for interactions in cycling and insight for complex bluff body aerodynamic interactions.

The drag behaviour as a function of spatial position has been quantified for a two rider formation. From a practical perspective in cycling it would be useful to extend this to groups of 3 or more cyclists such as a four rider pursuit team or large group numbers such as found in a peloton. This leads in to further investigation of interactions within a team to identify the physical parameters of the athletes that may tie into the complex coupling of drag within a team of cyclists. There is also the consideration of yaw effects as this is particularly relevant to road cycling events.

The flow similarity obtained with scale model cyclists in water channel tests, despite the lower Reynolds number, opens this technique as an avenue for further investigation given the more rapid data acquisition compared to wind tunnel testing. The understanding of flow changes with spatial position could be furthered by testing more axial positions and introducing lateral displacement. It would also be useful to capture three velocity components at both inlet and outlet for lead and trailing riders to be able to develop a full characterisation of the flow behaviour. This would allow the study of the evolution of vortices from the leading rider and their impact on the trailing cyclist. This work could also be extended by developing dynamic pedalling models and enhancing athlete and bicycle details. Developing a more comprehensive understanding of the three-dimensional flow field could lead to a model for predicting drag on the trailing rider as a function of spatial position and potentially frontal area.

Given the complexity of full scale testing there is considerable scope for further investigation in this area. This study limited the tandem formations to the minimum separation case as this was identified as having the greatest potential changes from the single rider case. It would, however, be useful to investigate additional downstream positions to look at how energy recovery from the freestream affects the trailing rider wake, similar to the scale results. In terms of experimental technique it would be of use to extend the imaging plane to capture the full wake down to the ground plane. Although it was shown that the chosen interrogation window captures the critical region of the wake in terms of coherent vortices, a full wake capture would enhance the understanding of dynamics of the lower legs. Additionally, increasing the spatial resolution of the sampling grid would enable more precise identification of the primary wake structures and potentially show the evolution of smaller scale structures in the wake. These are both limitations of testing with an athlete subject. However, given the symmetry associated with the periodic wake, it would be possible to use a half wake grid to increase resolution, as was applied in the postural investigation. Additional parameters that could be introduced to the problem include consideration of athlete geometry on the wake in tandem formations as well as the influence of pedalling cadence.

The study of rider base pressure would provide further detail in understanding the origins of drag changes in multi-rider formations. Using a pressure tapped mannequin at each rider position in multiple rider formations would provide a direct measurement technique to correlate with changes

in drag and a level of detail beyond that possible with velocity flow field data. Such testing could also be extended to tests including postural changes.

From a performance perspective in cycling it would be useful to investigate the potential for controlling interactions within a cycling team. For example, changing the posture of equipment of cyclists in a pursuit team or team trial to manipulate the distribution of drag over members within the team. This would enable tuning of resistance to allow optimum speed and recovery for each rider. The ability to control interactions both upstream and downstream within a team has the potential to provide significant performance benefits at the elite level.

## References

- Achenbach, E, 1971, Influence of surface roughness on the cross-flow around a circular cylinder, *Journal of Fluid Mechanics*, 46(2), p 321-335, doi: 10.1017/S0022112071000569
- Ahmed, SR, Ramm, R, Faltin, G, 1984, Some salient features of the time averaged ground vehicle wake, *SAE Technical Papers* 840300, doi:10.4271/840300
- Awbi, H, 1978, Wind-tunnel-wall constraint on two dimensional rectangular section prisms, *Journal of Wind Engineering and Industrial Aerodynamics*, 3(4), p 285-306, doi:10.1016/0167-6105(78)90034-X
- Barry, N, Burton, D, Crouch, T, Sheridan, J and Luescher, R, 2012, Effect of crosswind and wheel selection on the aerodynamic behaviour of a cyclist, *Procedia Engineering*, 34, p 20-25
- Barry, N, Burton, D, Sheridan, J and Brown, NAT, 2014, The effect of spatial position on the aerodynamic interactions between cyclists, *Procedia Engineering*, 72, p 774-779, DOI:10.1016/j.proeng.2014.06.131
- Barry, N, Burton, D, Sheridan, J and Brown, NAT, 2014, Aerodynamic performance and riding posture in road cycling and triathlon, *Proc. IMech, Part P: Journal of Sports Engineering and Technology*, DOI: 10.1177/1754337114549876
- Barry, N, Burton, D, Sheridan, J, Thompson, M and Brown, NAT, 2015, Aerodynamic drag interactions between cyclists in a team pursuit, *Sports Engineering*, 18(2), p 93-103, DOI: 10.1007/s12283-015-0172-8
- Baker, CJ, 1991, Ground vehicles in high cross winds. Part 1: Steady Aerodynamic Forces, *Journal of Fluids and Structures*, 5, p 69-90, DOI: 10.1016/0889-9746(91)80012-3
- Bergh, H and Tijdeman, H, 1965, Theoretical and experimental results for the dynamic response of pressure measuring systems, *National Aero and Astronomical Research Institute, Amsterdam*, Report NLR-TR F.238
- Betz, A, 1925, Ein Verfahren zur direkten Ermittlung des Profilwiderstandes, *Zeitschrift für Flugtechnik und Motorluftschiffahrt*, 16, p 42-44.
- Biermann, D & Herrstein Jr, WH, 1933, The Interference between struts in various combinations, *Report National Advisory Committee for Aeronautics*, Report No. 468
- Blair, KB & Sidelko, S, 2008, Aerodynamic performance of cycling time trial helmets, In: *The Engineering of Sport 7*, Edited by M. Estivalet & P. Brisson, p 371 - 377
- Blocken, B, Defraeye, T, Koninckx, E, Carmeliet, J and Hespel, P, 2013, CFD Simulations of the aerodynamic drag of two drafting cyclists, *Computers & Fluids*, 71, p 435-445, DOI:10.1016/j.compfluid.2012.11.012
- Blocken, B, Defraeye, T, Koninckx, E, Carmeliet, J and Hespel, P, 2011, Numerical study of the interference drag of two cyclists, *13<sup>th</sup> International Conference on Wind Engineering*
- Broker, JP, Kyle, CR and Burke, ER, 1999, Racing cyclist power requirements in the 4000m individual and team pursuits, *Medicine and Science in Sports and Exercise*, 31(11): 1677-1685
- Brune, GW, 1994, Quantitative low-speed wake surveys, *Journal of Aircraft*, 31(2), 249-255, doi: 10.2514/3.46481
- Burke, ER, 1986, *Science of Cycling*, Human Kinetics, California, USA
- Chabroux, V, Mba, MN, Sainton, P and Favier, D, 2010, Wake characteristics of time trial helmets using PIV-3C technique, In; *15<sup>th</sup> International Symposium on Applications of Laser Techniques to Fluid Mechanics*, Lisbon, Portugal

- Chabroux, V, Barelle, C and Favier, D, 2012, Aerodynamics of cyclist posture, bicycle and helmet characteristics in time trial stage, *Journal of Applied Biomechanics*, 28, p 317-323
- Chowdhury, H and Alam, F, 2014, An experimental study on aerodynamic performance of time trial bicycle helmets, *Sports Engineering*, 17(3), p 165-170, DOI 10.1007/s12283-014-0151-5
- Cooper, KR, 1993, Bluff-body aerodynamics as applied to vehicles, *Journal of Wind Engineering and Industrial Aerodynamics*, 49, p 1-21, DOI: 10.1016/0167-6105(93)90003-7
- Cooper, KR, 1998, Bluff-body blockage corrections in closed and open test section wind tunnels, In: *Wind Tunnel Wall Correction AGARD 336*, Advisory Group for Aerospace Research and Development, Edited by: B.F.R. Ewald
- Crouch, TN, Sheridan, J, Burton, D, Thompson, M and Brown, NAT, 2012, Dominant flow structures in the wake of a cyclist, *Proceedings of the 30<sup>th</sup> AIAA Applied Aerodynamics Conference*, New Orleans, LA, USA
- Crouch, TN, Sheridan, J, Burton, D, Thompson, M and Brown, NAT, 2012, A quasi-static investigation of the effect of leg position on cyclist aerodynamic drag, *Engineering of Sport 9*, Procedia Engineering, 34, p 3-8, doi:10.1016/j.proeng.2012.04.002
- Crouch TN, Burton, D, Brown NAT, Thompson MC and Sheridan J, 2014, Flow topology in the wake of a cyclist and its effect on aerodynamic drag, *Journal of Fluid Mechanics*, 748, p 5-35, DOI:10.1017/jfm.2013.678
- Davies, CTM, 1980, Effect of air resistance on the metabolic cost and performance of cycling, *European Journal of Applied Physiology*, 45, p 245-254
- Defraeye, T, Blocken, B, Koninckx, E, Hespel, P and Carmeliet, J, 2010, Aerodynamic study of different cyclist positions: CFD and full-scale wind-tunnel tests, *Journal of Biomechanics*, 43, p 1262-1268
- Defraeye, T, Blocken, B, Koninckx, E, Hespel, P, Verboven, P, Nicolai, B and Carmeliet, J, 2013, Cyclist drag in team pursuit: influence of cyclist sequence, stature and arm spacing, *Journal of Biomechanical Engineering*, 136(1), p 011005-1 – 9, doi: 10.1115/1.4025792
- Deng, J, Ren, A-L., Zou, J-F and Shao, X-M, 2006, Three-dimensional flow around two circular cylinders in tandem arrangement, *Fluid Dynamics Research*, 38, p 386-404, DOI:10.1016/j.fluiddyn.2006.02.003
- Di Prampero, PE, Cortili, G, Mognoni, P and Saibene, F, 1979, Equation of motion of a cyclist, *Journal of Applied Physiology*, 47 p 201 - 206
- Duncan, LT, 1994, The effect of deck spoilers and two-car interference on body pressure of race cars, *SAE Technical Paper 94-2520*, doi:10.4271/942520
- Edwards, AG and Byrnes, WC, 2007, Aerodynamic characteristics as determinants of the drafting effect in cycling, *Medicine and Science in Sport and Exercise*, DOI: 10.1249/01.mss.0000239400.85955.12
- Forrester, AIJ, 2008, *On the aerodynamics of bicycle wheels*, University of Southampton, UK
- Fouras, A, Lo Jacono, D, Hourigan, K, 2008, Target-free Stereo PIV: a novel technique with inherent error estimation and improved accuracy, *Experiments in Fluids*, 44, p 317-329, DOI:10.1007/s00348-007-0404-1
- García-López, J, Rodríguez-Marroyo, JA, Juneau, C-E, Pelelerio, J, Martínez, AC and Villa, JG, 2008, Reference values and improvement of aerodynamic drag in professional cyclists, *Journal of Sports Sciences*, 26(3), p277-286
- Gibertini, G & Grassi D, 2008, Cycling Aerodynamics, *Sport Aerodynamics*, Vol. 506, p 23-47, DOI: 10.1007/978-3-211-89297-8\_3

- Glauert, H, 1928, The effect of the static pressure gradient on the drag of a body tested in a wind tunnel, *Reports and Memoranda No. 1158 (Ae 323)*, Royal Air Ministry, UK
- Glauert, H, 1933, Wind tunnel interference on wings, bodies and airscrews, *Reports and Memoranda No. 1566*, Royal Air Ministry, UK
- Grappe, F, Candau, R, Bello, A and Rouillon, JD, 1997, Aerodynamic drag in field cycling with special reference to the Obree's position, *Ergonomics*, 40(12), p 1299-1311
- Griffith, MD, Crouch, T, Thompson, MC, Burton, D and Sheridan, J, Brown, NAT. 2014, Computational fluid dynamics study of the effect of leg position on cyclist aerodynamic drag, *Journal of Fluids Engineering*, 136(10). DOI: 10.1115/1.4027428
- Gross, AC, Kyle, CR, Malesvicki, DJ, 1983, The Aerodynamics of Human-Powered Land Vehicles, *Scientific American*, 249, p 142 -152
- Gu, Z, 1996, On the interference between two circular cylinders at supercritical Reynolds number, *Journal of Wind Engineering and Industrial Aerodynamics*, 62, p 175-190
- Hammache, M, Michaelian, M & Browand, F, 2001, Aerodynamic forces on truck models, including two trucks in tandem, *SAE Technical Paper 2002-01-0530*, 2002, DOI:10.4271/2002-01-0530
- Hooper, JD. and Musgrove, AR, 1997, Reynolds stress, mean velocity and dynamic static pressure measurement by a four-hole pressure probe, *Experimental Thermal and Fluid Science*, 15, p 375-383, DOI:10.1016/S0894-1777(97)00005-8
- Hori, E, 1959, Experiments on flow around a pair of parallel circular cylinders, *Proceedings of the 9<sup>th</sup> Japan National Congress for Applied Mechanics*, Tokyo, p 231-234
- Ioannou, PA, 1997, *Automated Highway Systems*, Plenum Press, New York, USA
- Ishigai, S, Nishikawa, E, Nishimura, K and Cho, K, 1972, Experimental study on structure of gas flow in tube banks with tube axes normal to flow (Part 1, Karman vortex flow around two tubes at various spacings), *Bulletin of the Japan Society of Mechanical Engineers*, 15(86), pp949-956
- Jermy, M, Moore, J and Bloomfield, M., 2008, *Translational and rotational aerodynamic drag of composite construction bicycle wheels*, Proc. IMechE Vol. 222 Part P: Journal of Sports Engineering and Technology, 222, p 91-102, DOI: 10.1243/17543371JSET17
- Kerschen, G, Golival, J-C, Vakakis, AF and Bergman, LA, 2005, The method of proper orthogonal decomposition for dynamical characterization and order reductions of mechanical systems; An Overview, *Nonlinear Dynamics*, 41, p 147-169, DOI: 10.1007/s11071-005-2803-2
- Kim, MK, Kim, DK, Yoon, SH and Lee, DH, 2008, Measurements of the flow fields around two square cylinders in a tandem arrangement, *Journal of Mechanical Science and Technology*, 22(2), p 397-407, DOI: 10.1007/s12206-007-1041-6
- Kitawaki, T & Oka, H, 2013, A measurement system for the bicycle crank angle using a wireless motion sensor attached to the crank arm, *Journal of the Science of Cycling*, 2(2), p 13-19
- Kusunose, K, 1997, Development of a universal wake survey data analysis code, *American Institute of Aeronautics & Astronautics*, A97-31757, p617-626, doi: 10.2514/6.1997-2294

- Kyle, CR, 1979, Reduction of wind resistance and power output of racing cyclists and runners travelling in groups, *Ergonomics*, 22(4), p 387-397, DOI: 10.1080/00140137908924623
- Kyle, CR & Burke, ER, 1984, Improving the racing bicycle, *Mechanical Engineering; The Journal of the American Society of Mechanical Engineers*, 106, p 34-45
- Kyle, CR, 1986, Mechanical factors affecting the speed of a cycle. In: Burke ER. *Science of Cycling Human Kinetics*, California, USA
- Kyle, CR and Weaver, MD, 2004, Aerodynamics of human-powered vehicles, Proceedings of Institution of Mechanical Engineers, Part A: *Journal of Power and Energy*, 218(141)
- Lin, J-C, Yang, Y and Rockwell, D, 2002, Flow past two cylinders in tandem: instantaneous and averaged flow structure, *Journal of Fluids and Structures*, 16(8), p 1059-1071, DOI:10.1006/jfls.2002.0469
- Martin, JC, Douglas, ML, Cobb, JE, McFadden, KL and Coggan, AR, 1998, Validation of a mathematical model for road cycling power, *Journal of Applied Biomechanics*, 14, p 276-291
- Martinuzzi, RJ and Havel, B, 2004, Vortex shedding from two surface mounted cubes in tandem, *International Journal of Heat and Fluid Flow*, 25(3), p 364-372, doi:10.1016/j.ijheatfluidflow.2004.02.003
- Maskell, EC, 1965, A theory of the blockage effects on bluff bodies and stalled wings in a closed wind tunnel, *Aeronautical Research Council Reports and Memoranda*, R & M 3400
- Maskell, EC, 1972, *Progress towards a method for measurement of the components of the drag of a wing of finite span*, Royal Aircraft Establishment, TR 72232, UK
- McCole, SD, Clane, K, Conte, JC, Anderson, R and Hagberg, JM, 1990, Energy expenditure during bicycling, *Journal of Applied Physiology*, 68, p 748-753
- Mercker, E and Wiedemann, J, 1996, *On the correction of interference effects in open jet wind tunnels*, SAE Technical Paper 960671, Society of Automotive Engineers
- Mercker, E, Cooper, KR, Fischer, O and Wiedemann, J, 2005, *The influence of horizontal pressure distribution on aerodynamic drag in open and closed wind tunnels*, SAE Technical Paper 2005-01-0867, Society of Automotive Engineers
- Morotn, BR, 1984, *The generation and decay of vorticity*, *Geophysical and Astrophysical Fluid Dynamics*, 28:3-4, p 277-308, doi: 10.1080/03091928408230368
- Munk, M, 1921, *Some new aerodynamic relations*, NACA Report 114
- Muson, BR, Young, DF and Okiishi, TH, 2006, *Fundamentals of Fluid Mechanics*, John Wiley & Sons, USA
- Oggiano, L, Leirdal, S, Saetran, L and Ettema, G, 2008, Aerodynamic optimization and energy saving of cycling postures for international elite cyclists, *The Engineering of Sport* 7, p 597-604
- Okajima, A, 1979, Flows around two tandem circular cylinders at very high Reynolds numbers, *Bulletin of the Japan Society of Mechanical Engineers*, 22 (166), doi:10.1299/jsme1958.22.504
- Pagliarella, R, 2009, *On the aerodynamic performance of automotive vehicle platoons featuring pre and post critical leading forms*, Thesis submission to RMIT University, Melbourne, Australia

Pannel, JR, Griffith, EA and Coals, JD, 1915, *Experiments on the interference between pairs of aeroplane wires of circular and lenticular cross section*, Reports and Memoranda – Aeronautical Research Council (Great Britain), Report 208

Rajamani, GK, 2006, *CFD analysis of Air Flow Interactions in Vehicle Platoons*, Thesis submission to RMIT University, Melbourne, Australia

Romberg, GF, Chianese, F Jr. & Lajoie, RG, 1971, *Aerodynamics of race cars in drafting and passing situations*, SAE Technical Paper 710213, DOI:10.4271/710213

Saetran, L and Oggiano, L., 2008, Skin Suit Aerodynamics in Speed Skating, In: *Sports Aerodynamics*, CISM International Centre for Mechanical Sciences, Springer, Vienna, 506, p 93-105, doi:10.1007/978-3-211-89297-8\_5

Sayers, AT and Stanley, P, 1994, Drag force on rotating racing cycle wheels, *Journal of Wind Engineering and Industrial Aerodynamics*, 53, p 431-440

Tew, GS and Sayers, AT, 1999, Aerodynamics of yawed racing cycle wheels, *Journal of Wind Engineering and Industrial Aerodynamics*, 82, p 209-222

Tropea, C, Yarin, AL and Foss, JF (eds), 2007, *Springer Handbook of Experimental Fluid Mechanics*, Springer Berlin Heidelberg, DOI: 10.1007/978-3-540-30299-5

Underwood, L, Schumacher, J, Burette-Pommary, J and Jermy, M, 2011, Aerodynamic drag and biomechanical power of a track cyclist as a function of shoulder and torso angles, *Sports Engineering*, 14, p 147-154

Underwood, L, and Jermy, M, 2013, Optimal handlebar position for track cyclists, *Sports Engineering*, 16, p 81-90, DOI: 10.1007/s12283-013-0111-5

von Schultz-Hausmann, FK and Vagt, J-D, 1988, Influence of test-section length and collector area on measurements in  $\frac{3}{4}$  open jet automotive wind tunnels, *Research in Automotive Aerodynamics SP-747*, Society of Automotive Engineers, USA, p99-107

Watkins, S & Vino, G, 2008, The effect of vehicle spacing on the aerodynamics of a representative car shape, *Journal of Wind Engineering and Industrial Aerodynamics*, 96 (6-7), pp. 1232-1239, DOI:10.1016/j.jweia.2007.06.042

Wilson, DG, 2004, *Bicycle Science*, The MIT Press, Cambridge, Massachusetts, USA

Wu, J, Sheridan, J, Welsh, MC and Hourigan, K, 1996, Three-dimensional vortex structures in a cylinder wake, *Journal of Fluid Mechanics*, 312, p 201-222

Zdravkovich, MM, 1977, Review – Review of flow interference between two circular cylinders in various arrangements, *Journal of Fluids Engineering*, 99(4), DOI: 10.1115/1.3448871

Zdravkovich, MM and Pridden, DL, 1977, Interference between two circular cylinders; series of unexpected discontinuities, *Journal of Wind Engineering and Industrial Aerodynamics*, 2(3), p 255-270, DOI:10.1016/0167-6105(77)90026-5

Zdravkovich, MM, 1992, Aerodynamics of bicycle wheel and frame, *Journal of Wind Engineering & Industrial Aerodynamics*, 40(1), p 55-70, DOI: 10.1016/0167-6105(92)90520-K

Zdravkovich, MM, Ashcroft, MW, Chisholm, SJ and Hicks, N, 1996, Effect of Cyclist's Posture and Vicinity of Another Cyclist on Aerodynamic Drag, *The Engineering of Sport 1*, Balkerna, Rotterdam

Zhou, J, Adrian, RJ, Balachandar, S And Kendall, TM, 1999, Mechanisms for generating coherent packets of hairpin vortices in channel flow, *Journal of Fluid Mechanics*, 387, p 353-396, DOI:10.1017/S002211209900467X

## Appendices

### Appendix A: Validation of Wind Tunnel Corrections for Multiple Tandem Cyclists

To test the validity of the correction methodology the Monash anthropomorphic cycling mannequin was tested separately on each of the 4 balances on the Multi-Rider Cycling Rig. This was to act as a representative reference body and compare the response of each balance. The results are plotted in Figure A.1 below. In addition to the raw  $C_D A$  and the final corrected value, the  $C_D A$  is also plotted when only applying the velocity perturbation or the horizontal buoyancy correction. This was provided to give an indication of the relative importance of each. Note that the correction factors in this work are calculated using the single body formula. As such the horizontal buoyancy correction will be the same, but the velocity perturbations are different for each individual as the mannequin was tested in isolation. It can be seen from this that the buoyancy correction is typically has a greater impact on the cyclist drag than velocity perturbations due to streamline distortion.

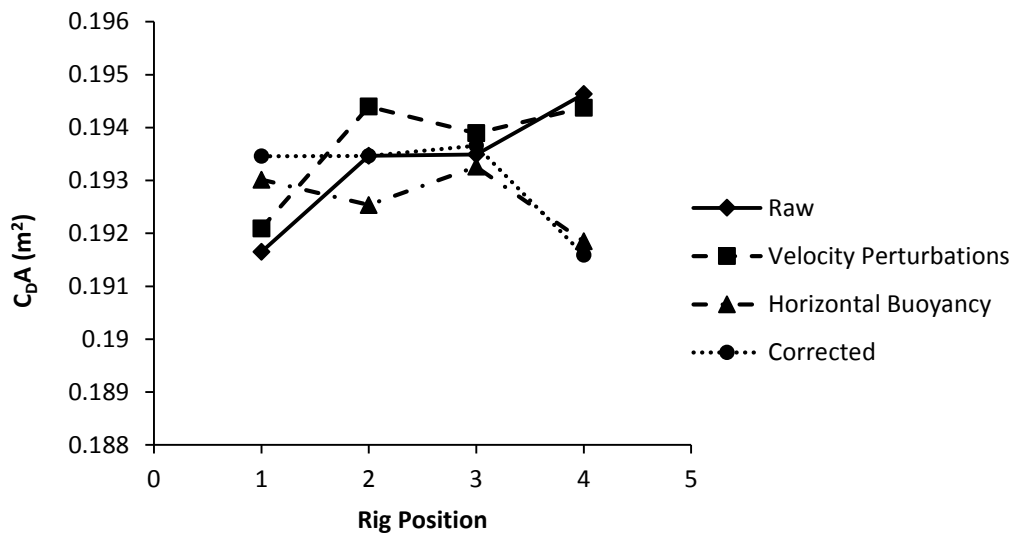


**Figure A.1** -  $C_D A$  for the Monash Anthropomorphic Mannequin mounted onto each position on the Multi-Rider Cycling Rig. Series show the relative effect of the velocity perturbation factors and the horizontal buoyancy corrections as well as the final corrected values. Raw refers to the measured  $C_D A$  before any corrections.

The result of the correction brings the drag measured at the first three positions into agreement within 0.0002 m<sup>2</sup> ( $C_D A$ ). However, it is noted that the drag measured for the mannequin in the final position is lower than the first three. It appears that horizontal buoyancy is overcorrecting the drag for that position. However, this difference for the mannequin in position 4 results in an error of only 0.75%.

As this work is primarily concerned with multiple rider formations a correlation test was also performed with two riders in positions 3 and 4. The mannequin was fixed in position 3 and Athlete B mounted in position 4. Drag was then measured with two ground plane conditions. This would force

a change in the pressure gradient over the rig, particularly the final rider, and test the robustness of the horizontal buoyancy correction. The drag of the athlete in position 4 with the mannequin mounted ahead in position 3 are plotted in Figure A.2 below.

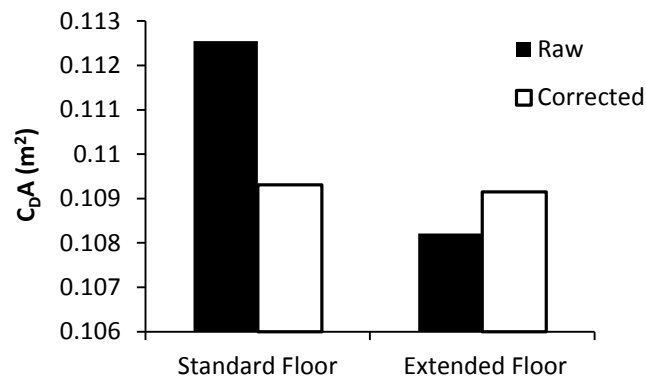


**Figure A.2** -  $C_D A$  of a trailing cyclist in Position 4 with a leading rider mounted ahead in Position 3.

It can be seen that the change in the floor condition has a significant effect on the raw drag measured by the force balance. However, after applying the appropriate correction factors (as outlined above) the two corrected values converge to within 0.1%. Given that this test was using an athlete in position 4, which introduces inherent uncertainty in positioning; this result suggests negligible difference between  $C_D A$  results. From these results it is concluded that the adapted correction methodology described above is suitable for application to the testing of multiple bluff bodies in tandem in an open jet wind tunnel.

## Appendix B: Calibration of Force Balance Rigs

### *Single Rider Cycling Rig*

The force balance was calibrated prior to each new experiment to ensure accurate force response of the load cells. A bespoke moment arm mechanism was used to convert an applied vertical mass into an axial load on the balance. Precise calibration weights were used to apply a stepped load to the system and the calibration factor for the voltage output of each load cell was determined. This was used for the two lateral load directions. Vertical load on the cells was calibrated by adding mass directly onto the cell. A sample calibration result is shown in Figure B.1 below. It can be seen that the force balance has a very linear response to the applied loads. Gradient of the calibration curve was then used to correct the voltage calibration factor on the output from the charge amplifier.

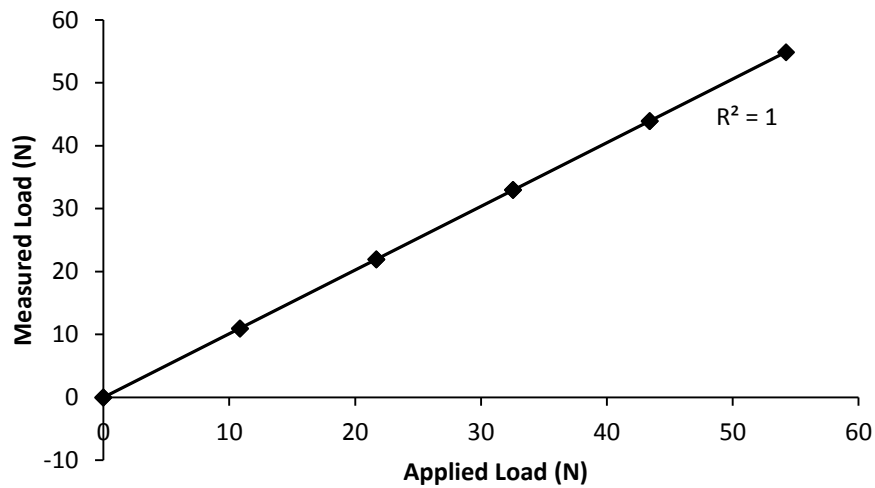


**Figure B.1** – Sample calibration curve for Single Rider Cycling Rig using Kistler load cells

### Multi-Rider Cycling Rig

Calibration of each rig was performed in the same manner to that described previously. The moment arm rig was used to apply a horizontal load to each bicycle rig force balance. The strain gauges provide a very stable response. At worst case the force balance response was 0.36% of the applied loads. This equates to +/- 0.054 N and is smaller than the experimental uncertainty typical for athlete testing, or even mannequin testing. Individual uncertainty is stated for each individual experimental description. Figure B.2 (below) shows a typical calibration response curve for the air bearing force balances. It can be seen that response is linear, with very small error from the applied load.

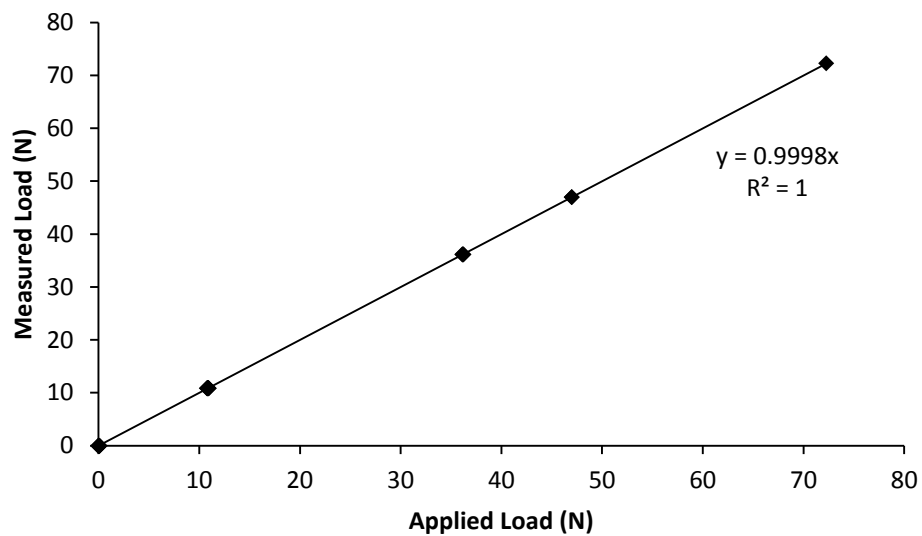


Figure B.2 - Sample calibration curve for Position 4 force balance in the Multi-Rider Cycling Rig

## Appendix C: Athlete Participant Images



**Figure C.1** – Images of Athlete used in this study (A-G)

## Appendix D: Aerodynamic Loads on Cyclists in a Tandem Formation

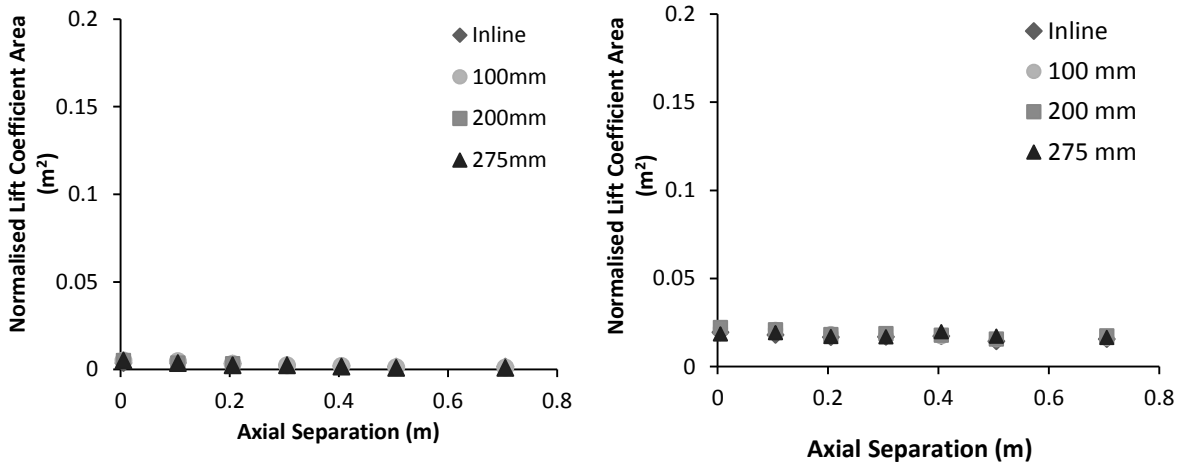


**Figure D.1** – Lift coefficient area ( $C_L A \text{ m}^2$ ) normalised against the single rider value.  
 Left – leading cyclist, Right – trailing cyclist in a two rider tandem formation

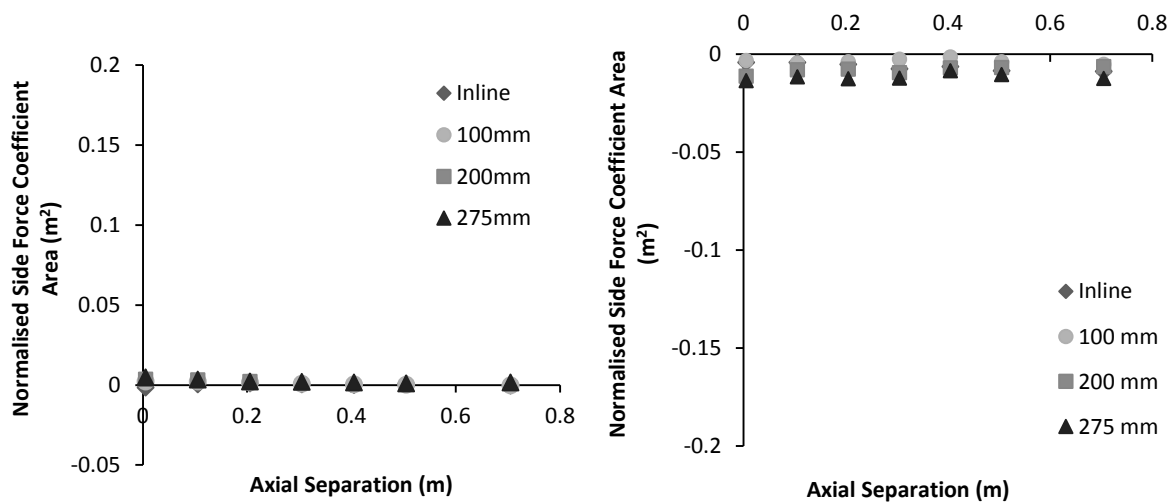


**Figure D.2** – Side force coefficient area ( $C_L A \text{ m}^2$ ) normalised against the single rider value.  
 Left – leading cyclist, Right – trailing cyclist in a two rider tandem formation

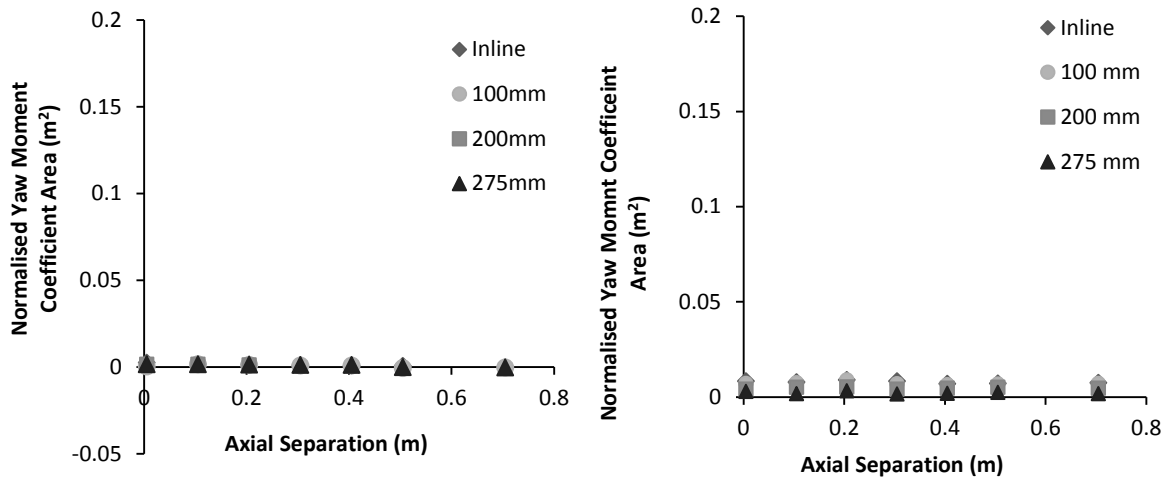


**Figure D.3** –Yaw moment coefficient area ( $C_{LA} m^2$ ) normalised against the single rider value. Left – leading cyclist, Right – trailing cyclist in a two rider tandem formation

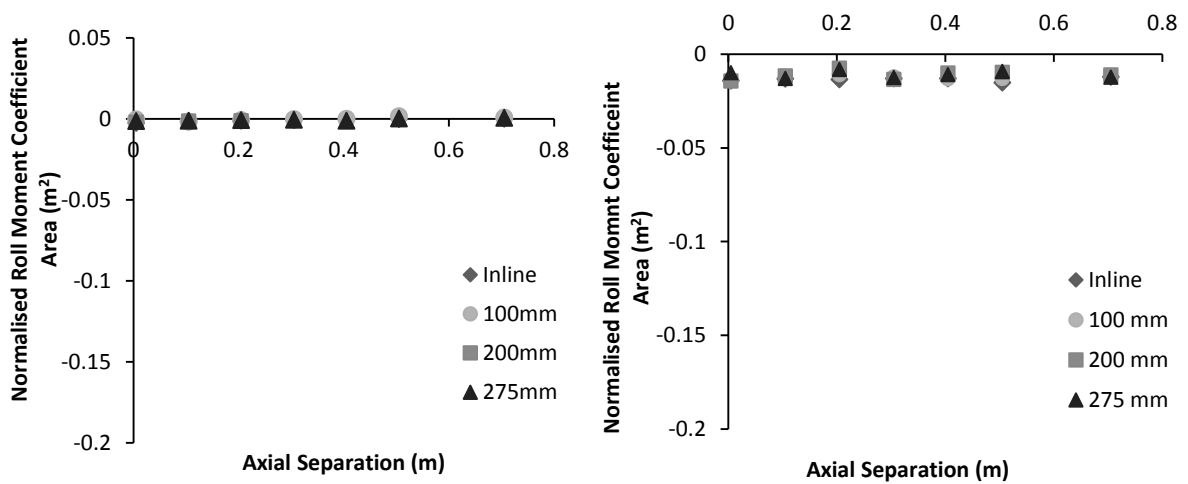


**Figure D.4** –Roll moment coefficient area ( $C_{LA} m^2$ ) normalised against the single rider value. Left – leading cyclist, Right – trailing cyclist in a two rider tandem formation

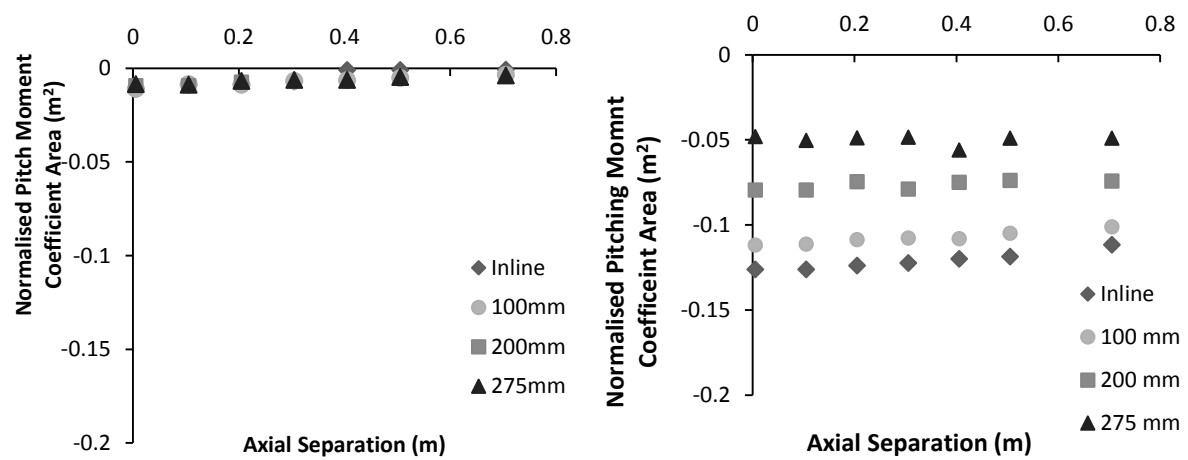


**Figure D.5** - Pitching moment coefficient area ( $C_{LA} m^2$ ) normalised against the single rider value. Left – leading cyclist, Right – trailing cyclist in a two rider tandem formation

## Appendix E: Velocity Profiles in the Wake of Scale Model Cyclists

### Symmetric Cyclists – Spanwise Velocity

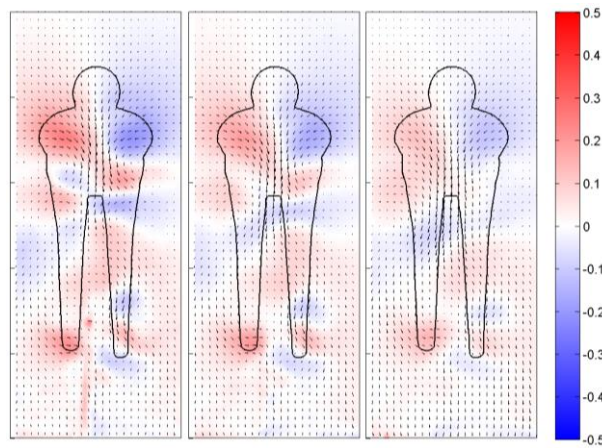


**Figure E.1** – Spanwise velocity ( $V$ ) in the wake of a single rider at  $15^\circ$ ; (L-R) 0.25C, 0.50C and 1.0C downstream of the rear of the cyclist

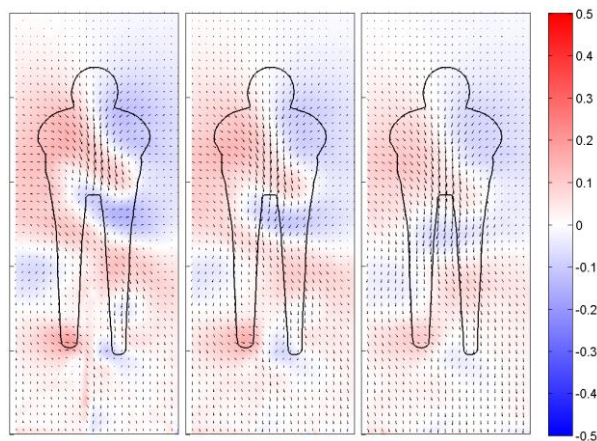


**Figure E.2** – Spanwise velocity ( $V$ ) in the wake of tandem symmetric-symmetric riders both at  $15^\circ$  at Spacing 1; (L-R) 0.25C, 0.50C and 1.0C downstream of the rear of the cyclist

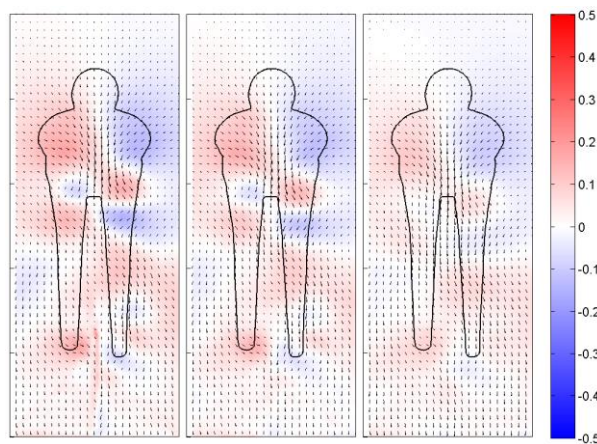


**Figure E.3** – Spanwise velocity ( $V$ ) in the wake of tandem symmetric-symmetric riders both at  $15^\circ$  at Spacing 2; (L-R) 0.25C, 0.50C and 1.0C downstream of the rear of the cyclist

## Asymmetric-Symmetric Cyclists – Spanwise Velocity

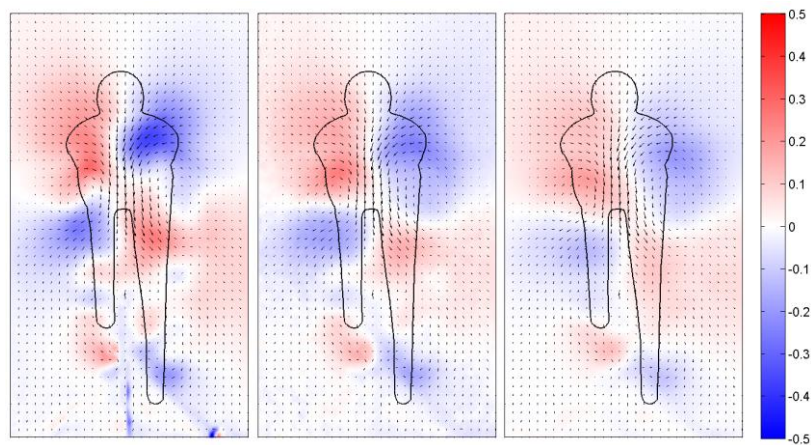


**Figure E.4** – Spanwise velocity ( $V$ ) in the wake of a single rider at  $75^\circ$  (**asymmetric**); (L-R) 0.25C, 0.50C and 1.0C downstream of the rear of the cyclist

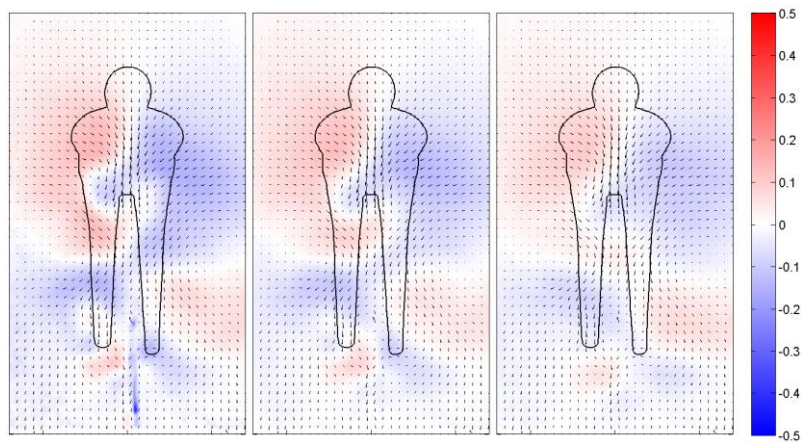


**Figure E.5** – Spanwise velocity ( $V$ ) in the wake of tandem **asymmetric-symmetric** riders ( $75^\circ - 15^\circ$ ) at Spacing 1; (L-R) 0.25C, 0.50C and 1.0C downstream of the rear of the cyclist

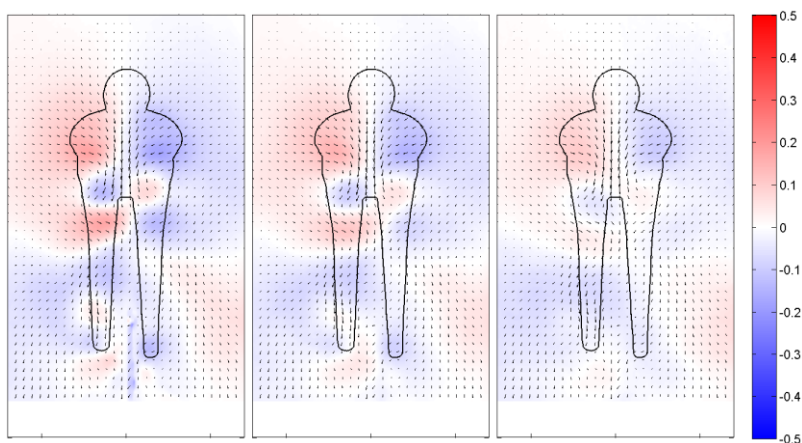


**Figure E.6** – Spanwise velocity ( $V$ ) in the wake of tandem **asymmetric-symmetric** riders ( $75^\circ - 15^\circ$ ) at Spacing 1; (L-R) 0.25C, 0.50C and 1.0C downstream of the rear of the cyclist

## Symmetric-Asymmetric Cyclists – Spanwise Velocity

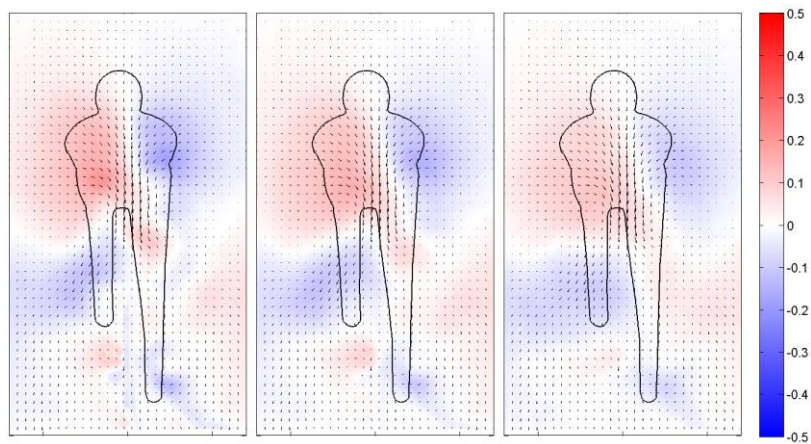


**Figure E.7** – Spanwise velocity ( $V$ ) in the wake of tandem **symmetric-asymmetric** riders ( $15^\circ - 75^\circ$ ) at Spacing 1; (L-R) 0.25C, 0.50C and 1.0C downstream of the rear of the cyclist

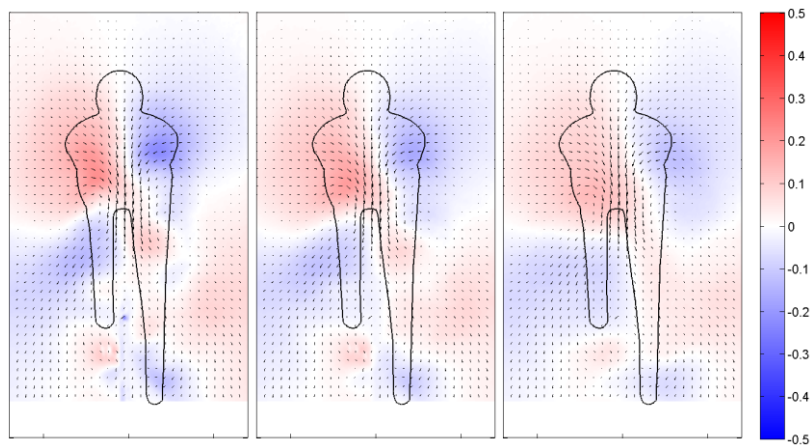


**Figure E.8** – Spanwise velocity ( $V$ ) in the wake of tandem **symmetric-asymmetric** riders ( $15^\circ - 75^\circ$ ) at Spacing 2; (L-R) 0.25C, 0.50C and 1.0C downstream of the rear of the cyclist

## Symmetric Cyclists – Vertical Velocity

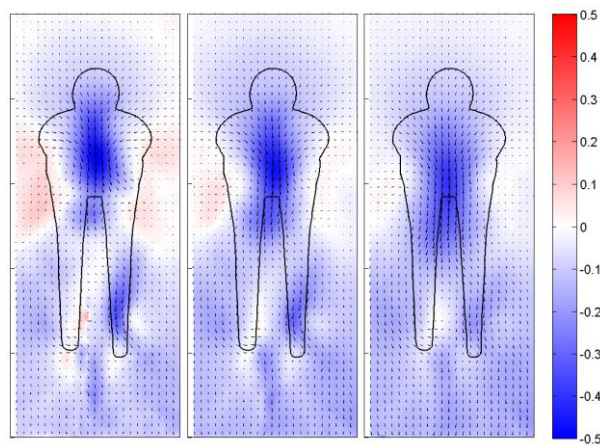


**Figure E.9** – Vertical velocity ( $W$ ) in the wake of a single rider at  $15^\circ$ ; (L-R) 0.25C, 0.50C and 1.0C downstream of the rear of the cyclist

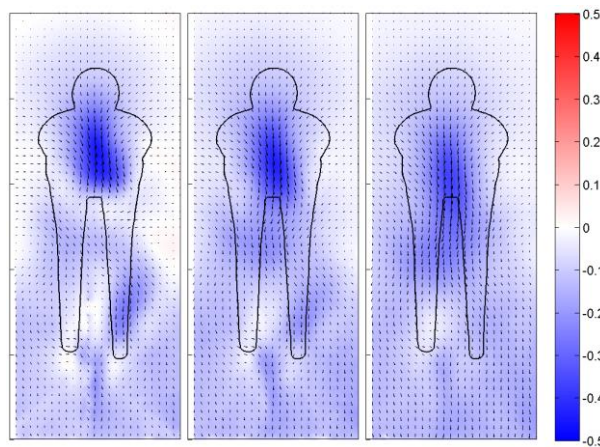


**Figure E.10** – Vertical velocity ( $W$ ) in the wake of tandem symmetric-symmetric riders both at  $15^\circ$  at Spacing 1; (L-R) 0.25C, 0.50C and 1.0C downstream of the rear of the cyclist

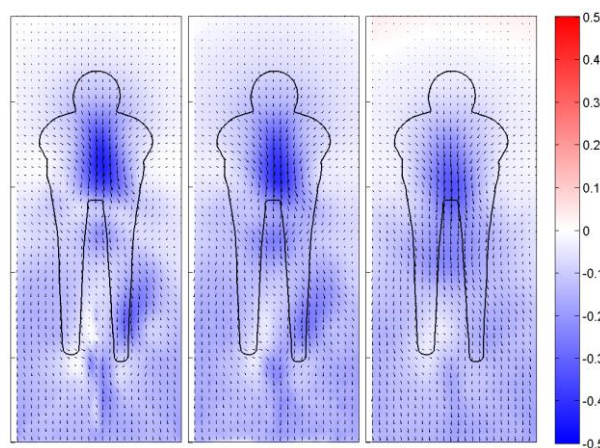


**Figure E.11** – Vertical velocity ( $W$ ) in the wake of tandem symmetric-symmetric riders both at  $15^\circ$  at Spacing 2; (L-R) 0.25C, 0.50C and 1.0C downstream of the rear of the cyclist

### Asymmetric-Symmetric Cyclists – Spanwise Velocity

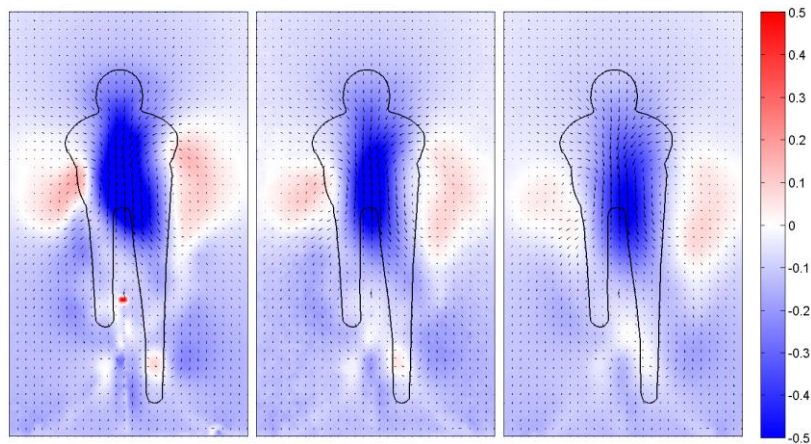


**Figure E.12** – Vertical velocity (W) in the wake of a single rider at  $75^\circ$  (**asymmetric**); (L-R) 0.25C, 0.50C and 1.0C downstream of the rear of the cyclist

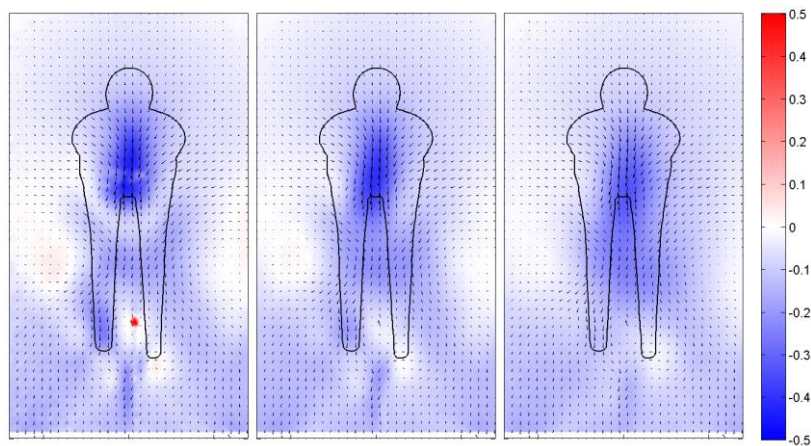


**Figure E.13** – Vertical velocity (W) in the wake of tandem **asymmetric-symmetric** riders ( $75^\circ - 15^\circ$ ) at Spacing 1; (L-R) 0.25C, 0.50C and 1.0C downstream of the rear of the cyclist

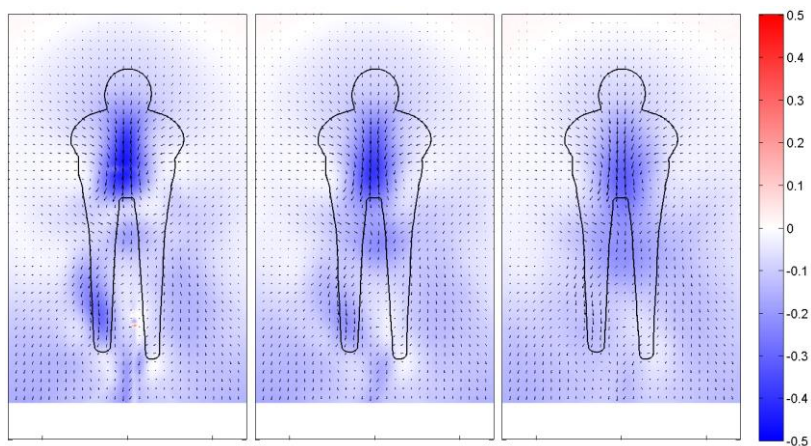


**Figure E.14** – Vertical velocity (W) in the wake of tandem **asymmetric-symmetric** riders ( $75^\circ - 15^\circ$ ) at Spacing 1; (L-R) 0.25C, 0.50C and 1.0C downstream of the rear of the cyclist

## Symmetric-Asymmetric Cyclists – Spanwise Velocity

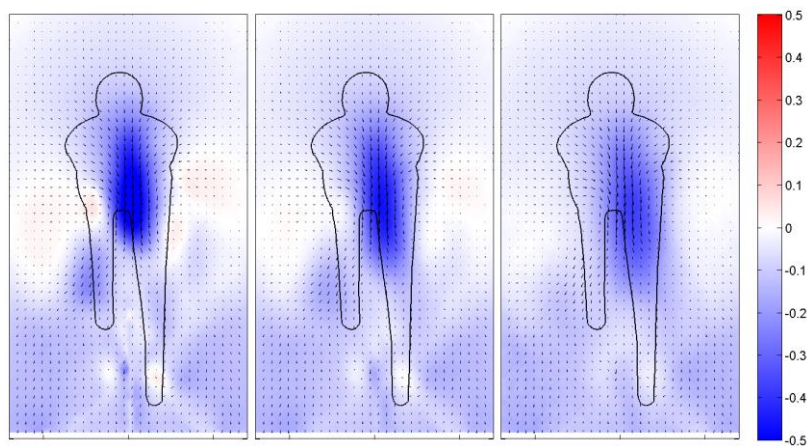


**Figure E.15** – Vertical velocity ( $W$ ) in the wake of tandem **symmetric-asymmetric** riders ( $15^\circ - 75^\circ$ ) at Spacing 1; (L-R) 0.25C, 0.50C and 1.0C downstream of the rear of the cyclist

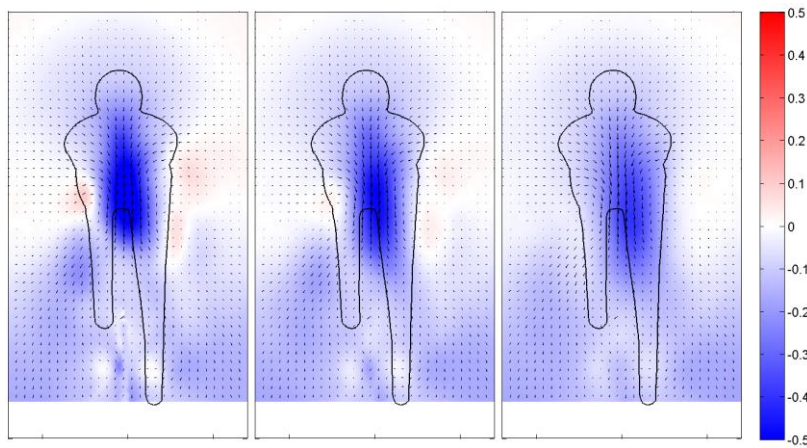


**Figure E.16** – Vertical velocity ( $W$ ) in the wake of tandem **symmetric-asymmetric** riders ( $15^\circ - 75^\circ$ ) at Spacing 2; (L-R) 0.25C, 0.50C and 1.0C downstream of the rear of the cyclist

## Appendix F: Streamwise Vorticity in the Wake of Scale Model Cyclists

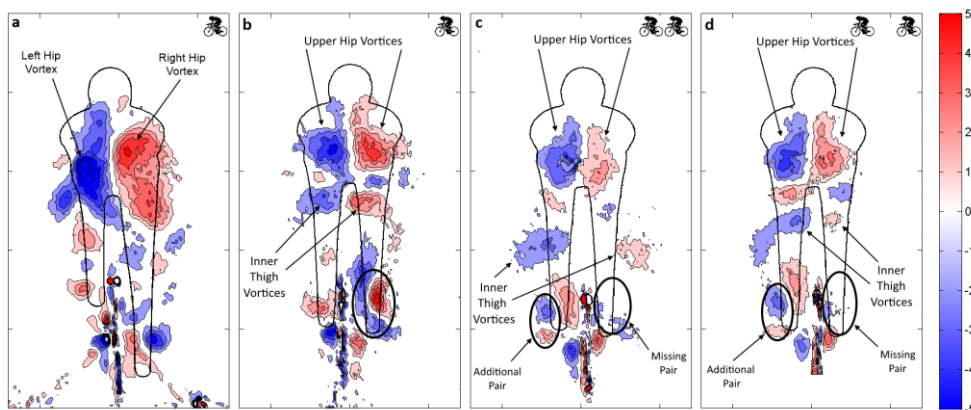


**Figure F.1 – Asymmetric-Symmetric:** Streamwise vorticity (non-dimensional) at  $x = 0.25C$  downstream of (a) a single rider at  $75^\circ$  crank angle, (b) a single rider at  $15^\circ$  crank angle, (c) a trailing rider at Spacing 1 at  $15^\circ$  with the leader at  $75^\circ$  and (d) a trailing rider at Spacing 2 at  $15^\circ$  with the leader at  $75^\circ$ .

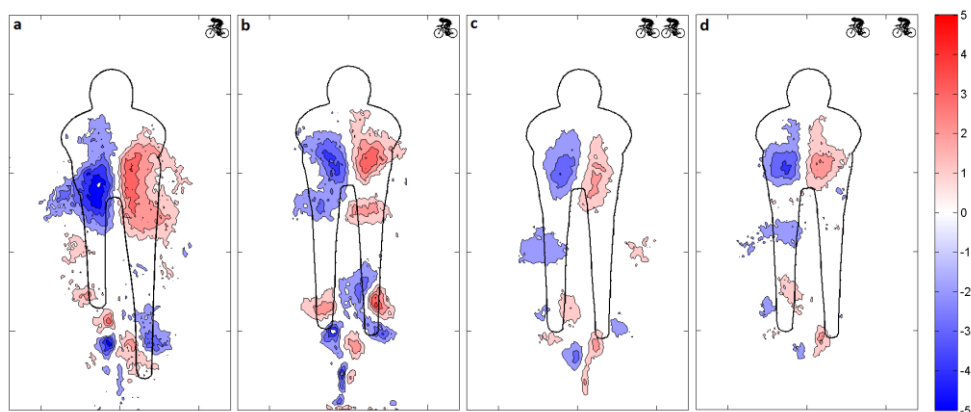


**Figure F.2 – Asymmetric-Symmetric:** Streamwise vorticity (non-dimensional) at  $x = 0.50C$  downstream of (a) a single rider at  $75^\circ$  crank angle, (b) a single rider at  $15^\circ$  crank angle, (c) a trailing rider at Spacing 1 at  $15^\circ$  with the leader at  $75^\circ$  and (d) a trailing rider at Spacing 2 at  $15^\circ$  with the leader at  $75^\circ$ .

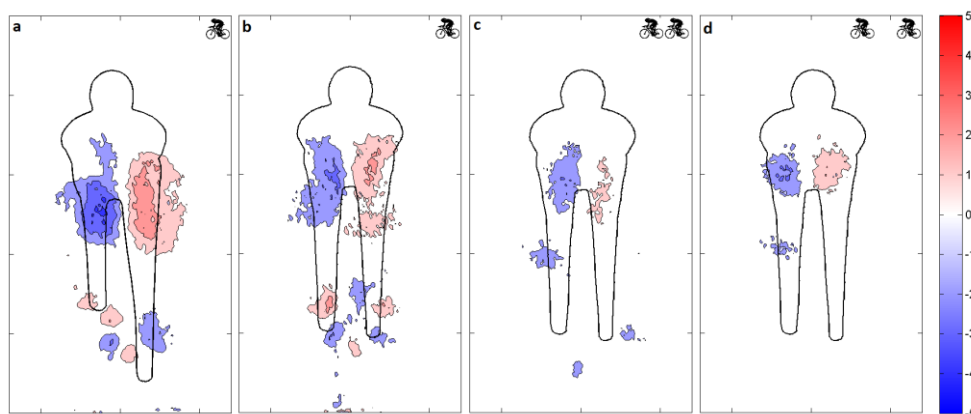


**Figure F.3 – Asymmetric-Symmetric:** Streamwise vorticity (non-dimensional) at  $x = 1.0C$  downstream of (a) a single rider at  $75^\circ$  crank angle, (b) a single rider at  $15^\circ$  crank angle, (c) a trailing rider at Spacing 1 at  $15^\circ$  with the leader at  $75^\circ$  and (d) a trailing rider at Spacing 2 at  $15^\circ$  with the leader at  $75^\circ$ .

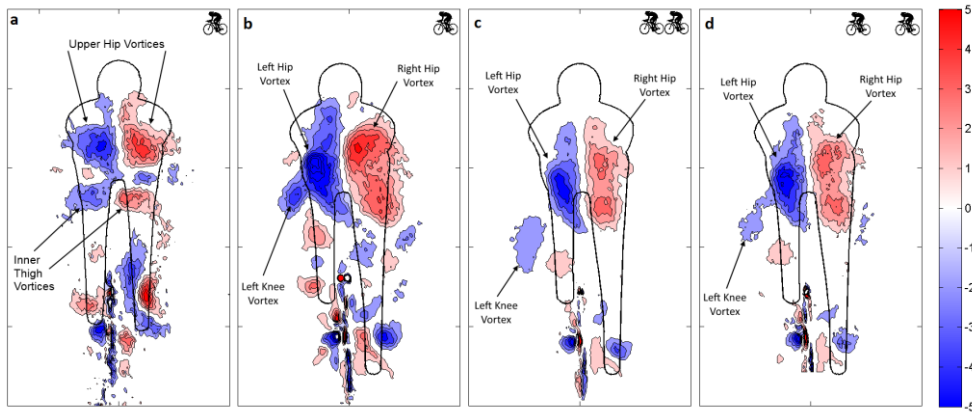


**Figure F.4 – Symmetric-Asymmetric:** Streamwise vorticity (non-dimensional) at  $x = 0.25C$  downstream of (a) a single rider at  $15^\circ$  crank angle, (b) a single rider at  $75^\circ$  crank angle, (c) the trailing rider at Spacing 1 at  $75^\circ$  with the leader at  $15^\circ$  and (d) the trailing rider at Spacing 2 at  $75^\circ$  with the leader at  $15^\circ$

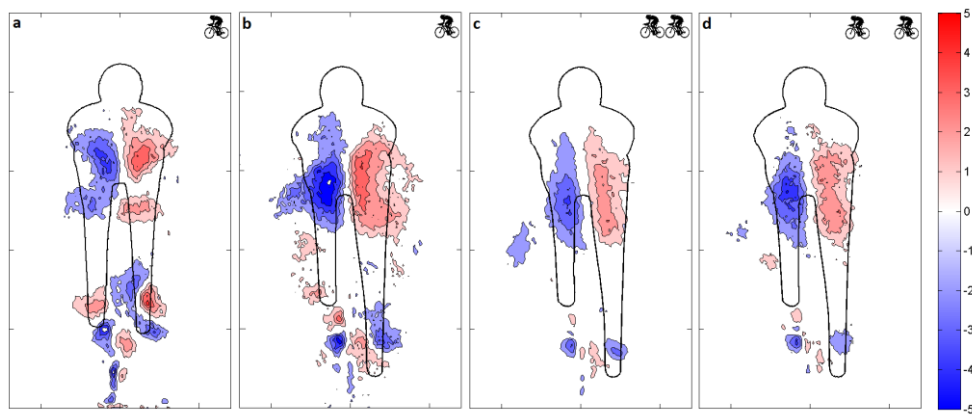


**Figure F.5 – Symmetric-Asymmetric:** Streamwise vorticity (non-dimensional) at  $x = 0.50C$  downstream of (a) a single rider at  $15^\circ$  crank angle, (b) a single rider at  $75^\circ$  crank angle, (c) the trailing rider at Spacing 1 at  $75^\circ$  with the leader at  $15^\circ$  and (d) the trailing rider at Spacing 2 at  $75^\circ$  with the leader at  $15^\circ$

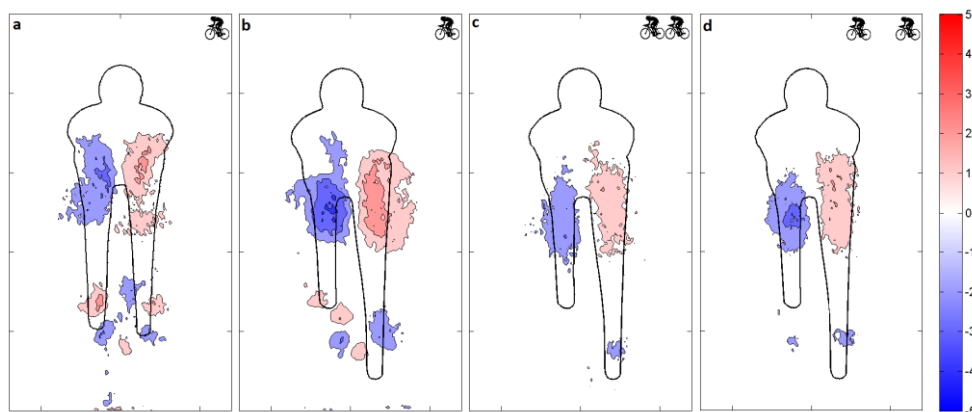


**Figure F.6 – Symmetric-Asymmetric:** Streamwise vorticity (non-dimensional) at  $x = 1.0C$  downstream of (a) a single rider at  $15^\circ$  crank angle, (b) a single rider at  $75^\circ$  crank angle, (c) the trailing rider at Spacing 1 at  $75^\circ$  with the leader at  $15^\circ$  and (d) the trailing rider at Spacing 2 at  $75^\circ$  with the leader at  $15^\circ$

## **Appendix G: Peak and Mean Vorticity in the Wake of Scale Model Cyclist**

**Table G.1** – Peak and mean streamwise vorticity within vortex boundaries from PIV cross sections in the wake of scale model cyclists

		Left Hip		Right Hip		Left Thigh		Right Thigh	
		Max	Mean	Max	Mean	Max	Mean	Max	Mean
	Single sym	-4.4764	-2.9935	4.8648	3.0569	-3.3153	-2.1018	3.8416	2.5217
Spacing 1	sym-sym	-3.3291	-2.281	3.486	2.3293	-1.6165	-1.2128	2.0452	1.5622
Spacing 2	sym-sym	-3.2507	-2.3196	3.7105	2.5419	-1.8881	-1.4835	2.6974	1.8487
Spacing 1	asym-sym	-3.4458	-2.3264	3.1237	2.1873	-2.2994	-1.7292	1.5975	1.2
Spacing 2	asym-sym	-3.9591	-2.7114	3.8363	2.6153	-2.5095	-1.9613	1.625	1.3237
	Single asym	-7.9657	-4.6958	5.4512	3.2363				
Spacing 1	sym-asym	-4.7366	-3.338	3.9882	2.5966				
Spacing 2	sym-asym	-5.4224	-3.4818	3.762	2.6331				

**Table G.2** – Peak and mean normalised streamwise vorticity within vortex boundaries from PIV cross sections in the wake of scale model cyclists. Normalised vorticity calculated from in-plane velocity fields normalised by trailing cyclist local inlet velocity, rather than freestream.

		Left Hip		Right Hip		Left Thigh		Right Thigh	
		Max	Mean	Max	Mean	Max	Mean	Max	Mean
	Single sym	-4.4764	-2.9935	4.8648	3.0569	-3.3153	-2.1018	3.8416	2.5217
Spacing 1	sym-sym	-4.5604	-2.978	4.7753	3.0785	-2.2144	-1.5224	2.8016	2.0423
Spacing 2	sym-sym	-4.0633	-2.7973	4.6382	3.1023	-2.3602	-1.7695	3.3717	2.2817
Spacing 1	asym-sym	-4.7202	-3.1368	4.2791	2.8794	-3.1499	-2.2284	2.1884	1.4923
Spacing 2	asym-sym	-4.9488	-3.3229	4.7954	3.2463	-3.1368	-2.3333	2.0313	1.5166
	Single asym	-7.9657	-4.6958	5.4512	3.2363				
Spacing 1	sym-asym	-6.4885	-4.401	5.4633	3.4244				
Spacing 2	sym-asym	-6.778	-4.2652	4.7025	3.2131				

## Appendix H: Power Spectral Density in the Wake of a Cyclist

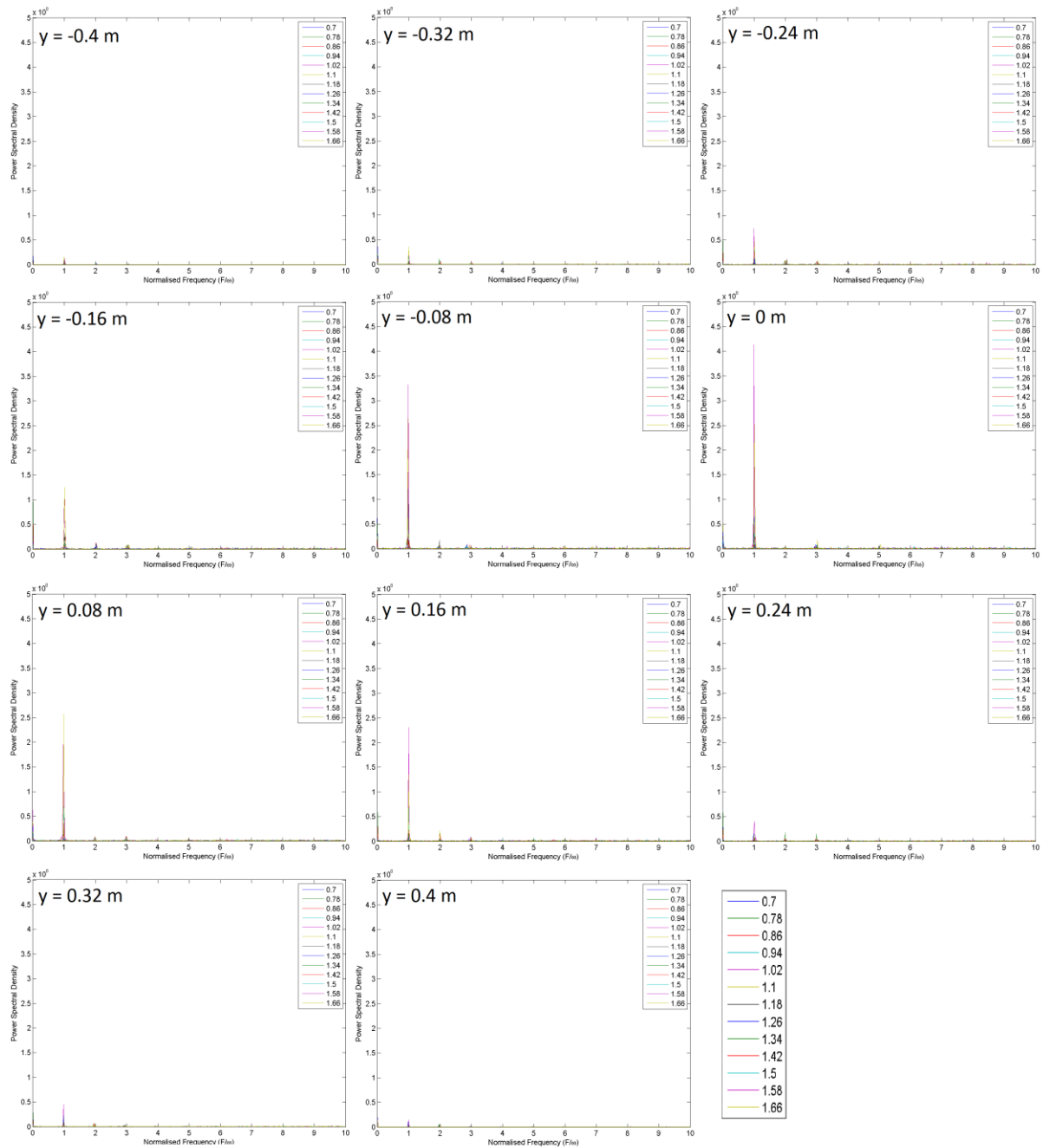


**Figure H.1** – Power spectral density of the spanwise component of velocity ( $V$ ) for each point in the interrogation window in the wake of a single pedalling cyclist. Data recorded with a cobra probe from discrete points in a wake survey. Series refer to vertical position with  $z = 0.7 - 1.66$  m.

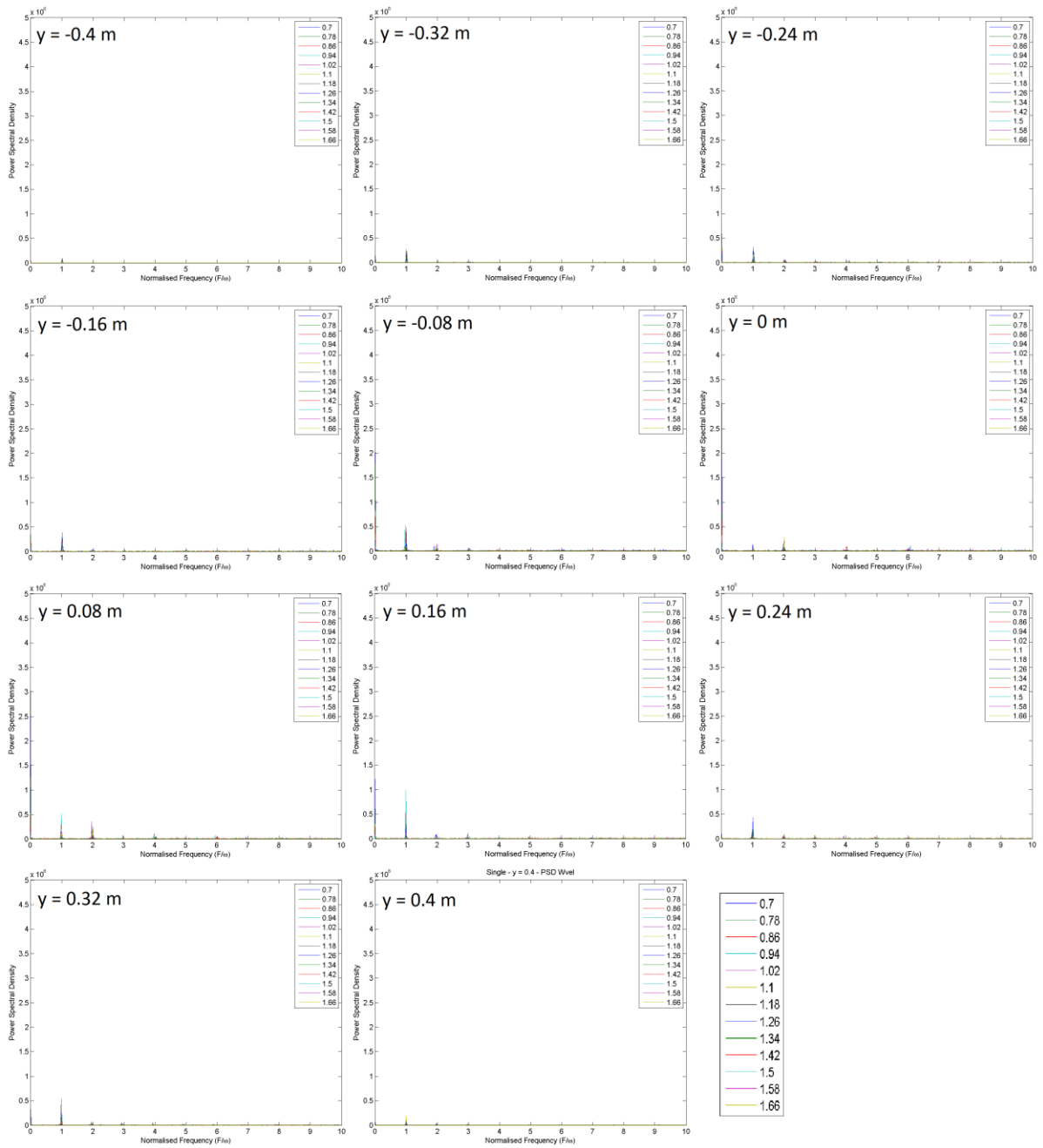


**Figure H.2** – Power spectral density of the vertical component of velocity (W) for each point in the interrogation window in the wake of a single pedalling cyclist. Data recorded with a cobra probe from discreet points in a wake survey. Series refer to vertical position with  $z = 0.7 - 1.66$  m.

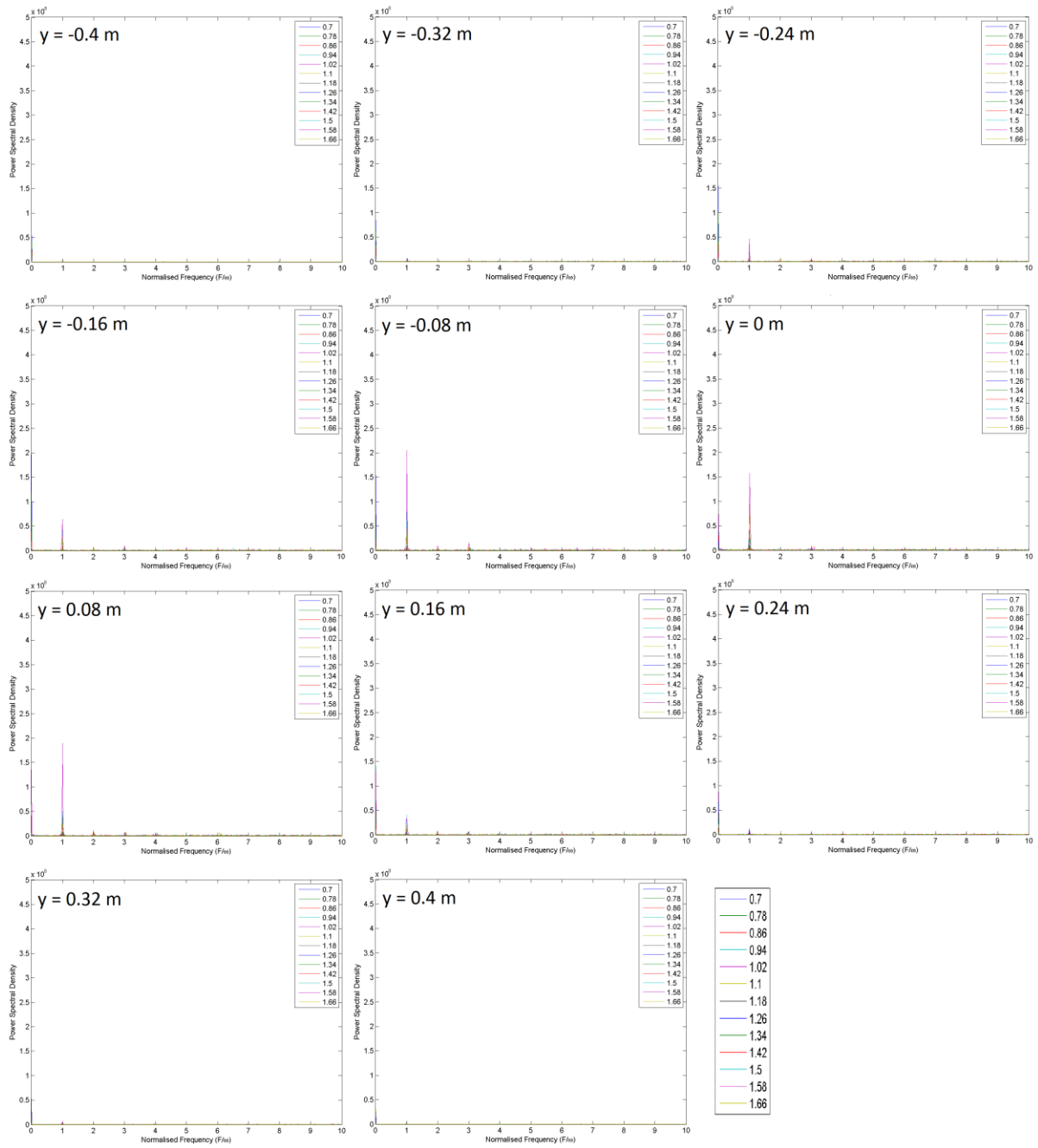


**Figure H.3** – Power spectral density of the spanwise component of velocity ( $V$ ) for each point in the interrogation window in the wake of a trailing pedalling cyclist in a tandem formation. Data recorded with a cobra probe from discrete points in a wake survey. Series refer to vertical position with  $z = 0.7 - 1.66$  m.

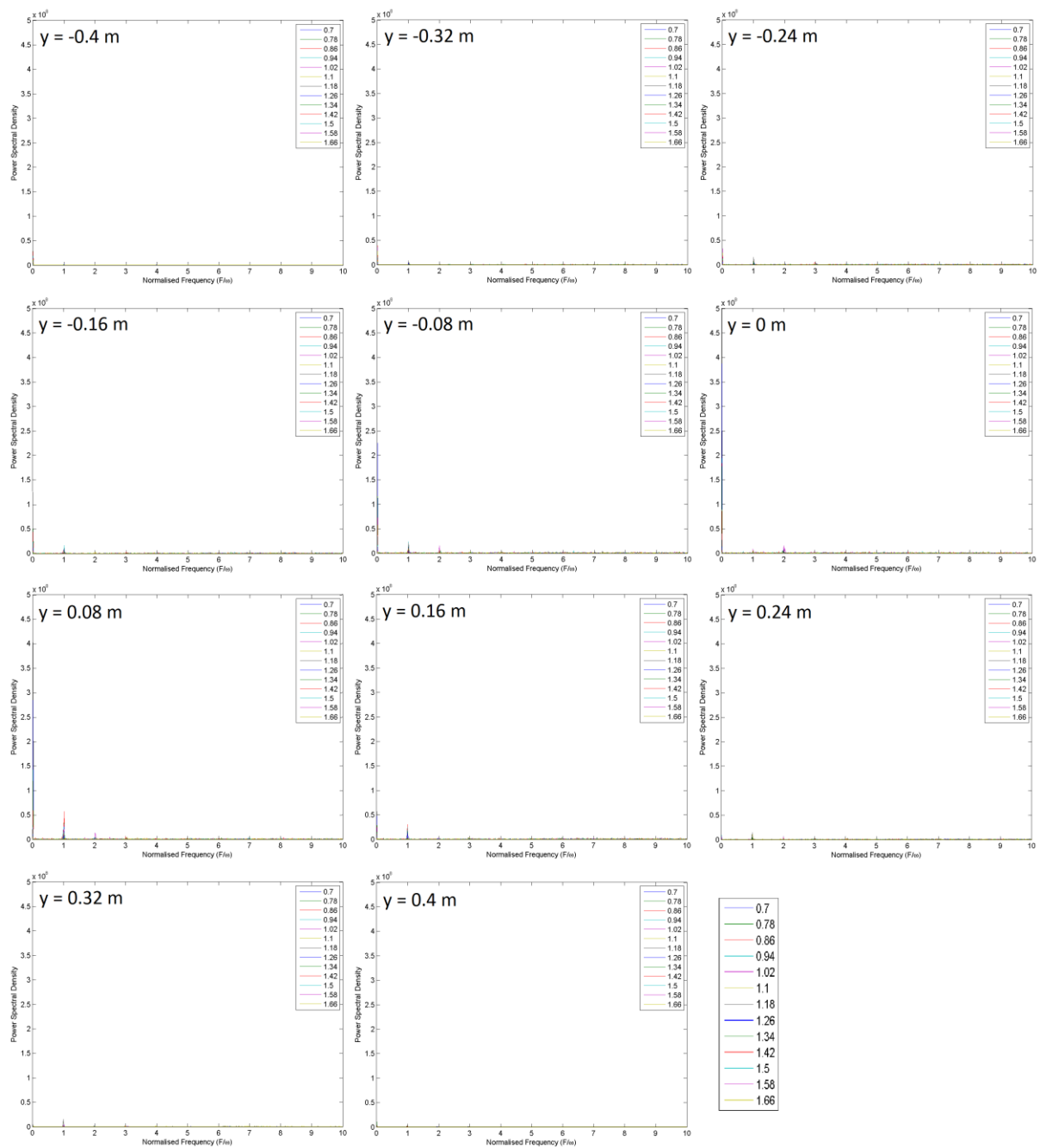


**Figure H.4** – Power spectral density of the vertical component of velocity ( $W$ ) for each point in the interrogation window in the wake of a trailing pedalling cyclist in a tandem formation. Data recorded with a cobra probe from discrete points in a wake survey. Series refer to vertical position with  $z = 0.7 - 1.66$  m.

## Appendix J: Phase Averaged Wake of a Pedalling Cyclist

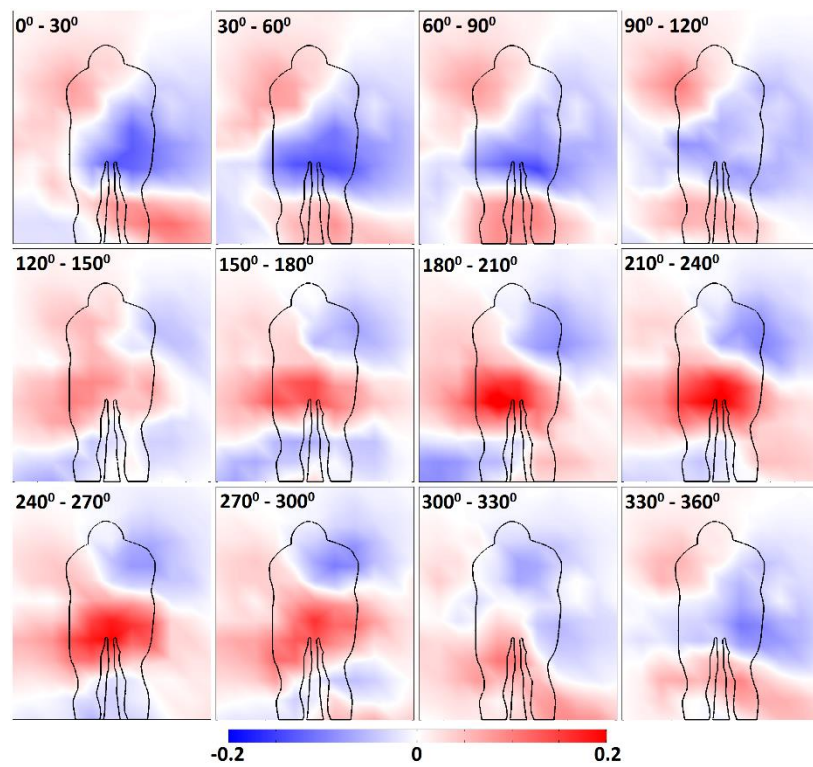


**Figure J.1** – Spanwise velocity ( $V$ ) in the wake of a single pedalling cyclist, phase averaged over  $30^\circ$  segments of the crank cycle

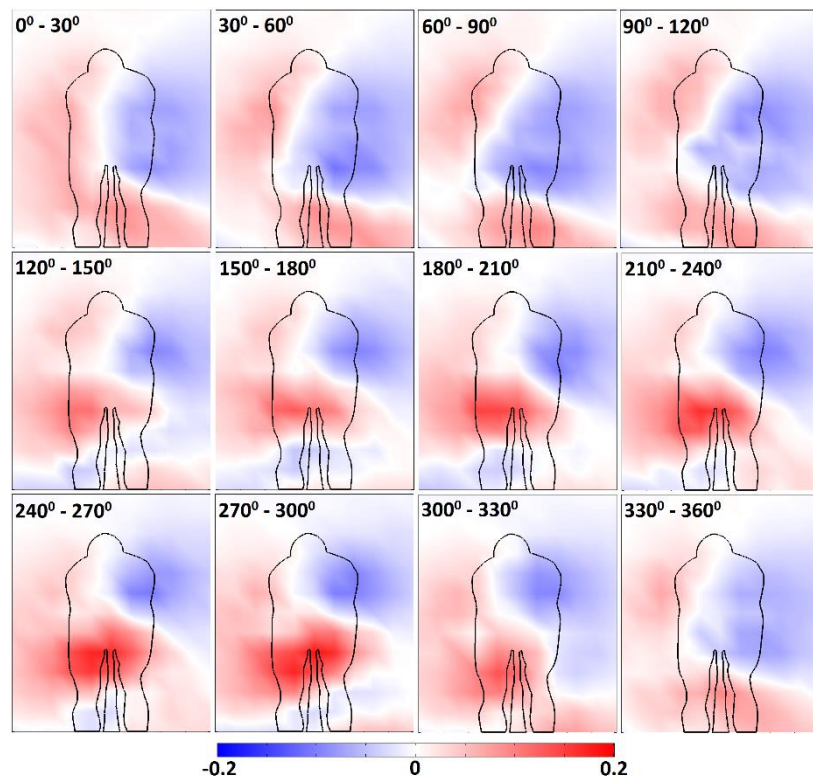


**Figure J.2** – Spanwise velocity ( $V$ ) in the wake of a trailing pedalling cyclist in a tandem formation, phase averaged over  $30^\circ$  segments of the crank cycle

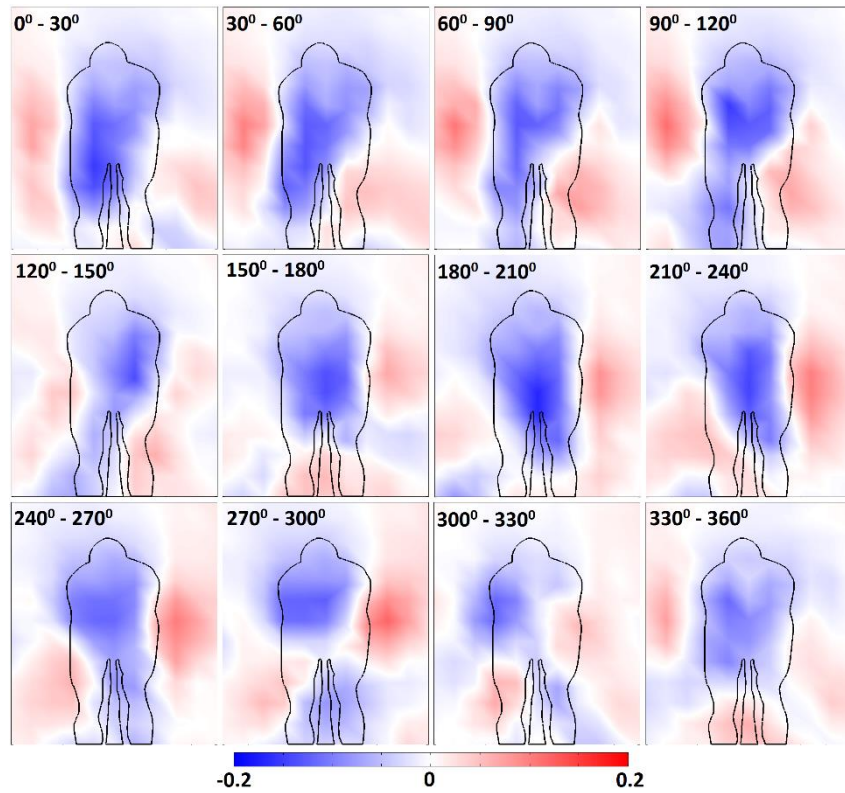


**Figure J.3** –Vertical velocity ( $W$ ) in the wake of a single pedalling cyclist, phase averaged over  $30^\circ$  segments of the crank cycle

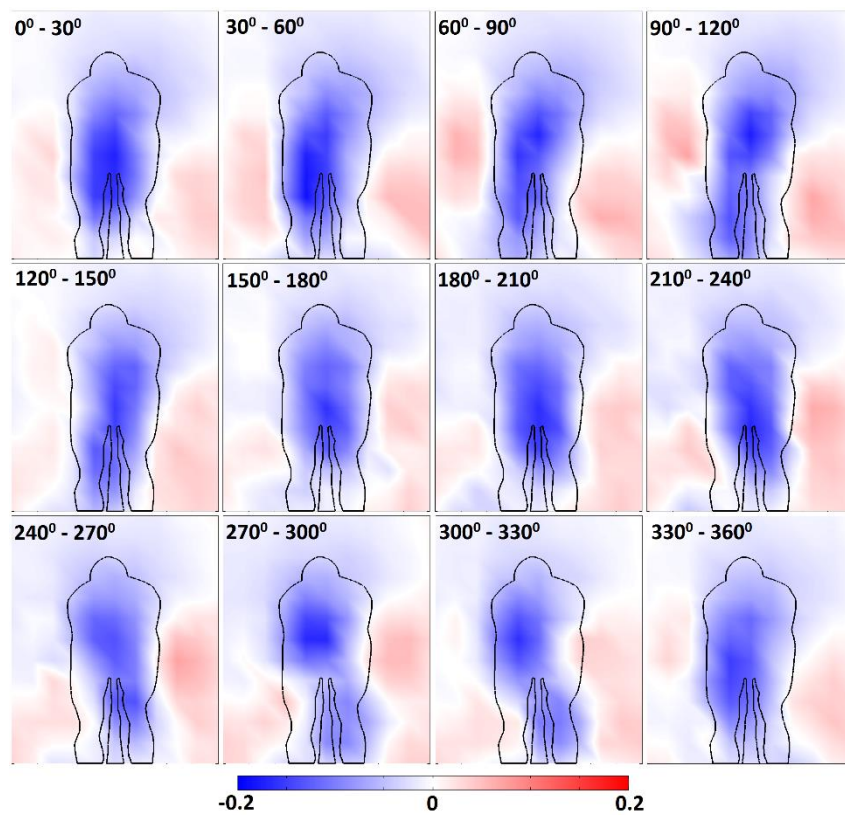


**Figure J.4** –Vertical velocity ( $W$ ) in the wake of a trailing pedalling cyclist in a tandem formation, phase averaged over  $30^\circ$  segments of the crank cycle

## Appendix K: The Effect of Posture on the Wake of a Cyclist

An investigation was conducted to investigate the influence of cyclist posture on cycling performance in road cycling and elite triathlon. Flow mapping was conducted in the wake of a dynamic cyclist by traversing a series of cobra probes in the wake. This process was similar to that described in Section 2.7.8. Athlete B was used as the cyclist but using a conventional draft-legal triathlon style setup. This involves a different bicycle (traditional road style), helmet and clothing to the time trial position used in other parts of this project. Four key postures were selected as representative postures used in road cycling and draft-legal triathlon. These are depicted in Figures K.1 and K.2 described in Table K.1.

**Table K.1** – Description of riding postures tested covering both cycling and draft-legal triathlon postures

	<b>Posture &amp; Description</b>	<b>Frontal Area (m<sup>2</sup>)</b>
1	Hands on hoods – reference posture	0.4941
2	Drops – conventional racing posture	0.4720
5	Hoods Grip –gripping brake hoods with horizontal forearms	0.4365
6	Aerobars – typical ITU draft-legal short aerobars	0.4174



**Figure K.1** - Front view of riding postures 1 -4 as listed in Table K.1 (above)



**Figure K.2** - Side profile view of riding postures 1 -4 as listed in Table K.1 (above)

The time averaged streamwise velocity profiles for the four postures are shown in Figure K.3 below and the normalised drag for each posture is reported in Table K.2. Given the symmetry of the time averaged dynamic wake only half the wake was captured.

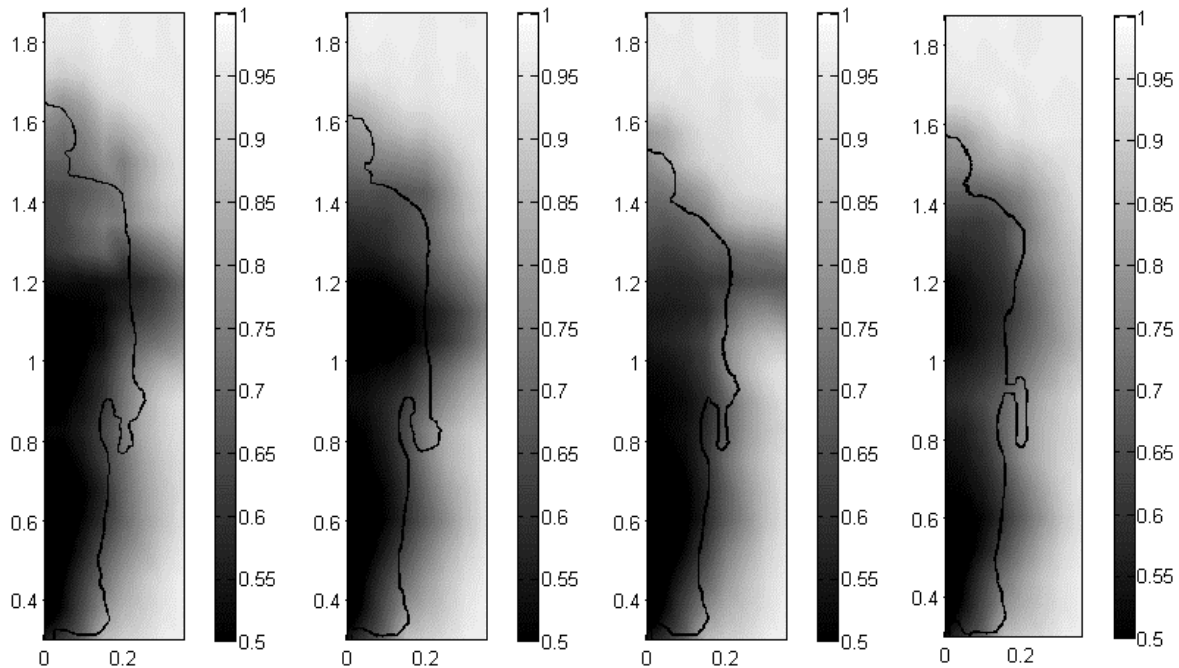


**Figure K.3** - Time averaged normalised streamwise velocity in the wake of a pedalling cyclist.

L-R: Postures 1 -4. Half wake shown with centreline at x=0.

**Table K.2**– Drag coefficient area and simulated power required for each posture (See Section 2.6.8) Delta values are for the change in  $C_{dA}$  referenced to Posture 1.

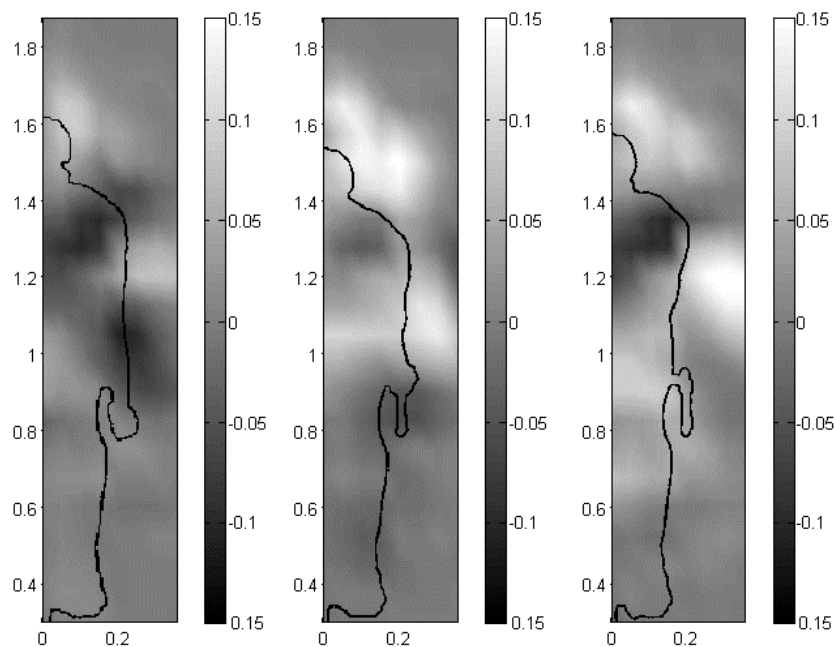
Posture	$C_{dA}$ ( $m^2$ )	Delta $C_{dA}$ ( $m^2$ )	Drag Saving (%)
1	0.343		
2	0.332	0.011	3.2
3	0.295	0.048	13.9
4	0.289	0.054	15.8

Dark regions in Figure K.3 indicate regions of velocity deficit from the freestream. It can be seen from the results that the centre of the wake in all cases contains the greatest velocity deficit. This is consistent with previous results for both the single and tandem results shown in Figure 5.4.1.

Moving from posture 1 to 4 the size of the high velocity deficit region decreases as the height and width of the rider silhouette is reduced. For postures 1 to 3 the riders head and shoulders are progressively lowered but arm position remains wide with the hands and elbows outside the width of the hips. As this happens the height of that primary velocity deficit region is reduced. Note that in lowering the head and shoulders the saddle and therefore hip height remains constant for all cases. In the case of Posture 4, the elbows are positioned inside the line of torso. The result is that the width of the low velocity wake region for Posture 4 is reduced as that isolated separation from the arms no longer persists downstream of the rider torso. To further highlight the differences in the wakes with

postural changes the wake of Posture 1 was used as a reference and subtracted from the other three cases (Figure K.4).

It is important to note that these results are captured over a different interrogation region to the results previously presented in Section 5.4. This was partly to accommodate the greater height of the athlete on this bicycle and in these postures. Due to the symmetry of the time averaged wake only one half of the wake is presented. The outline of the athlete is shown in each profile to highlight the difference in body posture in each frame. The previous data set presented for single and tandem cases were for athletes in a time trial posture and specific bicycle with faired helmets. These results utilise the same athlete (Athlete B), but on a road bicycle with conventional vented style helmet. Posture 4 is closest to the time trial posture in that the arms are inside the torso silhouette but a more upright position on the bicycle. Comparing the profile for Posture 4 with that of the single rider result from Figure 5.4.1, a strong degree of similarity is observed. Wake is widest at shoulder height and the lowest velocity occurs in the centre of the wake behind the hips.



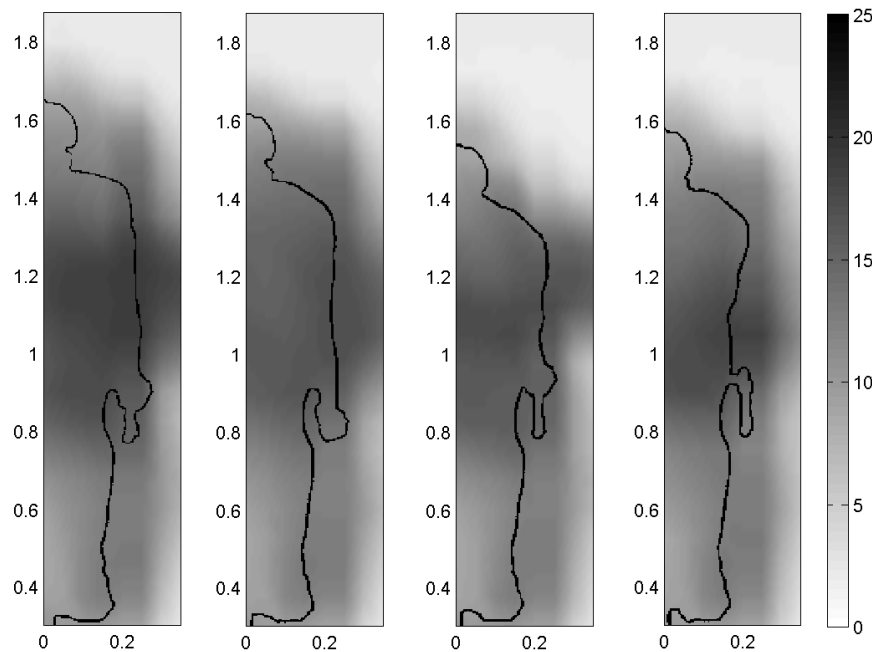
**Figure K.4** - Streamwise velocity difference; Streamwise velocity fields for (L-R) Postures 2, 3 and 4 after subtracting the velocity field of Posture 1

Figure K.4 shows the velocity difference between Postures 2-4 and Posture 1. Posture 1 is used as the reference as it is the most relaxed posture and also the highest drag case. Light regions in the profiles indicate where velocity is greater than measured in the Posture 1 wake. It can be seen that there are significant regions of higher velocity in the profiles of Posture 3 and 4; indicative of smaller energy loss.

By comparison, Posture 2 has only small changes compared to Posture 1. Some regions of higher velocity are evident, but there are also regions of lower velocity. This highlights just how sensitive the changes to the flow field are as a function of body shape and position. Net velocity change in the wake of the athlete at Posture 2 are significantly less than Postures 3 and 4 and this is reflected in the drag

measured for each position. Drag reductions of 3.2%, 13.9% and 15.8% were recorded for postures 2, 3 and 4 respectively, relative to Posture 1.

For Posture 4 there is a distinct region of lower velocity immediately behind the shoulder. This is likely the result of the change in the arm position. By moving the arms inside the line of the torso the presentation of the shoulder to the oncoming air is changed and a small local separation point is formed as a result.



**Figure K.5** - Turbulence intensity in the wake of a pedalling cyclist. L-R: Postures 1 -4. Half wake shown with centreline at  $x=0$ .

Figure K.5 shows the turbulence intensity in the wake of the athlete at Postures 1 to 4. The profile of Posture 4 exhibits a similar distribution to the single rider profile presented in Figure 5.4.6 for the athlete in the time trial setup with the highest turbulence intensity occurring in the centre of the wake behind the hips. Postures 1 to 3, which all have arms positioned wide of the hips, have a distinctly wider region of high turbulence. This is due to the localised separation from the arm, which convects downstream past the rider's hips and into the wake, rather than impacting on the front of the rider torso.

### Summary

It has been previously well established in literature that cyclist posture has a strong impact on their aerodynamic drag, and subsequently performance (Zdravkovich et al. 1996, Grappe et al. 1997, Gibertini and Grassi 2008, Gibertini et al 2008, Oggiano et al. 2008, García-López et al. 2008, Defraeye et al. 2010, Underwood et al 2011, Chabroux et al. 2012, Underwood and Jermy 2013). These results indicate that the change in drag arises due to the changing structure of the wake. From a performance standpoint, it can be stated that minimising the overall size of the wake region will have a positive

influence on cyclist drag; where the wake region is defined as the area of high velocity deficit and turbulence intensity. This can be achieved by lowering the cyclist's head and shoulders as well as bringing the elbows and arms inside the silhouette of the hips and torso.

If this result is considered in the context of multiple rider formations, it explains why the change in posture of one cyclist within a team can affect not only their own drag but also that of their team mates. As a cyclist changes their posture they also change the flow field around themselves. When riding in a team this will also alter the flow field around the team and the riders in close proximity. This is especially true of upstream riders as their wake effectively becomes the inlet conditions for the rider behind. However, understanding how the changes to the wake of one rider within a team formation will subsequently influence the surrounding riders requires a more detailed investigation and should be the subject of future work in this area.

The findings of this work have been published in Proceedings of the Institute of Mechanical Engineers, Part P: Journal of Sports Engineering and Technology (Barry et al. 2014).